MICROBEAM DESIGN IN RADIOBIOLOGICAL RESEARCH

A Thesis submitted for the degree of Doctor of Philosophy

by

Kevin John Hollis, B.Sc. M.Sc.

Department of Biology and Biochemistry, Brunel University

Cell and Molecular Biophysics Group, Gray Laboratory Cancer Research Trust

September 1995

Abstract

Recent work using low-doses of ionising radiations, both *in vitro* and *in vivo*, has suggested that the responses of biological systems in the region of less than 1 Gray may not be predicted by simple extrapolation from the responses at higher doses. Additional experiments, using high-LET radiations at doses of much less than one alpha particle traversal per cell nucleus, have shown responses in a greater number of cells than have received a radiation dose. These findings, and increased concern over the effects of the exposure of the general population to low-levels of background radiation, for example due to radon daughters in the lungs, have stimulated the investigation of the response of mammalian cells to ionising radiations in the extreme low-dose region.

In all broad field exposures to particulate radiations at low-dose levels an inherent dose uncertainty exists due to random counting statistics. This dose variation produces a range of values for the measured biological effect within the irradiated population, therefore making the elucidation of the dose-effect relationship extremely difficult. The use of the microbeam irradiation technique will allow the delivery of a controlled number of particles to specific targets within an individual cell with a high degree of accuracy. This approach will considerably reduce the level of variation of biological effect within the irradiated cell population and will allow low-dose responses of cellular systems to be determined. In addition, the proposed high spatial resolution of the microbeam developed will allow the investigation of the distribution of radiation sensitivity within the cell, to provide a better understanding of the mechanisms of radiation action.

The target parameters for the microbeam at the Gray Laboratory are a spatial resolution of less than 1 μm and a detection efficiency of better than 99 %. The work of this thesis was to develop a method of collimation, in order to produce a microbeam of 3.5 MeV protons, and to develop a detector to be used in conjunction with the collimation system.

In order to determine the optimum design of collimator necessary to produce a proton microbeam, a computer simulation based upon a Monte-Carlo simulation code, written by Dr S J Watts, was developed. This programme was then used to determine the optimum collimator length and the effects of misalignment and divergence of the

incident proton beam upon the quality of the collimated beam produced. Designs for silicon collimators were produced, based upon the results of these simulations, and collimators were subsequently produced for us using techniques of micro-manufacturing developed in the semiconductor industry. Other collimator designs were also produced both in-house and commercially, using a range of materials. These collimators were tested to determine both the energy and spatial resolutions of the transmitted proton beam produced. The best results were obtained using 1.6 mm lengths of 1.5 μm diameter bore fused silica tubing. This system produced a collimated beam having a spatial resolution with 90 % of the transmitted beam lying within a diameter of 2.3 ± 0.9 μm and with an energy spectrum having 75 % of the transmitted protons within a Gaussian fit to the full-energy peak.

Detection of the transmitted protons was achieved by the use of a scintillation transmission detector mounted over the exit aperture of the collimator. An approximately 10 μm thick ZnS(Ag) crystal was mounted between two 30 μm diameter optical fibres and the light emitted from the crystal transmitted along the fibres to two photomultiplier tubes. The signals from the tubes were analyzed, using coincidence counting techniques, by means of electronics designed by Dr B Vojnovic. The lowest counting inefficiencies obtained using this approach were a false positive count level of 0.8 ± 0.1 % and an uncounted proton level of 0.9 ± 0.3 %.

The elements of collimation and detection were then combined in a rugged microbeam assembly, using a fused silica collimator having a bore diameter of 5 μm and a scintillator crystal having a thickness of ~ 15 μm. The microbeam produced by this initial assembly had a spatial resolution with 90 % of the transmitted protons lying within a diameter of 5.8 ± 1.6 μm, and counting inefficiencies of 0.27 ± 0.22 % and 1.7 ± 0.4 % for the levels of false positive and missed counts respectively.

The detector system in this assembly achieves the design parameter of 99 % efficiency, however, the spatial resolution of the beam is not at the desired 1 μm level. The diameter of the microbeam beam produced is less than the nuclear diameter of many cell lines and so the beam may be used to good effect in the low-dose irradiation of single cells. In order to investigate the variation in sensitivity within a cell the spatial resolution of the beam would require improvement. Proposed methods by which this may be achieved are described.

Acknowledgements

It is with much pleasure that I thank Dr Barry Michael for his guidance, encouragement and enthusiasm throughout the experimental work involved in this project, and for his meticulous editing of this thesis. I am also indebted to Dr Steve Watts for his contribution to both the collimator simulation studies and his final edits to this work. In addition, my thanks to Dr Boris Vojnovic for his electronics expertise and stimulating discussions, and to Dr Melvyn Folkard, without whose excellent design skills this project would not have been possible. Thanks also go to the staff of the mechanical workshop, in particular Mr David Nash, for their machining abilities and patience in producing the apparatus designed for this project. I am also grateful to the staff of the Gray Laboratory for their friendship and support.

In addition I would like to thank my fellow PhD students and others for their camaraderie and to Mr Peter Russell for his financial support through my writing of this thesis.

This work was performed at the Gray Laboratory CRT, PO Box 100, Mount Vernon Hospital, Northwood, Middlesex, HA6 2JR and was funded by the Cancer Research Campaign and by grants from the Radiation Protection Action Programme of the European Community.

Contents

Chapter 1 : Introduction

1.1 Scientific Rationale

" Alpha-particle irradiation from radon progeny represents the largest source of effective dose to the general population of the United States (Miller et al., 1995) "

Human epidemiological studies of exposure to radon gas as a cause of increased cancer incidence give widely varying estimates of risk due to domestic exposure (Jacobi & Paretzke, 1985; Hofmann *et al.*, 1986; Bridges *et al.* 1991; Peto & Darby, 1994). However, *in vivo* laboratory experiments of radon breathing in rats shows a positive correlation for an increase in the numbers of pulmonary neoplasms with increasing concentration of radon inhaled (Chmelevsky *et al.*, 1982). The widespread exposure of large populations to low levels of radon gas may, by current risk estimates, be responsible for tens of thousands of cases of lung cancer in the United States alone (Brenner *et al.*, 1995). It is therefore imperative that further investigation of the risks resulting from exposure to low-doses of high-LET alpha-particles is undertaken.

In order to predict the biological effects of exposure to ionising radiations upon cells, and ultimately organisms, it is necessary to obtain both accurate experimental data concerning effects at relevant dose levels and to understand the complex mechanisms by which the effects of ionising radiation are mediated.

In the case of exposure to environmental levels of densely ionising radiation, for instance due to the inhalation of radon gas or exposure to high energy, high atomic number cosmic rays, it is highly unlikely that a cell will ever receive more than a single particle traversal during its life time (Brenner, 1993). This level of exposure corresponds to a dose of significantly less than 1 Gy. Data from exceptional cases of large numbers of people exposed to higher levels of ionising radiation, for instance atomic bomb survivors and uranium miners, have been used to attempt to predict the biological effects of low-dose level exposures to ionising radiation by back-extrapolation from the high-dose region. A complementary approach has been to use the broad-field irradiation of

cells in culture to quantify the effects resulting from these low-level exposures. Until recently however the high variation in the biological response of individual cells within a population, the random dose errors, and the low sensitivity of appropriate assays, have precluded attempts to quantify the dose-effect relationship at doses relevant to environmental exposure. Recently the use of improved assay systems, such as the single-cell analyzer imaging apparatus for cell survival (Marples & Joiner, 1993), have allowed *in vitro* experimentation at relevant dose-levels. The data obtained in these experiments suggest that back extrapolation from high-dose results to the low-dose region does not provide an accurate assessment of the cancer risk.

Low-LET radiations have been used with an automated single-cell survival assay and demonstrate a hypersensitive response in several cultured cell lines exposed to doses of less than 0.6 Gy of X-rays (Marples & Joiner, 1993; Lambin *et al.*, 1993; Singh *et al.*, 1994), showing that the linear quadratic fit extrapolated back to the low-dose region will underestimate the level of cell kill. In addition, James *et al.* (1991) have found that mice irradiated with 12 fractions of 0.04 Gy of γ-rays at 2 day intervals show a reduced number of double strand breaks in extracted spleen cells. Both these results suggests low-dose responses that could not be predicted from high-dose experiments.

High-LET radiations have also been used to demonstrate responses in the low-dose region which could not be predicted from results at higher doses. The yield of sister chromatid exchanges by α-particle irradiation has been shown to be higher in the low-dose region, at less than 0.1 Gy, than at higher doses (Nagasawa *et al.*, 1990). Further, if calculation of the number of particle traversals per cell nucleus is performed, the production of sister chromatid exchanges can be shown to occur in cells whose nuclei received a zero radiation dose (Nagasawa *et al.*, 1990; Nagasawa *et al.*, 1991; Nagasawa & Little, 1992). In agreement with this data is that of Hickman *et al.* (1994) showing an increase in the expression of p53 protein in significantly more cells than have suffered nuclear alpha-particle traversals. These data suggest the possibility of the transmission of biological effects between irradiated and unirradiated cells and therefore add further complication to the estimation of environmental radiation risk.

Additional chromosomal effects produced by high-LET radiations at low-dose have been found by Kadhim *et al.* (1992), showing a high frequency of non-clonal chromosome aberrations in the colonies formed from cells which have survived alpha particle traversals. This data suggest the possibility of the transmission of chromosomal instability from an irradiated parent cell to unirradiated daughter cells and therefore not only the irradiated cell but also its progeny must be considered in the assessment of radiation risk. The work of Thacker *et al.* (1988), showing an increase in the number of *hgprt*-deficient mutants by high-LET exposure, of Bettega *et al.* (1992), showing a super-linearity in the occurrence of oncogenic transformation by exposure to low-doses of α-particles, and of Martin *et al.* (1995), showing a maximum risk of transformation at 0.01 Gy for 90 keV μm^{-1} alpha-particles, suggest that back-extrapolation from the high-dose to the low-dose region may underestimate the real oncogenic risk from environmental exposure to high-LET radiations. The development of novel techniques to investigate the dose region below one Gray is therefore of critical importance in the determination of the oncogenic risk posed by environmental exposure.

In all broad field exposure to particulate radiation at low-dose levels an inherent dose error exists due to random counting statistics. For example, if a population of cells in culture are exposed to an average of one ^{210}Po α-particle traversal per cell (equivalent to ~ 0.4 Gy) then the Poisson distributed variation in particle traversals predicts that 37 % of the cells will receive no particles at all, 37 % will receive a single traversal and 26 % of the cells will receive two or more particle traversals, see Figure 1.1. Clearly the variation in the dose received by each cell will result in an increase in the variation of the biological response observed, and will therefore complicate the determination of the dose-effect relationship. In simple systems mathematical deconvolution methods may be used to elucidate a dose-effect relationship (Brenner, 1993), however, the complex interactions involved in biological systems prevent this approach giving a reliable prediction of biological effects.

The use of the microbeam irradiation technique will allow the delivery of a controlled number of particles to a specific target within an individual cell with a high degree of accuracy. The development of such a facility at the Gray Laboratory will enable low-doses of particulate radiation to be delivered to cells in such a way that no significant

dose variation exists within the population of irradiated cells. The accurate control of the delivered dose will allow the investigation of biological responses at levels relevant to environmental exposure without the inherent statistical uncertainty involved in broad field irradiations.

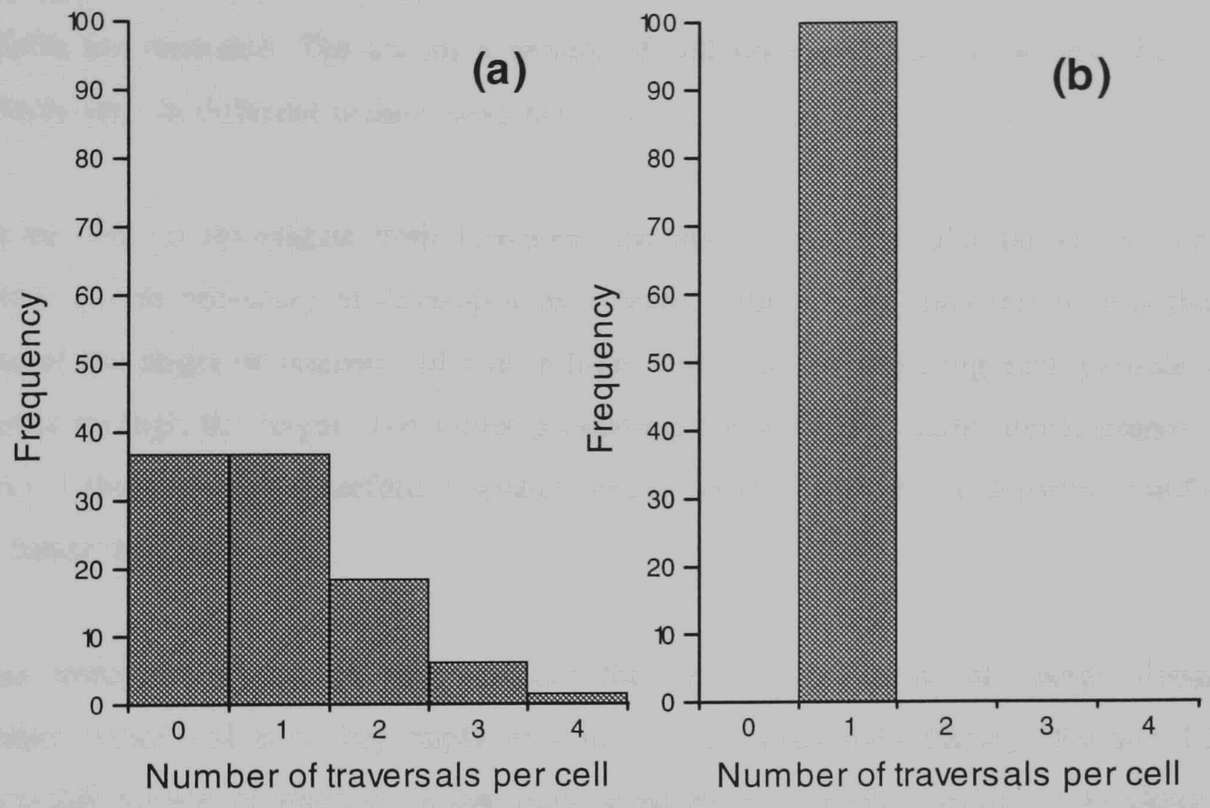

Figure 1.1 The distribution of particle traversals for an average of one particle per cell (**a**) using a broad-field, random, exposure and (**b**) using the microbeam irradiation technique.

In addition to quantifying the biological response of cells at low-dose levels it is necessary to understand the mechanisms by which the effects of radiation are mediated. One element in understanding these mechanisms is to elucidate the distribution of radiation sensitive sites within the cell. Further knowledge of the radiation sensitive sites within cells may also allow an improvement in the application of intra-cellular targeted radiotherapy treatments, such as immuno-targeting of Auger emitters to cancer cells and boron neutron capture techniques.

The notion of using a microbeam to investigate radiation sensitive targets within the cell is not a new one. As early as 1912 Tschachotin developed a focused ultraviolet light microbeam to investigate the distribution of radiation sensitivity within plant cells and considerable work was produced by Zirkle and others in the 1950's using both ultraviolet light and particulate microbeams. The distribution of radiation sensitive sites within the

cell remains a critical question which may be answered using the current generation of microbeams. The historical background of microbeam work into this question, along with questions raised by recent work in other fields, will be considered in Section 1.2. Using a microbeam approach it will be possible to investigate not only the effects of the localised irradiation of sub-cellular elements but also the mechanisms by which these effects are mediated. The use of a variety of cell lines will also show how the various effects vary in different cellular systems.

To be able to investigate both low-dose response and sub-cellular targets of radiation action it was necessary to develop a microbeam with a beam diameter of less than the size of the target of interest and with a high confidence of detecting each particle which passes through the target. The target parameters for the beam under development at the Gray Laboratory are therefore a spatial resolution of 1 μm and a detection confidence of better than 99%.

This introductory chapter will consider the physical processes of energy deposition within matter and how they apply to a microbeam irradiation facility (Section 1.3). A historical review of previous microbeam apparatuses is given (Section 1.4) along with a consideration of the recent advances in technology which have permitted a new generation of microbeam facilities to be constructed (Section 1.5). These recently developed facilities will be considered (Section 1.6), with a more detailed description of the Gray Laboratory microbeam (Section 1.7).

The work described in this thesis was to develop both the collimation and detection systems for the Gray Laboratory microbeam and to assemble these elements into a single unit capable of irradiating biological samples. Chapter 2 will describe the development of a Monte-Carlo style computer simulation programme and its use in the modelling of the performance of various collimator designs. The results of this work have allowed the design of commercially manufactured silicon collimators. These and other types of collimator were developed and are described in Chapter 3 with an analysis of the performance of each approach. The development of a highly efficient particle detector was also necessary for the production of a microbeam facility. The materials available for the production of a transmission proton detection system are discussed in Chapter

4 followed by a description of the design and development of an operational detector system in Chapter 5. The combination of the elements of collimation and detection into a functional microbeam assembly is described in Chapter 6 with an analysis of the microbeam performance obtained. Possible improvements to the design of the current microbeam assembly are then discussed in Chapter 7.

1.2 Determining the Radiation Sensitive Sites Within the Cell

The investigation of regions of cellular sensitivity has been a common aim of many experiments conducted using localised irradiation. Data have been obtained using several approaches and have produced information concerning a range of physiological endpoints. A review of some of this work, with an emphasis on previous microbeam work, into this critical question is presented here.

1.2.1 Microbeam irradiation

1.2.1 (a) Nuclear effects by nuclear irradiation

Since the assessment of biological endpoints using early microbeams was almost exclusively by observations made using visible light microscopy, much of the work involving nuclear irradiation has been performed on metaphase, condensed chromosomes. Two physiological effects which have been shown by several authors to result from cell irradiation are the production of DNA strands between daughter cells (chromosome bridges) and failed separation of chromosomes at mitosis (stickiness in anaphase). Zirkle & Bloom (1953) found this effect could be produced by irradiating prophase chromosomes with a few dozen protons and Bloom (1959) later demonstrated that the dose required to produce chromosome stickiness was approximately 20 protons delivered to two chromosomes whereas the dose required to produce chromosome bridges was three times this amount. Haynes (1961 *see refs within* Smith, 1964) also produced chromosome stickiness and bridges in metaphase chromosomes but using alpha particles at a flux of 15 particles μm^{-2}. The more extreme effect of chromosome condensation and clumping was also demonstrated using particle irradiation localised at the metaphase plate, by Smith (1959 *see refs within* Smith, 1964) using a range of doses of α-particles and by Davis & Smith (1957) with a much lower dose of ~ 4 α-particles at the same site. In addition, these experiments often showed deterioration in the function of the centrosome (Zirkle & Bloom, 1953; Davis & Smith, 1957) leading to irregularities at anaphase and formation of micronuclei if chromosome fragments were sufficiently separated from the rest of the genome (Bloom, 1955 *see refs within* Zirkle, 1957; Uretz *et al.*, 1954). Other experiments have shown similar effects using ultraviolet

light irradiation (Izutsu, 1961 *see refs within* Smith, 1964; Zirkle, 1953; Bloom, 1955 *see refs within* Zirkle, 1957). Irradiations using both particles (Uretz *et al.*, 1954) and U.V. light (Zirkle, 1953; Bloom, 1955 *see refs within* Zirkle, 1957) to the nuclear sap failed to show these chromosome effects.

A more direct form of chromosome damage has been demonstrated by Berns *et al.* (1969) using an argon laser and acridine orange sensitising dye. In these experiments chromosome breaks were produced on specific chromosome arms and lead to fragmentation at anaphase.

Another visible form of chromosome damage has been demonstrated to occur by ultraviolet irradiation of localised regions of metaphase chromosomes (Zirkle, 1953, 1956 *see refs within* Zirkle, 1957; Zirkle 1960 *see refs within* Smith, 1964; Uretz *et al.*, 1954, 1958; Perry, 1957; Bloom & Leider, 1962). The effect was observed under phase contrast microscopy as a paling of the chromosome at the site of irradiation followed by a spreading of the pale region along the chromosome. A decrease in the absorption of U.V. at the DNA absorption band around 260 nm has been shown, using U.V. spectroscopy, (Perry, 1957; Zirkle, 1957, 1960; Bloom, 1960a, 1960b; Brown & Zirkle, 1967) suggesting a loss of DNA-like material at the irradiation site. This was supported by a reduction in Feulgens staining in the paled region (Bloom, 1960a), even though the chromosome still had a continuous structural element as shown by calcium phosphate staining (Amenta, 1961 *see refs within* Smith, 1964; Bloom & Leider, 1962; Bloom, 1960a). The action spectrum for this effect peaks outside of the nucleic acid absorption region of 225 - 300 nm (Zirkle, 1960; Uretz & Zirkle, 1958 *see refs within* Smith, 1964) suggesting that direct DNA absorption of ultraviolet radiation was not responsible for the DNA steresis. Later work shows the opposite effect for higher order HeLa cells with increased optical density under phase contrast microscopy, increased Feulgens staining, and increased absorption at DNA/RNA wavelengths, suggesting an increased coiling or aggregation of the DNA (Naruse *et al.*, 1967).

The endpoint of mitotic delay was also observed to occur as a result of nuclear irradiation using both particles (Smith, 1959; Haynes, 1961 *see refs within* Smith,1964), U.V. light (Gaulden & Perry, 1958; Gaulden, 1960 *see refs within* Smith, 1964) and laser

radiation at 442 nm (Lin & Chan, 1984). Work by Carlson *et al.* (1961 *see refs within* Smith, 1964) showed that for U.V. this phenomenon was dose dependent and also demonstrated mitotic acceleration, rather than inhibition at low-doses. More detailed studies of the sensitive sites for this particular endpoint have been performed using both U.V. laser irradiation (Hatfield *et al.*, 1973) and argon laser irradiation (Ohnuki *et al.*, 1972; Berns, 1971). The work showed that either the nucleolus or near nucleolar chromosomes could be used to induce mitotic delay whereas nucleoplasmic or random chromosome irradiations were ineffective.

The nucleolus was also implicated in DNA/RNA synthesis using U.V. (Hatfield *et al.*, 1973), X-ray (Seed, 1960) and α-particle (Smith, 1961; 1962 *see refs within* Smith, 1964) microbeam irradiation by observing the effect of irradiation on ^{3}H-UdR uptake in the cells.

1.2.1 (b) Nuclear effects by cytoplasmic irradiation

The most commonly noted nuclear effect induced by cytoplasmic irradiation was that of spindle destruction by ultraviolet light leading to either abnormal or failed anaphase (Brown & Zirkle, 1967; Zirkle & Bloom, 1953; 1957; 1959; 1960; Bäjer, 1961; Geyer-Duszynska, 1959; 1961; Izutsu, 1961 *see refs within* Smith, 1964). Failed formation of the spindle was also observed if the cytoplasm was irradiated in prophase (Bloom *et al.*, 1955, 1956). Using ultraviolet spectroscopy the action spectrum for this effect has been shown to correspond to a protein-like component (Carlson & McMaster, 1953 *see refs within* Gray, 1956; Brown & Zirkle, 1967; Zirkle, 1960). Bloom (1959) also showed this effect using protons although the dose required, > 10^{6} particles, was exceptionally high.

Additional work by Zirkle (1970) showed that it was also possible to induce mitotic delay by cytoplasmic irradiation using U.V. light and Dendy (1961, 1962 *see refs within* Smith, 1964) has been able to demonstrate a reduction in DNA synthesis by cytoplasmic irradiation.

1.2.1 (c) Cytoplasmic/membrane effects by cytoplasmic/membrane irradiation

The most commonly reported cytoplasmic effect due to localised irradiation is that of blebbing and bubbling in the cytoplasm producing a local area of altered refractive index, and often sloughing off of cytoplasm (Uretz & Zirkle, 1957; Tschachotin, 1935, 1936 *see refs within* Zirkle, 1957). Jagger *et al.* (1969) showed, using high doses of ultraviolet irradiation, that sloughing off of pieces of cytoplasm leads to a long division delay and more recently these blebs have been shown to contain very high concentrations of Ca^{2+} ions (Trap & Berezesky, 1992).

Using laser microbeam irradiation it has also been possible to irradiate sub-cellular organelles. Kitzes *et al.* (1977) has shown that the irradiation of a single mitochondrion using an argon laser microbeam can change the membrane surface potential and the contractile response of rat myocardial cells.

1.2.1 (d) Cytoplasmic/Membrane Effects by Nuclear Irradiation

Again cytoplasmic blebbing has been reported to occur as a result of the irradiation of metaphase chromosomes by alpha particles (Smith, 1959 *see refs within* Smith, 1964; Haynes & Zirkle, 1961; Davis & Smith, 1957) . Targeting only the nucleolus has also been attempted and shows reduced amino acid uptake into the cytoplasm (Errera *et al.*, 1960) and reduced cytoplasmic RNA content (Perry, 1960).

1.2.1 (e) Direct comparison of nuclear and cytoplasmic sensitivity

Perhaps the earliest microbeam work addressing the question of the relative radiation sensitivities of the nucleus and cytoplasm was that of Tschachotin in 1920 (*see refs within* Zirkle, 1957) using a 5 μm diameter ultraviolet microbeam. The biological endpoint investigated was that of halting division in a sea-urchin blastomere. He found that division could be halted by a fixed exposure time if given to the nucleus, however, even double the dose given to the cytoplasm did not effect division. Using the metabolic endpoint of oxygen consumption however Tschachotin (1937 *see refs within* Zirkle, 1957) found that cytoplasmic irradiation reduced oxygen consumption whereas nuclear

irradiation showed no effect.

Using the endpoint of spindle destruction, Brown & Zirkle (1967) have shown that for ultraviolet radiation the dose required for either nuclear or cytoplasmic irradiation was the same. For an incident beam of protons however the same experimenters (Zirkle & Bloom, 1953) found no cytoplasmic effect upon the spindle even for thousands of particle traversals. Only the extreme dose of $> 10^6$ protons to the cytoplasm has been shown by Bloom (1959) to produce spindle destruction.

In agreement with the result of Tschachotin for the end-point of oxygen consumption, Errera & Vanderhaeghe (1957) has found the result that for the endpoint of protein production, the cytoplasm is more sensitive to U.V. light than either the nucleus or whole cell exposures.

The endpoint of DNA synthesis has been investigated by both Smith (1961; 1962 *see refs within* Smith, 1964) and Kuzin & Wainson (1966) in HeLa cells using α-particle microbeam irradiation. Smith found that the reduction of DNA synthesis could be achieved by either nuclear sap or nucleolar irradiation whereas cytoplasmic irradiation had no effect. The work of Kuzin & Wainson was more quantitative and showed that the nucleus was ten times more sensitive for this endpoint than the cytoplasm.

A modification to the U.V. light microbeam of Perry (1960) has been used by Jagger (Jagger *et al.*, 1969) to investigate the effects of ultraviolet light on division delay, cell kill and RNA synthesis in amoeba. The critical modification in this case was that rather than irradiating only a small part of either the nucleus or the cytoplasm Jagger used a beam larger than the size of the cell but with a nucleus obscuring element in the primary aperture, for cytoplasmic irradiation, and a primary aperture irradiating a large part of the nucleus and no cytoplasm, for nuclear irradiation. He found that nuclear irradiation could prevent RNA synthesis for up to 22 hours whereas cytoplasmic irradiation did not produce this effect. For the endpoint of cell kill however, Jagger found that an equal surface dose (Joules mm^{-2}) to either the nucleus or the cytoplasm produced an equal effect. Furthermore for the endpoint of division delay he found that the nucleus was six times less sensitive than the cytoplasm and that whole cell irradiation was more effective

than either nucleus or cytoplasm individually. Jagger also demonstrated that for the irradiation of the cytoplasm with a single field of the same size as that used for nuclear irradiation the dose required to induce an equal division delay was higher than that for the nucleus, demonstrating that not only the energy deposited but also the distribution of energy deposited within the target is critical in determining biological effect.

1.2.2 Partially penetrating particles

The use of a differential energy distribution within a biological target, resulting from partially penetrating radiation, was used as early as 1932 by Zirkle to investigate radiation sensitive sites. Much of this work has been carried out using ^{210}Po alpha particle sources due to the convenient range of the emitted α-particles, ~ 38 μm in muscle tissue (Ziegler & Biersack, 1985), however, electrons and the attenuation of soft X-rays through the target have also been used.

1.2.2 (a) Alpha particles

The early work of Zirkle (1932) was carried out using fern spores irradiated by a broad beam of partially penetrating alpha particles. He concluded that the inhibition and delay of the first division, inhibition of normal swelling and inhibition of chlorophyll production were all biological effects resulting from nuclear and not cytoplasmic irradiation. Petrova (1942 *see refs within* Zirkle, 1957) also found that in green algae cells uptake of urea and inorganic salts could only be reduced by nuclear and not by cytoplasmic irradiation, although cytoplasmic irradiation could produce cell kill at very high doses. Rogers & von Boerstel (1957; von Boerstel & Rogers, 1958) irradiated either the nuclear or cytoplasmic ends of *habrobracon* eggs. They found that for the endpoints of hatchability and cell death the nucleus was 10^6 times more sensitive than the cytoplasm.

The largest body of work in this field is that of T R Munro. Using ^{210}Po coated microneedles with different, but well defined, ranges for each needle, he was able to irradiate hamster and chick fibroblasts on a single cell basis and to observe the effects of the irradiation of different parts of the cell. Because of the time consuming irradiation

procedure each experiment involved only a few tens of cells. In addition, the geometry was approximately that of a point-like source close to the target and so the energy deposited at a given distance from the needle varied not only by the particle energy loss through the target material but also as 1/(distance)^2 from the needle. Munro investigated the dose relationship for the chromosomal endpoints of bridge formation, stickiness, clumping and failure of mitosis (Munro, 1958, 1959, 1961) and the production of division delay (Munro, 1970) and showed that even a dose of 250 - 1000 Gy given to the cytoplasm would not induce a division delay.

Later work of Cole (Datta *et al.*, 1976) found that if experimental data from the irradiation of CHO cells by ^{241}Am α-particles, was correlated with a computer modelled system, then a radiation sensitive region at 3μm into the cell, near the nuclear membrane, could be predicted. Raju *et al.* (1993) used the approach of calculating the energy deposited by α-particles in the nucleus of a number of cell lines having different geometries and found a correlation between cell kill and the energy deposited within the nucleus. There was however no suggestion of a radiation sensitive region near the nuclear membrane.

1.2.2 (b) Electrons

Irradiation of cells under vacuum by 1.5 to 90 keV electrons with corresponding penetrations of 0.07 to 125 μm has been used by Cole (1969; Cole *et al.*, 1969, 1974; Zermeno & Cole, 1969; Tobleman & Cole, 1974) to investigate the radiation sensitive sites in CHO and other cell lines. The comparison of a computer modelled system with experimental data suggested a highly sensitive thin layer inside of the nuclear membrane. He also noted that the response to 50 keV electrons was a low-LET type shouldered survival curve whereas for 10 keV electrons, having a range of ~ 2.4 μm, the response was a high-LET type with no oxygen enhancement of damage. This high-LET response at ~ 2.4 μm into the cell again suggests a highly radiation sensitive site near the nuclear membrane.

1.2.2 (c) Soft X-rays

Although soft X-rays do not have a defined range as exists for charged particles their

attenuation in biological material can be used to produce an energy deposition pattern which differentially irradiates one part of a target over another. Cornforth *et al.* (1989) used this property with various cell lines of differing geometries to demonstrate that the survival data obtained could be better fitted by using the dose to the nuclear volume rather than the entrance dose. However he suggested that further improvement could be made to the fit if only part of the nucleus was considered to be sensitive.

Mackie *et al.* (1993) used the property of iso-attenuation at two different X-ray energies to produce equal dose-depth distributions, but with differing secondary electron energies, which results in different locations within the cell for the highly damaging electron track ends. Using this approach did not demonstrate a significant difference between the two energies of radiation. Future work to determine target distribution will be attempted by shielding part of the nucleus using a banded structure across the cell. Irradiation of whole cells and of double the dose to half the cell will be performed and comparison made with physical models of radiation sensitivity.

1.2.3 Impact parameter

The culturing of plant spores on track etch plastic has been used to compare the effects of the distance from the centre of the spore at which a particle passes, the impact parameter, with the inactivation of the spore. This approach has been used in the BIOSTACK series of experiments on the Apollo space craft to investigate the effects of high energy heavy ions to which astronauts are exposed (Facius *et al.*, 1978). The impact parameter can be measured to an accuracy of 0.2 μm from the spores, which have a cytoplasmic core of only 0.22 μm^2. The results suggested two modes of inactivation, indicated by a change in the slope of the dose-survival curve at an impact parameter of ~ 1 μm. In addition, some inactivation was found even at impact parameters as large as 5 μm, even though the range of the secondary electrons produced in this case would not reach the inactivated spore. A proposed theory for the mechanism of this interaction is damage to the spore membrane by a shock wave as a result of the passage of the particle. These data have been reproduced in terrestrial experiments, using irradiation by heavy ions produced by a particle accelerator (Facius *et al.*, 1983) and show that even for a direct core hit the inactivation remains less than one, casting doubt

on the overkill hypothesis of radiation damage. Single-ion irradiation experiments have also been performed using accelerated heavy ions produced by the Darmstadt microbeam (Weisbrod *et al.*, 1992) and again show an inactivation probability of less than one for a direct hit to the core of the fern spore.

1.2.4 Radioisotope labelling

By the radio-labelling of certain biological molecules which bind to specific sub-cellular elements it is possible to produce highly localised irradiation at specific sites within the cell. A commonly used approach has been to use ^{125}Iodine which deposits 99% of its energy within a 40 nm radius (Hofer *et al.*, 1992). Dosimetry of the total isotope content of the cells can be made using gamma detectors and then computer simulations made to calculate the dose to the various cellular compartments, based on assumptions about the location of the radioisotope. One early example of the use of this approach was that of Marin & Bender (1963), using tritiated thymidine and its analogue uridine. They postulated that the ^{3}H-thymidine would be incorporated into the nuclear DNA at mitosis whereas the ^{3}H-uridine would be RNA incorporated throughout the cell cycle. Having calculated the dose received by the nucleus in each case they proposed that the difference in cell kill for equal nuclear dose which existed between the two cases must define the cytoplasmic contribution to radiation sensitivity.

Warters & Hofer (1977; Warters *et al.*, 1977) has used ^{125}Iodine labelled uridine deoxyribonucleic acid (^{125}I-UdR), tritiated thymidine (^{3}H-Thy) and ^{125}Iodine labelled concanavalin-A (^{125}I-ConA) to study cell death and division delay in CHO cells. These molecules selectively bind to either DNA (^{125}I-UdR & ^{3}H-Thy) or the plasma membrane (^{125}I-ConA) of the cells. The resulting cell kill was assessed using LD_{50} values from dose-survival curves. The data are summarised below :-

^{125}I-UdR	LD_{50} = 60	decays/cell	=	0.45	Gy @ DNA
^{3}H-Thy	LD_{50} = 1,350	decays/cell	=	3.8	Gy @ DNA
^{125}I-ConA	LD_{50} = 19,600	decays/cell	=	520	Gy @ membrane
				25	Gy @ cytoplasm
				4.1	Gy @ nucleus

By comparison with external X-rays (LD_{50} = 3.3 Gy) it can be seen that both membrane bound ^{125}I-ConA and DNA bound ^{3}H-Thy show similar cell kill for an equal dose to the nucleus, whereas the DNA bound ^{125}I-UdR shows a much higher biological effectiveness. A similar correlation was found between ^{125}I-ConA and external X-rays for the endpoint of division delay using the calculated dose to the nucleus.

^{125}I-UdR and ^{3}H-Thy have also been used by Hofer *et al.* (1975) to irradiate DNA within L1210 leukaemia cells in live mice with ^{67}Gallium citrate used to produce localised cytoplasmic irradiation. Cell death was measured by the trace amounts of ^{125}I excreted in the urine from the breakdown of dead cells and again shows ^{125}I to be the most effective isotope of the three. Later work (Hofer *et al.*, 1992) shows that the DNA bound ^{125}Iodine shows a high-LET type response whereas ^{125}Iodine bound to the plasma membrane, lysosomes, mitochondria or general cytoplasm all resulted in a shouldered survival curve characteristic of low-LET type radiation. In addition, Hofer demonstrated that after mitosis the cell becomes gradually more sensitive to DNA bound ^{125}Iodine, perhaps through an increased sensitivity of the DNA as it matures or an association of the DNA with a sensitive target, for example the nuclear membrane.

1.2.5 Observations suggesting non-DNA targets for radiation damage

In addition to these directly targeted approaches to the investigation of radiation sensitive sites there also exist more mechanistic studies suggesting that sites other than DNA may be critical in determining the response of cells to ionising radiation. Szekely *et al.* (1980) showed that the electrophoretic mobility of the membrane could be reversibly altered by X-ray doses of up to 5 Gy and irreversibly altered by higher doses. Rink (1975) has shown that the oxidation by ionising radiation of sulphydryl groups bound to membranes causes changes in cellular electrolyte levels and other authors have shown membrane responses at doses as low as 0.5 Gy (*see refs within* Ramakrishnan, 1993). These ideas support mechanisms proposed by Alper, postulating the presence of two sensitive sites within the cell (Alper, 1968, 1974, 1987). The mechanism of action of this membrane damage has been proposed as an ion homeostatic imbalance (Dean,1987). In addition, calcium ion concentration has been shown to regulate the action of certain phospholipases, proteases and endonuclease enzymes (Nicotera *et al.*,

1989; Eastman & Barry, 1992; Ramakrishnan *et al.*, 1993). It is therefore possible that DNA damage could be brought about by a localised change in Ca^{2+} concentration leading to regulation of endonucleases. A change in calcium ion concentration within the cell has been demonstrated by γ-irradiation and the use of the membrane protective vitamin-E analogue Trolox has been shown to reduce DNA fragmentation in thymocytes (Ramakrishnan *et al.*, 1993). In addition, visible blebbing of the cytoplasm due to irradiation has been shown to be associated with an increased calcium ion concentration and the blebs which break off from cells have been shown to contain high concentrations of Ca^{2+}, and may be a mechanism for the cell to restore its ionic balance (Trump & Berezesky, 1992).

Recent work of Wheeler *et al.* (1992) questions the direct correlation between DNA damage and cell death by comparing the survival response and the DNA damage response for cells irradiated at different temperatures and then moved to 37°C for a period of repair. If a direct correlation between cell death and DNA strand breaks exists then the response of both to a change in temperature should be identical. The difference in response of the two endpoints for 20°C irradiations perhaps suggests an additional, metabolic, pathway to DNA damage which is effected by the reduced temperatures. Some proposed targets and their associated pathways to cell death are suggested by Corcoran & Ray (1992) and are listed below,

Nucleus	-	Direct DNA damage / Ca^{2+} sensitive endonucleases.
Plasma membrane	-	Ion concentration loss / Damaged transport system.
Endoplasmic Reticulum and Cytoplasm	-	pH deregulation / Protein production / Loss of homeostasis / Loss of control of local Ca^{2+} ion concentration.
Mitochondria	-	Reduced ATP metabolism.

1.2.6 Conclusions

Early micro-irradiation experiments using high-LET charged particles indicate that the nucleus is the most radiation sensitive site within the cell and that other parts of the cell show little sensitivity. Other data, particularly using ultraviolet light irradiation, suggest

that other mechanisms may also be important for inducing cell death. In addition, work in the field of molecular biology has demonstrated the passage of intra-cellular signals between different compartments of the cell and can in some instances result in DNA damage within the nucleus. Clearly the investigation of the location of radiation sensitive sites within the cell remains a critical question in radiobiology, and one to which the current generation of microbeam apparatuses may give new insight.

1.3 Interactions of Ionising Radiation

The principle method of interaction of ionising radiation with matter is to increase the energy of a bound electron and so change the atomic state of the parent atom. If sufficient energy is imparted to the bound electron then it may be stripped away from the parent atom resulting in ionisation. This will consequently have an effect upon the chemical nature of the associated molecule and, if the effected molecule is an important biological target may result in a detectable biological effect. Both the absolute degree of ionisation and the pattern of energy deposition resulting from the passage of the ionising radiation will effect the response of the biological system. Parameters describing these properties have therefore been used in the hope of deducing the mechanism of radiation action from this relationship (e.g. Goodhead, 1989; Brenner & Ward, 1992).

In microbeam experimentation the pattern of energy distribution is significant in two respects. Firstly it may be used to elucidate the mechanism of radiation action. In addition, the lateral distribution of energy in the cell may have an effect upon the spatial resolution obtained from the microbeam apparatus. A brief description of the different types of interaction of ionising radiation with matter will therefore be given here, with consideration of the energy distribution which results.

Ionising radiations may be crudely separated into two categories. Those of charged particles (e.g. electrons, negative pi-mesons, protons, alpha particles) which deposit their energy by Coulomb interactions with the electrons of the target material (Section 1.3.1), and of uncharged particles (e.g. gamma rays, X-rays, neutrons) which deposit their energy indirectly by the production of secondary charged particles (Sections 1.3.2 - 1.3.4). The excitation and ionisation of matter by these processes will be considered briefly.

1.3.1 Coulomb / Rutherford scattering

The interaction of charged particles with matter may be described by the processes of elastic and inelastic Coulomb scattering with the nucleus and electrons of the target

atoms. For a particle having an energy greater than 2 MeV/u it is multiple inelastic collisions with electrons which is the dominant process for energy loss (Kraft *et al.*, 1992). The incident charged particle imparts energy to the atomic electrons of the target material by either glancing collisions, resulting in excitation of the parent atom, or by near collisions, usually resulting in impact ionisation of the electron (Zaider *et al.*, 1983). These near collisions produce free secondary electrons which usually have initial energies of greater than 100 eV. The equipartition principle of Bohr (Chatterjee & Schaefer, 1976) makes the approximation that there is an equal division of energy between that deposited in glancing collisions, which are numerous but of low energy, and that deposited in near collisions, which are less numerous but of a higher energy. The secondary electrons, δ-rays, created by higher energy interactions will themselves produce further ionisation and excitation along their path. The maximum energy which may be imparted to the ionised electron is determined by the velocity of the incident particle and is given by (Chatterjee *et al.*, 1973) :-

$$\epsilon_{max} = \frac{2\, m_0\, v^2}{1 - \beta^2} \qquad \text{- (1.1)}$$

where m_0 is the mass of the electron, $\beta = v / c$ and v is the velocity of the charged particle.

The distribution of energy losses for a 1 MeV proton in water vapour has been calculated as 19 % in excitation by the incident particle, 19 % in ionisation by the incident particle and 62 % in ionisation and excitation by the secondary electrons produced (Fäin *et al.*, 1974). As the secondary electrons slow down the pattern of their energy distribution will change and results in 30 to 50 % of the energy loss of the primary particle being deposited by electrons with energies of less than 5 keV (Goodhead, 1989). The energy spectrum of the secondary electrons produced is therefore extremely important in determining the pattern of energy loss within the target material. This spectrum will be dependent on both the incident particle velocity and the interaction cross-section of the particle with the atoms and molecules of the target material.

For protons and more massive charged particles it is reasonable to assume that, since their mass is much greater than that of the electron, their interaction with a single electron will have no significant effect upon their direction. Using this assumption it is possible to calculate the energy loss of the charged particle in the target medium, due to electron interactions. This is given, using classical mechanics by the Bethe formula, and a quantum mechanical correction can be made to this formula which results in the Bethe-Bloch formula (Evans, 1955) giving the stopping power of a charged particle in the target medium by :-

$$-\frac{dE}{dx} = \frac{4\pi Z^2 e^4 n}{m_0 v^2}\left\{\ln\left(\frac{2m_0 v^2}{I(1-\beta^2)} - \beta^2\right)\right\} \qquad \text{- (1.2)}$$

$$\textit{where} \quad n = \frac{N_0\, z\, \rho}{A}$$

where **Z** = the number of electronic charges carried by the incident particle

n = the electron density of the target material

e = the charge on the electron

z = the atomic number of the target material

$\mathbf{N_o}$ = Avogadros number

ρ = the density of the target material

A = the atomic weight of the target material

and **I** ,the mean excitation potential, is ~ 10 eV × **z** for **z** > 20.

For $\mathbf{E} >> \mathbf{m_0c^2}$, where $\mathbf{m_0}$ is the rest mass of the electron, a relativistic correction must also be used to compensate for electron density effects. In addition, when considering direct ionisation by incident or secondary electrons the initial assumption that the particle does not deviate due to the interaction with a bound electron is no longer valid and a further modification must be made.

1.3.2 Photoelectric effect

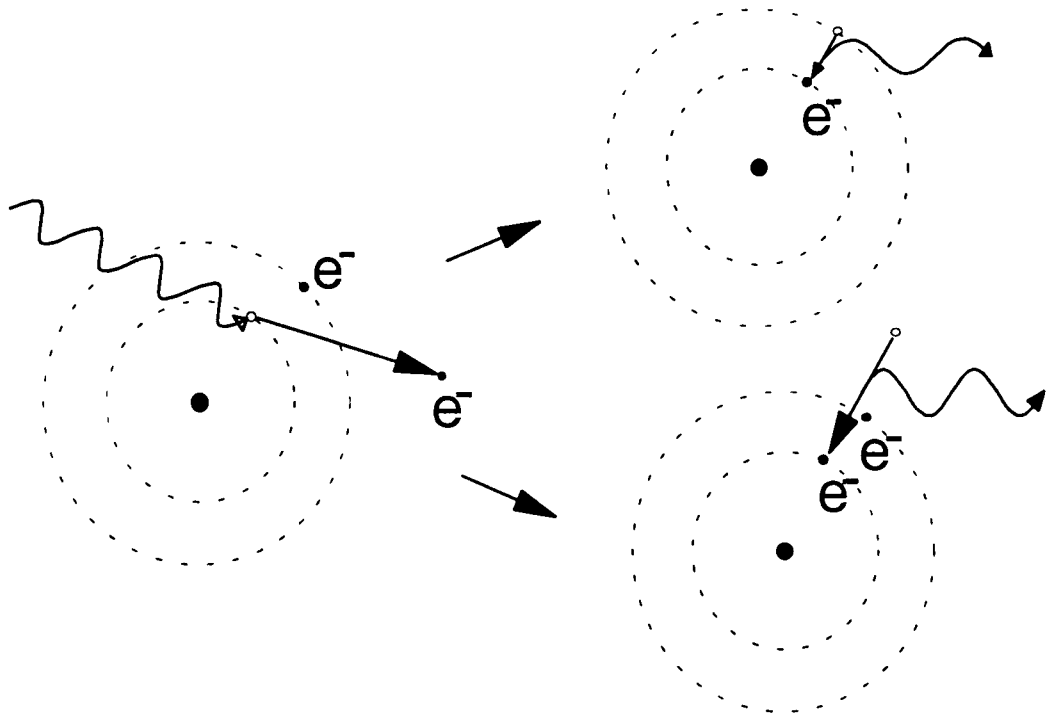

Figure 1.2 The complete absorption of a photon results in the ejection of a single photoelectron from the target atom. The remaining empty state may be filled by an electron from a higher energy level of the same atom or from the continuum band, in either case emitting a characteristic photon.

The photoelectric effect is the process by which an incident photon is completely absorbed and the energy lost to a bound electron of an atom of the target material. If the energy gained by the electron is greater than its binding energy then the electron will be ejected from the atom resulting in ionisation. This interaction is the predominant method of energy loss for photons with energies of less than 0.1 MeV. The electron most likely to be ejected from the parent atom is that of the inner (K-) shell, with 80 % of ejected electrons being from the K-shell when the incident photon energy is significantly larger than the K-shell binding energy (Evans, 1955). The kinetic energy of the ejected electron is given by :-

$$KE_e = h\nu_\gamma - E_b \qquad \text{- (1.3)}$$

where **h** is Plancks constant, ν_γ is the frequency of the incident photon, and E_b is the binding energy of the electron. Since an electronic state of the parent atom is left unfilled, relaxation can subsequently occur by the transition of an electron from a higher to a lower energy state. This transition results in the emission of a secondary photon by

the process of delayed fluorescence. The energy of the emitted photon is characteristic of the target atom and in soft tissues X-rays of ~ 500 eV make up a large part of this radiation. It is therefore possible for these X-rays to have sufficient energy to release a second, Auger, electron from its bound state. This process may be repeated, producing a cascade of electrons, until the energy of the characteristic fluorescent photon is no longer sufficient to release a bound electron from the target material. The photoelectron and Auger electrons will then produce further ionisation and excitation by the Coulomb interactions described in Section 1.3.1.

1.3.3 Compton effect

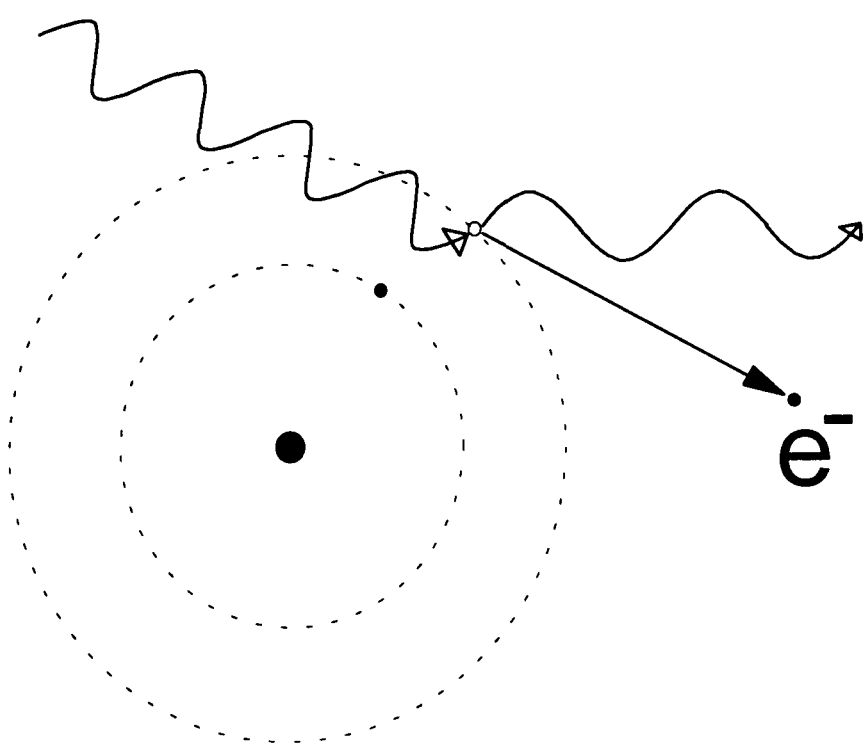

Figure 1.3 An incident photon interacts with a bound electron imparting some of its energy to the electron, so changing both its energy and direction.

The Compton effect is the process by which an incident photon undergoes scatter by an electron of the target material. The interaction results in an increase in the energy of the target electron and a change in both the energy and angle of the incident photon. If the energy imparted to the electron by this process is greater than its binding energy then ionisation will occur. The calculation of the change in energy and angle was calculated using classical electromagnetic principles by J J Thomson, however, this approximation is only valid for an incident photon energy which is much less than the rest mass of an electron. A relativistic correction given by Evans (1955) shows an energy transfer of :-

$$E'_{\gamma} = \frac{E_{\gamma}}{1 + \alpha(1 - \cos\theta)} \qquad \text{- (1.4)}$$

$$\textit{where } \alpha = \frac{E_{\gamma}}{m_0}$$

where θ is the change in the direction of the incident photon, E_γ is the energy of the incident photon and $E'\gamma$ is the energy of the scattered photon.

1.3.4 Pair production

This process is only relevant at high incident photon energies and is the production of an electron-positron pair from the energy of the incident photon, in the presence of an electric field, i.e. near an atomic nucleus. Since the rest mass of the electron is 0.51 keV the minimum photon energy which is necessary to produce an electron-positron pair is 1.02 MeV (γ-rays).

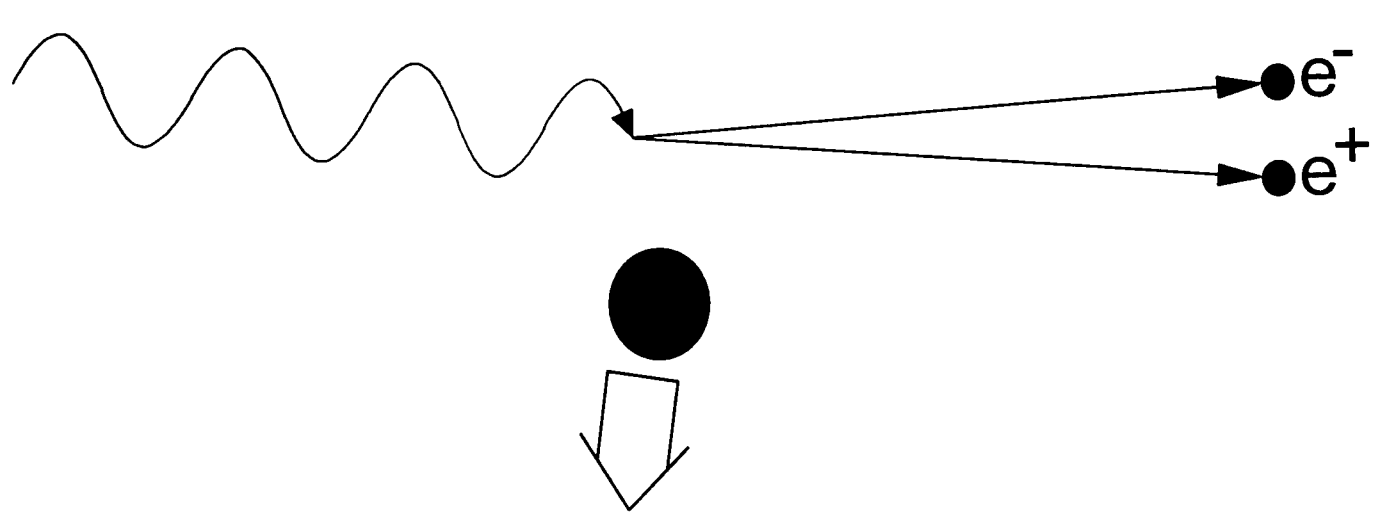

Figure 1.4 The production of an electron-positron pair from a high energy photon to an atomic nucleus. Momentum is conserved by nuclear recoil.

The relative significance of these three processes is dependent both on the energy of the incident photon and the properties of the material irradiated. For soft tissue the photoelectric effect dominates up to a photon energy of ~ 50 keV (hard X-rays). At energies higher than this the Compton effect becomes increasingly important and at a photon energy of ~ 10 MeV the process of pair production is approximately comparable to that of the Compton effect (Orton, 1986). Although these three processes are only

relevant to electromagnetic radiation it is worthy of note that if the bremsstrahlung photons given off by a decelerating charged particle are of sufficient energy then the both the Coulomb interaction and the photonic interaction processes will be involved in the energy deposition.

Another form of indirectly ionising radiation is that of neutral charged particles, for example neutrons. These particles interact with matter by elastic and inelastic collisions with the nuclei of the target material and produce secondary radiations which result in the ionisation of the target material.

1.3.5 Elastic nuclear collision

This is the dominant process of interaction for all neutrons, with the exception of thermal neutrons having energies of less than a few electron volts (Orton,1986). If a neutron collides with the nucleus of a target atom it will impart some of its momentum to the nucleus, obeying the laws of conservation of momentum and energy. For many biological materials hydrogen is a prominent constituent and so in this case the recoiling nucleus will be a proton. Typically the proton will gain 50% of the energy of the incident neutron and the processes of direct ionisation by the recoil proton will then become the form of ionising energy loss which will produce a biological effect, by the processes described in Section 1.3.1.

1.3.6 Inelastic nuclear collision

These processes, due to the fusion of a neutron with an atomic nucleus of the target material, result in a change in the structure of the target atomic nucleus and the emission of electromagnetic radiation and charged particles. These secondary radiations will then produce ionisation in the target material.

For thermal neutrons, of less than a few electron volts, the absorption of the low energy neutron results in the excitation of the nucleus. The subsequent relaxation of the nucleus results in the emission of a gamma-ray photon (radiation capture) or of charged particles (spallation). As the energy of the incident neutrons increases the result of the nuclear

interaction becomes more dramatic. For neutron energies greater than ~ 0.5 MeV the excited nucleus decays by photon emission, from a photon energy of ~ 100 keV for a high atomic number material to photon energies of ~ 5 MeV for low atomic number material. For neutron energies greater than ~ 5 MeV the interaction results in the fragmentation of the target atomic nucleus, also known as spallation. This results in the emission of electromagnetic radiation and light nuclear fragments such as protons, neutrons and alpha particles. For higher energies greater than ~ 100 MeV the nuclear spallation products are more massive. The products from these nuclear interactions result in dense ionisation giving neutrons the characteristic of a high-LET radiation.

1.3.7 The pattern of energy deposition in the cell

The various processes by which the ionising particles interact with matter result in a variation in the pattern of energy deposition for different incident radiations. This difference in the pattern of energy deposition within the cell is one element which is responsible for the differences in biological effectiveness between different types of radiation and may be a means of elucidating their mechanisms of action.

The processes described in Sections 1.3.1 to 1.3.6 result in localised distributions of energy deposition within the target due to either electromagnetic or particulate radiations. In the analysis of experimental data the localised pattern of energy deposition is often described by a single quantity which is an average over the length of the particle track, for example LET, or over the irradiated volume, for example dose. In a microbeam irradiation geometry however, the position of the particle track within the irradiated target is well defined. The effect of this is that the pattern of energy deposition in each irradiated cell will vary little across the irradiated cell population. Quantities of energy deposition averaged over the whole cell will therefore be inappropriate to describe the energy deposition of the incident radiation.

In addition to describing the radiation exposure of the target cells, it will be necessary to consider the effect that the distribution of energy will have on the spatial resolution of the microbeam itself. It would clearly be unwise to produce a microbeam of a size which was considerably smaller than the lateral spread of energy in the target. Equally

a microbeam which had a spatial resolution considerably larger than the size of the lateral spread of energy in a single track would have a wide range of possible energy deposition patterns for irradiations of more than a single particle, due to the position of charged particles within the beam. Consideration of the energy deposition distribution due to the charged particles used in the microbeam arrangement developed at the Gray Laboratory will therefore be given.

The pattern of energy deposition by charged particles has been investigated by both experimental means and by the simulation of particle tracks using Monte-Carlo type computer programmes based upon the theory of particle interactions with matter. Some useful data have been obtained using macroscopic proportional counters at low gas pressures. The dimensions of the energy depositions obtained may then be scaled down in size, equivalent to an increase in the pressure of the gas to unit density (e.g. Kanai & Kawachi, 1987; Braby & Ellett, 1972; Glass & Braby, 1969). However, a spatial resolution limit for the data obtained by this method exists at ~ 0.1 μm, due to the size of chamber necessary to retain a linear dose response in the proportional counter (Wilson & Partzke, 1980). Since the lateral spread in energy deposition for the charged particles used in this work is significantly smaller than this distance experimental data are not directly applicable to this work. The results of Monte-Carlo type simulations must therefore be used to give the required particle interaction data (*see refs within* Kraft *et al.*, 1992; Paretzke *et al.*, 1991; Zaider *et al.*, 1983; Charlton, 1986; Nikjoo & Goodhead, 1989, 1991; Leuthold & Burger, 1988; Williamson, 1987). These simulations use experimentally measured double differential interaction cross-sections in energy and angle for primary electron emission, elastic and inelastic scatter, excitation and ionisation, by the primary and secondary electrons (Kraft *et al.*, 1992) in the given target material, often vapour phase unit density water, for the appropriate incident particle. The particle interactions which are modelled using these codes are the direct ionisation and excitation by the incident particle, the energy and angle of the primary and secondary electrons and the energy deposition pattern of the secondary electrons generated.

The resulting energy distribution may be approximated to a dense core of ionisation, of only a few nanometres in diameter, due to the production of direct ionisation and low energy electrons by the incident charged particle, with more diffuse energy deposition

events at larger distances from the centre of the particle track, due to the production of higher energy secondary electrons, δ-rays. A nominal lower limit for the initial kinetic energy of these penumbral δ-rays has sometimes been drawn at ~ 100 eV (Nikjoo *et al.*, 1991). An approximate description of these regions is to consider the core as a top-hat type energy density distribution with the energy density of the penumbral region decreasing as an inverse-square relationship with radius (Chatterjee & Schaefer, 1976). Although this gives a crude approximation to the energy deposition over the whole track, for low-LET radiations or when considering only short track segments the concept of a core and penumbra is an artificial one (Kraft *et al.*, 1992).

The radius of the core and penumbra has been parameterised for particle energies of greater than 2 MeV / u by Chatterjee & Schaefer (1976) as :-

$$r_c = 0.0116 \times \beta \quad (\mu m)$$
$$r_p = 0.768\ E - 1.925\ \sqrt{E} + 1.257 \quad (\mu m) \qquad \text{- (1.5)}$$

where $\mathbf{r_c}$ is the core radius, $\mathbf{r_p}$ is the penumbral radius, $\beta = \mathbf{v} / \mathbf{c}$ for the incident particle, **v** is the velocity of the incident particle and **E** is the energy of the incident particle in units of MeV per atomic mass unit (MeV / u). In addition, the maximum radius of energy deposition has been defined by Krozubeck & Krasavin (1984) to be :-

$$r_{max} = 40 \times E^{1.75} \quad (nm) \qquad \text{- (1.6)}$$

and the maximum secondary electron energy has been defined by Chatterjee *et al.* (1973) as :-

$$\epsilon_{max} = \frac{2\ m_0\ v^2}{1 - \beta^2} \qquad \text{- (1.7)}$$

where $\mathbf{m_0}$ is the rest mass of the electron and **v** is the velocity of the incident particle. It is worthy of note that the maximum energy of the secondary electron emitted is not dependent upon the charge on the incident particle but depends solely on its velocity.

For a 4 MeV proton, used in this work, these equations correspond to a core radius of 1.47 nm and a penumbral radius of 479 nm (Chatterjee & Schaefer, 1976), a maximum radius of energy deposition of 452 nm (Kozubeck & Krasavin, 1984) and a maximum

secondary electron energy of 9.6 keV (Chatterjee *et al.*, 1973), corresponding to a maximum electron range of ~ 1 μm (Paretzke *et al.*, 1991).

The figures for the maximum diameter of the 4 MeV proton track, ~ 1μm, suggest that the energy deposition pattern will make a contribution to the spatial resolution of a nominal 1 μm diameter microbeam. However, the approximately equal energy partition between the low energy electrons of the core and the higher energy δ-rays (Chatterjee & Schaefer, 1976) results in ~ 50 % of the energy deposition occurring within a diameter of only a few nanometres and so the overall loss in spatial resolution will be minimal. At lower energies, or for heavier particles at similar energies, the particle velocity will also be less than that of a 4 MeV proton and hence the range of the secondary electrons will be reduced. The effect on spatial resolution due to energy spread around the track, will therefore also be minimal for these microbeams.

For the irradiation of biological targets by small numbers of particles in a well defined area the calculation of averaged quantities such as LET and dose are inadequate to describe the distribution of energy in the target. The data from some initial experiments have been presented as fluence-effect curves (Brooks *et al.*, 199; Prise *et al.*, personal communication) and an alternative parameter of 'hit size effectiveness function' has been proposed by Bond *et al.* (1985). The problem of quantifying energy deposition using a microbeam is one that will need to be addressed as further work is performed using microbeam techniques.

1.4 Historical Microbeams

1.4.1 An Overview

The technique of using microbeam irradiation to study the normal function and radiation response of individual cells dates back many years. As early as 1912 Tschachotin constructed an ultraviolet microbeam of ~ 5μm diameter and used this apparatus for several decades in the study of single cells (Tschachotin, 1959 *see refs within* Zirkle, 1957). During the 1950's an increased interest in microbeam irradiation resulted in the construction of many different types of microbeam using ultraviolet light, X-rays, electrons, protons, deuterons, and alpha particles. The most commonly constructed was the ultraviolet focused microbeam, built using the optical elements of a fluorescence microscope. Several particle microbeams including the proton microbeam of Zirkle & Bloom (1953) were also constructed around this time. Their uses were primarily to study the visible microscopic responses of cells to the various forms of incident radiation.

Perhaps because of the technical difficulties involved, the low number of cells that could be irradiated, and the development of improved cell culture techniques by Puck & Marcus, allowing the investigation of radiation response by the rapid irradiation of large numbers of mammalian cells *in vitro*, the use of these beams lasted little more than a decade. Work in the field of microbeam irradiation has continued by realising the potential of the laser as a source of high intensity, often monochromatic, light and the variety of wavelengths used has increased as new lasers have been developed. These laser microbeam apparatuses have also been used more recently for experiments as diverse as partial chromosome deletion, to the manipulation of whole cells using 'optical tweezers' (Berns *et al.*, 1991).

A summary of the achievements of microbeam construction will be given here with some consideration of the problems associated with the localisation of the various radiation types used.

1.4.2 Microbeam production

The characteristic property of a microbeam is the ability to localise a particular form of ionising radiation to an area of a few microns in diameter or better. This can be achieved either using shielding arrangements such as collimators and slits, or by focusing a radiation source to a micrometer sized image. The shielding approach has been used most often with particulate radiations and that of focusing with electromagnetic radiation sources. Both methods however are imperfect in that they not only restrict the beam to a limited area but also degrade the beam quality.

In the case of ultraviolet light and other electromagnetic radiations there are many processes which result in the deterioration of spatial resolution of the beam. Any optical element through which light passes will introduce a degree of scatter, absorption and internal reflection into the photon microbeam. If transmission optics are used then any lens in the system will produce aberrations which will introduce distortions into the shape of the focused beam. These distortions will be wavelength dependent and so will cause particularly serious problems for heterochromatic beams. In order to produce a 'hot-spot' of micrometer dimensions by focusing electromagnetic radiation, the object pin-hole diameter must be small and so will introduce both edge and Airy diffraction effects. These effects will be imaged onto the target and will therefore contribute to spreading of the microbeam produced. For a 2 μm hot-spot produced by demagnification of a 100 μm object pin-hole, Airy diffraction results in 15% of the energy of the incident beam lying outside of the primary maximum (Uretz *et al.*, 1954). The target material itself will also add to the degradation of the beam by scatter and the relative absorption of different wavelengths in heterochromatic beams.

For electromagnetic radiations of higher energies, X-rays and γ-rays, an additional contribution to the loss of spatial resolution will be made by the higher energy electrons produced by Compton scatter and the photoelectric effect. For example the mean secondary electron range due to the interaction of 8 keV X-rays with biological material is 1.7 μm (Seed, 1960). Electrons may also be produced in the material used for the cell support which may then be back-scattered into the target.

Another problem inherent in all focused light microbeams is that the irradiation geometry of the focused beam is of two cones which overlap at their apices to form a small volume of high radiation intensity. Material outside of the hot-spot at the focus of the beam will inevitably also be irradiated and an example of the relative intensities of other areas within the cone of radiation is shown in Figure 1.6.

Focused particle microbeams have also been designed and avoid the problem of scatter introduced by the use of a collimator. They do however introduce an alternative set of problems including the precise alignment of the focusing magnet and the design of a magnet to produce a highly uniform field. In addition, the production of the low-flux particle beams which are of use to the biological community is extremely difficult. This approach is commonly used in analytical physics apparatuses but is less convenient when constructing a facility to irradiate biological samples, since the facilities designed are, in general, sealed vacuum systems producing a horizontal focused beam of high intensity.

The use of a collimator to produce localised microbeam radiation also results in a loss of both spatial and energy resolution of the incident beam. The transmitted particles suffer energy loss, range straggling and scatter due to interaction with any material through which they pass. This results in an increase in the number of lower energy particles in the beam and causes an increase in the divergence of the collimated beam, which results in a gradual loss in spatial resolution as the distance from the collimator increases. The contribution of particle scatter to the transmitted beam may be either by interaction with the walls of the collimator itself or with material between the collimator exit aperture and the target, such as a vacuum window or transmission detector. In order to minimise these effects the amount of material between the particle source and the target must be minimised, for instance using thin vacuum windows and a short air path between the collimator and the target. In addition, the collimator geometry will be important in determining the degree of scatter which is introduced into the beam and designs for optimum collimator performance are discussed in Chapters 3 and 4.

Summaries of the various microbeam apparatuses previously developed and examples of the beam qualities produced are given in the following sections.

1.4.3 Ultraviolet microbeams

One method used to produce an ultraviolet microbeam was to illuminate an object slit with a bright source of ultraviolet light. The object slit was then demagnified to produce an intense spot in a volume whose size depended upon the level of demagnification. Since the apparatus was designed so that the hot-spot coincided with the focal point of a visible-light microscope it was possible to view and position the target cell using light microscopy and then to irradiate a specific site in the target whilst the target was being observed.

The first recorded use of this approach was that of Tschachotin in 1912 (*see refs within* Zirkle, 1957). By illuminating two pairs of perpendicular, adjustable slits using the spark from a mercury lamp and then defocusing the object slit using a quartz microscope objective he was able to produce a beam with a hot-spot of only a few microns in diameter. The target cells were mounted on a 5 μm thick mica sheet, under a visible light microscope and were irradiated from beneath the cell support. This allowed the target to be viewed at, and after, the time of irradiation with a minimum of mechanical disturbance.

A later design which was used by many other experimenters (von Boerstal & Wolff, 1955 *see refs within* Zirkle, 1957; Shimomura *et al.*, 1967) was that developed by Perry, Uretz and Bloom (Uretz *et al.*,1954; Zirkle & Bloom, 1953; Perry, 1957; Perry, 1960). Again a mercury lamp was used as the source of a continuous spectrum of light from 226 nm and the use of water cooling in this case allowed higher intensities to be reached. The object apertures were made from removable brass sleeves, which allowed a variety of sizes and shapes to be inserted, a 100 μm diameter object pinhole could be demagnified to produce a 2 μm diameter hot-spot. A considerable improvement of this design over that of Tschachotin was that the beam reducing optics were of the reflection rather than the transmission type and so completely achromatic. This configuration allowed the use of the same optics for both U.V. irradiation and visible light microscopy of the target. In addition, the use of different wavelengths of incident light could be used with no change in the focal plane of the hot-spot. A schematic of the arrangement is shown in Figure 1.5 (Perry, 1957).

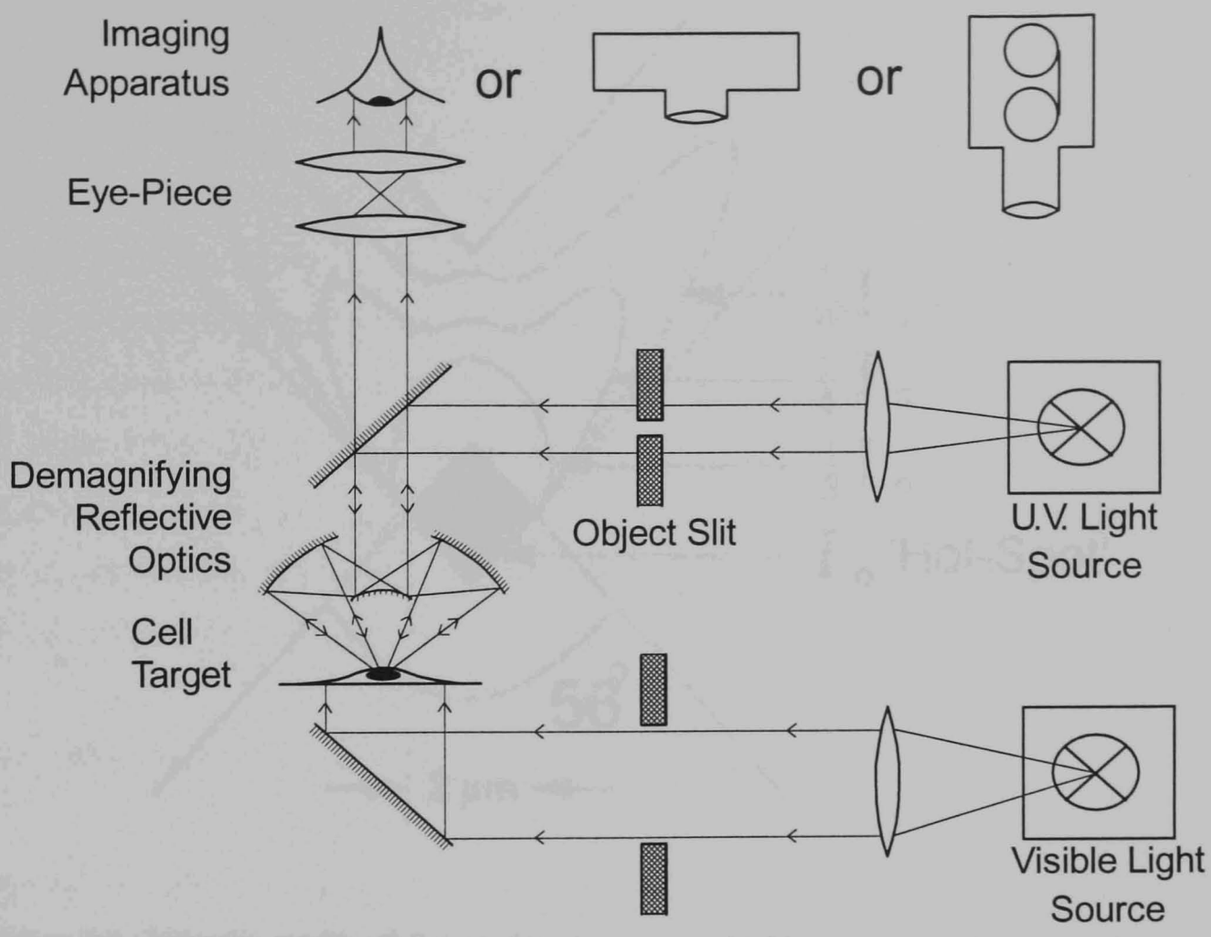

Figure 1.5 A schematic of the U.V. light microbeam designed by Perry (1957), using reflective optics. The sample could be monitored by eye, still photography or time-lapse cinematography.

The beam was capable of intensities of 0.015 $\mu J\ \mu m^{-2}\ s^{-1}$ at the hot-spot and with suitable filters could produce varying frequencies of incident light with a bandwidth of 3.7 nm. A two-dimensional intensity profile, resulting from the production of a hot-spot with a diameter of 2 μm, is shown in Figure 1.6 (Uretz *et al.*, 1954).

In addition to its use for microbeam irradiation the apparatus could be used for still or time-lapse photography of irradiated samples and for scanning densitometry.

An alternative approach to the problem of localised U.V. irradiation was that of Montgomery & Hundley (1961). Using reflective optics he demagnified the screen of a cathode ray tube, producing low-intensity ultraviolet light, onto the target area and then used an appropriate 'picture' to define the desired region of irradiation. Although ingenious this flying-spot microscopy technique produced only a very low intensity beam and irradiation times were therefore prohibitively long.

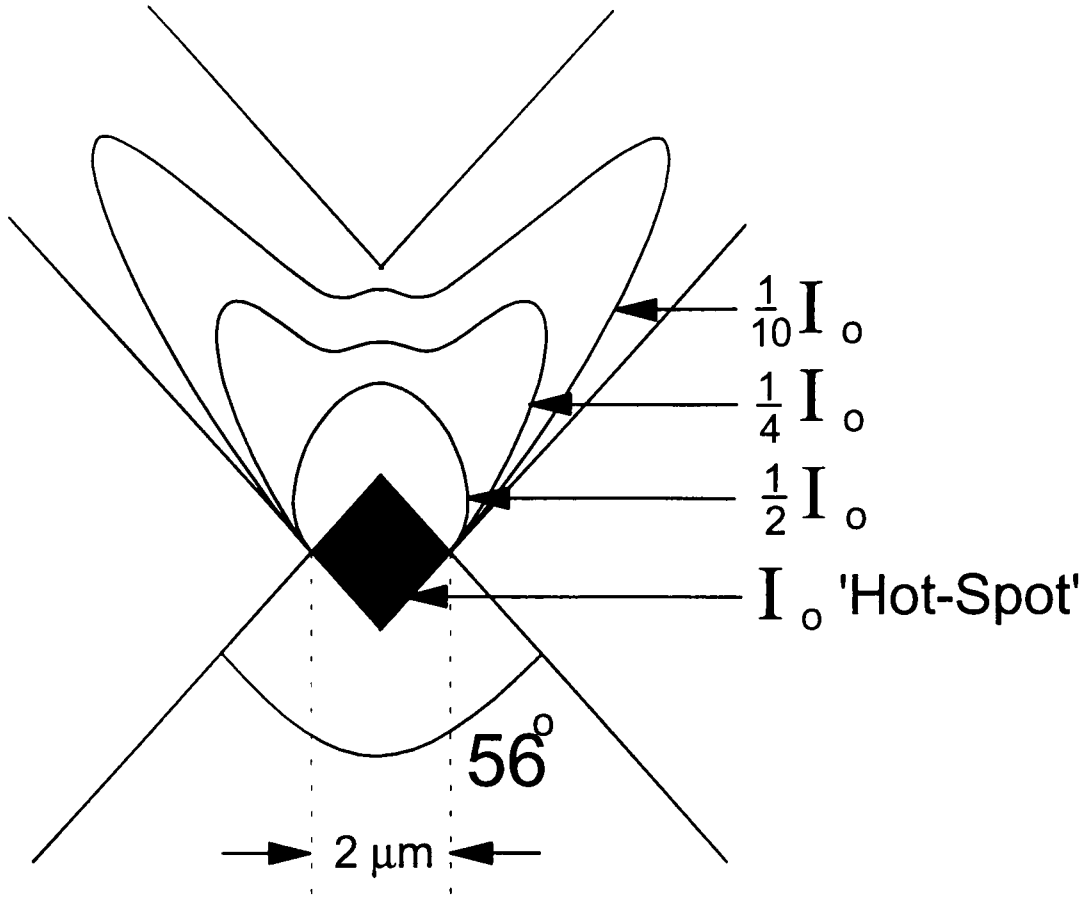

Figure 1.6 Intensity profile of the overlapping cones of a U.V. focused microbeam producing a hot-spot of 2 µm diameter. The iso-intensity bars for intensities of 1/2, 1/4 and 1/10 of the intensity in the hot-spot are shown.

1.4.4 X-ray microbeams

Examples of X-ray microbeams are scarce in the literature. The method used by Seed (1960) to produce an X-ray beam was to take an 8 kV X-ray source and to collimate the X-rays using a 1 mm long, drawn glass capillary with an exit aperture diameter of 1 µm. The acceptance angle of the rod was limited by the total external reflection angle of the glass and was calculated to be 36°, producing a dose-rate of 5 Gy min^{-1}. Due to scatter within the 2 µm thick cell support and the production of secondary electrons with a range of ~ 1.7 µm, the effective beam diameter was calculated to be 2.5 µm.

An alternative approach is that taken by Kirkpatrick & Pattee (1953), focusing X-rays using a pair of elliptical mirrors. Recent advances in silicon micro-machining technology now make it possible to focus X-rays using a Fresnel zone plate. The application of this technology to microbeam production has been discussed by Michette *et al.* (1993).

1.4.5 Laser microbeams

The development of the ruby laser in the late 1950's provided a convenient source of high intensity monochromatic radiation and was used by Bessis (1962 *see refs within* Smith, 1964) to produce a spot of 2 μm diameter at a wavelength of 694.3 nm. Later developments of higher power and shorter wavelength lasers allowed further beams to be built at energies more applicable to radiation damage in biological systems (Moreno & Salet, 1985; Lin & Chan, 1984; Berns, 1969; Kitzes *et al.*, 1977). Berns (1969) succeeded in using an argon laser, with harmonics in the ultraviolet, to produce a 0.6 - 0.8 μm diameter hot-spot at an energy flux of 1 mJ μm^{-2}. These beams have a wide variety of uses from whole cell manipulation to gene deletion (Berns, 1974, 1991).

1.4.6 Electron microbeams

Due to the high level of scatter of electrons these beams were not popular as a source of localised irradiation. An example of an electron microbeam is that of Pohlit (1954 *see refs within* Zirkle, 1957) using a 30 - 150 keV electron source to produce a 1 μm diameter beam at dose-rates of up to $2x10^5$ Gy s^{-1}. At these energies the scatter of the electrons would be several microns (Paretzke *et al.*, 1991), so broadening the 1 μm spot considerably with depth into the target.

1.4.7 Proton microbeams

The only well documented example of a low-energy proton microbeam is that of Zirkle & Bloom (1953; Bloom, 1959). A schematic of the beam apparatus is shown in Figure 1.7.

A broad beam of 2 MeV protons was produced using a Van de Graaff particle accelerator and emerged to atmosphere through a 5 μm thick window. A collimator assembly, in air, was then used to localise the proton beam. The collimator consisted of either a pair of highly polished steel or brass adjustable slits producing a ribbon shaped beam, or of a triangular collimator with a side length of ~ 2.5 μm in steel or brass. The production of this collimator was by colliding a highly polished flat with a sharp blade,

to produce a V-groove. A second highly polished flat was abutted onto the first to produce a triangular tube. The material used for the V-groove collimators was either brass or steel and the length of the collimator was between 60 and 300 μm. The energy spectrum and spatial resolution of the beam, prior to traversing the 5 μm mica cell support, are shown in Figures 1.8 and 1.9. Energy data was obtained by measurements of track length in nuclear emulsion plates.

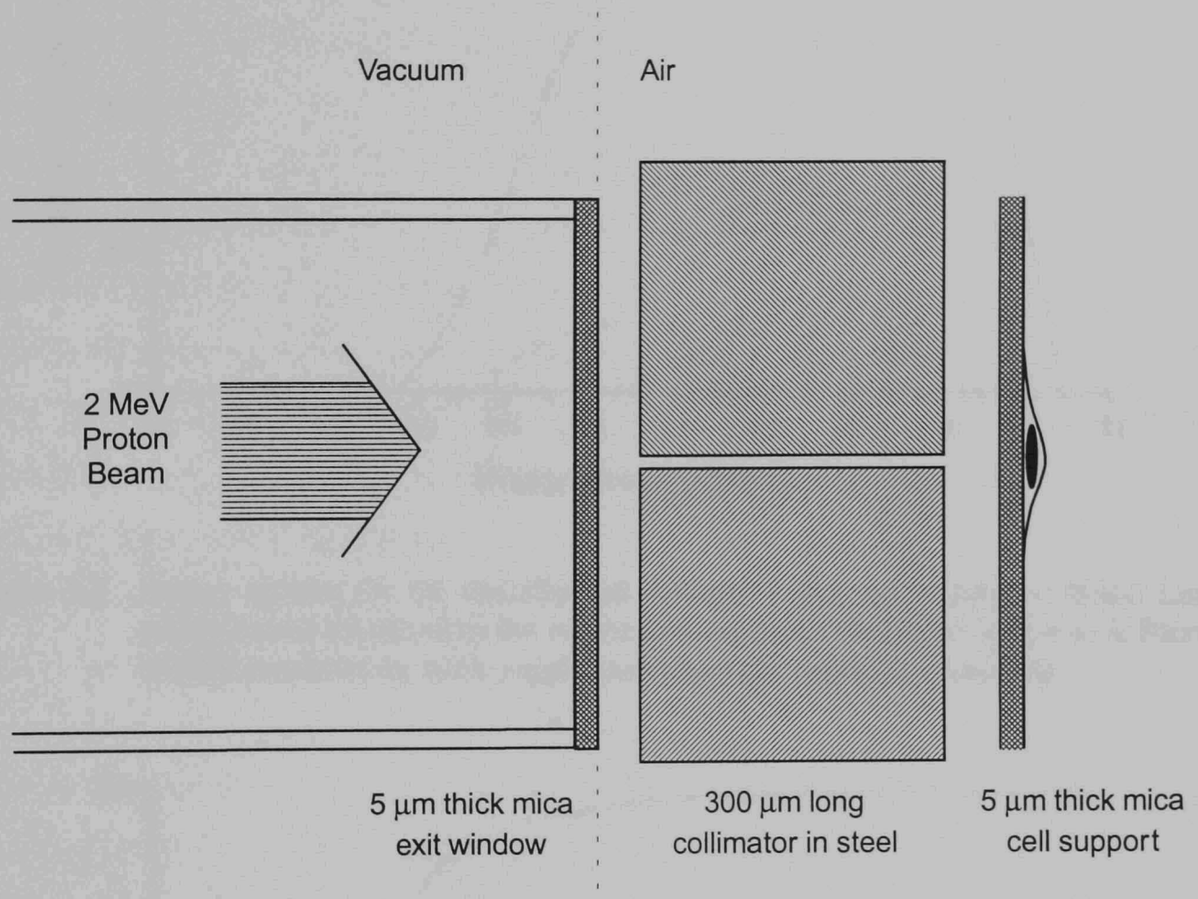

Figure 1.7 A schematic of the proton microbeam apparatus developed by Zirkle & Bloom (1953) to irradiate single cells.

Irradiations were performed using two microscope stages. The target was initially aligned on the viewing stage using microscope cross-hairs and then transferred to a second stage for irradiation. By careful machining of the stage the error in alignment was kept to less than 0.6 μm. Control of the dose given was by timed exposures and so variations in the dose delivered due to random errors, described by Poisson statistics, were inevitable in this arrangement. In addition to the random variation inherent in timed exposures, the Van de Graaff accelerator produced protons in bunches, restricting the minimum dose possible to approximately 20 protons. Because the stage co-ordinates were not absolute with respect to the microscope objective the location of individual irradiated targets could not be revisited. It was therefore necessary to observe each

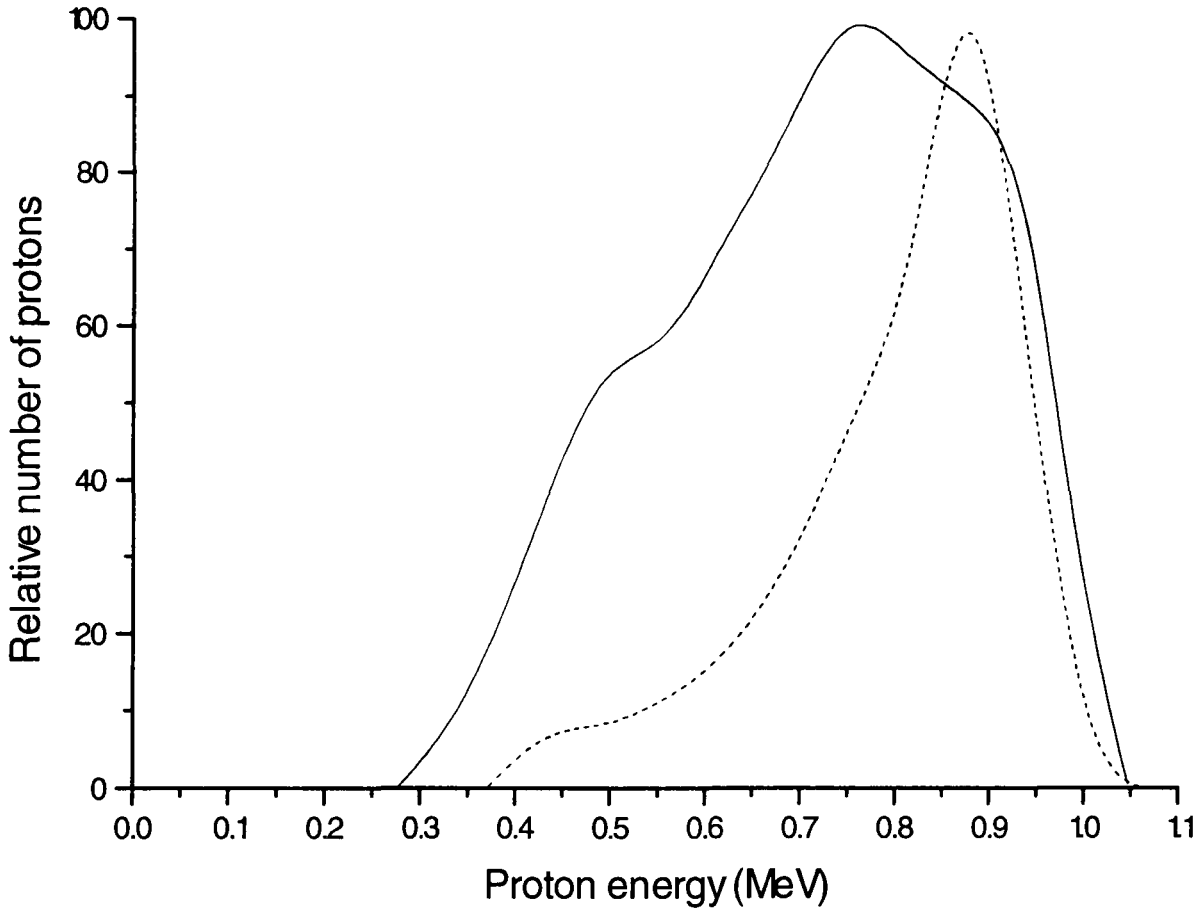

Figure 1.8 Energy spectra for the uncollimated (Dashed Line) and collimated (Solid Line) proton beams produced by the microbeam apparatus developed by Zirkle & Bloom (1953), measured by track length analysis in photographic emulsions.

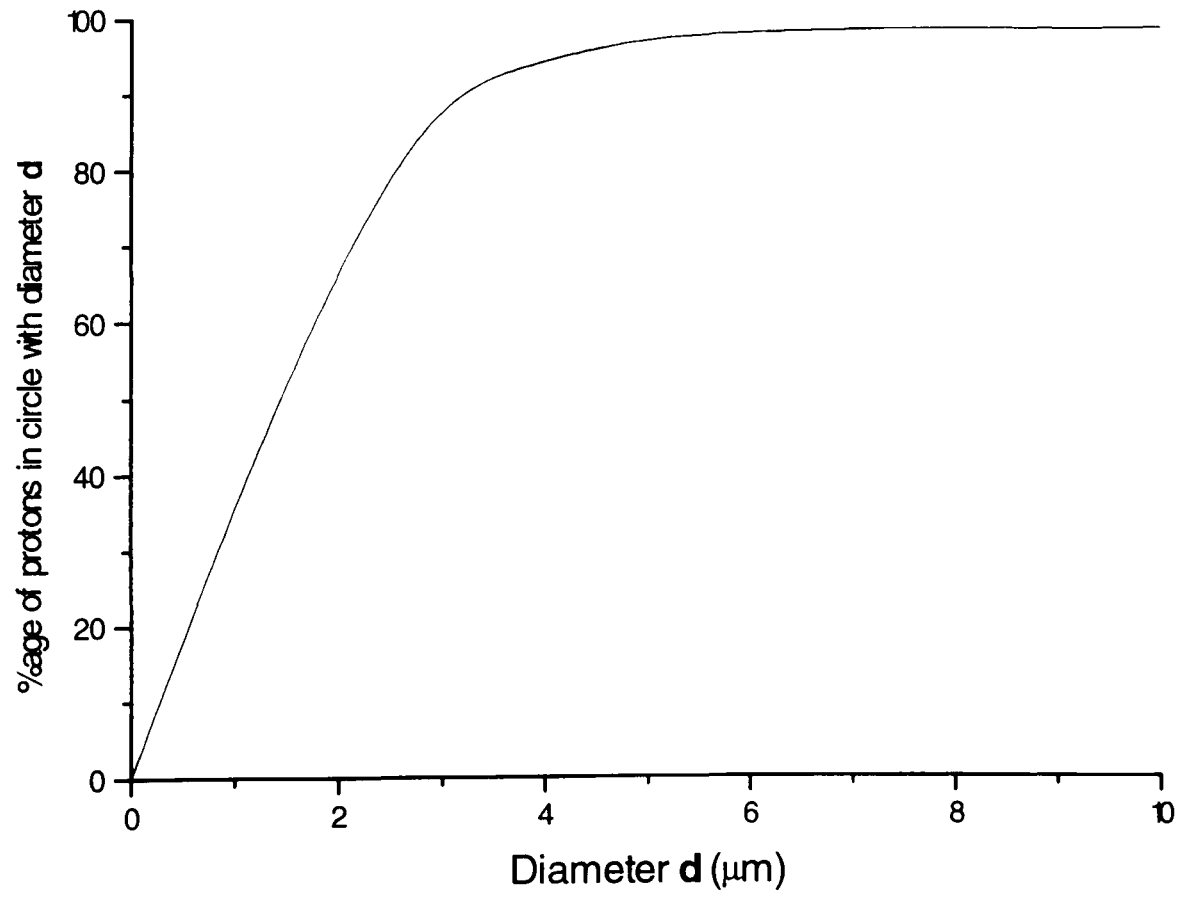

Figure 1.9 Spatial resolution of the collimated proton microbeam developed by Zirkle & Bloom (1953), measured by track analysis in photographic emulsions.

irradiated target until the biological endpoint had been observed. Visible changes observable by light microscopy could be recorded by either sketch or 35 mm still photography. The laborious methods involved in this apparatus considerably limited the number of cells which could be irradiated in each experiment

A higher energy proton beam was produced by Morgan (1962 *see refs within* Smith, 1964). In this case a broad beam of 2 MeV deuterons from a particle accelerator was used to irradiate helium gas. The resulting nuclear reaction resulted in the emission of 15 - 16 MeV protons. Two pairs of highly polished 1.5 mm thick metal slits were used to collimate the protons to a 2 by 10 μm ribbon. The arrangement for cell irradiation was similar to that of Zirkle & Bloom (1953). A considerable advantage of this system was that the highly penetrating protons could be detected by using a crystal scintillator to detect the protons which traverse the relatively thin target and this allowed an absolute value for the delivered dose to be obtained. Biological data using this microbeam do not however appear in the literature.

1.4.8 Alpha particle microbeams

The availability of alpha particle laboratory sources allowed microbeams to be constructed without the inconvenience and expense of particle accelerators. There were therefore several examples of these beams published in the literature. The alpha particle beams were similar in principle to the proton beam of Zirkle previously described and all use ^{210}Po sources producing α-particles of up to 5.2 MeV. The method of collimation in each case was by a several micron diameter hole in a thin metal sheet. Davis & Smith (1957) used a 1 - 1.5 μm diameter hole in 20 μm thick gold, producing a beam divergence of 3° angular full width at half maximum at the exit surface of the collimator. Haynes & Zirkle (1960) used a 1.5 μm diameter hole in 25 μm thick copper and Kuzin & Wainson (1966) produced a 4 μm diameter beam using a 1-2 μm hole in 100 μm thick bronze. In each case irradiation was by timed exposures and often long irradiation times were necessary due to the inevitable low flux of transmitted alpha particles through the collimator.

1.4.9 Heavy ion microbeams

More recently a localised heavy-ion irradiation facility has been constructed (Kraske *et al.*, 1990) at Darmstadt, Germany. This apparatus allows the irradiation of biological targets with particles of up to 1.4 MeV/u and with atomic masses from carbon to uranium, corresponding to LET's of 500 to 1200 keV μm^{-1} respectively. The spatial resolution of this beam is approximately two microns in diameter. Collimation was used to localise the incident particles, in this case using 0.7 to 2.0 μm holes etched in 30 μm thick mica. The penetration depth of these high energy particles is sufficient to allow their detection after traversal of the target and the low count rate allows easy control of the dose given using a mechanical shutter. Contamination from lower energy particles scattered within the collimator is present but the level of beam degradation is unreported.

In addition to these systems constructed for the irradiation of biological samples there also exist microbeams which are used as tools for the physical analysis of materials. These high spatial resolution microbeams are generally produced by focusing a high intensity particle or photon beam, generated by a particle accelerator. The energy and spatial resolutions attained at these facilities are generally superior to those of the biological beams reported. However, these beams are not suitable for biological work, due to their high flux and the necessity to irradiate samples under vacuum and so will not be considered here.

In summary, a considerable number of microbeam facilities have been constructed for use in biological experiments. The simplest of these were the focused ultraviolet light systems based on the optical elements of fluorescence microscopes. Particle microbeams have also been constructed, however these suffered from poor energy spectra, low count-rates and a lack of particle detection. The technological advances that have been made over the last thirty years now make the construction of particle microbeams a feasible proposition for the study of low-dose responses and spatial sensitivity within mammalian cells. The new technologies which have made this possible are considered in Section 1.5.

1.5 New Technology

The early microbeams described in the previous section were used in many experiments to determine the radiation response of various cellular elements at different doses (see Chapter 1.2), however, all suffered from several common problems. One deficiency of all these systems was the inability to revisit a particular irradiated cell at a time after irradiation. It was therefore necessary to observe each irradiated cell continuously after irradiation until the result for a particular biological endpoint had been ascertained. This could take many hours per cell. The result was that a low number of cells were irradiated in each experiment, for example a total of ~ 300 partially irradiated cells inclusive of all endpoints in the work of Zirkle & Bloom (1953).

Recent advances in technology now allow the automated irradiation of many cells in a short period of time and the accurate re-visiting of the irradiated cells to observe their biological responses. It has therefore become possible to irradiate many hundreds of cells in a single experiment and then to remove the cells from the irradiation apparatus prior to assaying the cells for a particular endpoint at a later time. There are many technological advances which have permitted this development in single cell irradiations, all of which rely upon the speed of modern computers and their ability to control experimental apparatus. Modern microscope stages are now designed with triple-axis, motorized drives accurate to a tenth of a micron over a range of several centimetres. These stages can be controlled using a computer software package which can also be used to provide a user friendly interface for the stage control. In order to locate the desired target a high quality image can be obtained using modern microscope optics and solid state imaging devices. The image acquisition can also be performed under computerised control and the use of current image processing packages allows the automated recognition of objects. If the beam itself is also under computer control then it becomes possible to irradiate many cells with a high positional accuracy, in a short period of time, and with a minimum of human interaction, thus eliminating a potential source of error.

A second problem facing early particle microbeam experimenters was that of dose delivery. In all cases the dose given was controlled by timed irradiations and so

incorporated not only the Poisson statistical error but also errors due to the heterogeneity of the beam produced by the particle accelerator used. This problem has been alleviated in modern microbeam apparatus by the use of various methods of particle detection (see Sections 1.6, 1.7, and Chapters 4 and 5) and fast electronics to control beam delivery. The various technological advances which have allowed this include the development of small diameter optic fibres, miniaturisation of photomultiplier tubes, solid state photon counting apparatus, improved scintillator efficiency and fast shuttering for beam control.

In addition to these technologically based problems there were also biological limitations to the early work. The most important of these was the simplicity of the biological endpoints available. With the exception of the metabolic endpoints of urea, salt metabolism, oxygen metabolism, and the uptake of elements required for DNA/RNA synthesis, the other endpoints studied were visible changes in the structure or mitotic ability of the target cells. These endpoints gave little information concerning the effect of radiation upon the normal function of cells and often required high doses to be observed.

Many single cell assays are now available which can be used even at very low doses to evaluate the effect of radiation upon the target cells. Several of these assays are able to detect low levels of damage to the DNA within the nuclei of cultured cells. Both the nuclear halo and single cell gel electrophoresis (comet assay) methods use cell lysis and the direct observation of the movement of DNA from the cell nucleus. The degree of spreading, in the case of the comet assay under the influence of an electric field, reflects the degree of DNA damage. Direct observation of chromosomes and breaks in their structure may be observed at mitosis by several methods. Spindle inhibition and exposure to hypotonic salt solution leads to an increased separation of condensed, damaged chromatin at anaphase, alternatively premature chromosome condensation can be used before metaphase to stimulate chromosome condensation into a visible state. The number of fragments created by DNA breaks can then be counted after staining with DNA binding fluorescent dyes. A more complex staining method is used in fluorescence *in situ* hybridisation (FISH). Using fluorescent markers for individual regions of individual chromosomes it is possible not only to measure the number of aberrations but also their location in the genome.

Immunofluorescent stains can be used to measure the location and quantity of individual proteins, e.g. p53 and cytoskeletal proteins, within single cells allowing the analysis of cell physiology after irradiation. In the future molecular biological techniques such as reverse transcriptase polymerase chain reaction and kinase assays may be available *in situ* for single cells (Metting, 1994), which would give further information concerning the regulation of specific processes in irradiated cells. These methods could therefore be used to give a more complete picture of the complex pathways involved in radiation response. Metabolic function can also be evaluated using fluorescent markers for ATP, Ca^{2+} and BUdR taken up during the unscheduled DNA synthesis associated with repair. In addition to these sensitive assays based on cell metabolism and DNA damage, the well established functional endpoints of mitotic ability, survival and, by growing cell lines from individual irradiated cells, mutation frequency, can also be measured on a cell by cell basis.

The final advantage which exists for modern microbeam experiments is the availability of many established mammalian cell lines of varying origin and radiosensitivity, and the potential to grow primary cell samples from fresh tissue. The biological responses of these cell lines are more likely to predict the *in vivo* responses to ionising radiations in humans than the plant cells, eukaryotes and cells from lower organisms which were irradiated in early microbeam work.

1.6 Modern Microbeams

Four ion microbeams have recently been constructed for application to radiobiological work (Braby, 1993; Folkard *et al.*, 1993; Randers-Pehrson *et al.*, 1993; Fischer *et al.*, 1993) and have been used for preliminary biological experiments (Brooks *et al.*, 1994; Prise *et al.*, personal communication). In addition, a focused X-ray beam has been produced for radiobiological work (Kobayashi & Iida, 1993) and further microbeam apparatus are under construction (Watanabe *et al.*, 1993; Belli, 1993). Each apparatus has been designed using different methods of collimation and detection, the key elements of which will be reviewed here with a summary of the beam parameters obtained.

1.6.1 The Columbia University, RARAF microbeam

The source of particles for the Columbia microbeam is a 4.2 MV Van de Graaff accelerator capable of producing beams of protons, deuterons, helium-3 and helium-4 ions with a range of LET's from 20 to 225 keV μm^{-1}. The vertical, parallel beam produced is controlled using a fast electrostatic switch and a slower beam stop. The spatial resolution of the microbeam is determined by a double collimator arrangement in two stainless steel foils. A laser-drilled hole in 500 μm thick stainless steel, with an entrance aperture of 5 μm has been produced to be collinear with a second laser-drilled hole in 500 μm thick stainless steel, having an exit aperture of 6 μm. A spacer of 300 μm is used between the steel sheets to allow the divergence of scattered particles from the first collimator, so preventing them from entering the second collimator. Using a silicon detector an energy spectrum has been obtained which indicates that 90% of the particles which exit the collimators are within the full energy peak, for an incident α-particle beam. Collimator alignment is achieved by using a ball and socket type mount with adjusting screws to orientate the collimator with the incident particle beam. The location of the collimator position is by visible light microscopy, using a laser beam to illuminate the exit hole from below. A microscope mounted above the exit aperture is used to view the position of the collimator and epi-fluorescence is used to locate the target cells. During irradiation particle detection is achieved using a transparent, gas-filled proportional counter located in front of the objective lens of the microscope. Particles must therefore have sufficient energy to traverse the target cell and a thin layer

of culture medium in order to be detected. Using automated image recognition and automated microscope-stage control, irradiations of approximately 400 cells per hour can be achieved. The beam has an overall spatial resolution, including alignment errors of 8 μm diameter (Randers-Pehrson *et al.*, 1993; 1994).

1.6.2 The Pacific Northwest Laboratory microbeam

The PNL microbeam uses a tandem 2 MV Van de Graaff accelerator as a source of protons, deuterons, helium-3, helium-4 and lithium ions. Collimation of the incident beam has been achieved using two pairs of orthogonal knife edge slits which can be adjusted to apertures of less than 1 μm. In addition, a thin copper foil with a laser drilled 5 μm hole is used to eliminate edge scattered particles resulting from scatter within the lower slit collimator. Particle detection is achieved using a transmission scintillation detector between the exit aperture and the target cells. A 7 μm thick sheet of plastic scintillator is mounted over the exit aperture of the collimator and emits photons as a result of energy deposition by an α-particle traversal. The emitted photons are then collected by an array of photomultiplier tubes positioned around the objective lens of the viewing microscope. Beam control is achieved by a fast piezo-electric shutter, allowing count rates of up to 500 particles per second to be used. Although the system uses video and computer aided imaging some user interaction is necessary for cell irradiation and so the time necessary to irradiate a single cell is at least 20 seconds (Braby, 1993).

1.6.3 The Darmstadt microbeam

This beam also uses collimation to produce a high spatial resolution beam of heavy ions. In this case collimation has been achieved by using a three stage process. Two sets of X-Y slits at six metres apart are used initially to obtain a high degree of parallelism in the incident ion beam and to reduce its width to 0.25 mm^2. A drawn glass capillary has then been used to further reduce the beam diameter to 40 μm. The final stage of collimation has been achieved using parallel sided holes etched in 30 μm thick mica, with diameters of 0.7 to 2.0 μm. The spatial resolution of this arrangement is shown in Figure 1.10 and shows a beam diameter of ~ 2 μm (Kraske *et al.*, 1990).

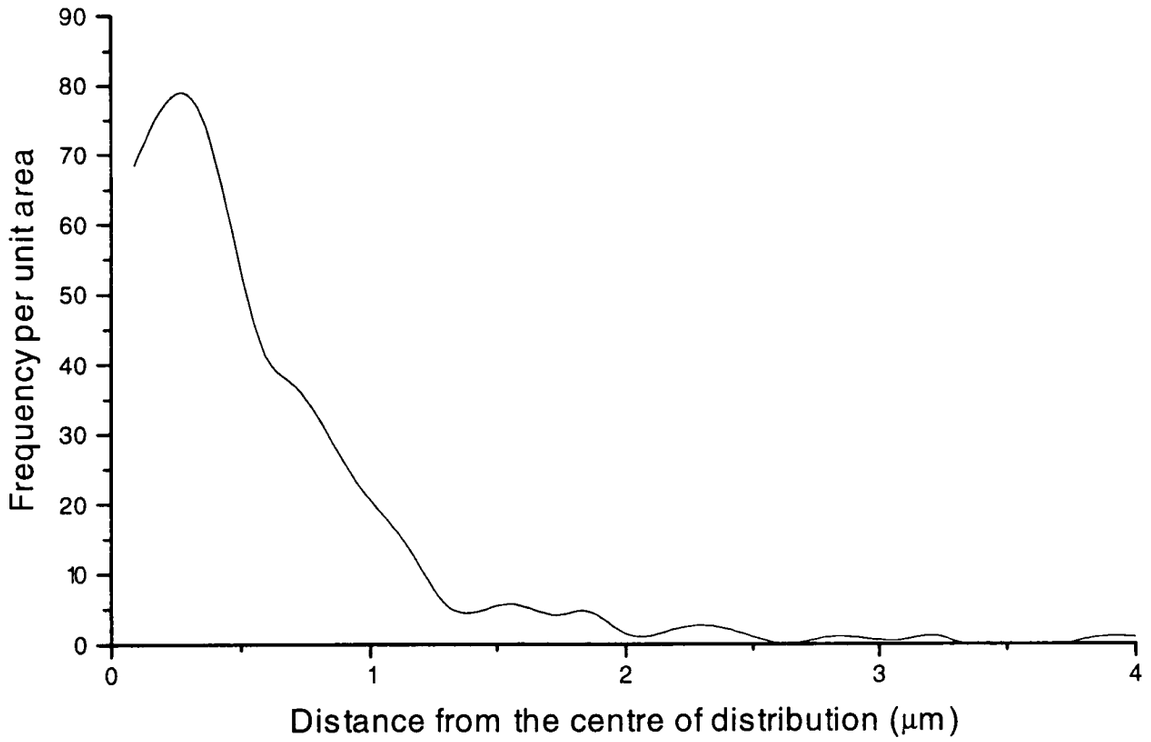

Figure 1.10 Spatial resolution of the heavy-ion microbeam produced at GSI Darmstadt.The data was converted to frequency per unit area from the published frequency data.

The particles are accelerated by the UNILAC linear accelerator at GSI Darmstadt and have an energy of 1.4 MeV/u for atomic masses from carbon to uranium, corresponding to LET's from 500 to 12,000 keV μm^{-1}. The penetration of these high energy particles is sufficient to allow their detection after traversing the target cells, using a surface barrier particle detector. Although the spatial resolution of the beam is high the rate at which samples may be irradiated is limited by the low count rate of the beam to ~ 40 cells per hour (Kraske *et al.*, 1990).

1.6.4 The Photon Factory focused microbeam

This beam is an example of a focused X-ray microbeam which, although at present used mainly for elemental analysis of biological samples, could be adapted for the irradiation of single cells. The X-ray beam is produced by the synchrotron radiation facility at Tsukuba, Japan, and is focused to a spot of ~ 5 μm in diameter by imaging a pair of slits forming an aperture of ~ 200 μm × 200 μm, using a pair of cylindrical multilayer mirrors in the Kirkpatrick-Baez configuration. The calculated and experimentally measured beam widths produced are shown in Figure 1.11.

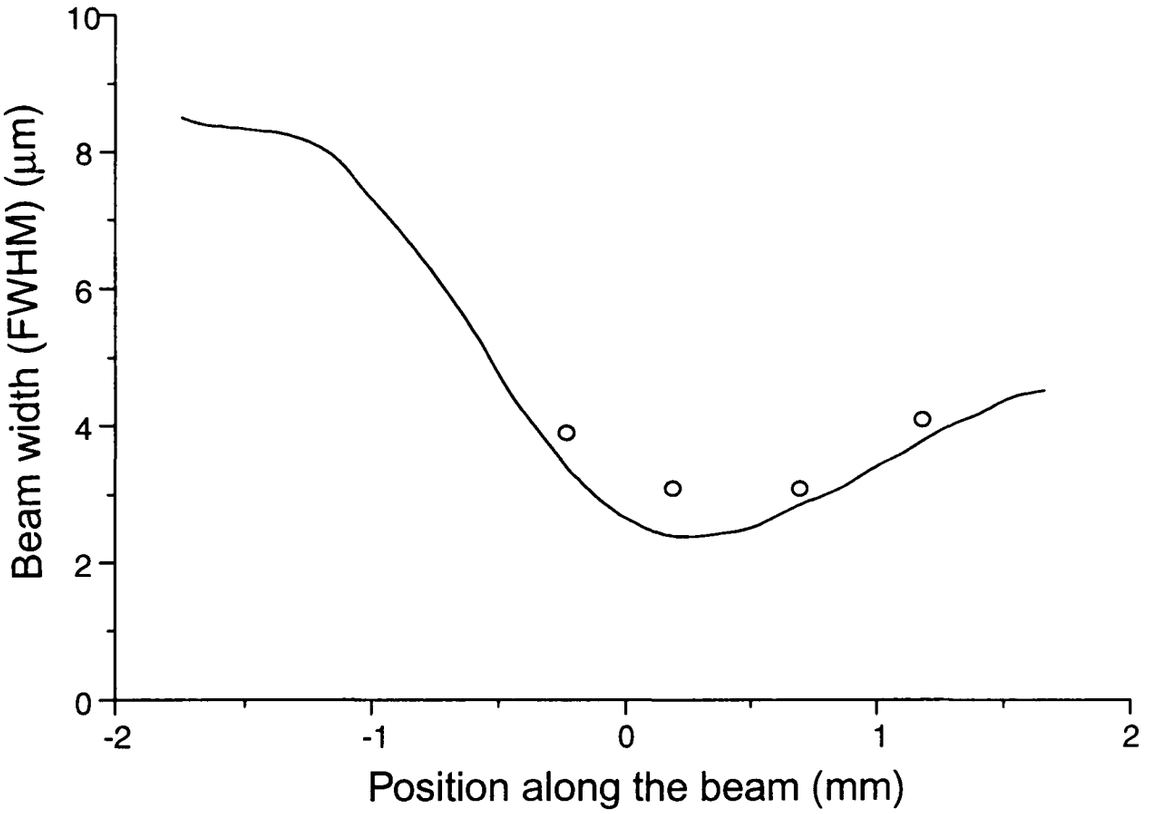

Figure 1.11 Calculated (Solid Line) and measured (Open Circles) Photon Factory microbeam widths as a function of the position along the beam. Zero is the focal point.

In addition to these working microbeams, including the Gray Laboratory microbeam which will be discussed in detail in Chapter 1.7, others are in various stages of development. At Legnaro, Italy, an attempt is under way to produce a focused particle microbeam using a 2 MV Van de Graaff accelerator (Belli, 1993) and at Takasaki, Japan a second heavy ion beam is under development (Watanabe *et al.*, 1993). Future ideas also include the production of a focused soft X-ray microprobe using zone-plate technology at the Gray Laboratory (Folkard *et al.*, 1993) and for an in-flight impact facility, based upon a flow cytometer machine geometry, at Legnaro, Italy (Colautti *et al.*, 1993).

These beams will together allow the investigation of critical radiobiological questions and will enable comparison of the data obtained at the various facilities.

1.7 The Gray Laboratory Microbeam

1.7.1 Ion beam production and control

The Van de Graaff accelerator used to produce the incident particle beam at the Gray Laboratory is a single-ended 4 MV machine capable of accelerating protons to 4.25 MeV and doubly charged helium-3 ions to 8.5 MeV (Michael *et al.*, 1994). A pre-existing positive beam line, previously used for broad-field irradiation, has been modified and a 90° bending magnet inserted to produce a vertical beam emerging in a dedicated laboratory area, see Figure 1.12. The power of the bending magnet limits the energies of the protons and helium ions which may be used to 4.0 MeV and 5.6 MeV respectively. A beam-stop is used to permit the continued use of the room beneath the microbeam laboratory for broad-field irradiations, without radiation contamination in the room above, (Folkard *et al.*, 1993) and is also included in the safety interlock system of the beamline. Both steering and magnetic focusing elements are installed along the beam line and these are used to shape and position the emerging beam. Beam monitoring is achieved using a quartz viewing crystal at the exit of the bending magnet and by current monitors attached to two pairs of perpendicular slits higher in the beam-pipe. Control of particle irradiations will be achieved by deflecting the beam using a fast electrostatic shutter (Vojnovic *et al.*, 1993), a transient 20 kV potential applied to the electrostatic steering plates in ~ 1 μs, and then the operation of a slower mechanical shutter with an operating time of 50 ms (Folkard *et al.*, 1993) to turn off the beam.

The vertical position of the final microbeam collimator-detector assembly is achieved using a three position Z-drive designed by M Folkard (1993) and is shown in Figure 1.13. This arrangement allows the retraction of the final few centimetres of the beamline to permit movement of the target support without damage to the collimator-detector assembly or disturbance of the target itself.

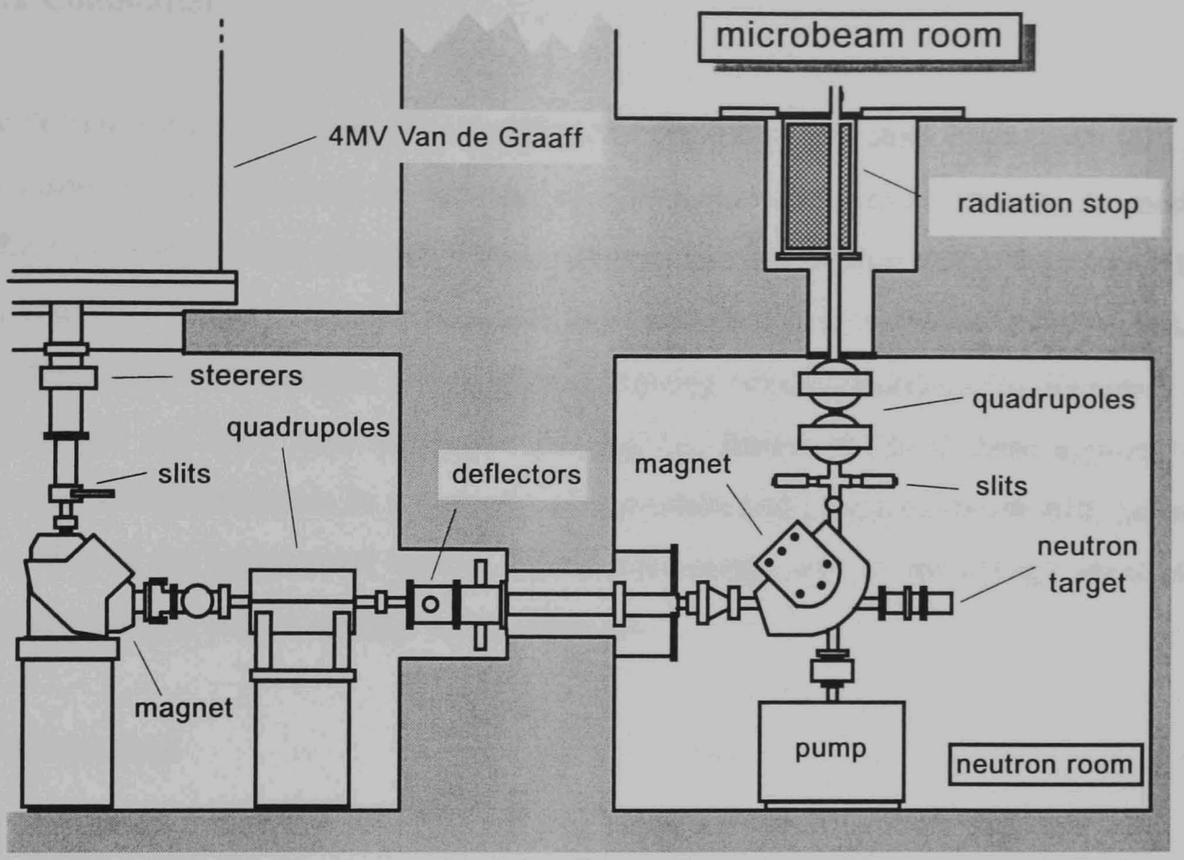

Figure 1.12 Geometry of the beam-line used to produce a vertical positive ion beam at the Gray Laboratory.

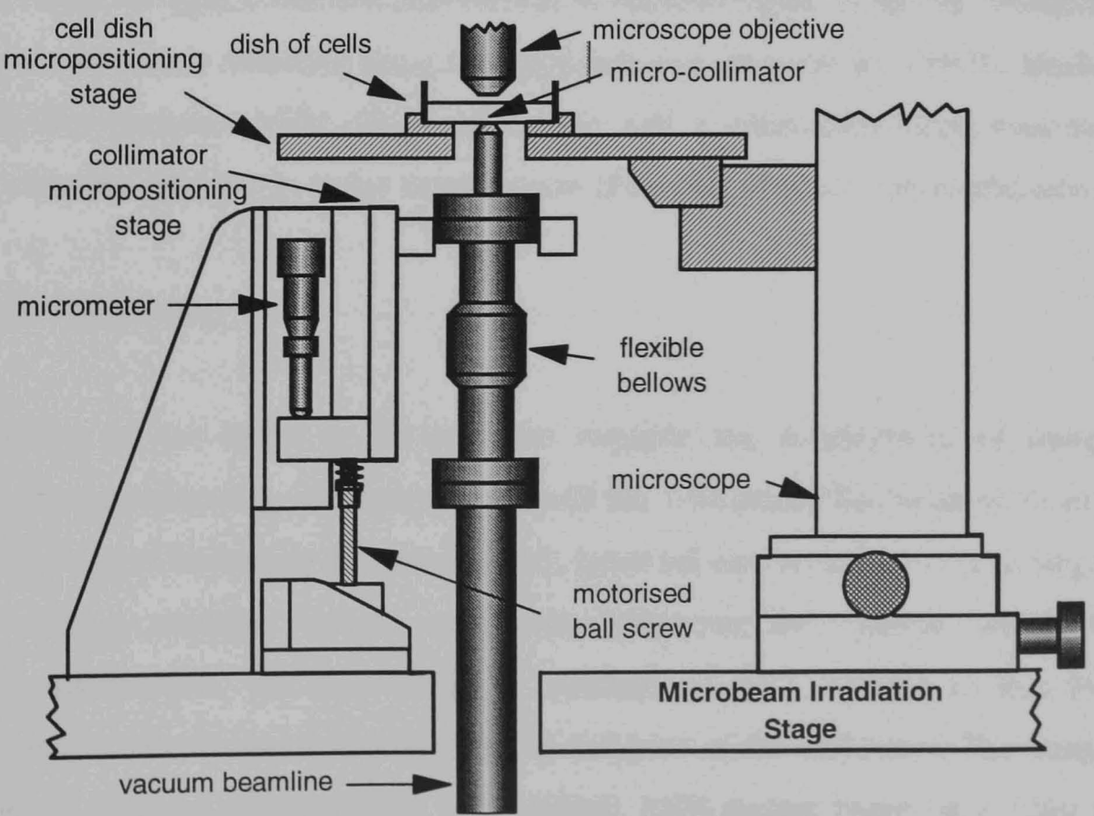

Figure 1.13 Vertical 3-position Z-drive designed by M Folkard (1993) for the positioning of the final collimator-detector assembly.

1.7.2 Collimation

The design and development of collimation for the Gray Laboratory microbeam will be discussed in Chapters 2 & 3. The use of a computer simulation program to model collimator designs (see Chapter 2) has allowed the construction of a commercially manufactured silicon collimator having a triangular profile of 3 μm side length (Hollis, this thesis). Also commercial glass capillaries having circular profiles with diameters of 5.0 and 1.5 μm have been developed (Hollis, this thesis). Both of these approaches collimate the proton beam to a high spatial resolution and produce a beam with greater than 95% of the transmitted protons in the full-energy peak of the energy spectrum, obtained using a silicon surface barrier detector.

1.7.3 Detection

The design and development of a charged particle transmission detector will be discussed in Chapters 4 and 5. A transmission detector has been developed using a thin crystal of zinc sulphide doped with silver atoms, which is coupled to 30 μm diameter glass optic fibres for light collection and transfer to photomultiplier tubes for detection. The efficiency of proton detection using this approach was shown to be > 99 % (Hollis, this thesis). For particles which fully traverse the cell a microscope-turret mounted ionisation chamber detector is under development (Folkard, personal communication).

1.7.4 Target Alignment

The positioning of the target to be irradiated required the development of image acquisition, image processing, software control, and the commercial hardware necessary to position the target accurately (Vojnovic *et al.*, personal communication). The target is viewed using a modified upright microscope (Olympus, BH2 Series) with epi-fluorescence attachments. The microscope is mounted on an X-Y stage so that the objective lens can be positioned directly over the exit hole of the collimator. The image of the target is acquired using a Xillix Microimager 1400 system based on a 1280 × 1024 pixel, 7 μm × 7 μm pixel size, charge coupled device connected to a 486 PC fitted with a Matrox 1280 imaging board. Some image processing was possible using the pre-

existing system software, however, a significant amount of modification has been necessary to attain adequate cell recognition (Vojnovic, Locke & Gilbey; 1993). Having located the target it may then be positioned over the collimator exit aperture using a commercial microscope stage (Marzhauser), having a step size of 0.25 μm and driven under software control from within the image processing software package.

1.7.5 Irradiation Procedure

Initial alignment of the collimator is necessary using optimisation of both count rate and the energy spectrum of the beam, measured using a surface barrier detector. Next the X-Y position of the viewing microscope is adjusted to place the exit hole of the collimator at approximately the centre of the field of view. The vertical position of the collimator is then adjusted to ~ 20 μm below the focal plane of the objective lens, using the in-house designed and built Z-drive (Folkard, 1993).

Initialization of the positioning stage to allow the use of absolute co-ordinates of the target position is achieved by the use of a custom made plate having two well defined corners. These corners are located by a purpose written software procedure and their relative positions are used to define both an absolute position and the angular deviation between the stage and the CCD camera (Vojnovic, personal communication).

Having set-up both the collimator and the microscope stage the initialisation plate may then be replaced by a stainless steel walled, mylar-bottomed dish of cultured cells. The dish is then raster-scanned to identify the position of each cell to be irradiated. Each field is analyzed individually by the imaging software to locate all objects within the field and then geometric object parameters are used to determine whether the object is a single cell suitable for irradiation and to obtain its centre of mass. The co-ordinates of each object in the irradiation area are stored and are then used to revisit all of the objects recognised as cells to allow rapid irradiation.

Having completed the irradiation the cell dish may be removed, after lowering the collimator approximately 20 mm to allow the dish to clear the objective lens. Each cell dish assembly is uniquely labelled and so can be returned to the microscope stage at a

later time to assay for the appropriate biological endpoint, using the stored co-ordinates to re-visit the locations of the irradiated cells.

Using this system it is possible to irradiate approximately 200 cells per hour, depending on the proton dose given.

Chapter 2 : Simulation of Collimators

2.1 Introduction

Several different geometries and materials have been used to collimate particles for microbeam apparatuses (Zirkle, 1953; Haynes & Zirkle, 1960; Kuzin & Wainson, 1966; Berns, 1974). However, the use of these different designs has been determined by the availability of materials and machining processes rather than by theoretical design. In order to optimise the performance of the collimator system for the Gray Laboratory microbeam, a computer model was developed (Watts, personal communication). This model was used to simulate the performance of various collimator geometries and also to study the effect of variations in the parameters of both the incident beam and the collimator itself upon the quality of the microbeam produced. The beam quality can be described using parameters for both the energy and the spatial resolution of the beam. A perfect collimator would collimate the incident beam to a spatial resolution defined by the ratio of its width to its length, the aspect ratio, and with no energy loss of the transmitted particle. However, all materials will introduce scattered particles into the beam either by collision with the collimator wall and scatter back into the collimated beam or by the transmission of particles through the exit surface of the collimator, see Figure 2.4. The proportion of scattered particles within the beam determines the quality of the beam produced by a particular collimator and will depend upon both the collimator geometry and the material from which it is fabricated. The simulation programme described in this chapter has been written by Dr S J Watts (Brunel University, UK) and was developed by the author as part of this work. It was used to model the effect of particle scattering on the transmitted beam for a range of collimator geometries and incident beam parameters.

2.2 Principles of Collimation

The track of a particle through matter and its energy loss as it traverses a given material are determined by individual interactions with the atoms of the target material. For 4 MeV protons the primary interactions will be elastic scattering with the nuclei and inelastic scatter with the atomic electrons of the material. The scattering resulting from

the Coulomb interaction of a single particle with a single atom, see Figure 2.1, is described by the Rutherford formula (Fernow, 1986) :-

$$\frac{d\sigma}{d\Omega} = z_1^2 \, z_2^2 \, r_e^2 \left(\frac{mc}{\beta p}\right)^2 \frac{1}{4 \sin^4(\theta/2)} \qquad \text{- (2.1)}$$

$$\textit{where} \quad d\Omega = 2\pi \, \theta \, d\theta$$

$$\textit{and} \quad d\sigma = 2\pi \, b \, db$$

where z_1 is the charge of the incident particle, z_2 is the charge of the target atom, **m** is the mass of the incident particle, r_e is the classical electron radius, **p** is the momentum of the incident particle, θ is the scattering angle and $\beta = v/c$. The equation describes $d\sigma/d\Omega$ which is the probability that an incident particle with normal incidence between **b** and **b + db** will be scattered into an element of solid angle between θ and $\theta + d\theta$. The integral of $d\sigma/d\Omega$ defines σ which is the probability that an incident particle will be scattered into an element of solid angle between 0 and θ.

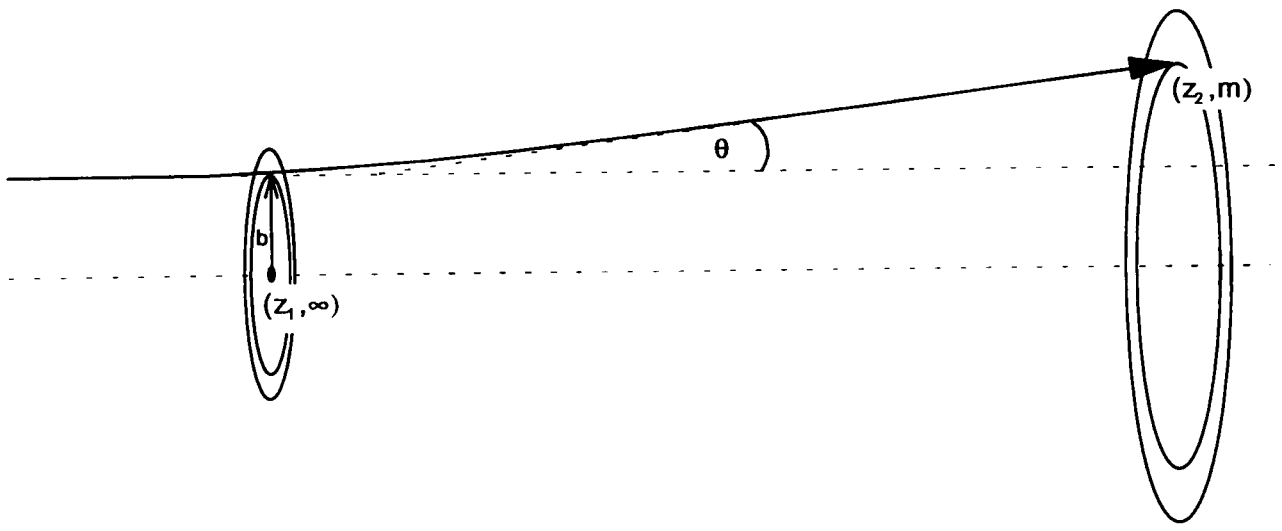

Figure 2.1 A schematic of the interaction of a single incident particle having a charge z_2, mass **m** and impact parameter **b** with a single atomic nucleus having charge z_1. The particle is deflected through an angle θ.

The modelling of a particle track in matter may be achieved by the calculation of individual atomic collisions with the atoms of the material, however, this process is mathematically demanding and requires considerable computation time. An empirical approximation may be made for small angles of scatter, $\theta < 10°$, in materials with an atomic number higher than 20, and for a limited range of scatterer thickness between $10^{-3} \times L_{rad}$ and $10 \times L_{rad}$, where L_{rad} (radiation length) is a material specific quantity derived

from the energy loss of high energy electrons in electron-photon showers. This simplification approximates the range of scattering angles, for particles transmitted through a thickness **x** of scattering material, to a Gaussian distribution having a root mean square scattering angle, θ_{rms}, given by (Aguilar-Benitez *et al.*, 1992) :-

$$\theta_{rms} = z_{inc} \frac{14.1}{p\ \beta} \sqrt{\frac{x}{L_{rad}}} \left(1 + \frac{1}{9} \log_{10} \frac{x}{L_{rad}} \right) \qquad \text{- (2.2)}$$

where θ_{rms} is the scattering angle, z_{inc} is the charge on the incident particle, **x** is the thickness of scatterer and L_{rad} is the radiation length of the scattering material.

The mean energy loss, **dE**, of a particle with energy **E** in distance **dx** of the material is calculated using the Bethe formula (Knoll, 1979) :-

$$-\left(\frac{dE}{dx}\right) = 4\pi \frac{z^2\ e^4\ n}{m_0\ v^2} \left[\ln \left(\frac{2\ m_0\ v^2}{I\ (\ 1 - \beta^2\ )} \right) - \beta^2 \right]$$

$$\textit{where} \quad \gamma = \frac{1}{\sqrt{1 - \beta^2}} \qquad \text{- (2.3)}$$

$$\textit{and} \quad \beta = \frac{v}{c}$$

where **z** is the charge on the incident particle, **e** is the charge on an electron, **n** is the electron density of the material, $\mathbf{m_0}$ is the rest mass of the electron, **v** is the velocity of the incident particle and **I** is the mean excitation potential. The approximation to the scattering angle distribution does not include the tail produced by single high angle scatter events due to near nuclear collisions. It will therefore underestimate the degree of scatter produced in a given material. The approximation has been tested by comparison with TRIM, a widely used a particle transport code (Ziegler, 1977). The comparison of results from these two simulation programmes is made in Figure 2.2 and 2.3, for an incident beam of 4 MeV protons traversing 70 μm of silicon.

As predicted, the simulation underestimates the mean angle of scatter for this thickness of silicon due to the absence of events producing large scattering angles in the

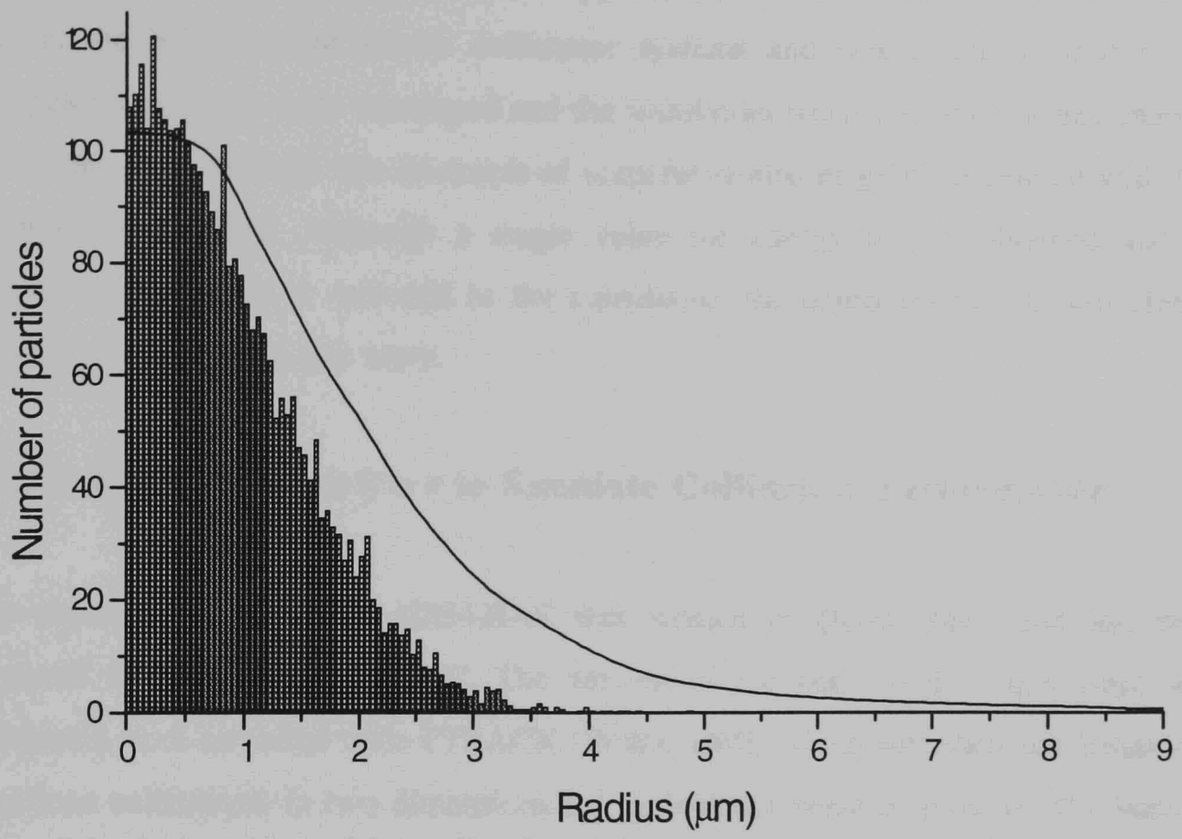

Figure 2.2 A comparison of the predicted spatial resolution of an incident 4 MeV proton beam after transmission through 70 μm of silicon using the TRIM ion transport code (Solid Line) or the code developed by Dr S J Watts (Bars).

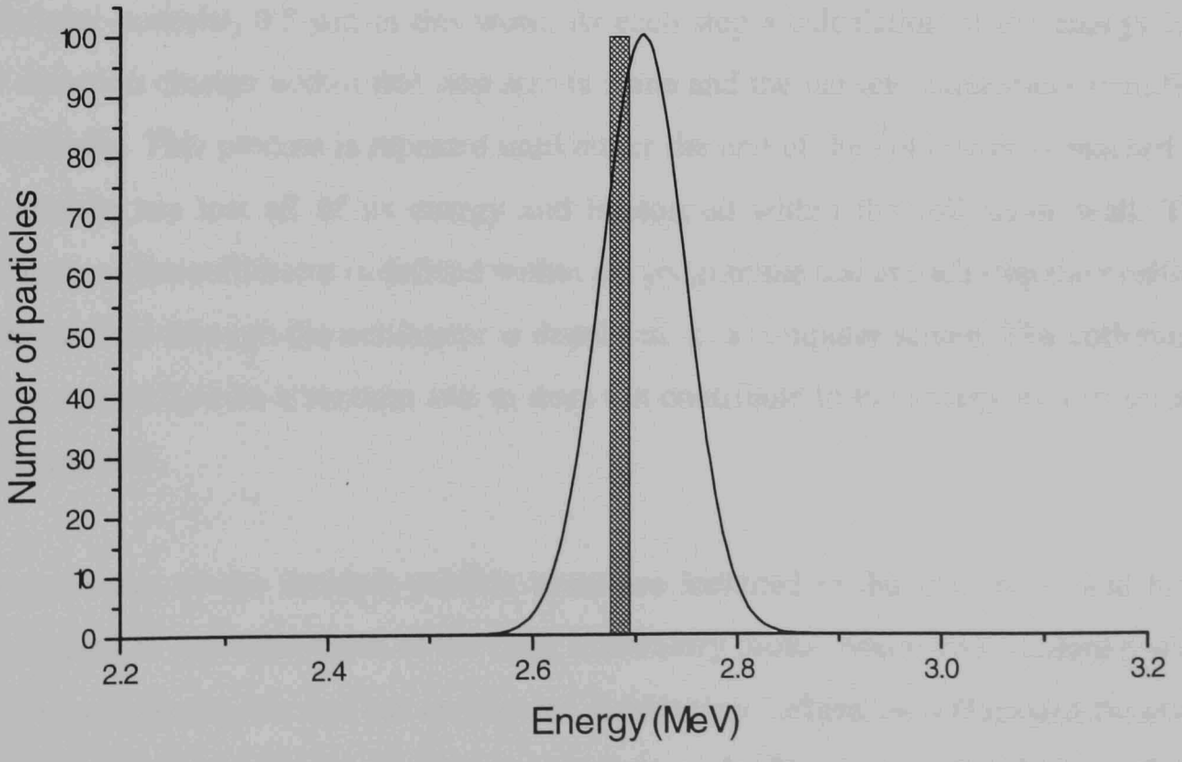

Figure 2.3 A comparison of the predicted energy resolution of an incident 4 MeV proton beam after transmission through 70 μm of silicon using the TRIM ion transport code (Solid Line) or the code developed by Dr S J Watts (Bars).

approximation used. For this study the approximation will be sufficiently accurate to predict the behaviour of silicon collimator systems and was therefore used in the computer simulation code developed and the simulation work described in this chapter. The energy loss through this thickness of scatterer is also in good agreement with that calculated by TRIM. Although a single value for energy loss is obtained and no statistical fluctuation is included in the calculation the approximation is sufficiently accurate to be used in this work.

2.2 Computer Programme to Simulate Collimator Performance

The simulation programme KJH4.BAS was written in *Quick Basic* and has been executed using a 33MHz 486-PC. The version of the code used in this work was developed from an initial code PTRACK (Watts, 1993) which simulates the behaviour of silicon collimators in two dimensions for an incident beam of protons. The various parameters of the incident beam and collimator may be modified either as user defined inputs or within the code.

The programme functions by taking a series of short steps of fixed length through the collimator material, 0.5 μm in this work. At each step a calculation of the energy loss and direction change within that step size is made and the particle parameters modified accordingly. This process is repeated until either the end of the collimator is reached or the particle has lost all of its energy and is stopped within the collimator wall. The geometry of the collimator is defined within the programme and at each step the position of the particle through the collimator is displayed on a computer screen. The collimator hole is assumed to be a vacuum and so does not contribute to the energy loss or scatter of the particle.

The properties of the incident particle beam are included in the simulation and have been chosen to represent those of the Gray Laboratory proton beam. The incident proton beam is monoenergetic and has an angular distribution defined by a Gaussian function the width of which may be modified within the code. The spatial distribution of the beam is a top-hat distribution whose width is chosen to be significantly larger than the collimator width simulated.

If a particle is transmitted through the collimator then its energy, position and direction are stored to a data file for later analysis. In order to obtain sufficient numbers of transmitted particles several tens of thousands of incident particles were modelled for each collimator. For each simulation, the computer time required to obtain sufficient data was approximately 7 hours.

A summary of the programme structure is shown below.

```
        Define initial parameters of particle and collimator material
        Define collimator geometry
        For I = 1 to N (number of particles)
        Reset initial parameters
10      Calculate energy loss for particle
        Calculate distribution of scattering angles
        Generate a random scattering angle from the distribution
        Subtract energy loss
        Add scattering angle to particle trajectory
        Calculate new particle co-ordinates
        Map position of particle to screen
            IF particle has reached the collimator end  THEN
            Write energy, position and direction to file
            Goto 20
            ELSE IF Particle has zero energy THEN
            Goto 20
            ELSE
            Goto 10
20      NEXT I
```

An example of the screen output from the programme is shown in Figure 2.4. The example given is for a 5 μm wide beam of 4 MeV protons incident upon a 1 μm wide, 1000 μm long silicon collimator. The figure shows examples of particles which are stopped in the collimator walls, scattered back from the wall into the proton beam, transmitted through the exit surface of the collimator, and transmitted directly through the collimator hole.

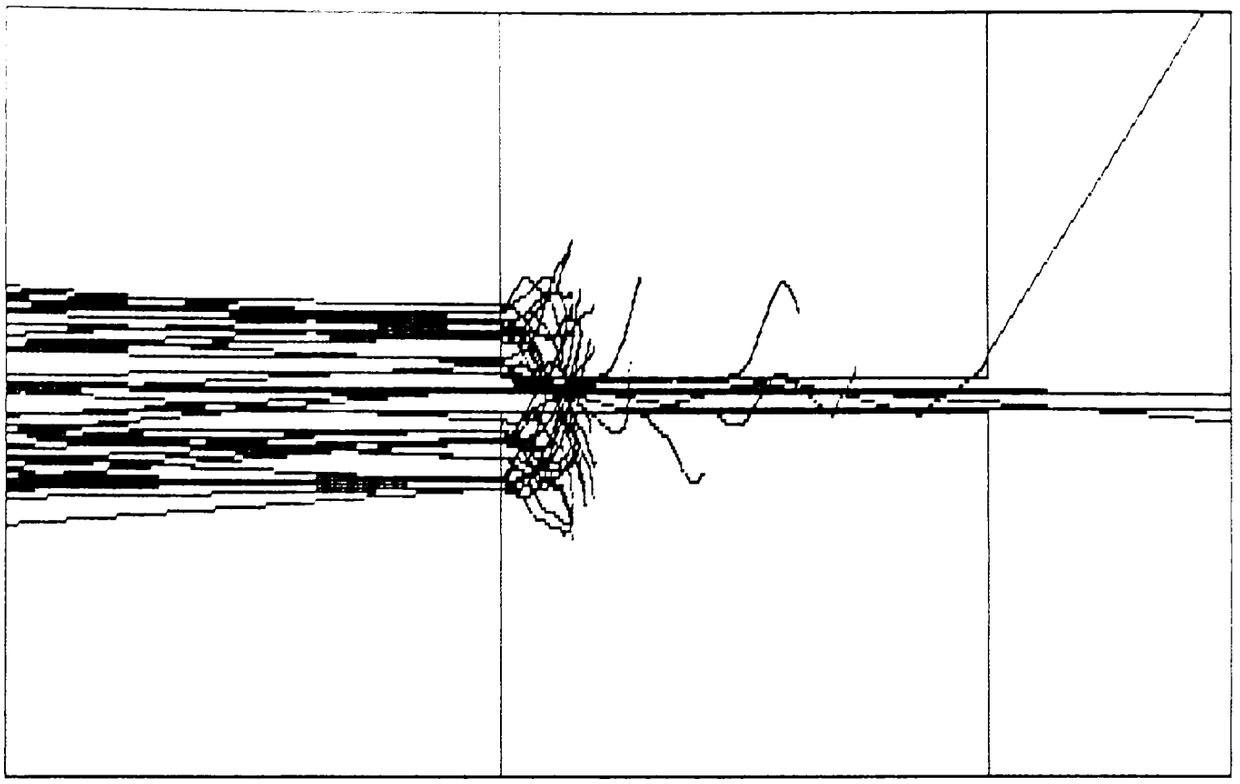

Figure 2.4 An example of the screen output from the programme KJH4.BAS developed from the PTRACK simulation written by Dr S J Watts. The example shown is for a beam of 4 MeV protons with a width of 5 μm incident upon a 1 μm wide, 1000 μm long silicon collimator.

Many modifications have been made to the original code to improve its range of applicability, to improve its speed of calculation and to allow its use by users unfamiliar with the programme. A complete annotated example of a programme designed to simulate the performance of a single straight sided collimator in silicon with user defined inputs for both the collimator and the incident proton beam parameters is given in Appendix I. A summary of the simulation programmes developed in this work for the various collimator geometries and incident beam parameters modelled and a description of their functions are given in Appendix II.

2.4 Data Obtained from the Simulation Programme

The final parameters of each particle transmitted through the collimator are stored to file for analysis. These data describe a beam profile at the exit hole, how the beam spreads as it emerges from the collimator and the energy distribution of the transmitted particles. An example of the profiles obtained from the analysis of these data are given in Figures 2.5, 2.6 and 2.7.

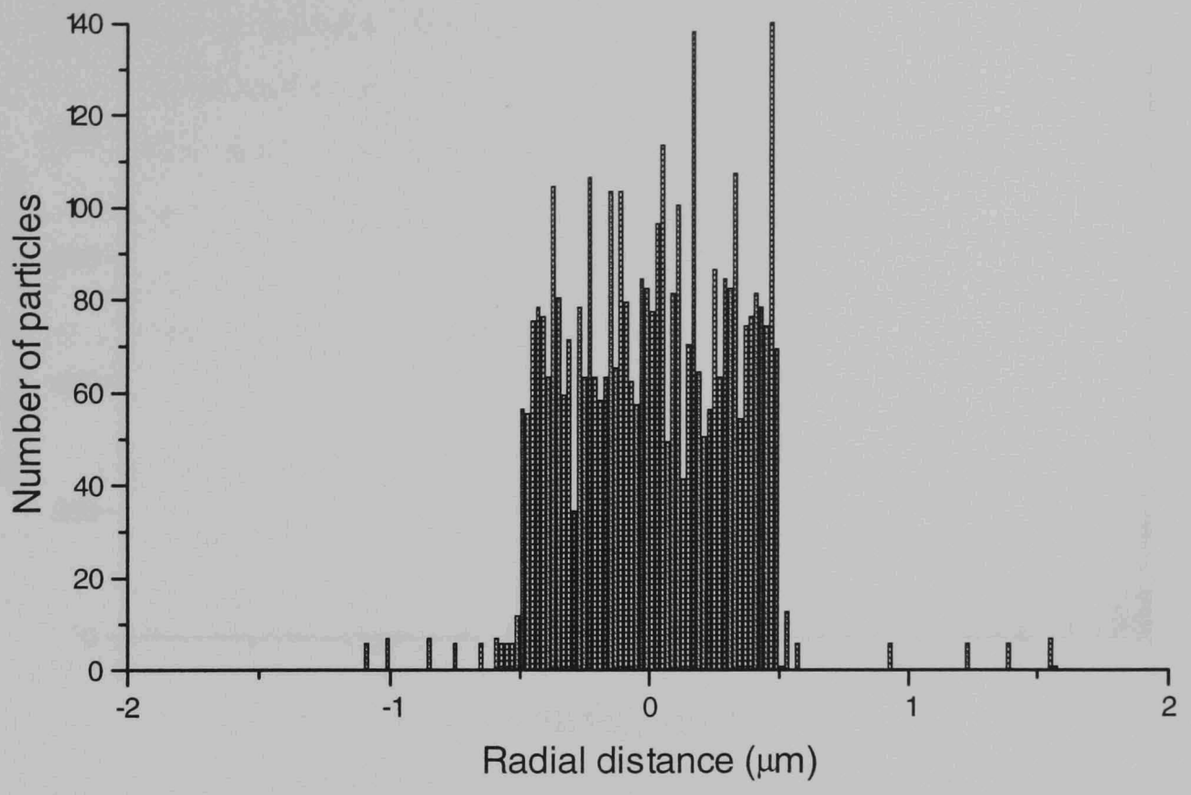

Figure 2.5 An example of the spatial data obtained from the programme KJH4.BAS for a 4 MeV proton beam incident upon a 1 μm wide silicon collimator, at the exit surface of the collimator modelled.

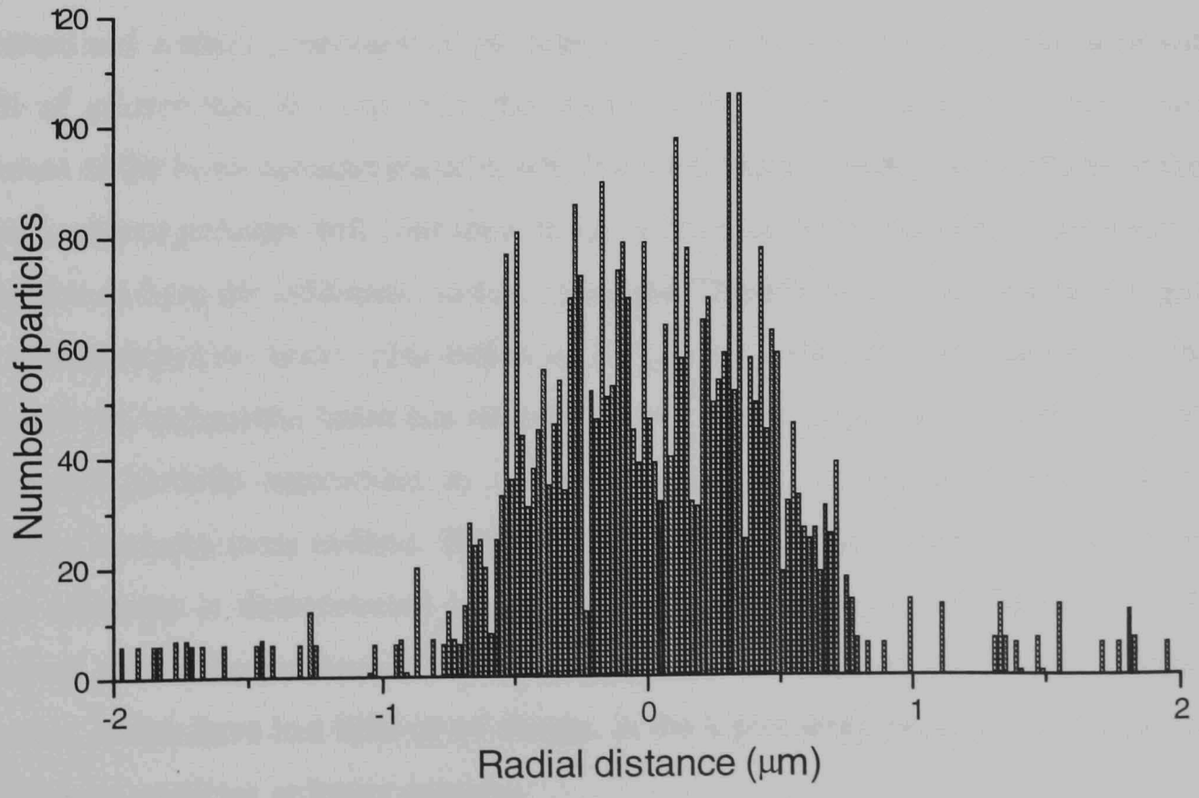

Figure 2.6 An example of the spatial data obtained from the programme KJH4.BAS for a 4 MeV proton beam incident upon a 1 μm wide silicon collimator, at 500 μm from the exit surface of the collimator modelled.

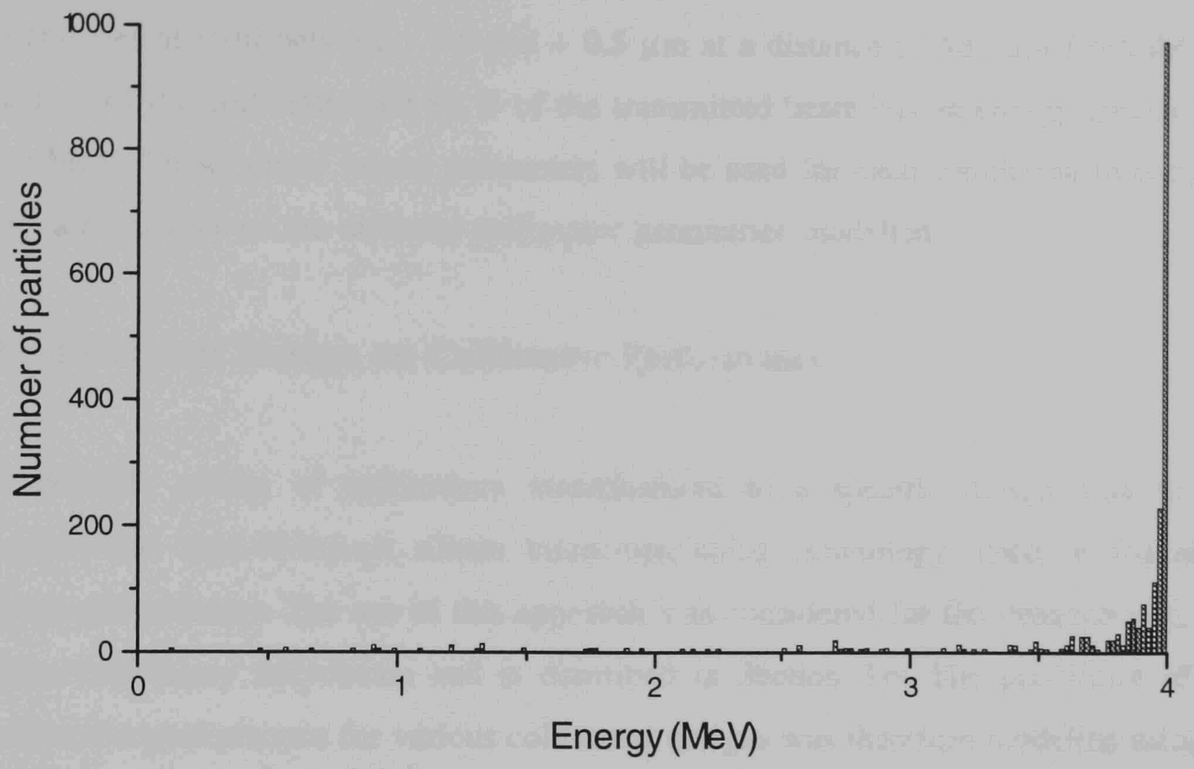

Figure 2.7 An example of the energy data obtained from the programme KJH4.BAS for a 4 MeV proton beam incident upon a 1 μm wide silicon collimator.

Figure 2.5 shows the spatial distribution of the transmitted beam at the exit surface of the collimator. It shows a beam with a central element emerging from the collimator aperture and a small proportion of particles emerging through the collimator wall with radii of greater than 0.5 μm from the centre of the 1 μm wide hole. If the central element of the beam contains particles which were scattered lower in the collimator then these scattered particles will contribute to an increase in the transmitted beam width as the distance from the collimator surface increases. This effect is demonstrated in Figure 2.6 which shows the spatial distribution at 500 μm from the collimator surface. At this distance the transmitted beam has become larger and the presence of a core of highly collimated particles surrounded by a halo of scattered, and therefore lower energy, particles becomes more evident. The relative proportion of the scattered to unscattered beam elements is demonstrated by the energy spectrum shown in Figure 2.7. The spectrum shows the presence of a high proportion of unscattered and lightly scattered particles, which have lost little or no energy, in the high energy peak, with a proportion of scattered particles at lower energies.

The quality of the beam produced in this example may be described using both spatial

and energy parameters, which may be calculated from the data. In this case 65 % of the beam lies at radii between - 0.5 and + 0.5 μm at a distance of 500 μm from the exit surface of the collimator and 88 % of the transmitted beam has an energy greater than 3.9 MeV. These single valued parameters will be used for each simulation to compare the performance of the different collimator geometries modelled.

2.5 Effects of Design on Collimator Performance

A possible source of collimators manufactured to a specific design was to use commercial state-of-the-art silicon micro-machining technology, used in the semi-conductor industry. The use of this approach was considered for the production of the Gray Laboratory microbeam and is described in Section 3.6. The prediction of the collimator performance for various collimator designs was therefore modelled using an incident 4 MeV proton beam and a silicon-walled collimator. The incident beam width was chosen to be significantly larger than the collimator entrance aperture and with a divergence of 0.067° full width at half maximum, as an approximation to the divergence of the Gray Laboratory beam, estimated using in-line beam monitors.

2.5.1 Effects of length on collimator performance

The length of a collimator has a strong influence on its performance. A study was therefore undertaken using the simulation of a 4 MeV proton beam incident upon parallel-sided silicon collimators of various widths and lengths. The data obtained from these simulations were used to calculate parameters for both the energy and spatial resolutions of the transmitted beam for each collimator modelled. Defined limits of energy loss and lateral spread of the collimated beam were used to provide single parameter descriptions of the collimator performance. The results of these analyses for collimator widths of 1 μm and 3 μm are shown in Figures 2.8 and 2.9.

The data in Figure 2.8 show that for the collimation of a 4 MeV incident beam by a parallel-sided silicon collimator with a width of 1 μm the optimum energy resolution can be achieved using a collimator of 650 μm in length. The penetration of 4 MeV protons in silicon is ~ 146 μm and so at shorter lengths the energy resolution decreases rapidly.

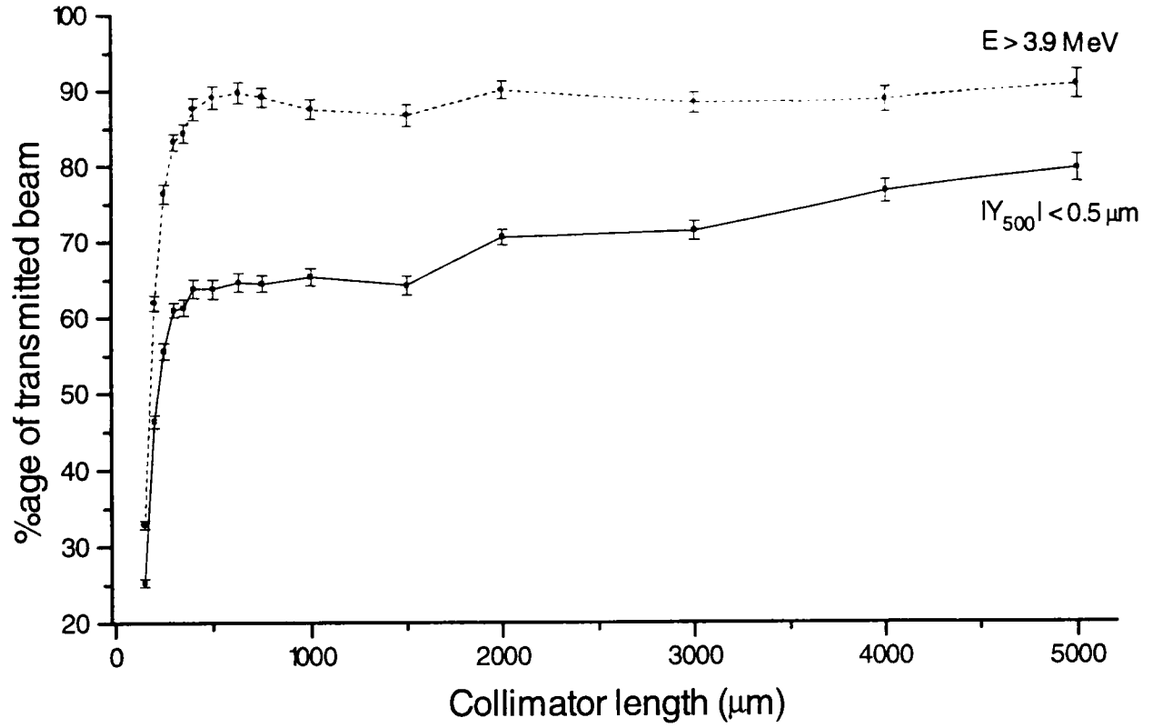

Figure 2.8 The effect of length upon the performance of a 1 μm wide collimator in silicon for an incident beam of 4 MeV protons. The spatial resolution is represented by the percentage of the transmitted beam having a radius of < 0.5 μm at a distance of 500 μm from the exit surface of the collimator (Solid Line). The energy resolution is represented by the percentage of the transmitted beam having an energy of > 3.9 MeV (Dashed Line).

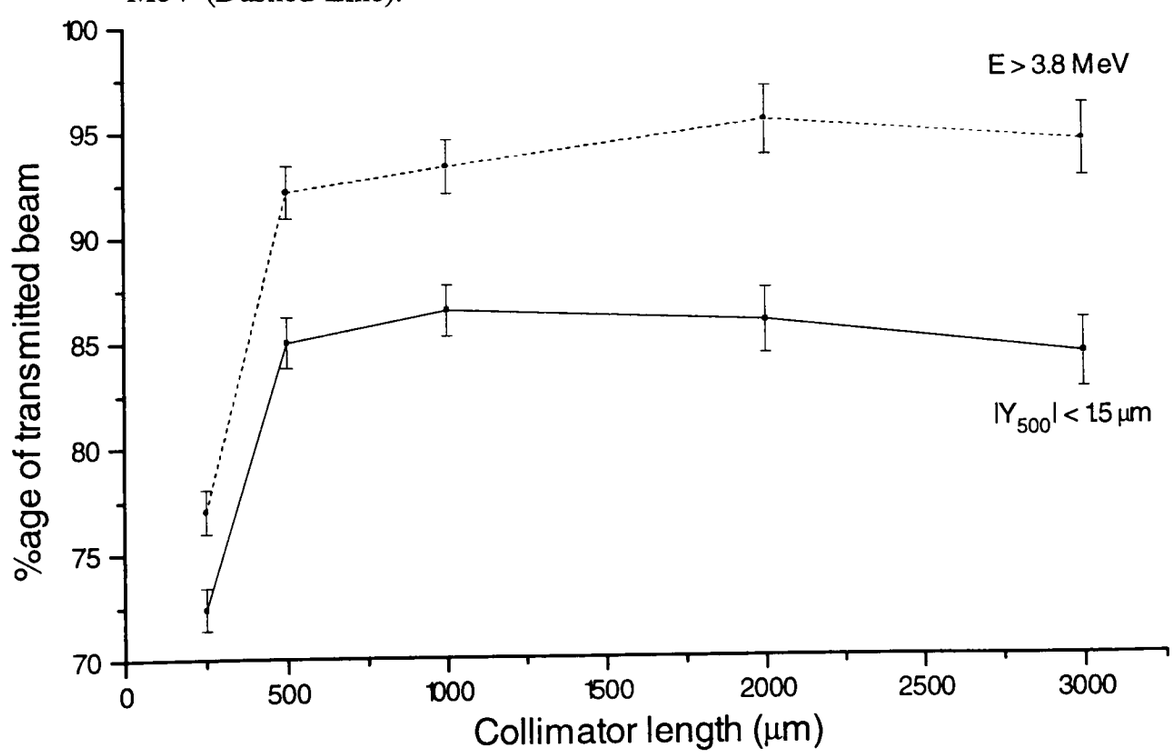

Figure 2.9 The effect of length upon the performance of a 3 μm wide collimator in silicon, for an incident beam of 4 MeV protons. The spatial resolution is represented by the percentage of the transmitted beam having a radius of < 1.5 μm at a distance of 500 μm from the exit surface of the collimator (Solid Line). The energy resolution is represented by the percentage of the transmitted beam having an energy of > 3.8 MeV (Dashed Line).

At longer lengths the energy resolution reaches a plateau and no further gain is achieved. The spatial resolution of the beam shows the same rapid decrease in performance at lengths of less than 650 μm, however, a gradual improvement is obtained by an increase in the collimator length beyond 650 μm. A 10 % gain in the spatial resolution of the transmitted beam is obtained by an increase in collimator length from 650 to 5000 μm and demonstrates a reduction in the divergence of the transmitted beam for an increase in the aspect ratio of the collimator modelled. An anomaly appears to be present in the region of 1500 μm to 2000 μm, however, further simulation and comparison with detailed experimental data would be necessary to clarify whether this is a real effect, an artefact of the model used or simply a random statistical fluctuation.

The data in Figure 2.9 show similar results for a collimator width of 3 μm.

In summary, if designing a parallel-sided collimator in silicon for the collimation of a 4 MeV proton beam then collimator lengths of at least 650 μm will be required to produce the optimum energy resolution and a further reduction in the divergence of the collimated beam will be obtained by the use of even longer lengths.

2.5.2 Effects of misalignment on collimator performance

The previous section has demonstrated that collimators of considerable length are necessary to obtain optimum collimator performance, however, the longer a collimator is the more difficult it will be to align with the incident proton beam. The effects of collimator misalignment on the quality of the transmitted beam were therefore investigated by the simulation of different degrees of beam misalignment for a 1 μm wide, 1000 μm long silicon collimator and a 4 MeV incident proton beam with a full width at half maximum divergence of 0.067°. The quality of the transmitted beam was assessed using the same parameters as those described in Section 2.4.1. The data are presented in Figure 2.10.

The data demonstrate a reduction in the beam quality for an increase in the misalignment between the collimator and the incident beam. For the collimator parameters used in this simulation a misalignment of 0.1° results in a loss in collimator

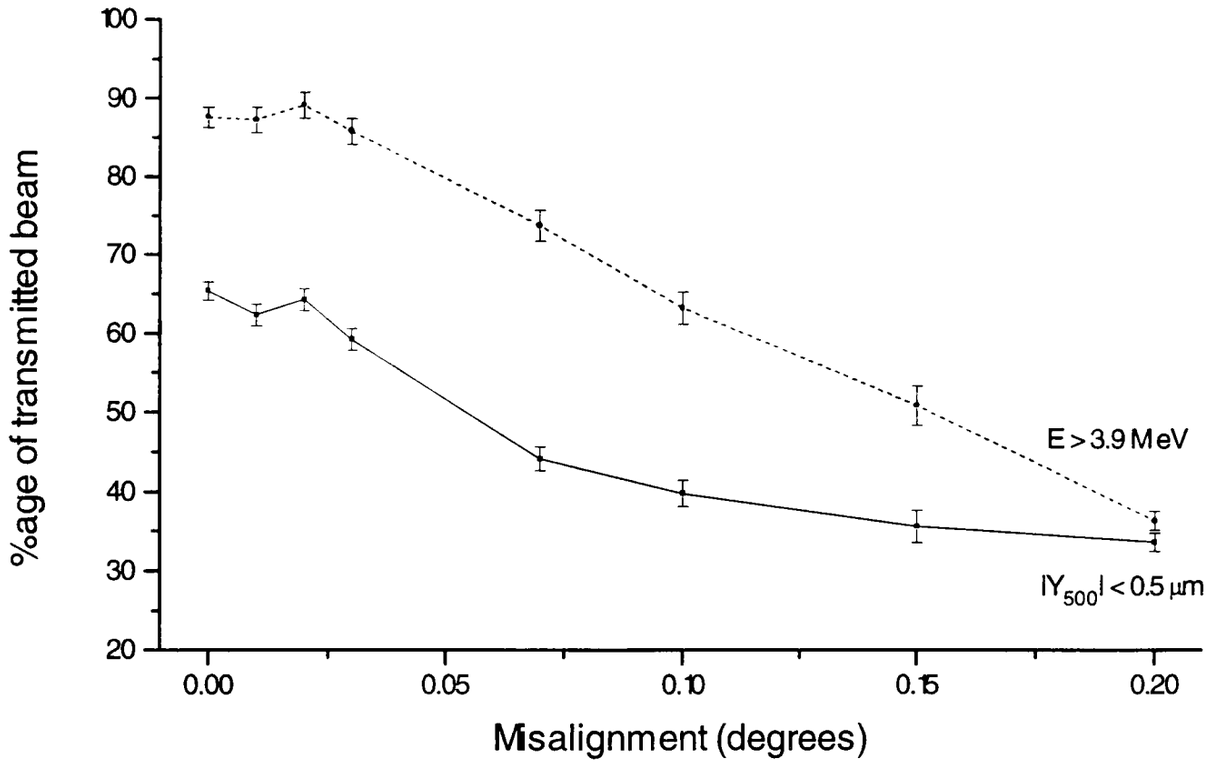

Figure 2.10 The effect of misalignment with the incident beam upon the performance of a 1 μm wide, 1000 μm long collimator in silicon, for an incident beam of 4 MeV protons. The spatial resolution is represented by the percentage of the transmitted beam having a radius of < 0.5 μm at a distance of 500 μm from the exit surface of the collimator (Solid Line). The energy resolution is represented by the percentage of the transmitted beam having an energy of > 3.9 MeV (Dashed Line).

performance of 25 % in the spatial resolution and 25 % in the energy resolution of the transmitted beam. A plateau in the collimator efficiency is present at angles of less than 0.025° and correlates well with the geometrical line-of-sight occlusion of the collimator to the beam direction at an angle of, $\tan^{-1}(0.5/1000) = 0.029°$. In these simulations no consideration was given to the result of misalignment on the count-rate of the collimated beam. However, in an experimental situation this would of course become an important consideration.

In summary, the alignment of the collimator with the beam has a significant effect on beam quality and so must be carefully considered in the design of experimental apparatus to support micro-collimators.

2.5.3 Effects of incident beam divergence on collimator performance

Having determined the optimum collimator parameters for an incident 4 MeV proton beam it was also necessary to establish the effect that variations in the quality of the incident beam would have on the emergent beam. The effect of the incident beam divergence on the quality of the collimated beam was investigated for a 4 MeV proton beam incident upon a 1 μm wide, 1000 μm long collimator in silicon. The results obtained are summarised in Figure 2.11.

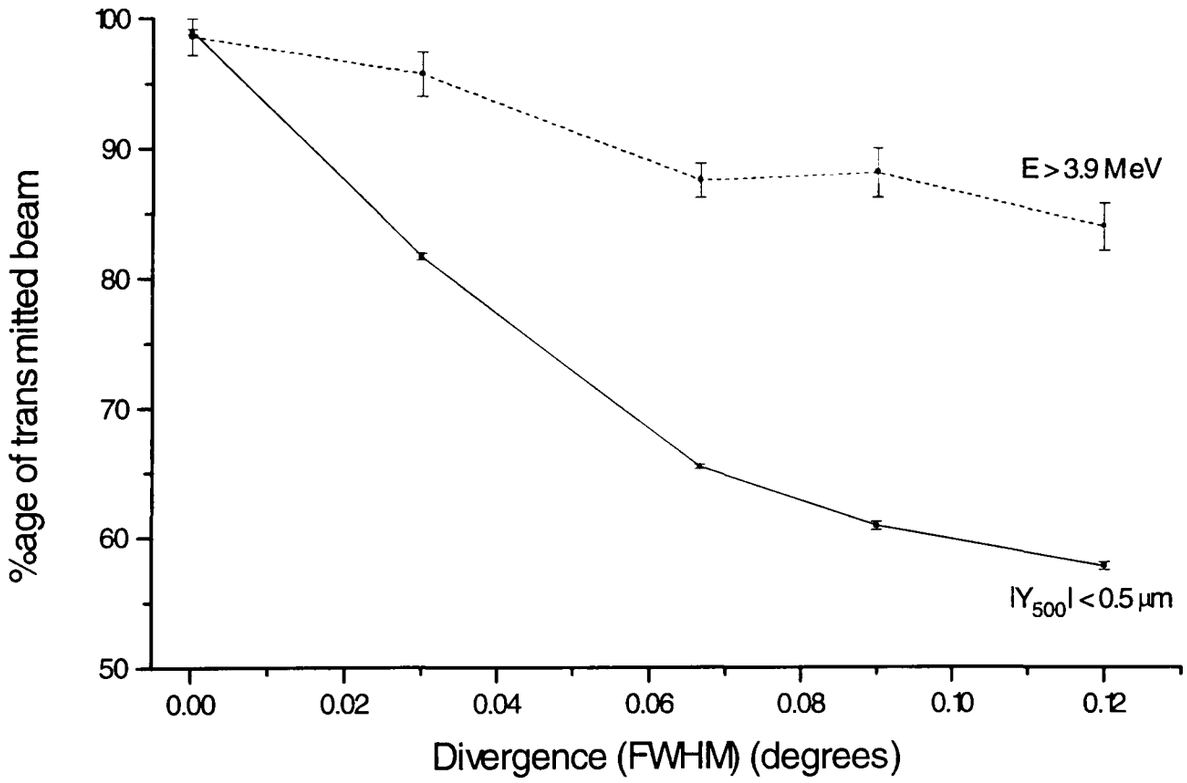

Figure 2.11 The effect of the incident beam divergence upon the performance of a 1 μm wide, 1000 μm long collimator in silicon, for an incident beam of 4 MeV protons. The spatial resolution is represented by the percentage of the transmitted beam having a radius of < 0.5 μm at a distance of 500 μm from the exit surface of the collimator (Solid Line). The energy resolution is represented by the percentage of the transmitted beam having an energy of > 3.9 MeV (Dashed Line).

The data show that as the incident beam divergence increases the quality of the collimated beam is reduced as a result of an increased amount of scatter within the collimator material. At a full width at half maximum incident beam divergence of 0.067°, used in many of the simulations in this work, the loss in beam quality over that of a parallel proton beam is 10 % in the energy resolution and 35 % in the spatial resolution of the collimated beam.

It can be seen from the data that significant improvements in the quality of the collimated beam may be obtained by reducing the divergence of the incident beam. Therefore effort must be made to optimise the parallelism of the incident beam in any apparatus used to produce a microbeam by collimation.

2.6 Improved Collimator Designs

The modelling described in the previous sections used only the case of single, straight-sided collimators. By the use of more complex designs it may be possible to improve the performance of a collimator beyond that of a simple, straight-sided device with an equivalent total length. Many designs were modelled some of which will be considered here.

2.5.1 Effects of introducing voids on collimator performance

The use of a void in a collimator is, in effect, the production of a two-collimator arrangement in which the first collimator produces an incident beam with a low divergence, which therefore improves the quality of the beam incident upon the second collimator and so improves the performance of the second collimator. An alternative approach is to consider the first collimator as the primary collimating element and the second collimator as an anti-scatter device, removing reduced-energy particles which are introduced into the transmitted beam by scatter within the first collimator. This approach is used by both the PNL and Columbia microbeam facilities.

Simulations were performed using a variety of collimator geometries. Three examples are given here of two-collimator designs using parallel sided silicon collimators having total lengths of 1000, 3000 and 5000 μm. The incident beam used in the simulations was a 4.0 MeV proton beam having an angular divergence of 0.067°. The data were analyzed using the same parameters for energy loss and spatial resolution as those described in Section 2.4.1 and the results are shown below in Table 2.1.

1st Collimator Length (μm)	Void Length (μm)	2nd Collimator Length (μm)	%age of beam with E > 3.9 MeV	%age of beam with $\|Y_{500}\|$ <0.5μm
1000	3000	1000	95.8 ± 1.8	95.2 ± 1.8
5000	-	-	93.9 ± 1.9	93.5 ± 1.9
1000	1000	1000	90.8 ± 2.1	72.9 ± 2.1
3000	-	-	89.3 ± 1.9	75.4 ± 1.9
333	333	333	91.1 ± 1.4	67.4 ± 1.4
1000	-	-	89.6 ± 1.9	65.5 ± 1.9

Table 2.1 Data obtained for the simulation of single, parallel-sided collimators having a width of 1 μm and lengths of 1000, 3000 and 5000 μm compared to the data obtained for two-collimator assemblies of equal width and overall length.

The data show that in almost all cases the addition of a void into the collimator arrangement appears to produce at most a modest improvement of ~ 2 % in both the energy and spatial resolutions of the collimated beam. However, for the number of transmitted particles modelled in this study the result is not at a high level of statistic significance. Further work using larger numbers of particles would perhaps clarify this result.

The data suggest that the improvements obtained by the use of collimator voids must be carefully weighed against the increased difficulty of collimator alignment produced by the use of double collimator assemblies and the increased difficulty of production of more complex designs.

2.6.2 A curved, magnetically-tuned collimator design

A particle moving at right angles to a uniform magnetic field travels in a circular path with a defined radius, assuming a constant particle energy. If the particle is scattered by atomic collisions within the magnetic field then it will lose energy and undergo a change in its radius of curvature. If a collimator were produced with a curvature matching that

of the track of the particle beam, either by tuning the beam energy or the magnetic field, then particles scattered within the collimator would suffer a critical change in the radius of curvature along which they were travelling. This would increase the chance of them colliding with the walls further along the collimator and so reduce the number of scattered particles emerging in the transmitted beam, see Figure 2.12. The advantages of this type of collimator were proposed by Dr S J Watts (personal communication). Modifications to the existing code have allowed the simulation of collimators with radii of curvature of 289.1 mm, corresponding to that of a 4 MeV proton in a 1 Tesla magnetic field. The results for curved collimators having lengths of 1500 and 5000 μm are shown below in Table 2.2.

Collimator Length (μm)	%age of beam with E > 3.9 MeV	%age of beam with $\|Y_{500}\| < 0.5\mu m$
Curved 1500	98.4 ± 0.8	94.5 ± 0.8
Straight 1500	83.4 ± 1.1	61.1 ± 0.9
Curved 5000	98.9 ± 3.3	97.4 ± 3.3
Straight 5000	90.9 ± 1.9	79.9 ± 1.8

Table 2.2 Data obtained for the simulation of single, parallel-sided collimators having a width of 1 μm and lengths of 1500 and 5000 μm compared to the data obtained for curved collimators having an equal length and width, in a 1 Tesla transverse magnetic field.

The data show that a considerable improvement in collimator performance is obtained for a curved collimator in a magnetic field over a straight collimator of equivalent length, for lengths of both 1500 and 5000 μm. For the parameters chosen to describe the transmitted beam the improvement in energy resolution is 15 % for the 1500 μm collimator and 9 % for the 5000 μm collimator. The improvement in the spatial resolution of the transmitted beam is 33 % for the 1500 μm and 17 % for the 5000 μm long example.

The results demonstrate that if this design could be constructed then a significant gain in beam quality could be achieved. The construction would depend upon the production

of a highly uniform and tunable magnetic field with minimal protrusions above the surface of the collimator. In addition, the design would require considerable accuracy in the relative alignments of the beam, collimator and magnetic field.

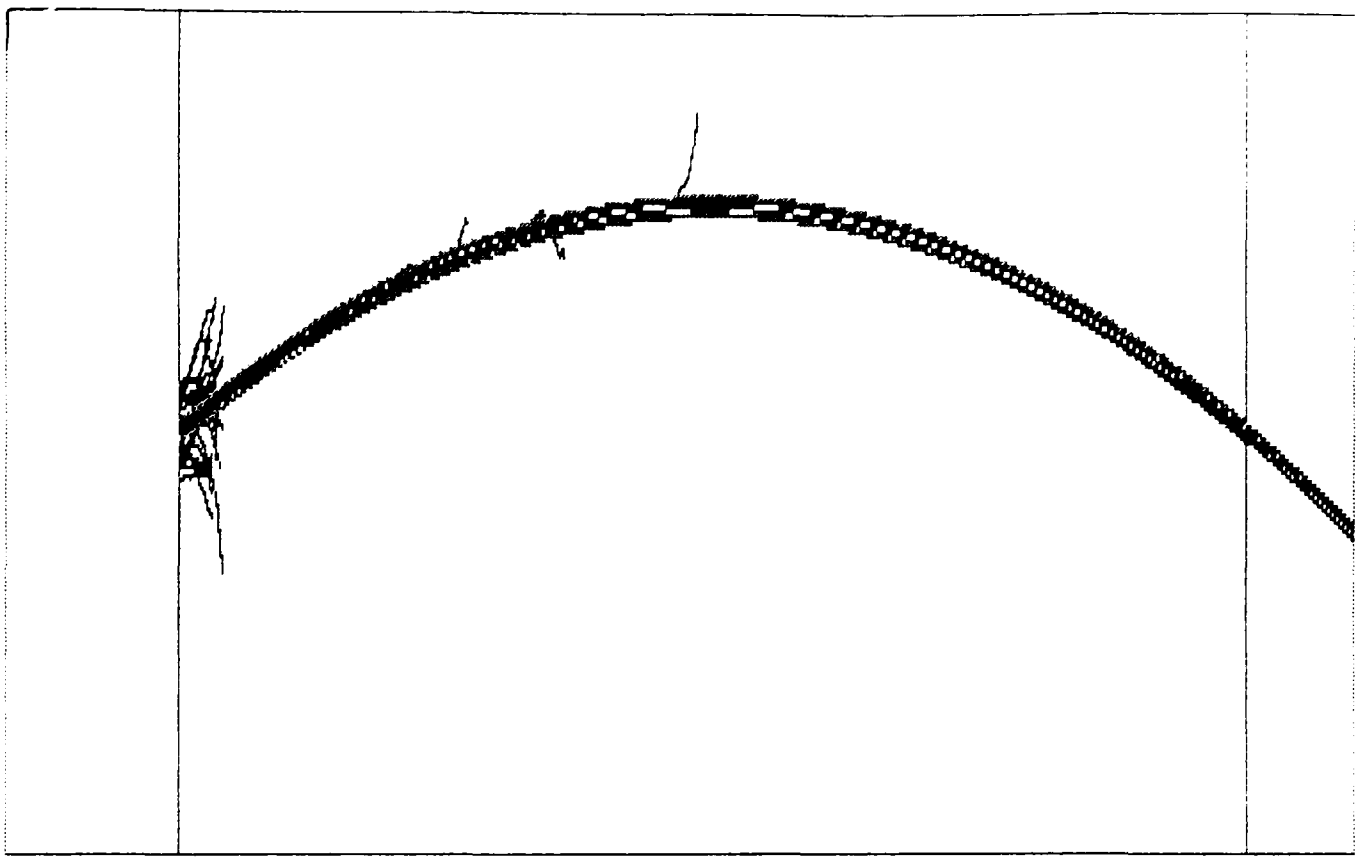

Figure 2.12 An example of the screen output from the programme KJH50.BAS developed from the PTRACK simulation written by Dr S J Watts. The example shown is for a beam of 4 MeV protons with a width of 5 μm incident upon a 1 μm wide, 5000 μm long curved silicon collimator.

2.7 Conclusions

It is apparent from this work that the production of a high quality microbeam is dependent on the many parameters of the collimator, its mounting assembly and the incident proton beam. The simulations performed gave approximations to the optimum values of the parameters investigated and suggested designs which may be used to improve the performance of microbeam collimator systems. The parameters used were however considered independently and variations in the values of the fixed parameters in each simulation may have an effect upon the optimum values obtained for the variable parameter. For example, a change in the incident beam divergence may effect the optimum collimator length which would in turn alter the effect of collimator

misalignment.

These studies have provided a basic understanding of collimator behaviour. Optimum values of length were obtained for two collimator widths and the expected performance of various collimator designs was obtained. This information will be valuable in the design of collimator systems for the Gray Laboratory microbeam facility.

2.7 Further Work

These simulations have provided a basis for the prediction of collimator performance. However, further work using the current simulation code could provide further insights into the design of collimator systems.

In order to understand how the optimum collimator parameters vary with changes in the incident beam parameters, simulations using a range of beam divergences, energies and particle types would be necessary. The collimator geometry could then be tailored to the particle beam used. In addition, studies involving alternative collimator materials, having different characteristics of particle scattering and energy loss, would be useful to determine if further improvements in collimation are possible with other manufacturing techniques based on the use of different collimator materials.

A limitation encountered in these studies has been that to reduce the statistical errors in the data to less than 2 % would require the simulation of many thousands of particle tracks which would require a prohibitively long computing time. The use of a more powerful computer or a faster computing language would alleviate this problem.

In addition to the use of the current version of the simulation programme to obtain further information about the behaviour of collimator systems it would be possible to make improvements to the code to make more accurate predictions of collimator performance.

The approximations made for the effect of multiple particle scattering in this simulation limit the accuracy of the predictions made. The use of detailed calculations of particle

tracks using more rigorous approximations for scatter and energy loss would increase the level of confidence in this work. Work to make these improvements has been performed by H Gohla (1995) at Brunel University under the supervision of Dr S J Watts. The data obtained using the detailed simulation code agree closely with that of other particle simulation codes available (Watts, personal communication). The results of the detailed code also agree well with those of the approximations used in this study, endorsing the use of this programme in the simulation of collimator systems.

A further improvement to the current code would be to expand the simulation from two-dimensions to three-dimensions. The effect of this change is shown below to decrease the ratio of the exit aperture to the wall material by a factor of two.

Two-Dimensions :- Exit width : Wall Length

$$d : 2L$$

Three-Dimensions :- Exit area : Wall area

$$\pi (d/2)^2 : \pi d L$$

$$\Rightarrow \quad d/4 : L$$

$$\Rightarrow \quad d : 4L$$

This change may therefore result in the introduction of more scattered particles into the transmitted beam and so implies a reduced performance for a three- rather than two-dimensional simulation. Further work is necessary to investigate this effect on collimator performance.

The implementation of these changes to the simulation programme will result in a more accurate simulation of collimator behaviour but may be constrained by the time required for the simulation of sufficient particle numbers unless faster computing methods are applied.

Chapter 3 : Collimation

3.1 Introduction

The production of particle microbeams by collimation was used as early as 1953 by Zirkle, resulting in an α-particle microbeam of having a radius of ~ 2.5 μm. This facility and others like it have been reviewed in Section 1.4. In each case the beam relied on the use of a small hole in a thin piece of highly stopping material. The method of production of these holes was highly individual to each facility and demonstrated the ingenuity used to construct microbeam apparatus.

The microbeam constructed by Zirkle used either adjustable slits or a V-groove clamped against a flat plate to produce a high aspect ratio triangular collimator. The V-groove in this case was produced by 'a controlled collision' between the plate and a highly polished blade. More commonly the collimator used was a several micron diameter aperture in a thin metal disc. The apertures used have been produced by many methods including the puncture of an aluminium or lead disc by a finely ground steel needle (Haynes & Zirkle, 1960) resulting in a 1.5 μm exit aperture, by ion-beam drilling in bronze (Kuzin & Wainson, 1966) resulting in a 1-2 μm diameter aperture, by depositing tin onto an electroformed 6 μm electron microscope grid until the aperture was only 1 μm in diameter (Berns, 1974) and by squeezing lead plates around a fine fibre which was then removed leaving a fine bore hole (Berns, 1974).

Although ingenious, these methods have only been successful in the production of holes which were relatively short, < 100 μm. The collimator lengths were adequate for the collimation of α-particles, however, the simulation work described in Chapter 2 suggests that for the higher penetration of 4 MeV protons collimators of considerably longer lengths are required.

Several methods of production of collimator holes of various dimensions are described here with an analysis of their performances and conclusions concerning their applicability to the production of a 3.5 MeV proton microbeam.

3.2 Laser Drilled Holes in Glass

3.2.1 Method

The use of high power lasers to drill micron sized holes in thin materials has been used in many applications where uniform circular apertures are required, for instance in optics applications. However, the drilling of high aspect ratio holes of only a few microns in diameter is less well established since it has fewer commercial applications. An attempt was made for us by Excitech (UK) Ltd to produce high aspect ratio holes by laser drilling. The nature of the drilling process makes glass more suitable for drilling than metal, however, since the range of 4 MeV protons in borosilicate glass is 119 μm the aspect ratio of the collimator must be at least 50:1 for a 2 μm hole. A preliminary attempt was therefore made by drilling holes in 140 μm thick borosilicate glass. The geometry of the holes produced was conical, with a 30 μm diameter circular entrance aperture, a 5 μm diameter circular exit aperture, and a length of 140 μm. Eighteen holes were drilled in a single microscope slide cover-slip and by cutting the glass single holes were obtained in glass pieces of ~ 5 mm square.

A single drilled hole was mounted onto a stainless steel end-cone using Torr Seal (Varian Vaccum Products, USA) vacuum cement. The removable end-cone was then mounted onto the end of the proton microbeam line to test the performance of the collimator. The end-cone had a 500 μm diameter, 1 mm thick hole drilled vertically into its upper surface over which the collimator was aligned, see Figure 3.1. Using this arrangement scattered protons from the mounting assembly did not contribute to the transmitted beam and so did not result in a loss of collimator performance.

Although no alignment adjustment of the collimator relative to the incident beam was possible using this arrangement the mounting of the glass directly onto the perpendicular top surface of the end-cone produced sufficiently accurate alignment to allow the transmission of the proton beam. Additional adjustments to optimise the collimator performance were then made using the beam steering elements.

The transmitted protons were detected using a microscope-lens-turret mounted silicon

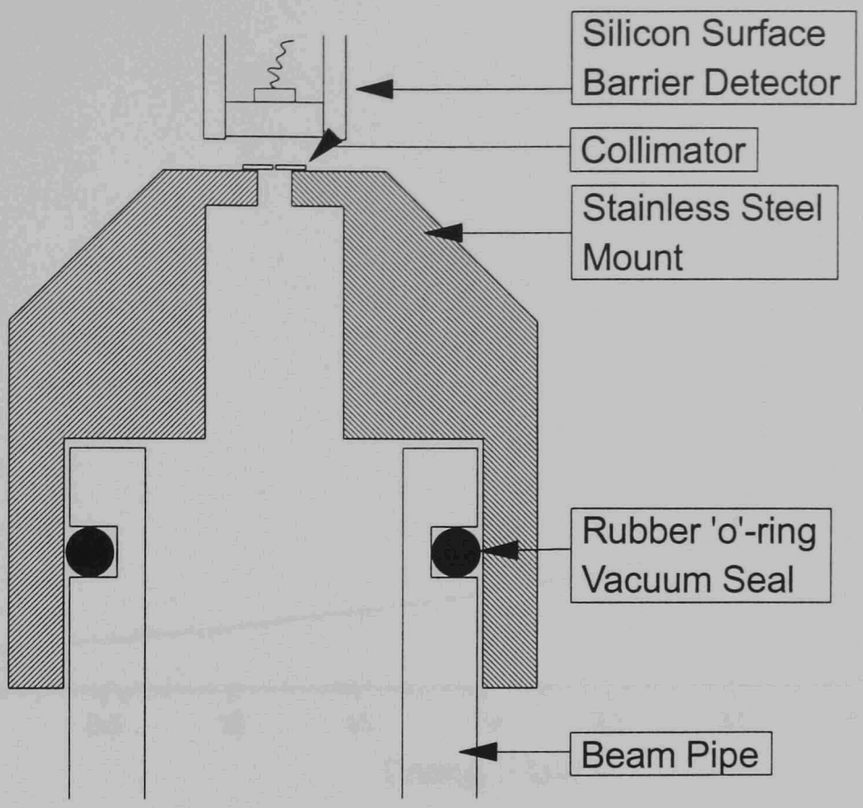

Figure 3.1 The mounting arrangement used to test the performance of laser-drilled collimators in 140 μm of borosilicate glass for an incident beam of 3.5 MeV protons.

surface barrier detector connected to commercial nucleonics pulse shaping and amplification units. The energy spectrum was obtained using pulse height analysis by a Norland 5300 multichannel analyzer and the spatial resolution of the collimated beam was determined using CR39 track etch plastic.

Since no window was used in this arrangement the hole remained open to atmosphere throughout the experiment and was constantly pumped by a turbo-molecular pump. The loss of vacuum in the system due to the presence of the 5 μm hole was not significant.

3.2.2 Results

Data were obtained for this collimator for an incident proton beam of 3.5 MeV. The energy spectrum of the transmitted beam is shown in Figure 3.2.

The spectrum shows a high energy peak with a maximum at 3.5 MeV, due to particles transmitted directly through the collimator aperture without colliding with the walls and of lightly scattered particles. A significant fraction of the transmitted beam is present at

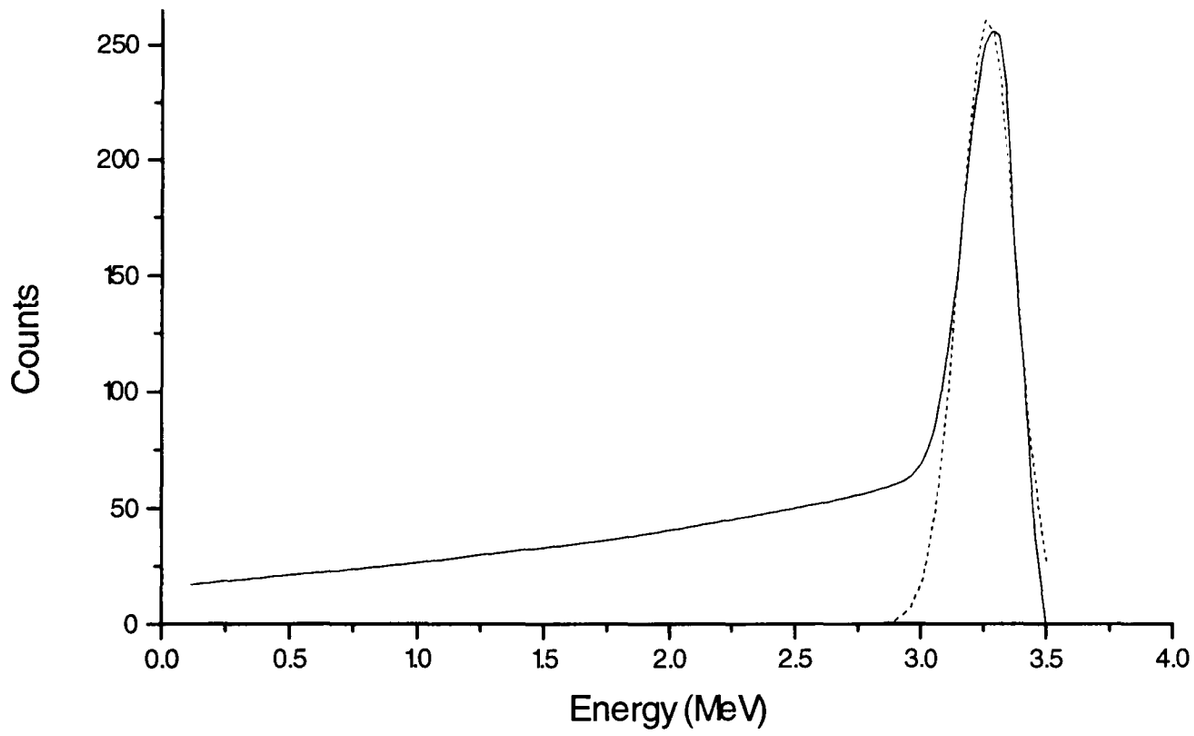

Figure 3.2 The energy spectrum obtained for the transmitted beam produced by a laser drilled boroslicate glass collimator having an exit aperture diameter of 5 μm and a length of 140 μm, for an incident beam of 3.5 MeV. The dotted curve shows a Gaussian fit to the high energy peak.

lower energies corresponding to highly scattered particles. By the fitting of a Gaussian distribution to the high energy peak and the integration of the peak and the full energy spectrum, using a commercial PC-based graph package (Origin, Microcal, USA), the proportion of the transmitted beam lying in this high energy peak region was calculated to be 40 %.

The spatial resolution of the beam was investigated by using timed irradiations of CR39 track etch plastic at various vertical distances from the exit surface of the collimator, using 200 protons per irradiation. By the use of the imaging software associated with the microbeam apparatus the beam size was measured directly from the pits in the track etch plastic. Examples are given for the beam size at distances of 0, 50 and 500 μm from the collimator surface in Figures 3.3a), b) and c).

The irradiation in Figure 3.3a) shows that as the beam emerges at the exit surface of the collimator it has a diameter significantly larger than the diameter of the exit hole. Although this effect may be exaggerated by a small initial gap of ~ 10 μm between the

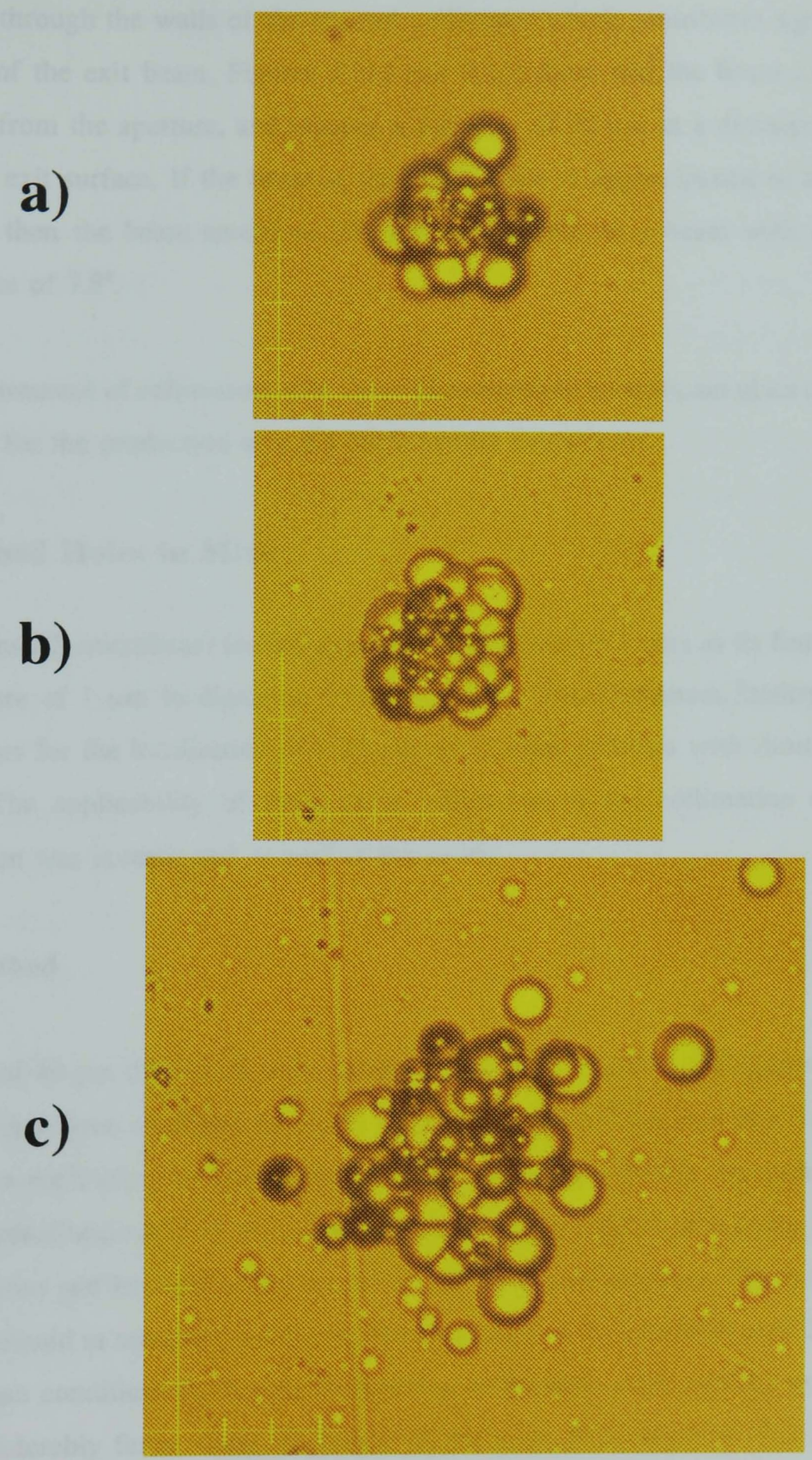

Figure 3.3 The spatial resolution of the transmitted beam produced, in CR39 track etch plastic, by a laser-drilled borosilicate glass collimator having an exit aperture diameter of 5 μm and a length of 140 μm, for an incident beam of 3.5 MeV protons, at distances of **a**) 0, **b**) 50, and **c**) 500 μm from the surface of the collimator, using timed irradiations of ~ 200 protons. Scale bars are 16 μm per division.

exit aperture and the track etch plastic, there is clearly considerable transmission of particles through the walls of the tapered collimator which contributes significantly to the size of the exit beam. Figures 3.3b) and 3.3c) show that the beam expands as it emerges from the aperture, and reaches a diameter of 90 μm at a distance of 200 μm from the exit surface. If the beam at the exit surface is approximated to be 35 μm in diameter then the beam spread at 200 μm corresponds to a beam with a half-angle divergence of 7.8°.

The performance of collimators with these dimensions in borosilicate glass is clearly not adequate for the production of a 3.5 MeV proton microbeam.

3.3 Etched Holes in Mica

The Darmstadt microbeam facility described in Section 1.6.3 uses as its final collimator an aperture of 1 μm in diameter, formed in mica. The Darmstadt facility uses these collimators for the localisation of high atomic number particles with short penetration depths. The applicability of these mica collimators to the collimation of a proton microbeam was investigated as part of this work.

3.3.1 Method

Samples of 40 μm thick mica were obtained from Dr J Vetter at GSI Darmstadt. These samples have been irradiated by 11.43 MeV per nucleon ^{197}Au ions at a density of 10^3 to 10^4 ions cm^{-2}, using the Darmstadt heavy ion accelerator facility. By etching the mica in 8 % hydrofluoric acid at room temperature it was possible to etch along the tracks of the gold ions and laterally out to the planes of the crystal structure. The resulting holes were rhomboid in cross-section due to the orientation of the crystal planes. The etch rate under these conditions in the lateral direction of the hole width was 55 nm $hour^{-1}$ and was considerably faster along the length of the track. Etch times of 7½, 22, 31½ and 55½ hours were chosen in order to produce hole widths of 0.4, 1.2, 1.7 and 3.0 μm respectively. The rhomboid cross-section of the hole was clearly visible using visible light microscopy.

The mica was mounted over a 0.5 mm hole in the stainless steel end-cone described

previously and alignment was achieved by the optimisation of the incident beam direction using the beam steering elements.

3.3.2 Results

Since the range of 3.5 MeV protons in mica is greater than 40 μm it was necessary to reduce the energy of the incident proton beam to 2 MeV, corresponding to a range of 34 μm in mica having a density of 3.0 g cm^{-3}. The 0.5 mm mounting hole allowed the irradiation of several collimators with side lengths of ~ 2 μm and so single exposures resulted in the irradiation of multiple sites in the CR39 track etch plastic. The energy spectrum of the collimated beam was again obtained using a silicon surface barrier detector, however, the previously used multichannel analyzer was replaced by a more accurate PC-based system allowing the acquisition and storage of precise energy data. The spectrum obtained by the irradiation of several mica collimator holes simultaneously, for an incident 2 MeV proton beam, is shown in Figure 3.4.

The energy spectrum shows at least two elements, perhaps corresponding to the presence of several transmitted proton beams from the mica holes mounted over the 0.5 mm diameter mounting hole. The beam quality for each individual collimator is therefore difficult to determine.

The spatial resolution of the beam was again obtained using CR39 track etch plastic. The studies show that as the beam leaves the surface of the collimator it has a diameter of ~ 38 μm determined by an irradiation of ~ 200 protons and at a distance of 100 μm from the exit surface of the collimator the beam enlarges to ~ 45 μm in diameter. Although the initial beam size is comparable to that of the laser drilled borosilicate glass collimator tested previously, the divergence of the beam appears to be significantly improved. However, the performance of this collimator relative to that of others discussed is difficult to assess since this study was undertaken at an incident proton energy of only 2 MeV rather than the 3.5 MeV proton beam used in all other work described in this chapter. The beam size at the exit aperture suggests that the degree of transmission through the exit surface of the collimator is high and so the collimator would be unsuitable for our purposes. In addition, the irradiation of a large area of the

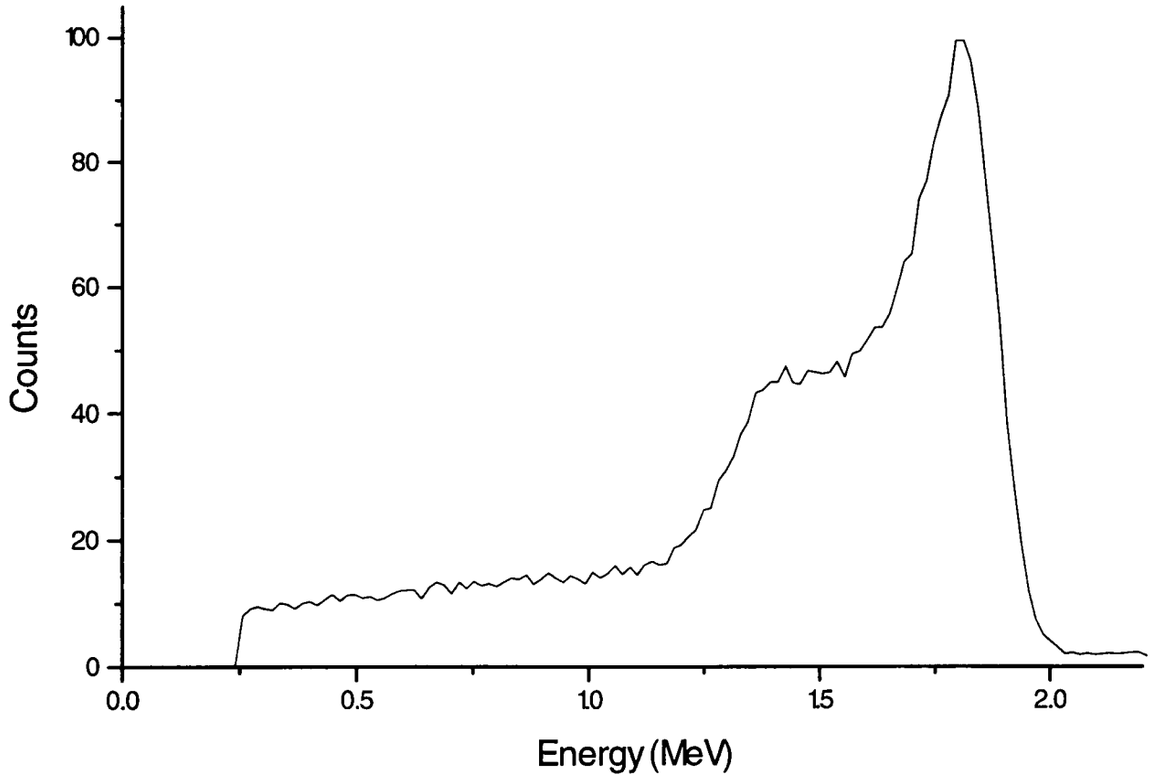

Figure 3.4 The energy spectrum obtained for the transmitted beams produced by several mica collimators, having widths of ~ 2 μm and lengths of 40 μm, for an incident beam of 2 MeV protons.

mica revealed heterogeneity in the thickness of the mica which resulted in the transmission of protons through areas of the mica even at these low energies. This would pose a serious problem unless considerably thicker mica could be obtained in which high aspect ratio holes could be produced.

3.4 Drawn Micro-Capillary Tubes

The use of micro-capillary tubing tapering to an exit hole of 1 μm has previously been used in the production of a channelled X-ray microprobe (Seed, 1960). A modification of this principle was used to produce a particle collimator for the Gray Laboratory microbeam.

3.4.1 Method

The micro-capillary collimators were produced using a commercially available pipette puller (Model PN-3, Narishige Ltd, Japan). A borosilicate glass capillary of 1.6 mm

outside diameter (Vitrex, Camlab, UK) and 0.5 mm inside diameter was mounted in the puller. The mechanism of the device clamped one end of the capillary firmly and used electromagnets to apply a tension to the other end. A platinum foil heater then applied a localised heat around the centre of the capillary tube. When the glass had reached a fluid state the force on the tube was sufficient to draw out the glass to a shape determined by the electromagnets. By the careful control of the heater element and the electromagnets, capillary tubes with the dimensions shown in Figure 3.5 could be produced. The ratio of the hole diameter to the wall thickness remained as 1:1 throughout the length of the tube.

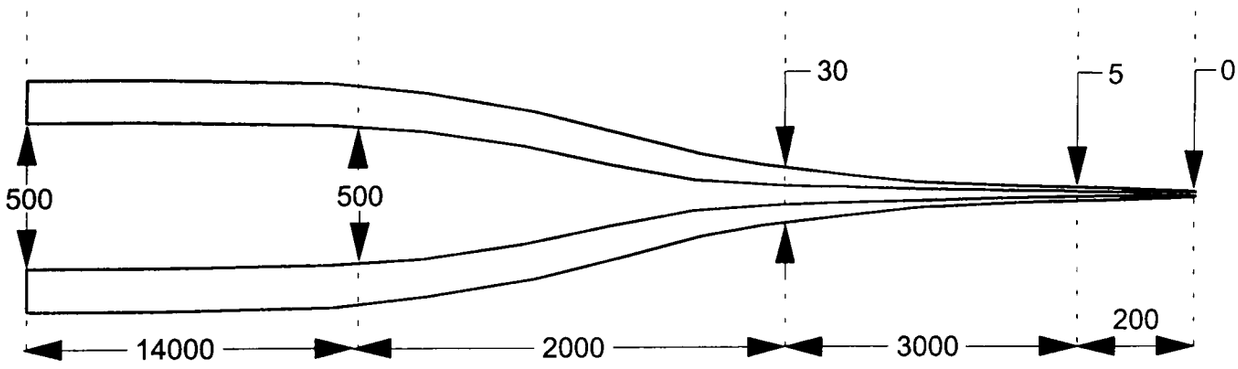

Figure 3.5 The dimensions of the tapered micro-capillary tubes which were used as potential collimators for the Gray Laboratory microbeam. Dimensions are in μm.

By the removal of the tip of the glass pipette it was possible to produce an aperture of only a few microns in diameter. However, the range of 4 MeV protons in glass is much greater than the wall thickness. It was therefore necessary to thicken the walls of the capillary by the addition of material to the external surface, prior to the removal of the tip of the pipette. The substance used to thicken the wall of the collimator was a liquid polymer (Loctite 350, Loctite, UK) which cured to a solid under illumination by ultraviolet light from a fluorescence microscope. This polymer was applied gradually to avoid the production of transverse forces on the glass as a result of supporting a large mass of liquid, which may have introduced a curve into the collimator. Having embedded the collimator the polymer was gradually polished away from the end of the capillary until an aperture was produced. The aperture could be seen using visible light microscopy.

The production of these collimators is summarised in Figure 3.6.

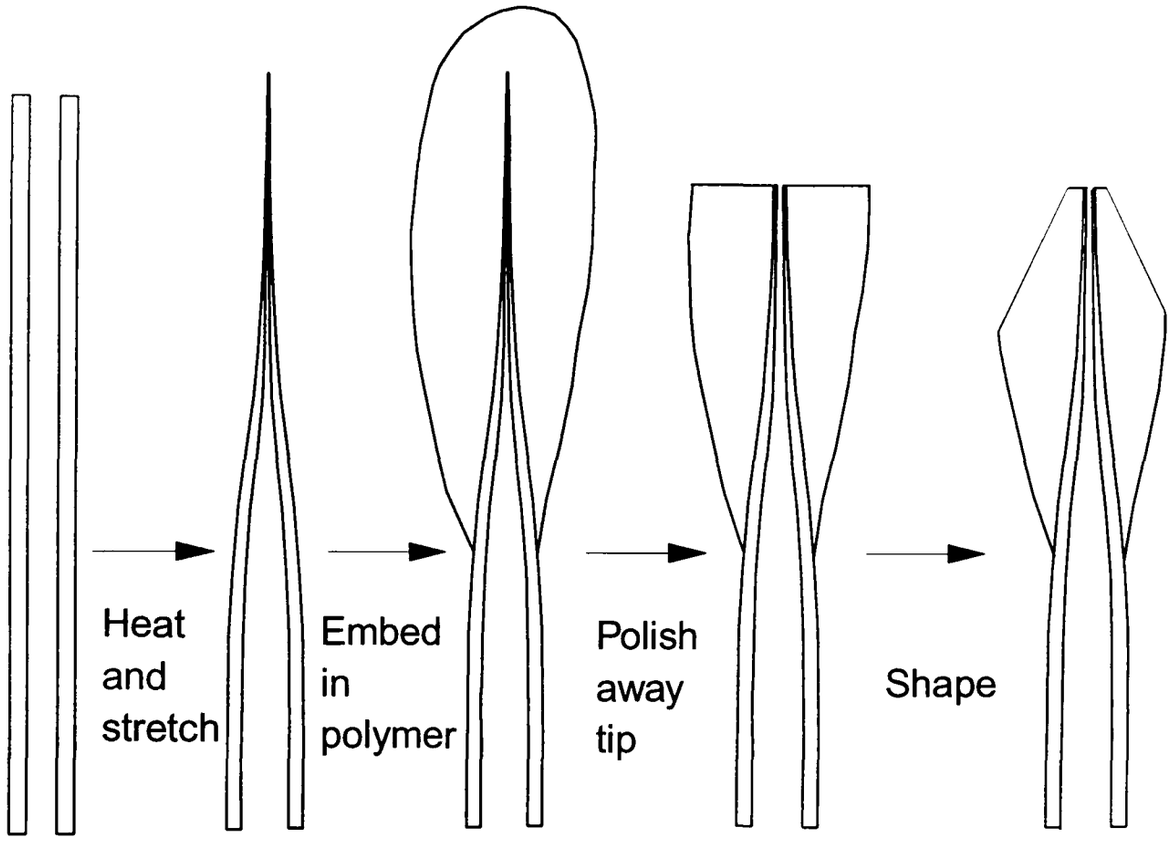

Figure 3.6 A schematic of the production of collimators using borosilicate micro-capillary tubing.

The production of collimators by this method required the removal of both polymer and capillary glass from the tip of the pipette by abrasion. The surface was then polished to a glass-like finish in order to locate the collimator exit aperture using visible light microscopy. This process inevitably resulted in a high proportion of the collimators having less than optimum performance due to the presence of polishing debris in the collimator hole. Many methods of clearing these holes were attempted, using ultrasonic agitation in alcohol, hydrochloric acid and detergents and by the use of a pressure differential in conjunction with these agents. Although no method had a high efficiency in this task, an acceptably high success rate of collimator production was obtained by the development of the method which is described below.

The micro-capillaries were drawn and embedded as previously described and the capillary was mounted within a larger diameter glass tube using ultraviolet curing, glass-bonding adhesive (Loctite 350, Loctite, UK). The larger diameter glass tube allowed the connection of this assembly to a helium gas cylinder using flexible reinforced plastic

tubing. A pressure of 10 to 20 p.s.i. was then applied to the assembly to maintain a clear path through the collimator during abrasion. With this pressure applied, the end of the collimator was gradually abraded using 10 μm grain size optical polishing paper. At regular intervals the tip of the assembly was placed into a solution of filtered detergent in an ultrasonic agitator. The use of detergent and ultrasound served two purposes. The first was that of a cleaning effect upon the surface, removing the debris left by the process of abrasion. The second was that when an aperture was produced in the end of the collimator the gas emerging from the micrometer-sized hole produced small bubbles on the surface of the polymer and so was a reliable indication of the presence of a clear path through the assembly. This enabled the production of smaller diameter apertures since the hole could be detected with ease. In addition, time was saved since the holes which remained blocked were not tested using a proton beam. The use of the positive pressure of the helium gas also increased the efficiency of collimator production by reducing the likelihood of debris entering the hole. Having determined that the collimator was clear, the surface of the collimator was then progressively polished using optical polishing papers of 5, 1 and 0.5 μm grain size. Inevitably some of these collimators become blocked by this polishing process, however, in some cases the use of prolonged ultrasonic agitation in detergent solution, in conjunction with the application of a positive pressure was sufficient to clear a blocked collimator. Having completed this process the collimator was briefly washed in alcohol with ultrasonic agitation to remove final debris and detergent solution.

Even using this rigorous method of collimator production the probability of the collimator having an acceptable energy resolution was still only 1 in 7 of those collimators which reached the stage of testing with a proton beam. The method was therefore highly labour intensive and resulted in a low yield of collimators.

In order to test these collimators they were mounted in a vacuum tight assembly and aligned with the 3.5 MeV proton beam. A mounting arrangement was designed for this purpose, the design for which is shown in Figure 3.7. The design was based upon a ball and socket type of joint, pivoting about the O-ring vacuum seal with adjustment of the collimator direction by manually operated screws actuating against the beam pipe. A later modification to this design used an extended tube to obtain greater accuracy in the

alignment of the collimator and is shown with dotted lines. The use of this modification allowed collimator alignment with an accuracy of 0.5 degres per screw turn.

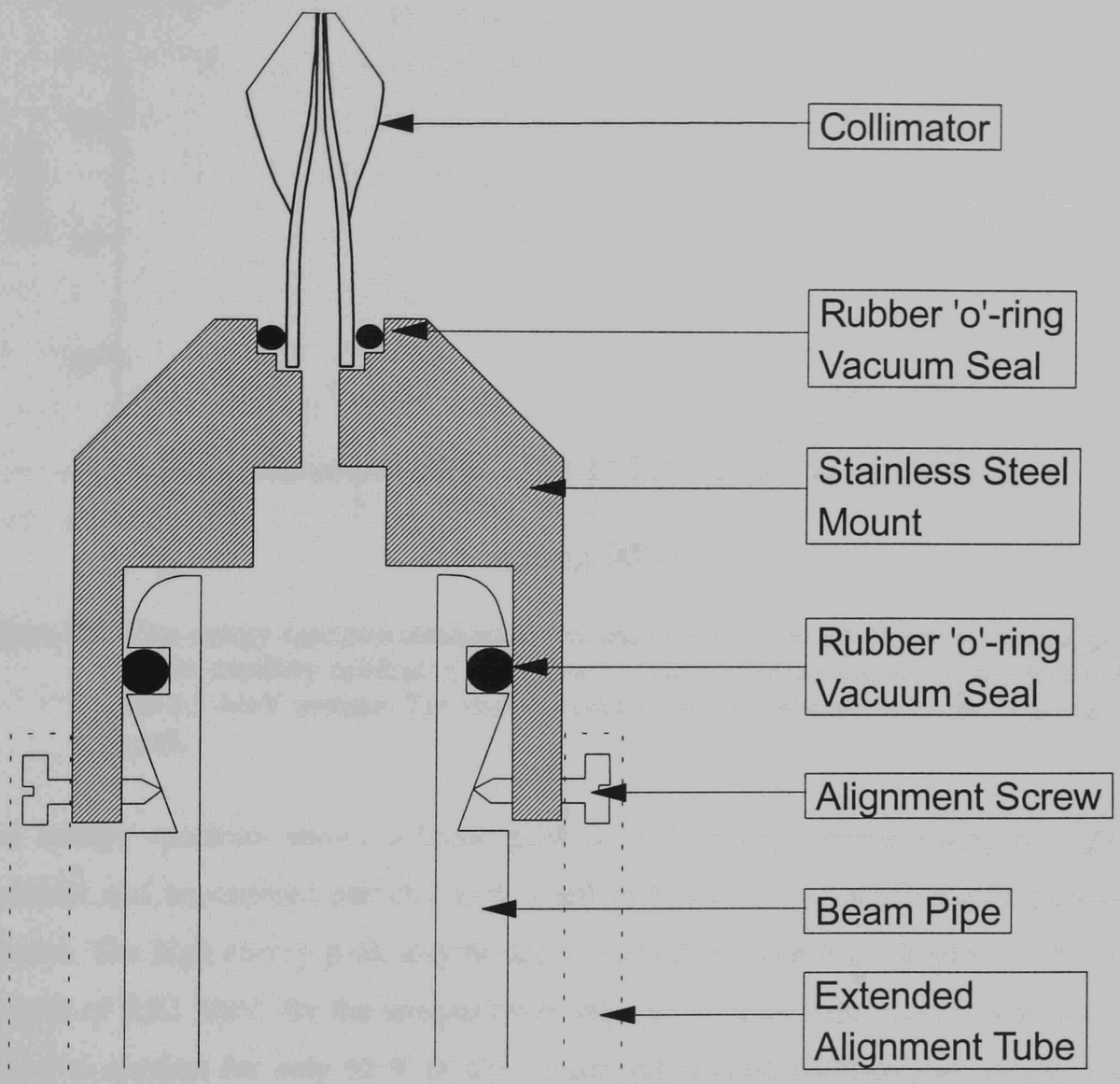

Figure 3.7 The design of the stainless steel end-cone assembly used to mount and test the glass micro-capillary collimators. The design allows the alignment of the collimator with the incident beam by the use of adjusting screws.

3.4.2 Results

Using this approach it was possible to produce collimators with diameters as small as 5 μm. The energy spectrum for a collimator with a diameter of 4.9 μm, obtained using a silicon surface barrier detector, is shown in Figure 3.8.

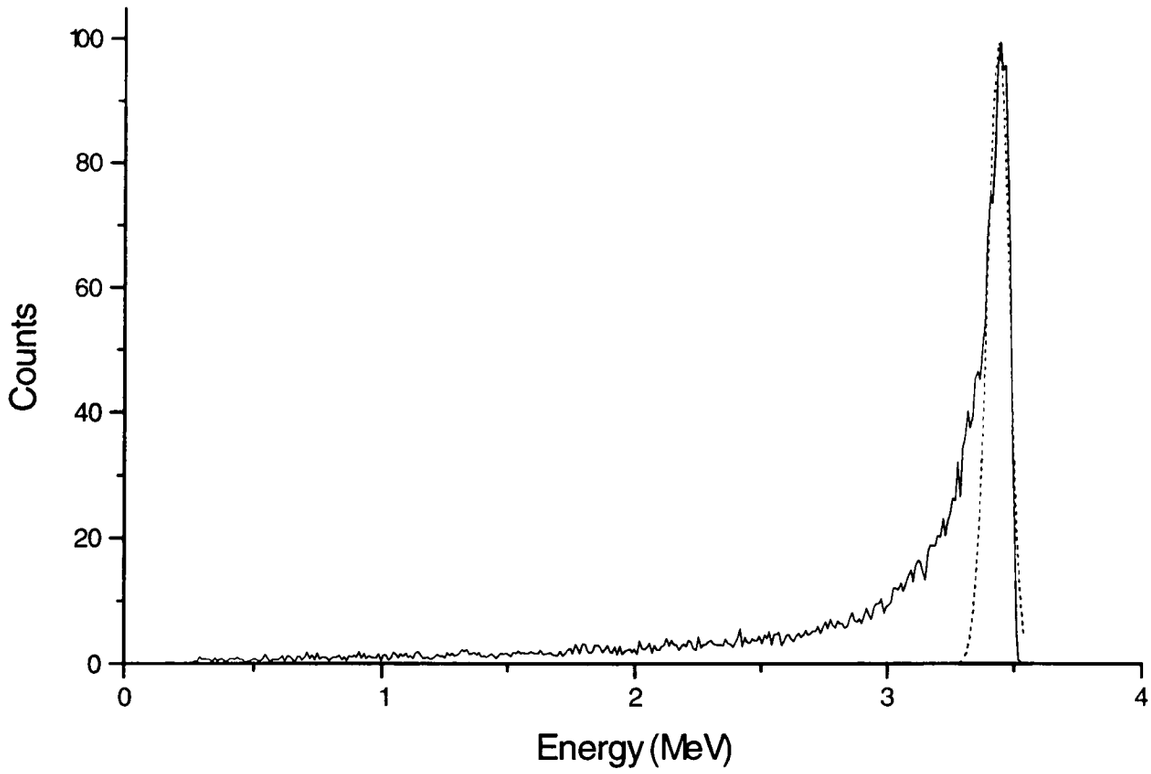

Figure 3.8 The energy spectrum obtained for the transmitted beam produced by a drawn glass micro-capillary collimator, having an exit aperture of 4.9 μm, for an incident beam of 3.5 MeV protons. The dashed curve shows a Gaussian fit to the high energy peak.

The energy spectrum shows a broad peak at high energy corresponding to lightly scattered and unscattered particles with a tail of lower energy, more highly scattered protons. The high energy peak may be approximated to a Gaussian distribution having a width of 0.22 MeV. By the integration of the spectrum the high energy peak can be shown to account for only 42 % of the transmitted protons, indicating the presence of a high proportion of scattered particles.

The corresponding spatial resolution of the beam was assessed using the irradiation of CR39 track etch plastic with various numbers of protons at different distances from the exit surface of the collimator and are shown in Figures 3.9a), b) and c).

Figure 3.19a) shows the irradiation of CR39 track etch plastic at the exit surface of the collimator by a timed irradiation of ~ 20 protons at two sites separated by 50 μm. It can be seen that the beam consists of a dense core of unscattered and lightly scattered particles with a diameter of ~ 7 μm and that superimposed upon the core is a background of more highly scattered particles with a beam diameter of ~ 20 μm. Figure 3.9b) shows

an irradiation of ~ 120 protons at the exit surface of the collimator. The lower energy particles present in the beam produce a more densely ionised track in the plastic leading to a larger pit diameter. The size of these pits obscures the observation of the smaller pits produced by high energy protons. The beam diameter therefore increases to ~ 30 μm as a result of the presence of these lower energy, scattered particles. These scattered particles will contribute significantly to an increase in the size of the collimated beam as the distance from the collimator is increased. This is shown in Figure 3.9c) by an irradiation of ~ 120 protons at a distance of ~ 500 μm from the exit hole. The beam divergence has resulted in an increase in the beam diameter to ~ 120 μm. Since the low energy, highly scattered particles diverge considerably the core of high energy, unscattered particles is less obscured in this case. Although the scattered particles have significantly increased the overall size of the beam, the core of high energy particles has a diameter of only ~ 20 μm showing a low divergence of the unscattered particles.

In order to avoid the masking effects of the large pits due to scattered, low energy particles, repeated irradiations of track etch plastic at the exit surface of the collimator were performed using small numbers of particles. Timed irradiations corresponding to ~ 20 protons were made and the diameter of the beam at each irradiation site was measured using the microimager software. The results of these measurements are plotted in Figure 3.10 and show a wide range of beam diameters with a peak at ~ 18 μm.

Although these collimators may have an adequate performance for some single cell irradiation experiments it is unlikely that this approach would attain the 1 μm collimation desired for the Gray Laboratory microbeam.

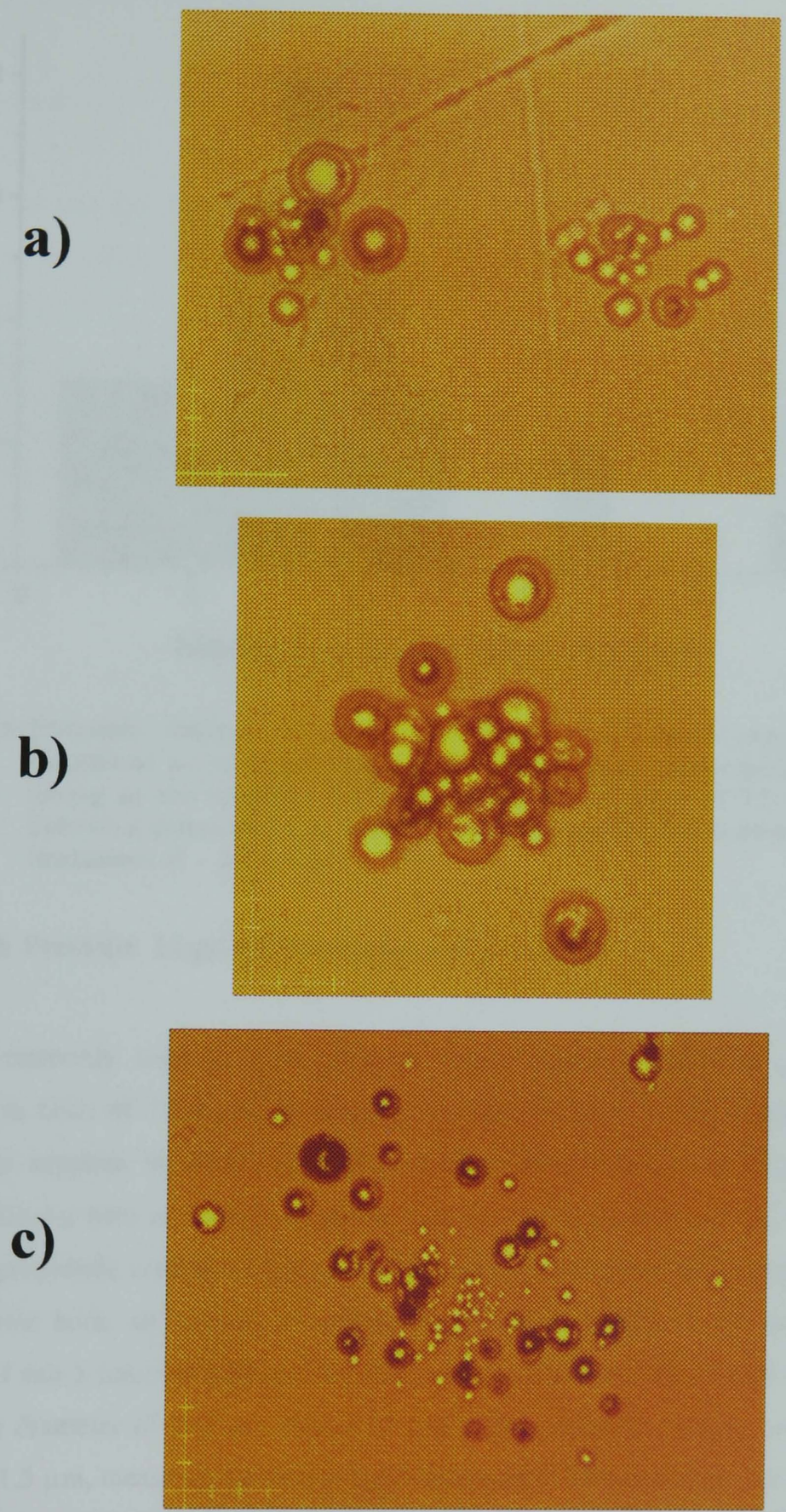

Figure 3.9 The spatial resolution of the transmitted proton beam in CR39 track etch plastic, produced by a drawn glass micro-capillary collimator having an exit aperture of 4.9 μm, for an incident beam of 3.5 MeV protons, using irradiations of **a**) ~20 protons at the exit surface of the collimator, **b**) ~120 protons at the exit surface of the collimator and **c**) ~120 protons at 500 μm from the exit surface of the collimator. Scale bars are **a**),**b**) 4 μm per division, **c**) 8 μm per division.

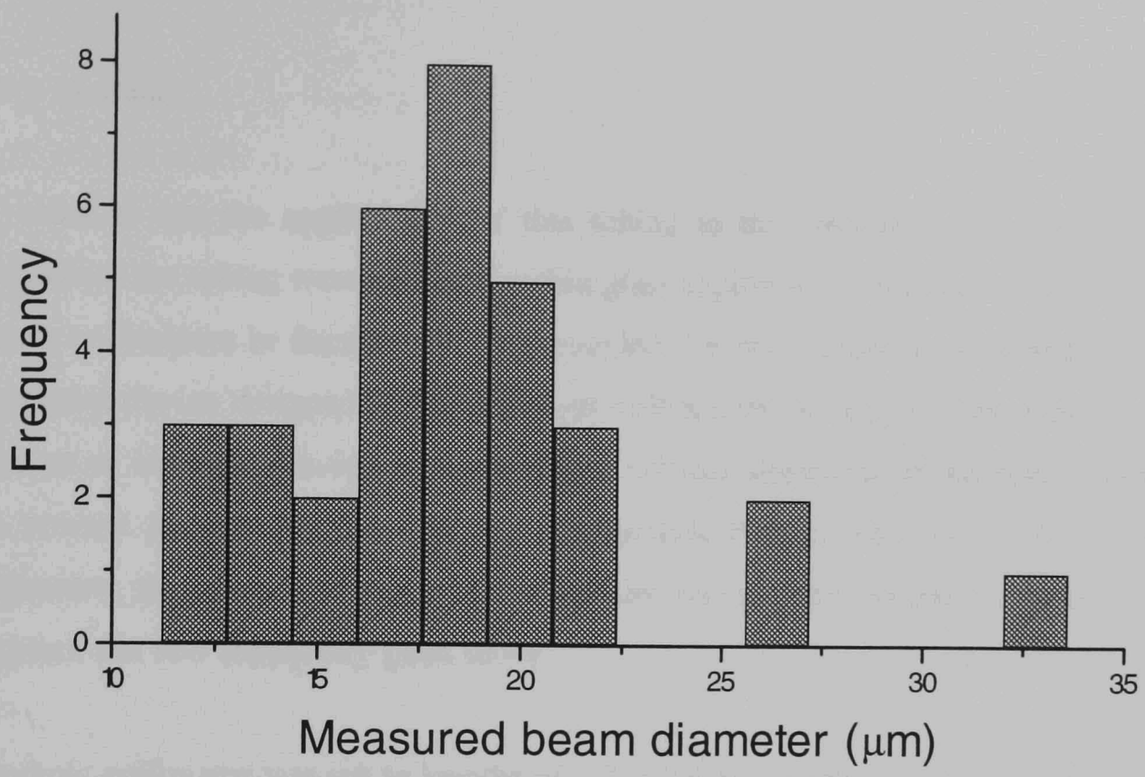

Figure 3.10 Frequency diagram of repeat measurements of the spatial resolution of the transmitted proton beam produced by a drawn glass micro-capillary collimator having an exit aperture of 4.9 μm, for an incident beam of 3.5 MeV protons. Individual proton pits were measured using the microimager software for multiple irradiations of ~ 20 protons.

3.5 High Pressure Liquid Chromatography Tubing

Tubing commonly used in high pressure liquid chromatography is commercially available in coils of 10 meters in length. The smallest bore tubing available for this application supplied by S.G.E. (UK) Ltd is made from fused silica glass and has a uniform circular bore of 5 μm in diameter with an outside diameter of 285 μm and a 10 μm thick polyimide coating. In addition to the availability of similar tubing having a 10 μm diameter bore, an attempt was made for us, by SGE Ltd., to produce a unique example of sub-5 μm bore tubing of similar overall dimensions. The resulting tubing has an outside diameter of 225 μm with a 10 μm thick polyimide coating and a uniform bore of ~ 1.5 μm, measured by visible light microscopy. The uniformity in the diameter of the bore, inspected at intervals along the length of the tubing, and the highly circular appearance of the aperture suggests that the method of production produces a smooth walled, uniform tubing which may be suitable for the collimation of 3.5 MeV protons. In addition, the wall of the tubing is ~ 100 μm thick and is sufficiently thick to fully stop

protons in the collimator wall.

3.5.1 Method

In order to test the applicability of this tubing to the collimation of protons, short sections of the tubing were mounted within glass capillaries of the type used to produce drawn collimators in Section 3.3. This enabled the collimators to be tested using the alignment device designed for the previous collimators. A second glass tube was also used as an insert to provide an approximate vertical alignment of the hplc collimator. To prevent protons from exiting the arrangement through any route other than the collimator, the glass tubing was surrounded by vacuum cement and vacuum wax run between the two supporting glass tubes.

The hplc collimator was cut to lengths of 1.7 ± 0.3 mm using a fibre optic cleaver and these sections were then manipulated into place using fine tweezers under a binocular microscope, and a steady pair of hands! The process of cutting the tubing lengths was made easier by mechanically removing the polyimide coating with a sharp scalpel blade. This also resulted in a more perpendicular and burr free exit surface for the collimator.

Much of the data was obtained using windowless collimators since the degradation of the vacuum by these apertures did not cause a significant problem in the running of the Van de Graaff accelerator. However, it was also possible to attach windows to the collimators in this arrangement. This was achieved by loosely clamping a sheet of 2.5 μm thick mylar over the end of the collimator mounting arrangement by means of an appropriately sized ring of shrink fit plastic tubing. The application of gentle heating using a hot air gun then caused the mylar to become highly malleable as a result of which it melded itself around the collimator end. The shrink fit tubing also tightened due to the heating and so strengthened the attachment of the mylar to the tubing.

The use of adhesives within the collimator mounting arrangement resulted in the blockage of a number of collimators, however, the success rate for the production of collimators which transmit particles was significantly higher using this method than that of the drawn capillary collimator approach described in Section 3.4.

3.5.2 Results

Data were obtained for both the energy and spatial resolutions of the collimated beam for hplc tubing with bore diameters of 10, 5 and 1.5 μm, using a silicon surface barrier detector connected to a PC-based multichannel analyzer, and CR39 track etch plastic studies. The results are shown in Figures 3.11 to 3.14.

The energy spectra for all of these bore sizes, shown in Figures 3.11a), b) and c), are significantly improved over those of previously tested collimators. In each case the high energy peak due to unscattered and lightly scattered particles is narrower and makes up a larger fraction of the transmitted beam. For the collimators shown the full width at half maximum of the high energy peak is 0.04 ± 0.01 MeV and constitutes 74 % of the collimated beam.

The spatial resolutions of the beams obtained are of a correspondingly high quality. Figures 3.12a), b) and c) show the exit beam size for a timed exposure corresponding to an irradiation by 20 protons for the 10 μm and 5 μm bore capillary and 10 protons in the case of the 1.5 μm bore capillary. In each case the tight core of high energy particles is predominant with very few scattered particles present in the beam. As the number of protons was increased to 500, in Figures 3.13a), b) and c), the presence of a small number of lower energy, scattered particles becomes evident resulting in a broadening of the beam due to protons transmitted through the collimator material at the surface. The proportion of these scattered particles is, however, very low.

Multiple irradiations of 10 protons per point were used to assess the beam size at the exit surface of the collimator. The distance between the two outermost pits in each 10 proton irradiation was measured using the software attached to the microbeam and the data obtained are shown in Figures 3.14a), b) and c). The reduction in the transmitted beam size with a decrease in the size of the capillary bore is shown. The smallest beam diameter was obtained using the 1.5 μm bore capillary and showed an outer beam diameter distribution with a mean of 2.3 ± 0.9 μm. The increase in the beam size over that of the diameter of the capillary bore may have been due to scatter within the collimator and transmission of particles through the surface of the collimator, however,

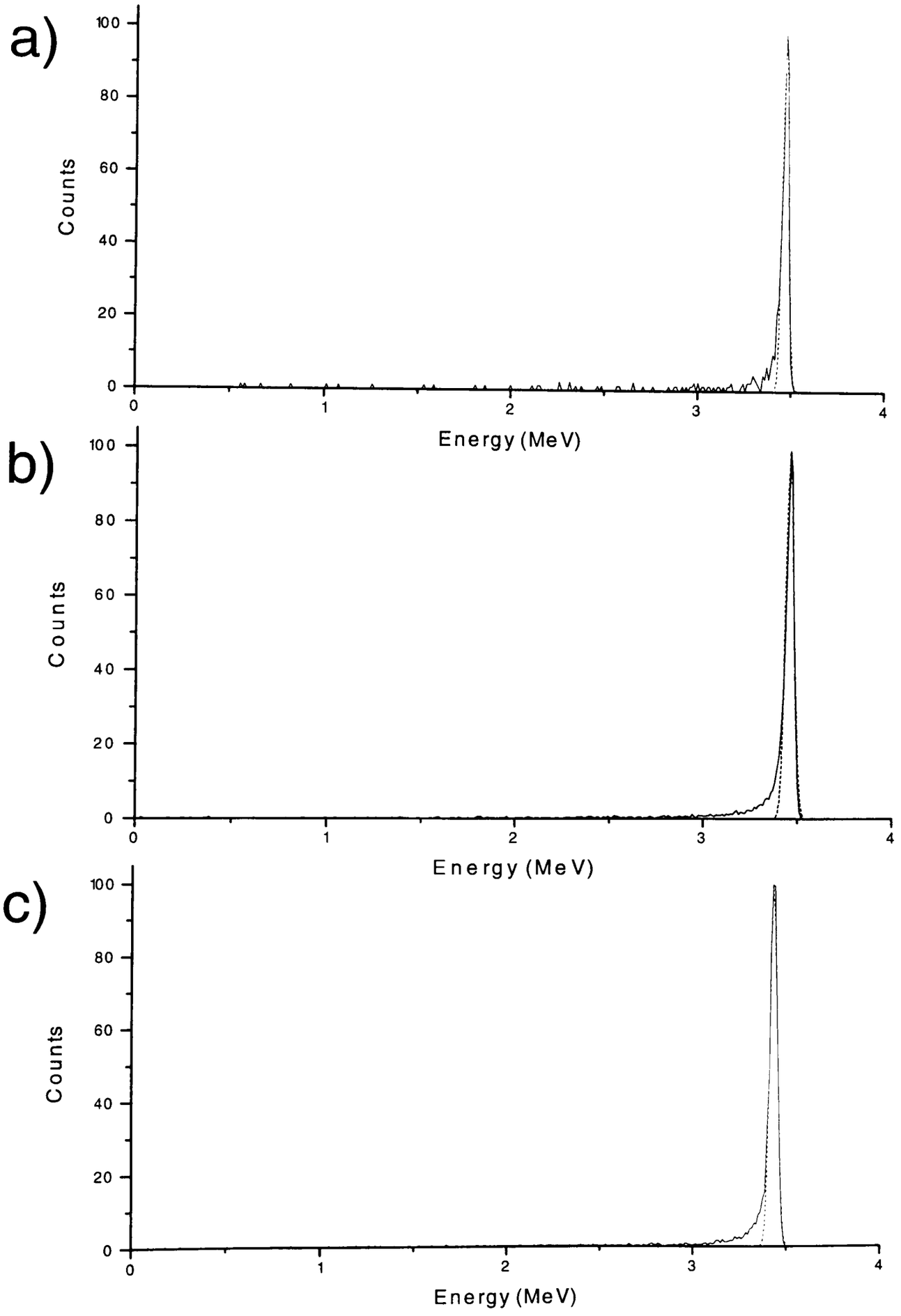

Figure 3.11 The energy spectra of the transmitted beam produced by hplc tubing collimators with bore diameters of **a)** 10 μm, **b)** 5 μm and **c)** 1.5 μm, for an incident beam of 3.5 MeV protons. In each case the high energy peak was fitted by a Gaussian distribution (Dashed Line).

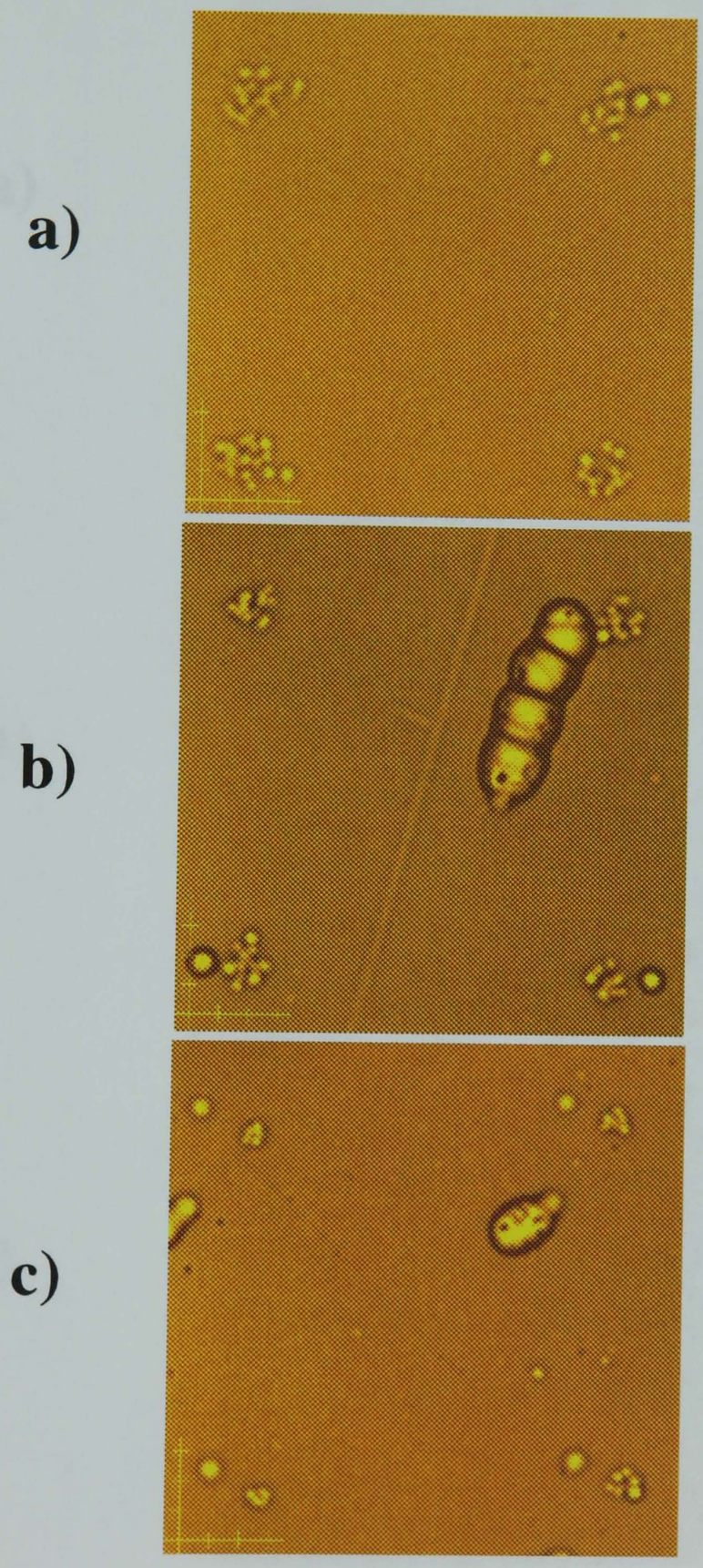

Figure 3.12 The spatial resolution of the transmitted beam produced by hplc tubing collimators with bore diameters of **a**) 10, **b**) 5, and **c**) 1.5 μm, for an incident beam of 3.5 MeV protons, using timed exposures corresponding to irradiations of **a**) 20, **b**) 20 and **c**) 10 protons, in CR39 track etch plastic with the plastic positioned as close to the exit surface of the collimator as possible. Scale bars are 4 μm per division.

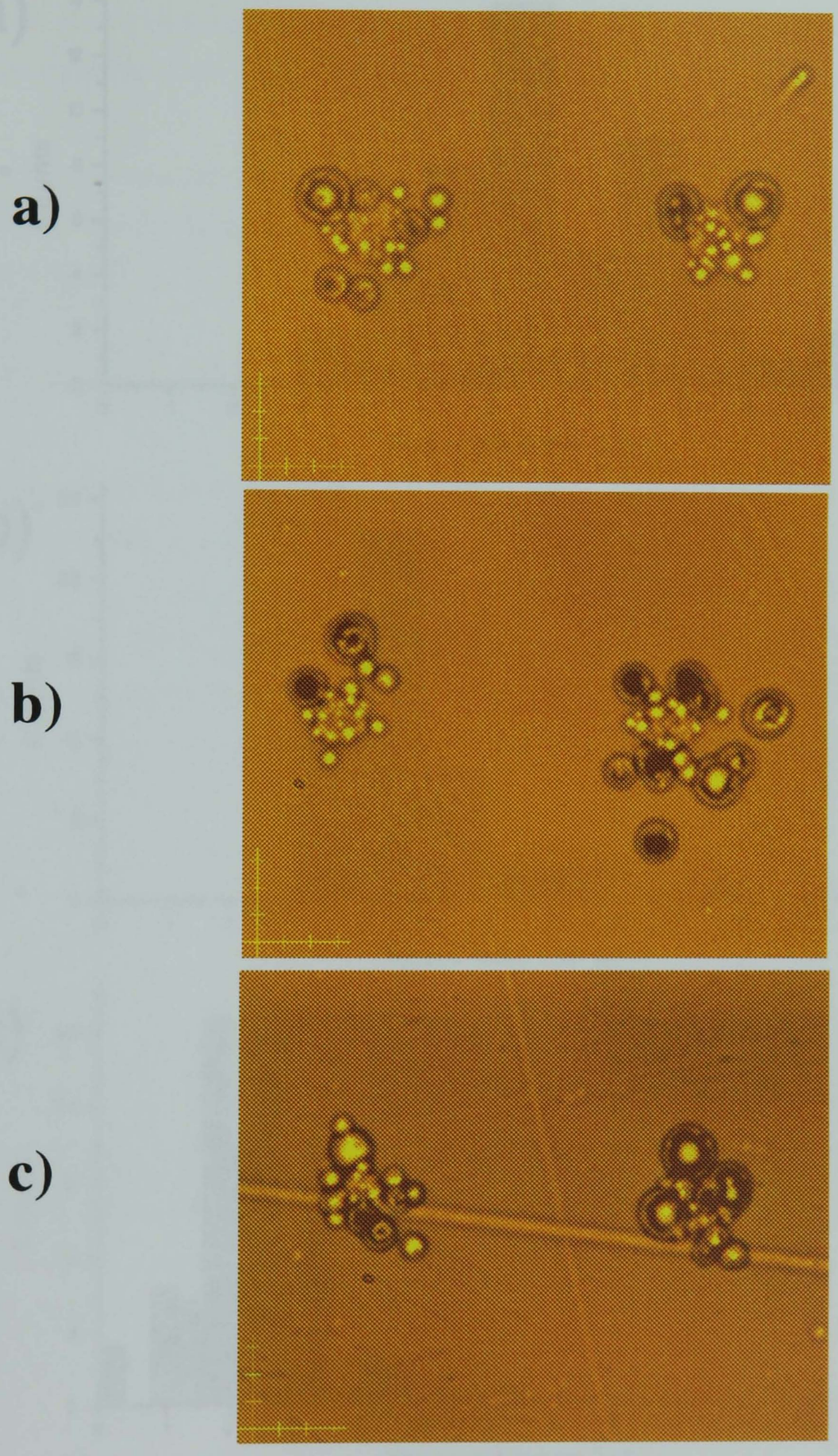

Figure 3.13 The spatial resolution of the transmitted beam produced by hplc tubing collimators with bore diameters of **a)** 10, **b)** 5, and **c)** 1.5 μm, for an incident beam of 3.5 MeV protons, using timed exposures corresponding to irradiations of 500 protons, in CR39 track etch plastic with the plastic positioned as close to the exit surface of the collimator as possible. Scale bars are 4 μm per division.

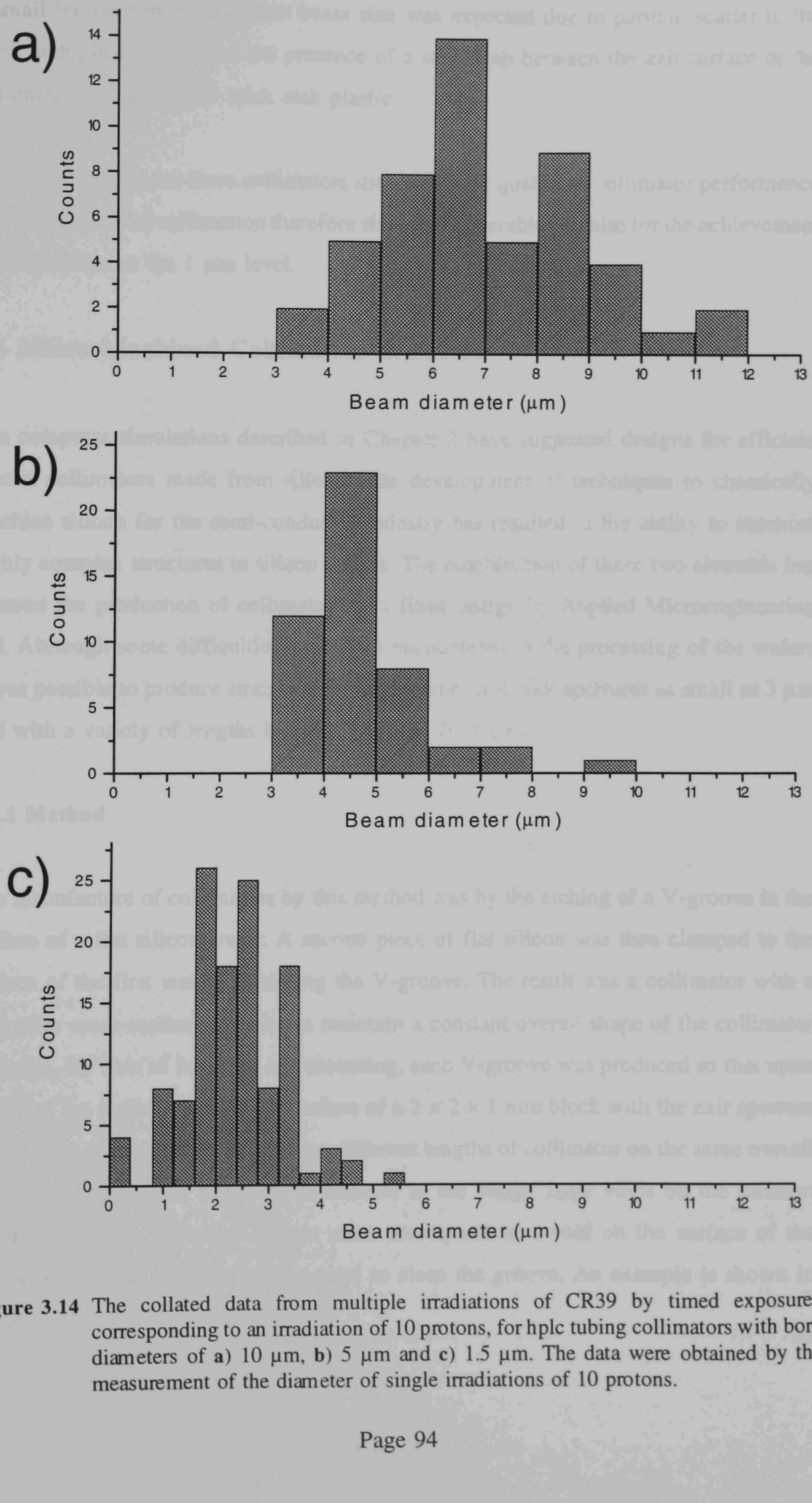

Figure 3.14 The collated data from multiple irradiations of CR39 by timed exposures corresponding to an irradiation of 10 protons, for hplc tubing collimators with bore diameters of **a**) 10 μm, **b**) 5 μm and **c**) 1.5 μm. The data were obtained by the measurement of the diameter of single irradiations of 10 protons.

a small increase in the apparent beam size was expected due to particle scatter in the track etch plastic itself and the presence of a small gap between the exit surface of the collimator and the CR39 track etch plastic.

The data obtained for these collimators showed a high quality of collimator performance and this method of collimation therefore shows considerable promise for the achievement of collimation at the 1 μm level.

3.6 Micro-Machined Collimators in Silicon

The computer simulations described in Chapter 2 have suggested designs for efficient proton collimators made from silicon. The development of techniques to chemically machine silicon for the semi-conductor industry has resulted in the ability to machine highly complex structures in silicon wafers. The combination of these two elements has allowed the production of collimators to a fixed design by Applied Microengineering Ltd. Although some difficulties have been encountered in the processing of the wafers it was possible to produce straight sided collimators with exit apertures as small as 3 μm and with a variety of lengths between 140 and 2000 μm.

3.6.1 Method

The manufacture of collimators by this method was by the etching of a V-groove in the surface of a flat silicon wafer. A second piece of flat silicon was then clamped to the surface of the first wafer, so closing the V-groove. The result was a collimator with a triangular cross-section. In order to maintain a constant overall shape of the collimator substrate, for ease of handling and mounting, each V-groove was produced so that upon dicing of the wafer it was on the surface of a 2 × 2 × 1 mm block with the exit aperture at one edge of the square. To produce different lengths of collimator on the same overall block size it has been necessary to include in the design large voids on the incident beam side of the collimator. These must correspond to a void on the surface of the corresponding flat block of silicon used to close the groove. An example is shown in Figure 3.15.

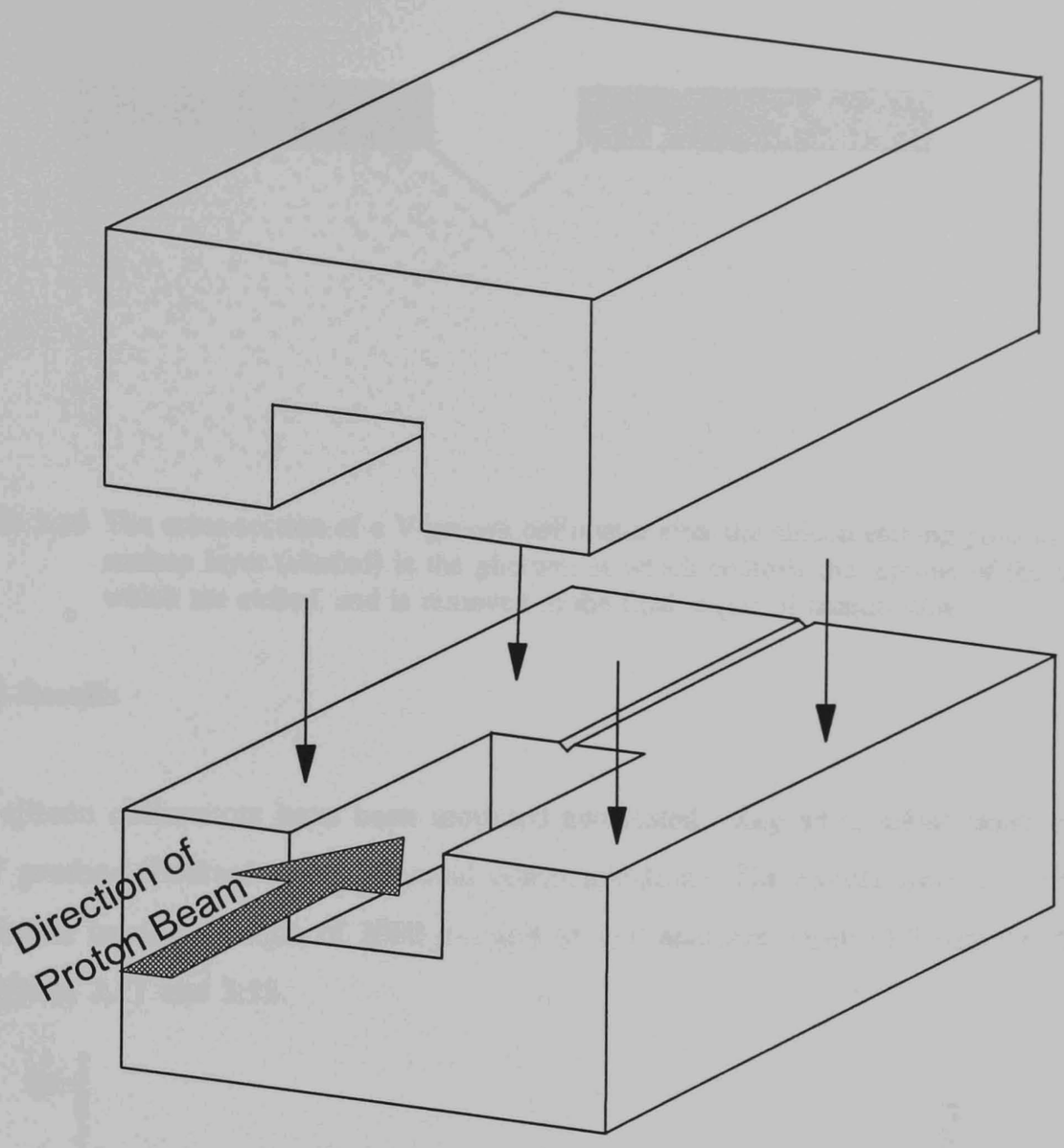

Figure 3.15 The geometry of a silicon manufactured collimator in the surface of a 2 × 2 × 1 mm piece of high purity silicon with a second flat piece of silicon above, to close the V-groove and so produce a collimator with a triangular exit aperture.

The method used to manufacture the V-grooves was by the production of a mask on the surface of the silicon using electron beam writing. The mask revealed the silicon wafer only in regions where the silicon was to be chemically etched. The etching process acted along the crystal planes of the silicon and so limited the depth of the etching process, as shown in Figure 3.16. The crystal planes were inclined at an angle of 54.7° to the surface of the silicon and so the triangle produced was isosceles with a depth of 0.706 times less than the width at the surface of the groove.

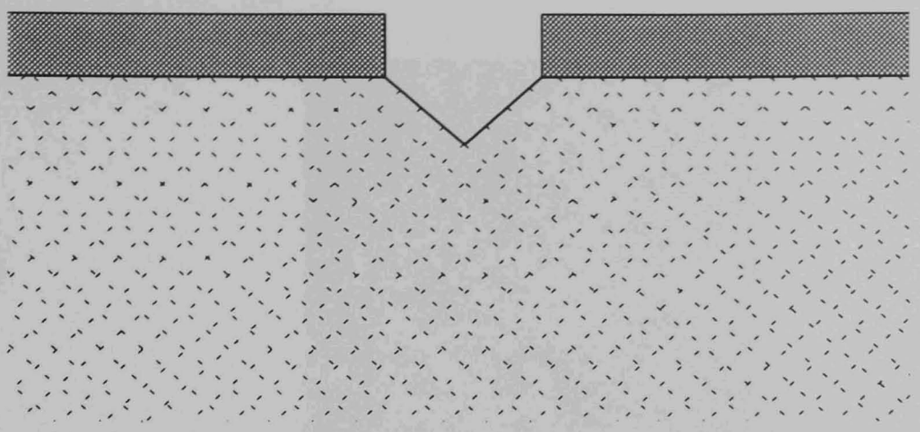

Figure 3.16 The cross-section of a V-groove collimator after the silicon etching process. The surface layer (shaded) is the photoresist which controls the regions of the silicon which are etched, and is removed in the final stages of manufacture.

3.6.2 Results

The silicon collimators have been mounted and tested using an incident beam of 3.5 MeV protons (Folkard *et al.*, personal communication). The results from a V-groove collimator having a length of 2000 μm and an exit aperture width of 3 μm are shown in Figures 3.17 and 3.18.

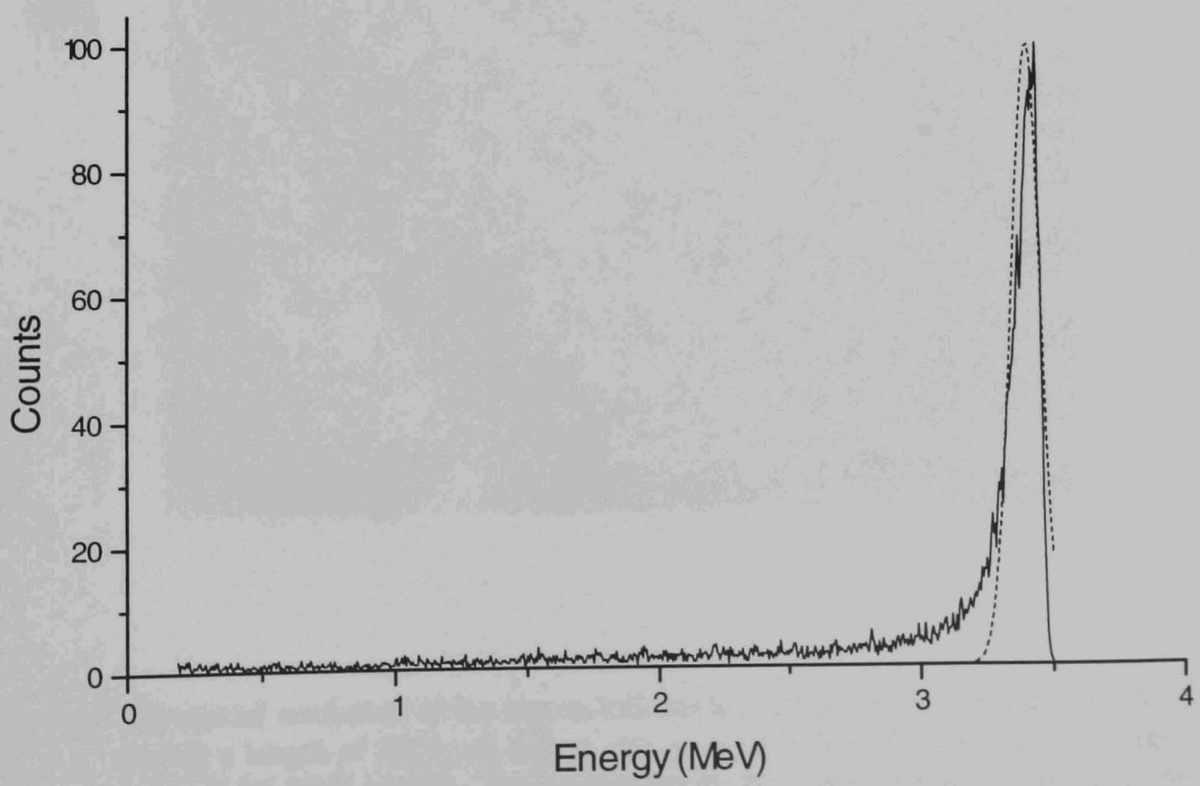

Figure 3.17 The energy spectrum of the transmitted beam produced by a silicon collimator having a length of 2000 μm and an exit aperture width of 3 μm. A Gaussian distribution was fitted to the high energy peak (Dashed Line).

a)

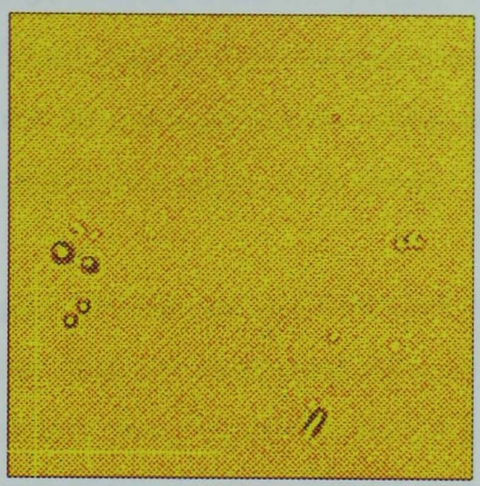

b)

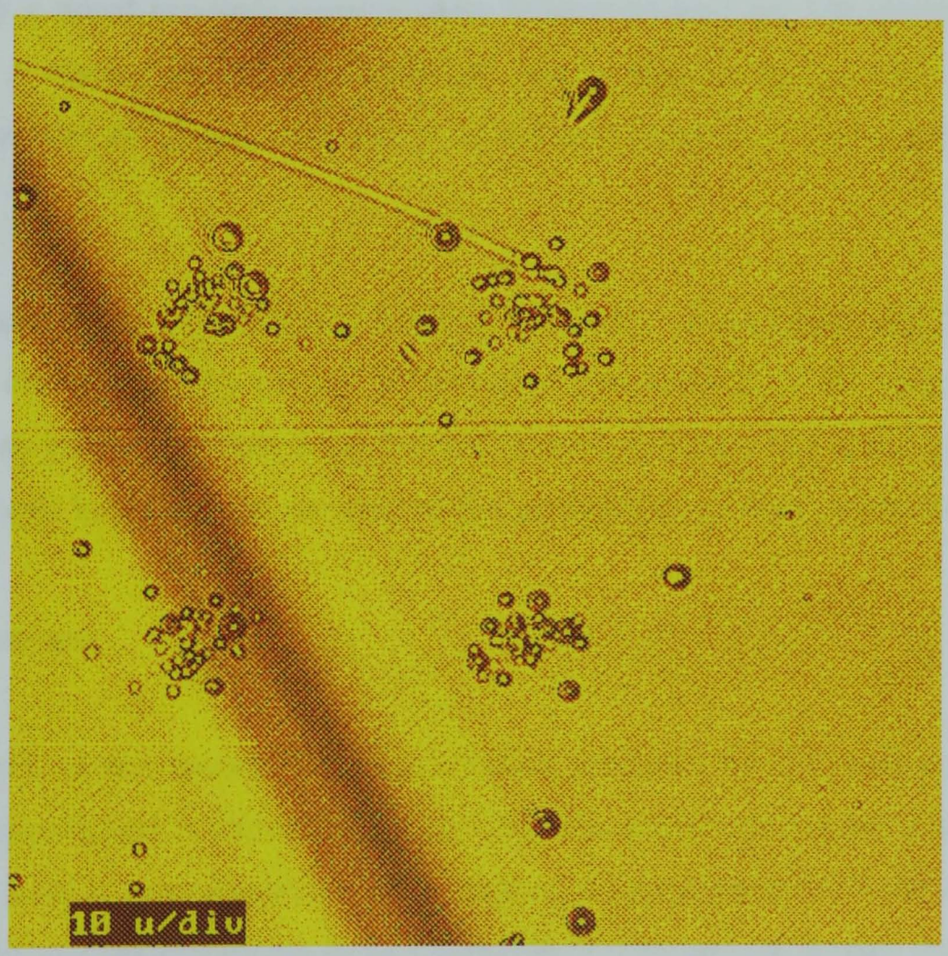

Figure 3.18 The spatial resolution of the transmitted beam produced by a collimator in silicon having a length of 2000 μm and an exit aperture width of 3 μm, for an incident beam of 3.5 MeV protons. The irradiations are by timed exposures corresponding to **a**) 20 protons and **b**) 200 protons, in CR39 track etch plastic with the track etch plastic positioned as close as possible to the exit surface of the collimator. Scale bars are 16 μm per division.

The energy spectrum shows a high energy peak with a contribution to the spectrum by scattered protons at lower energies. For this collimator the width of the high energy peak is 0.11 MeV and accounts for 64 % of the transmitted beam. The proportion of scattered particles in this case is significantly higher than that obtained using the chromatography tubing collimators and so it can be expected that the collimator will also show a lower performance in terms of the spatial resolution of the beam.

The spatial resolution was again obtained using CR39 track etch plastic. Figure 3.18a) shows the beam size for a timed exposure corresponding to an irradiation of 20 protons. In this case the core of high energy particles appears to be 6 μm in diameter with lower energy scattered particles outside of this diameter. The beam shown in Figure 3.18b) was produced by a timed exposure corresponding to an irradiation by 200 protons at four points with a spacing of 100 μm. Again the core of high energy protons is visible, having a diameter of 12 μm, with a halo of scattered particles at radii outside of the core.

The collimator shows a performance between that of the drawn pipette capillaries and that of the chromatography tubing. With further development of the manufacturing process it may become possible to produce collimators with more favourable geometries and smaller exit holes in order to improve the performance of these collimators.

3.7 Conclusions

A comparison of the transmitted proton beams produced by the several types of collimator investigated is shown in Figure 3.20. The energy spectra are plotted on a logarithmic scale to demonstrate the proportion of scattered particles in the beam and the size of the exit beam is shown by an irradiation of ~ 20 protons in track etch plastic. In addition, repeated irradiations were made for the various sizes of hplc tubing collimators, using a range of timed proton exposures. The total beam diameter was measured for each irradiation site and the average of these gave the mean beam diameter for an irradiation by a given number of protons. The mean diameters of the irradiated areas for the various sizes of collimator tested is shown in Table 3.1.

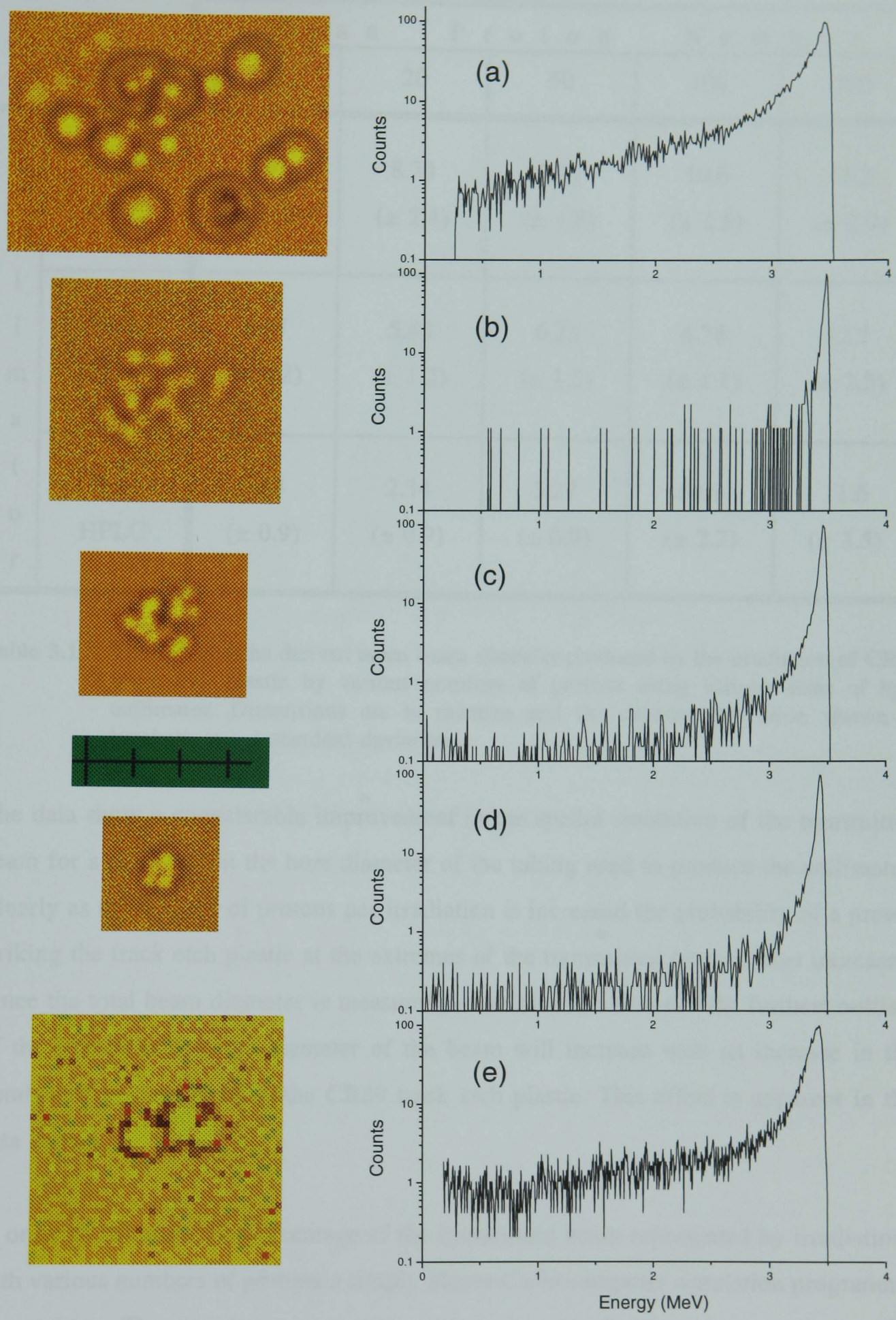

Figure 3.20 A summary of both the spatial and the energy data obtained for **a**) a drawn micro-capillary collimator having an exit aperture diameter of 5 μm, **b**) an hplc fused silica tubing collimator having a bore of 10 μm, **c**) an hplc fused silica tubing collimator having a bore of 5 μm, **d**) an hplc fused silica tubing collimator having a bore of 1.5 μm, and **e**) a silicon micro-manufactured collimator having an exit aperture width of 3 μm. Scale bar is 4 μm per division.

		Mean Proton Number				
		10	20	50	100	500
Collimator	10 μm HPLC	6.91 (± 2.0)	8.74 (± 2.4)	9.27 (± 1.8)	10.6 (± 2.5)	15.2 (± 2.9)
	5 μm HPLC	4.67 (± 1.2)	5.43 (± 1.2)	6.23 (± 1.3)	6.78 (± 1.1)	12.7 (± 2.5)
	1.5 μm HPLC	2.34 (± 0.9)	2.34 (± 0.9)	3.27 (± 0.9)	5.09 (± 2.2)	11.6 (± 3.5)

Table 3.1 The value of the derived mean beam diameter produced by the irradiation of CR39 track etch plastic by various numbers of protons using various sizes of hplc collimator. Dimensions are in microns and the experimental error, shown in brackets, is ± 1 standard deviation.

The data show a considerable improvement in the spatial resolution of the transmitted beam for a reduction in the bore diameter of the tubing used to produce the collimator. Clearly as the number of protons per irradiation is increased the probability of a proton striking the track etch plastic at the extremes of the transmitted beam is also increased. Since the total beam diameter is measured as the distance between the furthest outliers of the irradiated area the diameter of the beam will increase with an increase in the number of protons striking the CR39 track etch plastic. This effect is apparent in the data shown.

In order to calculate the percentage of the transmitted beam represented by irradiations with various numbers of protons a simple Monte-Carlo computer simulation programme was written. The simulation programme selected a sample of random numbers, of a chosen size, from a Gaussian distribution. The maximum and minimum values from the random sample of numbers were recorded and used to calculate the range of the sample. This process was repeated 2,500 times for each sample size chosen, to obtain an accurate mean range of the data. The proportion of the original Gaussian distribution

which was represented by the mean range of the data was then calculated. An example of a single sample of five numbers is shown schematically in Figure 3.21.

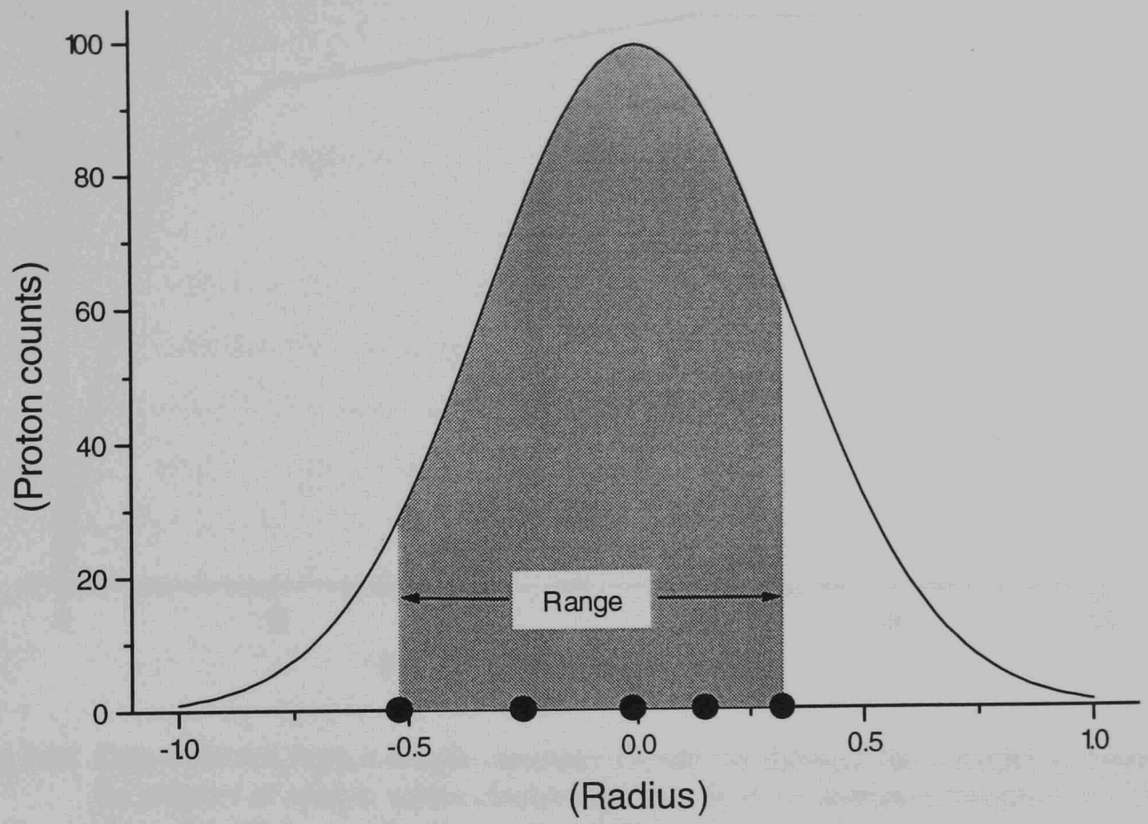

Figure 3.21 A schematic representation of the process involved in calculating the proportion of the transmitted beam profile represented by the irradiation of CR39 track etch plastic with a given number of protons.

The diagram shows an example in which a random sample of five numbers (-0.51, -0.25, -0.01, 0.15, 0.32) was chosen from the Gaussian distribution shown. From these numbers the range of the example data was calculated to be 1.66 and the area of the Gaussian represented by this range is shown by the hashed area.

The proportion of the area of the original Gaussian distribution represented by each sample size is shown in Figure 3.22. If the profile of the transmitted experimental proton beam can be approximated to a Gaussian profile then the data obtained from this simulation will also provide an accurate indication of the proportion of the transmitted beam represented by an irradiation with a chosen proton number.

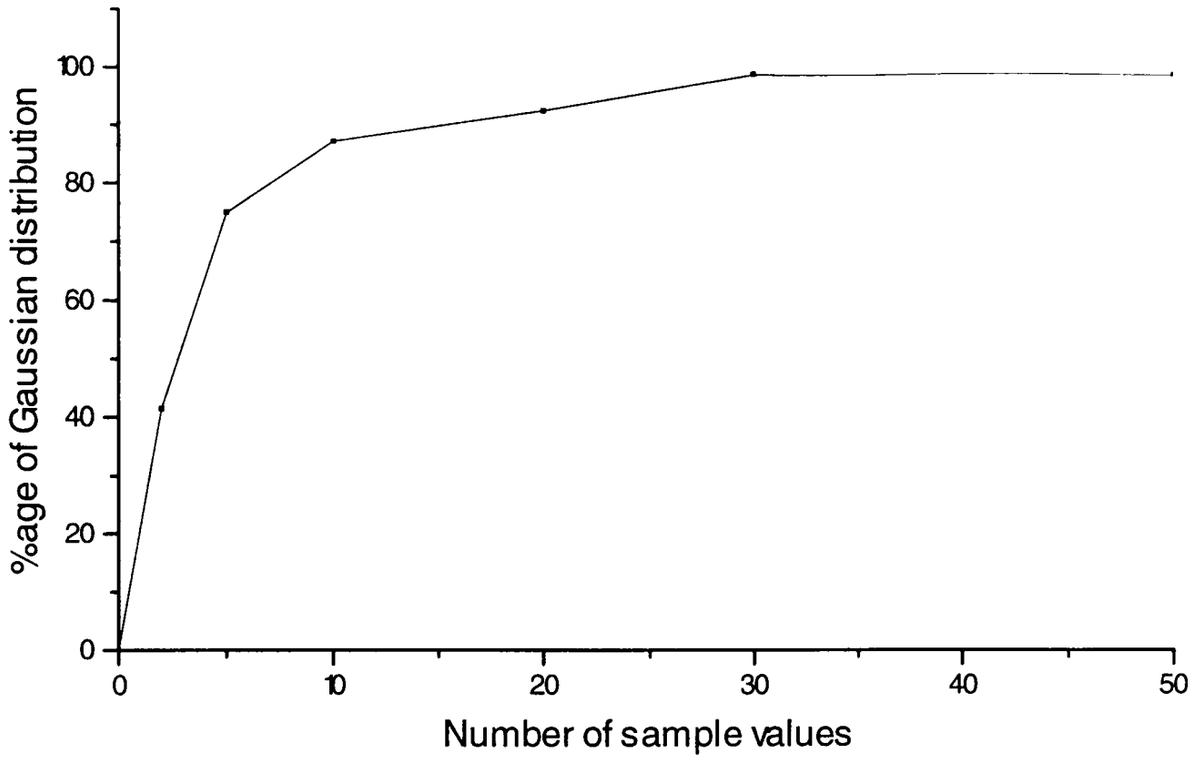

Figure 3.22 Data obtained from a simple computer simulation showing the correlation between the number of sample values chosen randomly from a Gaussian distribution and the area of the Gaussian distribution to which the range of the data corresponds.

It can be seen from Figure 3.22 that the best representation for the width containing 90 % of the transmitted beam is given by the mean diameter of multiple point irradiations by ~ 10 protons. The mean beam sizes obtained by repeated irradiations with ~ 10 protons are given in Table 3.1 and show experimentally obtained 90 % beam widths of 6.9, 4.7 and 2.3 μm for hplc tubing bore sizes of 10, 5, and 1.5 μm respectively.

In summary, several types of collimators have been tested in this work to attempt to collimate a 3.5 MeV proton beam to a dimension of 1 μm. The use of chromatography tubing has come closest to achieving this goal, having an exit aperture of 1.5 μm and an energy spectrum with 75 % of the transmitted beam lying within a narrow high energy peak. A further attempt by S.G.E. Ltd to produce tubing with a bore of less than 1 μm may well be successful and would hopefully produce a similar energy resolution to that obtained at 1.5 μm with a consequent improvement in the spatial resolution of the transmitted beam.

Although having a poorer spatial resolution, the approach using silicon collimation is the most versatile for the production of collimators with novel designs and may be

developed further in the future. However, the cost of the processing involved is considerable and the performance of the collimators does not as yet match that of the chromatography tubing.

3.8 Further Developments

The collimators which were designed and tested in this chapter were all based upon the principle of obtaining the optimum performance of a single collimator. The simulation work undertaken in Chapter 2 shows that the use of voids in collimators may produce a small improvement in the performance of the collimator. It would be possible to produce a double collimator system using the laser drilled hole method by the use of two co-linear holes. This is the approach which has been used in the production of the collimator for the Columbia laboratory microbeam. The introduction of voids into the chromatography tubing would be more difficult but could perhaps be achieved by the rigid mounting of a single length of tubing followed by the removal a middle section from the single tube resulting in two co-linear collimator tubes. The simplest method of manufacture which could be used to produce double collimator designs is that of silicon micro-machining, which would require only the redrawing of the electron written design mask to implement.

Another method suggested in Chapter 2 to improve the performance of the collimation is to use a curved collimator in a magnetic field. Again this could be included in the writing of the electron mask for the production of collimators in silicon and samples of these collimators having lengths of 5 mm and radii of 289.1 mm were produced. An alternative approach would be to introduce a circular bend into a length of chromatography tubing however this would require a more rigorous design to ensure a circular path and to align the collimator with the magnetic field. In both cases the design of a mounting arrangement to produce a uniform magnetic field aligned with the plane of the collimator will require considerable skill.

3.9 Comparison of Results Obtained from Experiment and Simulation

Experimental data for both the spatial and energy resolutions of the transmitted beams produced by several types of collimator were obtained in this work. It was therefore possible to compare the experimental data obtained with the expected performance of the collimators, calculated using the simulation programme described in Chapter 2.

Comparison of the performance of a drawn glass micro-capillary collimator having a 5 μm exit aperture, was made with the simulation of a tapered collimator of similar geometry in silicon. In order to make a comparison between the two-dimensional spatial data obtained from the simulation and the three-dimensional spatial data obtained by experiment, the experimental data were represented as the number of protons per unit area. The results are shown in Figures 3.23 and 3.24.

The energy spectra obtained from the experiment and from the simulation programme show a similar shape although the experimental spectrum has a better energy resolution with a sharper high energy peak. Both spectra demonstrate the presence of a significant number of scattered particles with reduced energies. The spatial resolution also shows some discrepancy between the two data sets, however, in this case the experimental data show a poorer spatial resolution than that of the simulation. An excess of scattered particles at radii greater than 4 μm is present in the data obtained by experiment. The difference between the predicted performance and that shown by experiment may be due in a large part to the lower stopping power of the polymer which makes up the thickness of the collimator wall, relative to that of the silicon walled collimator used in the simulation. The range of 4 MeV protons in the polymer is 220 μm compared to 150 μm for silicon. Since the transmission of the particles through the collimator tip makes a significant contribution to the increase in beam size, the increased penetration of the protons through the polymer will make a significant difference to the size of the transmitted beam. This may also explain the superior energy resolution of the experimental data, since the transmitted particles which emerge through the exit surface of the collimator will have suffered less energy loss than particles with an equal path length in silicon. An additional contribution to the difference between the spatial resolutions obtained may be due to the overlap of pits at the centre of the beam. The

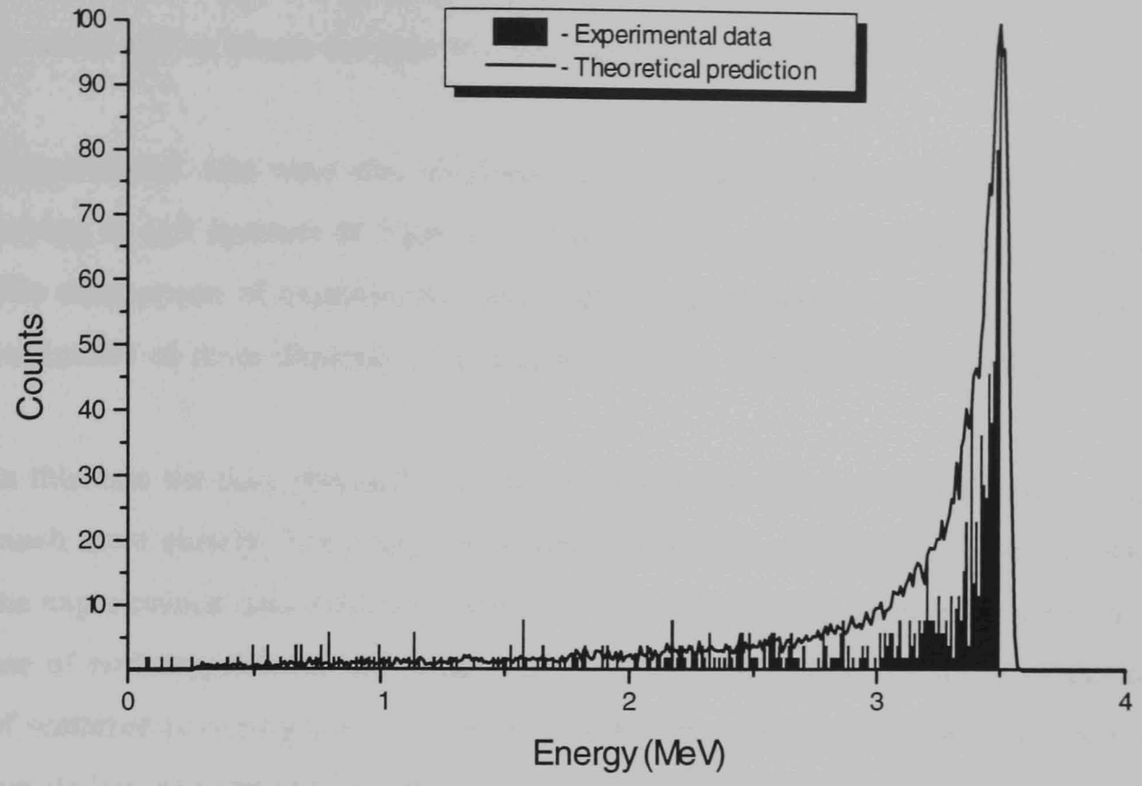

Figure 3.23 A comparison of the energy spectrum of the transmitted beam produced by a drawn glass micro-capillary collimator having an exit aperture of 5 μm (Bars), with the energy spectrum predicted by a Monte-Carlo simulation programme for a collimator of similar dimensions in silicon (Solid Line).

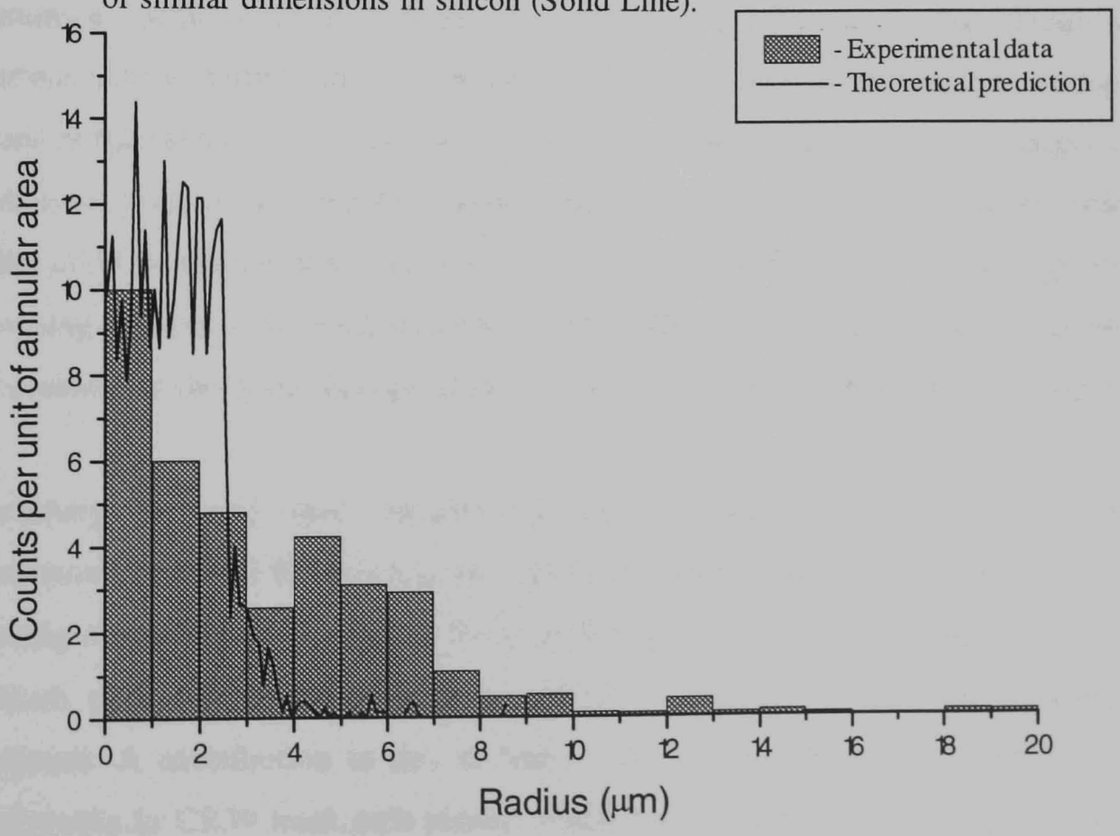

Figure 3.24 A comparison of the spatial resolution of the transmitted beam produced by a drawn glass micro-capillary collimator having an exit aperture of 5 μm (Bars), with the spatial resolution predicted by a Monte-Carlo simulation programme for a collimator of similar dimensions in silicon (Solid Line).

dense core of high energy protons prevents the observation of double hits at the same location and so biases the data towards the observation of proton hits at larger radii.

Experimental data were also obtained for a straight sided fused-silica glass collimator having an exit aperture of 5 μm and a length of 1.6 mm, constructed using hplc tubing. The comparison of experimental data with the data obtained from the simulation of a collimator of these dimensions in silicon is shown in Figure 3.25 and 3.26.

In this case the data obtained from the simulation programme fit the experimental data much more closely. The energy spectrum obtained from the Monte-Carlo simulation fit the experimental data extremely well over four orders of magnitude, as is shown by the use of both logarithmic and linear scales in Figure 3.25. The prediction of the number of scattered protons present in the beam at low energies is calculated accurately by the simulation programme for all energies present in the transmitted beam. The data obtained for the spatial resolution of the transmitted beam also show a better correlation between the two data sets than for the previous comparison. However, the simulation programme again predicts a beam size which is smaller than that obtained by experiment. One contribution to this effect is the difficulty of identifying overlapping protons at the centre of the beam which will add a bias towards protons at larger radii. In addition, protons with the full incident energy of 3.5 MeV produce a pit which is smaller and less distinct than the pit produced by a proton with a lower energy, due to the etching process of the track etch plastic. This effect will favour the identification and measurement of the lower energy, scattered protons present in the beam at larger radii.

In summary, the energy spectrum obtained from the simulation programme predicts the experimental data well for collimators constructed using materials with energy loss and scattering characteristics similar to those of silicon. However, the spatial resolution of the beam produced by the simulation appears to be smaller than that obtained by experiment. A contribution to this difference is made by the characterisation of the proton tracks in CR39 track etch plastic. Since the difference between the data sets is small for collimators constructed using materials with similar properties to those of silicon, the programme may be used to predict the optimum geometries of glass and silicon collimators for microbeam design.

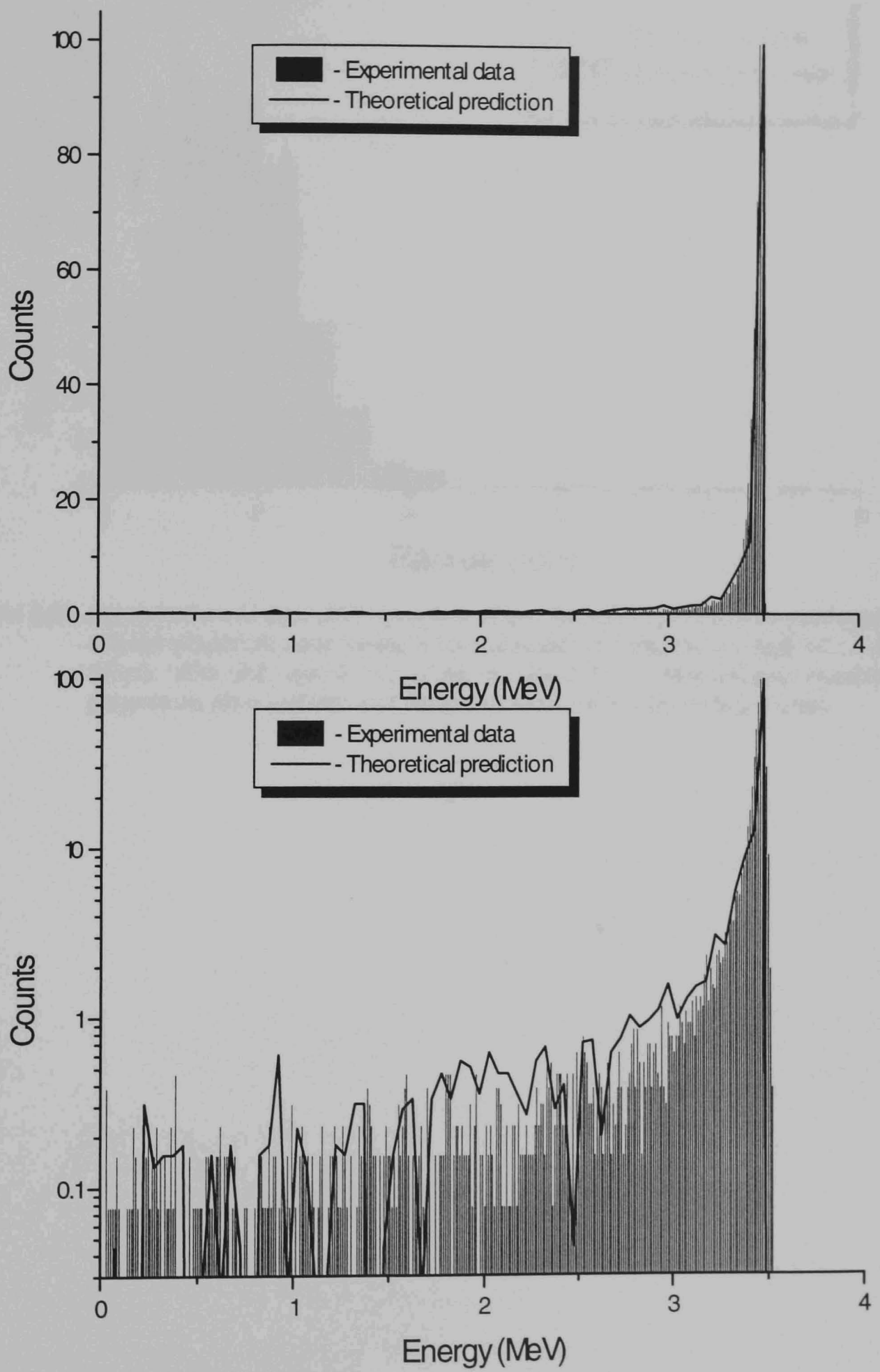

Figure 3.25 A comparison of the energy spectrum of the transmitted proton beam produced by a fused-silica collimator having a bore diameter of 5 μm and a length of 1.6 mm (Bars), with the energy spectrum predicted by a Monte-Carlo simulation programme for a collimator of similar dimensions in silicon (Solid Line), a) on a linear scale and b) on a logarithmic scale.

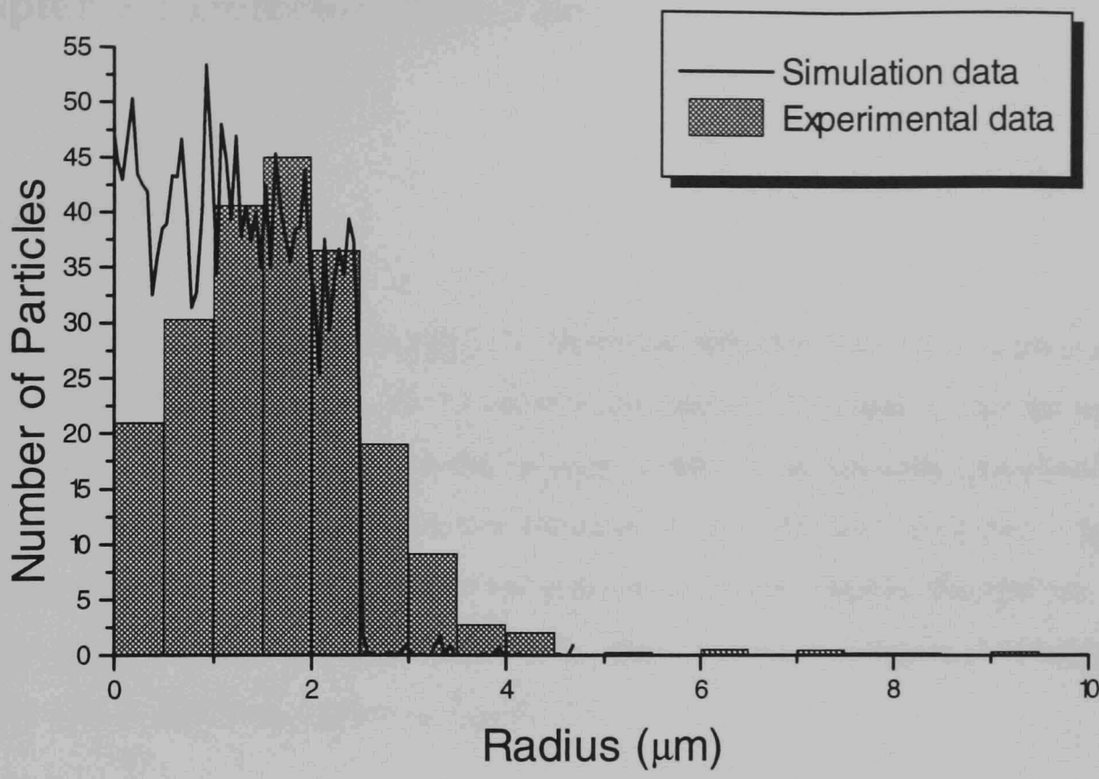

Figure 3.26 A comparison of the spatial resolution of the transmitted proton beam produced by a fused-silica collimator having a bore diameter of 5 μm and a length of 1.6 mm (Bars), with the spatial resolution predicted by a Monte-Carlo simulation programme for a collimator of similar dimensions in silicon (Solid Line).

Chapter 4 : Detector Materials

4.1 Introduction

The use of a proton microbeam to study the biological effects of low-doses of particulate radiations on cells requires the use of an efficient particle detection system to ensure minimal errors in the dose given to the individual cells of an irradiated population. If no particle detector was used then the variation in the delivered dose for a timed exposure at a defined dose-rate would be determined by the Poisson distribution. The variation would therefore be considerable in the case of irradiation by small numbers of particles and is discussed further in Section 1.1.

The geometrical configuration of the microbeam assembly allows access for a particle detector in two positions, before and after the particle has traversed the cell, see Figure 4.1.

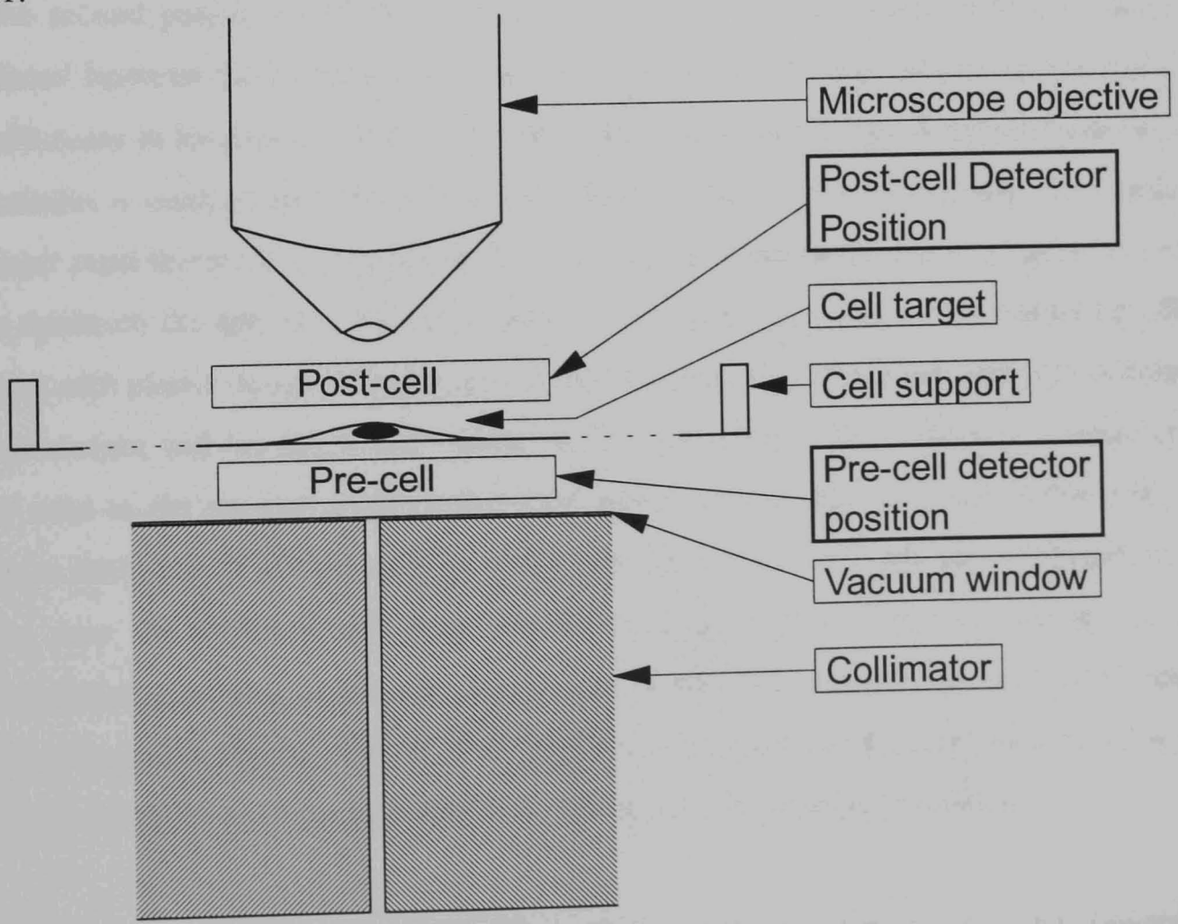

Figure 4.1 A schematic of the possible positions for a particle detector for the Gray Laboratory microbeam facility, showing the elements limiting the available space in each position.

In both positions considerable practical difficulties exist in the design of a suitable detector system. In the post-cell position the physical access is restricted by the objective lens and the presence of cell culture media over the target cells. In addition, the penetration of 4 MeV protons is only 140 μm in unit density material and so much of the culture media would need to be removed or displaced for the penetrating particle to have any remaining energy for detection. Removing the cell media during irradiation is likely to effect the biological responses of the cell and will also alter the focal plane of the image. The use of a particle detector in this position also precludes the use of particles with penetration depths of less than the cell thickness. A possible design for a detector in this position would be to remove the objective lens and replace it with a particle detector. This approach would however require a change in the apparatus between imaging the target cell and its irradiation and would lengthen the time required for each irradiation. This problem would be alleviated by the use of an accurate repositioning apparatus. The co-ordinates of the cells could be logged initially and then revisited blind, with a particle detector in place of the objective lens.

The second possible position for a particle detector is a transmission type of detector placed between the collimator exit and the base of the cell dish. However, the use of a collimator to localise the position of the proton beam results in a divergent beam which contains a small proportion of scattered particles which diverge rapidly. The cellular target must therefore be as close to the exit surface of the collimator as possible in order to minimise the spread in the collimated beam. The beam profiles obtained using CR39 track etch plastic described in Chapter 3 indicate that the distance between the collimator exit surface and the target cell should be less than 30 μm. The design of a detector to be used in the pre-cell position therefore poses considerable difficulty. However, the space limitation is not the only consideration for a detector in the pre-cell position. In this case the detector will result in both energy loss and particle scatter of the transmitted particles, which will degrade the spatial resolution of the collimated beam. This increase in the divergence of the proton beam will accentuate the necessity for the target cell to be as close as possible to the exit of the collimator system.

A particle detector in the post-cell position has been designed for the Columbia microbeam (Randers-Pehrson, 1994) and a pre-cell detector system has been designed

for the PNL microbeam (Braby, 1993), see Sections 1.6.1 and 1.6.2.

In order to allow the use of particles which do not fully penetrate the target cell and its culture media, the pre-cell position was chosen as the preferred site for particle detection. The properties of materials which may be used will be considered in this chapter, followed by a description of the detector development in Chapter 5.

4.2 Choice of Detector Type

A transmission detector in the pre-cell position was chosen as the preferred option for maximum versatility in the microbeam experiments possible at the Gray Laboratory. Therefore the primary consideration limiting the type of detector which may be used is that of space. Three commonly used types of charged particle detector are scintillation counters, gas-filled detectors and silicon detectors. The choice of detector type which is most suited to the detection of 4 MeV protons was determined by detector efficiency, cost and geometrical considerations.

In order to use a silicon detector the thickness of silicon used would be limited to ~ 10 μm due to the effect of scatter within the detector material on the collimated beam. This poses several difficulties. Although commercial silicon detectors with this thickness are available the mounting arrangements used protrude a considerable distance above the surface of the silicon and so are unsuitable for this application. In order to develop a silicon detector in-house it would be necessary to construct a system from an unmounted silicon wafer which was then polished to a thickness of 10 μm. This is near to the limit of silicon detector production and so both the cost involved in the initial purchase and the fragility of the detector make this an impractical alternative. An additional problem of silicon detectors is that to perform efficiently the lattice structure must be free from defects. Protracted irradiation of a beam in a spot several microns in diameter would eventually cause a destruction of the lattice structure over the collimator position so reducing the efficiency of the detector. This approach has therefore not been adopted.

The construction of a gaseous transmission detector is a second possibility which is made extremely difficult by the geometry imposed upon it. The simplest geometry for

a gaseous detector is that of a parallel-plate ionisation chamber, having a unity gain. The energy required to produce an ion pair in most detector gases is ~ 30 eV (Tait, 1980). The energy deposited by a 4 MeV proton in 30 μm of argon at standard temperature and pressure is 330.6 eV (Ziegler, 1985) and so the number of ion pairs produced in the gas would be 11. Since the noise level of a low-noise preamplifier is equivalent to approximately 500 ion pairs (Tait, 1980) it would be necessary to introduce a signal gain into the system by the use of a thin wire proportional counter geometry. Construction of a thin wire proportional counter having a thickness of less than 10 μm would be extremely difficult. In addition, a gaseous detector normally requires a constant flow of gas to maintain a high counting efficiency. These considerations make this approach to the development of a gaseous transmission particle detector unrealistic.

The third option is that of a scintillation detector. This approach has several advantages over that of a gaseous or solid-state detector. Scintillating materials are commercially available in thin geometries of 10 μm thickness at a low cost. The performance of these materials is well characterised and the signal sizes expected from the materials available is sufficient for the efficient detection of 4 MeV protons, see Sections 4.4 and 4.5. The collection of the emitted photons is made feasible by recent developments in fibre optic technology and the availability of photomultiplier tubes which provide a low-noise, high-gain method of converting the photon pulse into an electrical signal. These practical considerations favour a scintillation counting approach for the development of a pre-cell particle detector for the microbeam system.

4.3 Scintillation Theory

When a charged particle passes through a material it loses energy primarily through Coulomb interaction with the atomic electrons, causing ionisation and excitation of the constituent atoms or molecules of the material. In some cases the excited atoms will relax back to the ground state by the emission of a photon. In order for a material to scintillate efficiently, the relaxation of the excited atoms to the ground state must be preferentially by the emission of a photon rather than by other non-radiative processes, for example energy loss through molecular vibrations. In addition, the absorption of the emitted light by the scintillator must be low otherwise the emitted light will not escape

the material. Since for most materials the absorption and emission spectral lines are close together the re-absorption of the emitted photons is usually high and as a result efficient scintillating materials are rare.

Two categories of scintillating materials exist, organic and inorganic materials. The process of scintillation in the two cases is different and so will be considered separately.

4.3.1 Organic scintillators

The most common organic scintillators commercially available are the plastic type and consists of a mixture of scintillating molecules in a polymer base material which is transparent to the emitted light. The process of scintillation in an organic scintillator occurs by the direct excitation of a molecule of the scintillator by an incident charged particle. The excitation and radiative relaxation processes of the molecule are shown diagrammatically in Figure 4.2.

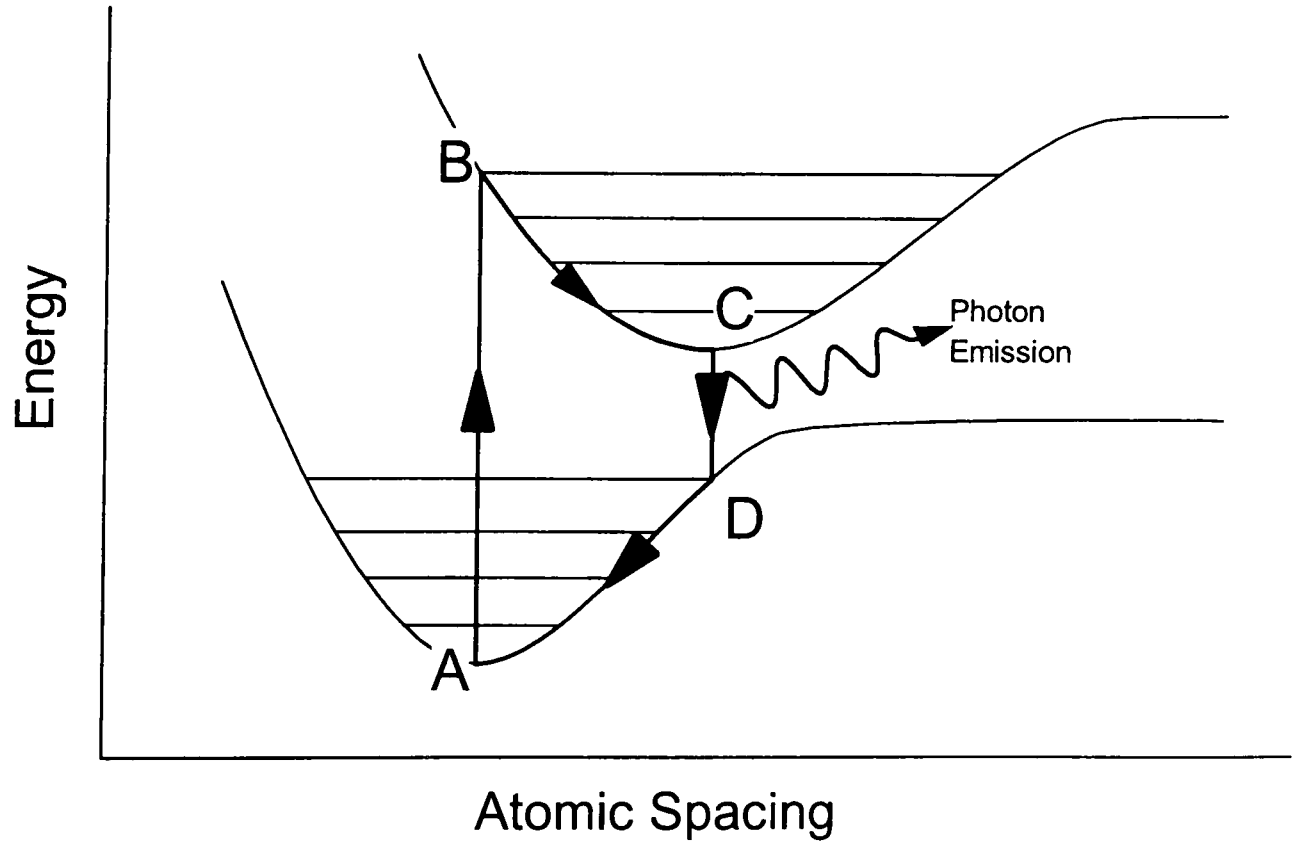

Figure 4.2 A diagrammatical representation of the excitation and radiative relaxation processes involved in the scintillation process of an organic scintillating material.

The incident charged particle excites an atom of scintillator from the ground state, A, into its first excited state, B. By the Franck-Condon principle the transition is too rapid

for a change in the atomic separation of the molecule to occur and consequently the atom at B is in an excited vibrational state. The atom subsequently relaxes by inter-atomic collisions and a consequent loss of vibrational energy, until it reaches a semi-stable state at C. The atom may then decay back to the ground state at D by the emission of a photon, at a rate determined by the stability of state C. The atom at D will again be excited vibrationally and will subsequently decay back to state A by the loss of vibration energy to neighbouring molecules. Due to the additional loss of vibrational energy the radiative process from state C to state D has a lower energy difference than is required for the excitation from state A to state B, and so it is not possible for the emitted photon to re-excite this transition in another molecule of scintillator. The re-absorption of the emitted photon by other scintillator molecules is therefore small.

The process of fluorescence in these molecules is highly efficient, ~ 90 % at the characteristic excitation wavelength. However, the scintillation process is far less efficient due to the necessity for the incident charged particle to excite a molecule of scintillator directly. The efficiency of conversion of the energy lost by the charged particle to energy emitted as photons from the material is therefore only ~ 4 % for anthracene, one of the most efficient organic scintillators (Gilmore, 1992).

4.3.2 Inorganic scintillators

The principle difference between the process of scintillation by an inorganic material rather than a polymer is that the energy of the charged particle may be deposited anywhere within the crystal lattice and may then be transferred to a scintillation site elsewhere in the material. This contrasts with the case of organic polymers where the scintillating molecule must be excited directly. Again the steps in the scintillation process are best expressed diagrammatically, see Figure 4.3.

A valence band electron of the crystal lattice is excited into the empty states of the conduction band and therefore becomes free to move from atom to atom within the lattice. Since the valence band is fully occupied, except for the very few holes resulting from the ionisation of electrons to the conduction band, the electron will remain mobile in the lattice until it encounters an empty state at a lower energy for which a transition

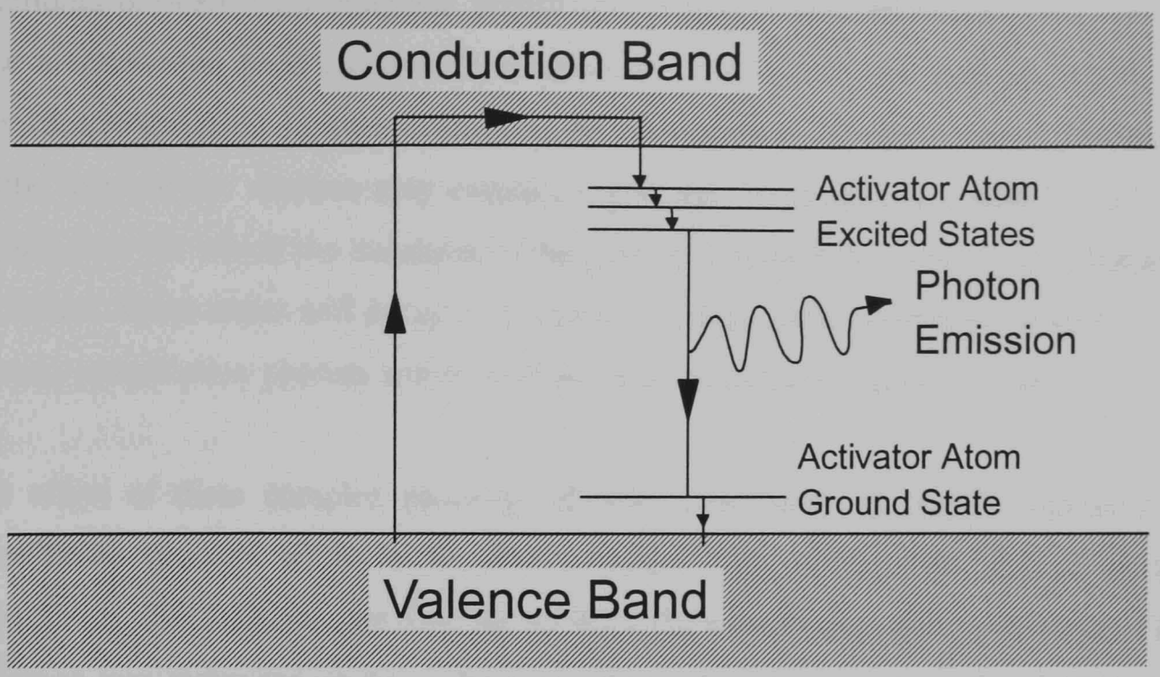

Figure 4.3 A diagrammatical representation of the excitation and radiative relaxation processes involved in the scintillation process of an inorganic scintillator material.

from the conduction band is permitted. The doping of the intrinsic crystal with activator ions, or scintillation sites, results in the production of electronic states in the band-gap between the valence and conduction bands of the intrinsic material. A mobile conduction band electron may therefore decay into these empty states at the site of an activator atom. The electron may then decay from the excited state of the activator atom to its ground state by the emission of a photon, and then by non-radiative decay back to the valence band of the intrinsic atoms. Again the energy of the emitted scintillation light will be less than that required to excite an electron into the conduction band of the intrinsic material and so the emitted photon is unlikely to be reabsorbed by the material.

Since the energy deposition site for charged particles in these materials is non-specific the efficiency of conversion of the deposited particle energy into emitted photons is generally higher than that of organic scintillators. However, there are competing processes within the crystal structure which reduce the efficiency of photon production. These processes are non-radiative routes for the ionised electron to return to its ground state and are due to the presence of lattice imperfections. The lattice imperfections, which may be flaws in the crystal structure or the presence of impurities, introduce additional energy states into the band gap of the material. These energy levels may act as electron traps, preventing or delaying the scintillation process, or may allow the decay of the ionised electrons back to the valence band by non-radiative processes. An

additional problem with inorganic scintillators is that of delayed fluorescence. In this case a conduction band electron decays into an excited activator state for which the transition to the ground state is prohibited. By the statistics of thermal energy fluctuation of the material the electron may eventually gain sufficient energy to excite it into an atomic state for which the transition to the ground state by the emission of a photon is permitted. These states will decay over a relatively long period compared to that of the primary scintillation process and so will result in an extended photon pulse.

The effect of these complex pathways of atomic relaxation is that the emission of scintillation photons tends to be over a longer time period than that of plastic scintillators. For example, the time for 90 % of the scintillation light to be emitted for ZnS(Ag) was measured to be as long as 100 μs for some of the large light pulses recorded in this work. The overall conversion efficiency from particle energy loss to emitted photons however remains high, with better than 20 % efficiency for intrinsic ZnS crystals.

In the design of a detector for the Gray Laboratory microbeam project both inorganic and organic scintillators have properties which both favour and oppose their use. Some consideration of the properties of two scintillator materials with high conversion efficiencies in each class is given here.

4.4 NE102 Organic Scintillator

NE102 is a polyvinyltoluene based polymer with a density of 1.032 g cm^{-3} and a refractive index of 1.56. It has a light output which is 65 % of that of anthracene and its wavelength of maximum emission is 423 nm (N.E. Technology, UK). The conversion efficiency with which NaI(Tl) converts energy deposited into emitted photons is ~ 13 % (Tait, 1980) and is equivalent to 230 % of the efficiency of anthracene (N.E.Technology Data Sheet).

The conversion efficiency for NE102 is therefore, **13 % × 65 / 230 = 3.67 %.**
The energy loss of 4.0 MeV protons in 1 μm of NE102 is **15 keV** (Ziegler, 1985).
The energy converted into photons in 1 μm of NE102 is therefore,

$$15 \text{ keV} \times 3.67 / 100 = 0.55 \text{ keV}.$$

The photon energy at the maximum emission wavelength is,

$$h\,c / \lambda$$

$$= 6.626\text{x}10^{-34} \times 3\text{x}10^{8} / 423\text{x}10^{-9}$$

$$= 4.70\text{x}10^{-19} \text{ Joules}$$

$$= 2.94 \text{ eV}.$$

The average number of photons produced in 1 μm of NE102 by the passage of a 4 MeV proton is therefore,

$$550 / 2.94 = \underline{187.4 \text{ photons.}}$$

A second consideration in determining the thickness of NE102 which may be used to detect particles is the effect of the detector on the divergence of the proton beam. Monte-Carlo simulations of various thicknesses of the polymer base material, toluene, were performed using the TRIM ion transport package (Ziegler, 1985). The data obtained for an incident point source of 3.5 MeV protons with normal incidence to the scintillator are presented in Figure 4.4.

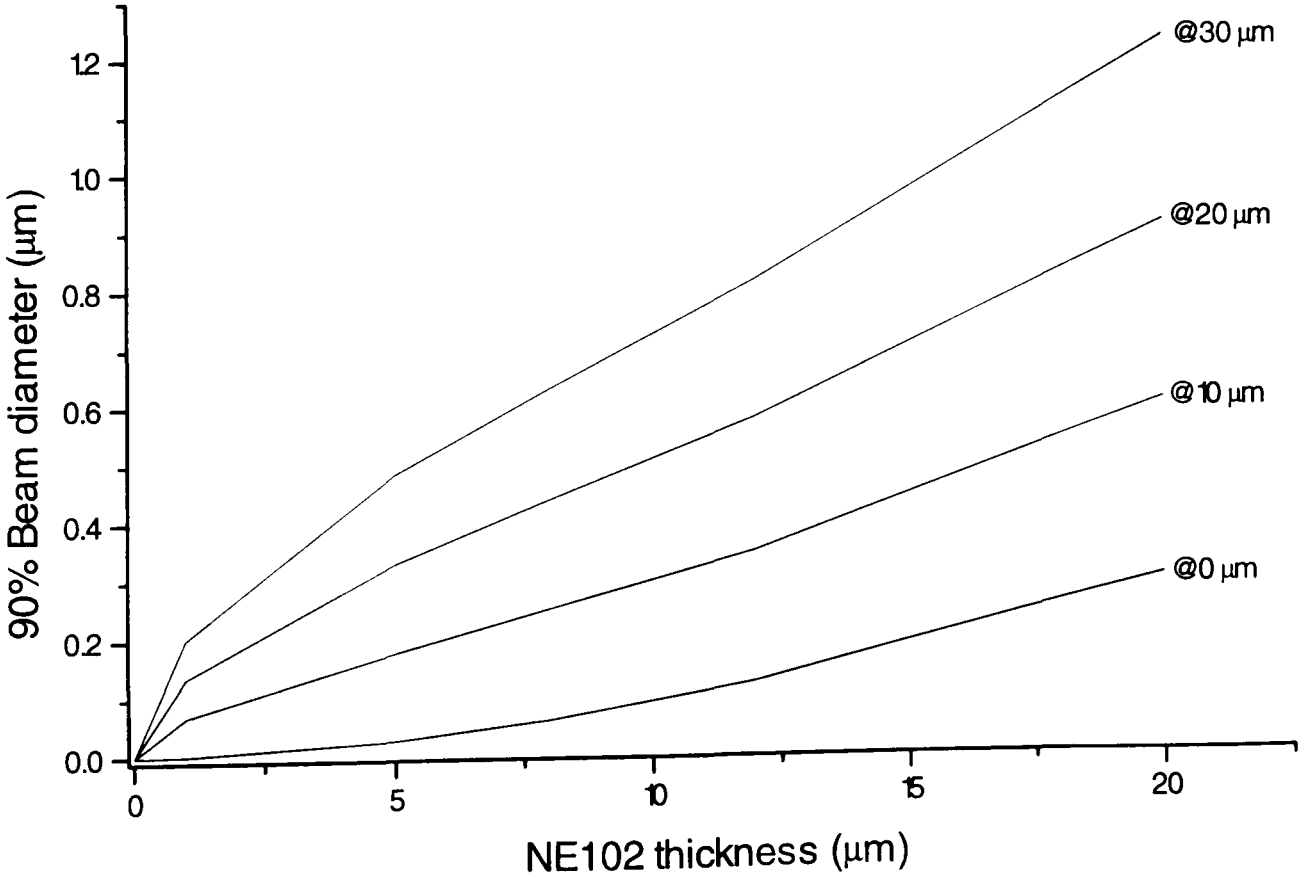

Figure 4.4 A summary of the effect of various thicknesses of toluene, obtained from the simulation of a point source of 3.5 MeV protons, using the TRIM Monte-Carlo simulation programme (Ziegler, 1985). The figure shows the diameter containing 90% of the transmitted beam at distances of 0, 10, 20 and 30 μm from the exit surface of the material.

A foil of NE102 scintillator having a thickness of 10 μm is commercially available and the data show that for this thickness of NE102, at 10 μm from the exit surface 90 % of the transmitted beam has a lateral deviation of less than 0.2 μm and by 30 μm from the scintillator the beam has expanded by 0.6 μm. The thickness of NE102 which is used will be determined by a consideration of the number of photons produced, the efficiencies of photon collection and detection, the effect of the polymer on the transmitted charged-particle beam and the proximity of the target cell to the exit surface of the scintillator.

4.5 ZnS(Ag) Inorganic Scintillator

ZnS doped with silver activator atom is a crystalline solid and is available only as a powder of small crystals. It has a density of 4.09 g cm^{-3} and a refractive index of 2.356. It has a light output of 300 % of that of anthracene and its wavelength of maximum emission is 450 nm.

The energy conversion efficiency for ZnS(Ag) is therefore,

13 % × 300 / 230 = 17 %.

The energy loss of a 4 MeV proton in 1 μm of ZnS(Ag) is **22.67 keV** (Ziegler, 1985). The energy converted into photons in 1 μm of ZnS(Ag) is therefore,

22.67 keV × 17 / 100

= 3.855 keV.

The photon energy of maximum emission is given by, **h c / λ**

= 4.42x10^{-19} Joules

= 2.76 eV.

The average number of photons produced in 1 μm of ZnS(Ag) by the passage of a 4 MeV proton is therefore,

3855 / 2.76 = <u>1397 photons.</u>

Again the effect on beam divergence has been considered using the TRIM ion transport package. The results are shown in Figure 4.5.

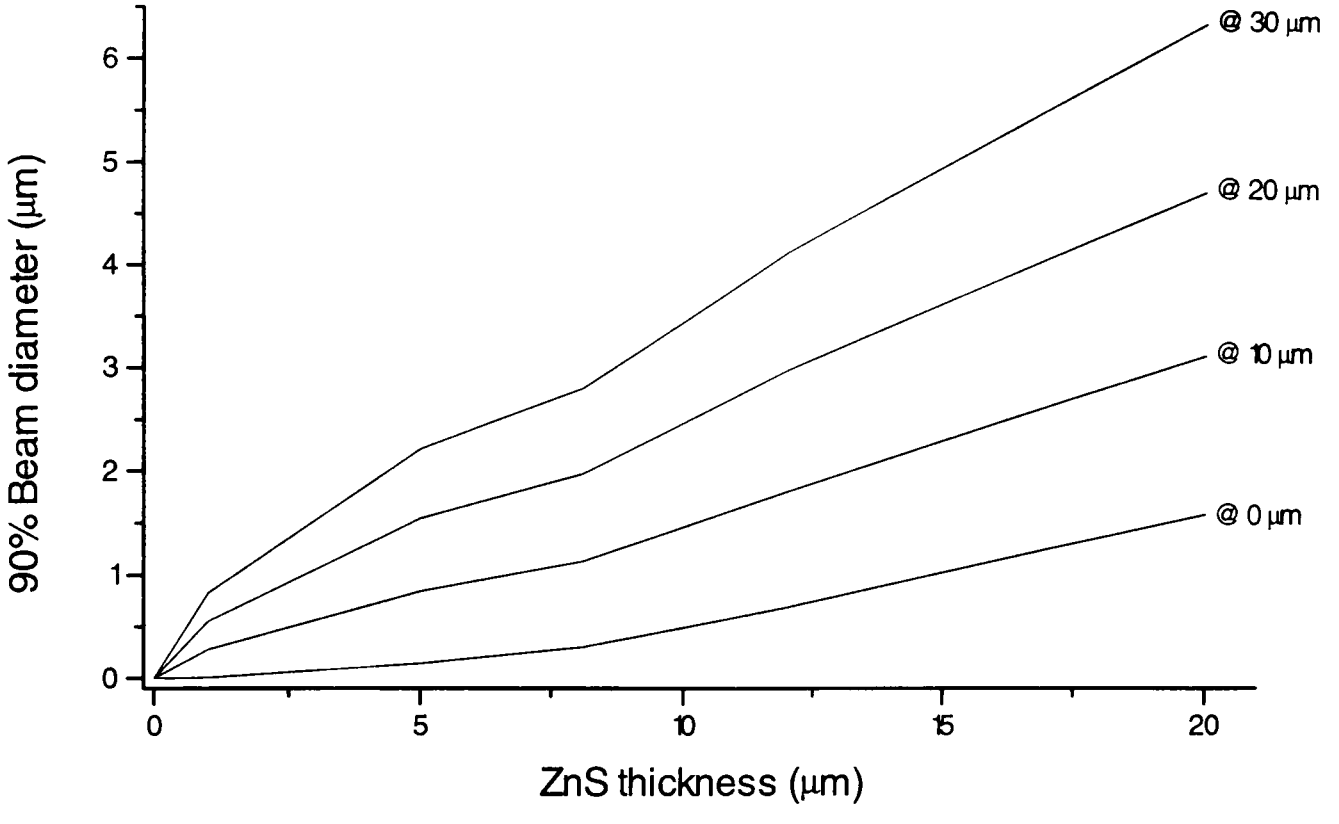

Figure 4.5 A summary of the effect of various thicknesses of ZnS, obtained from the simulation of a point source of 3.5 MeV protons, using the TRIM Monte-Carlo simulation programme (Ziegler, 1985). The figure shows the diameter containing 90% of the transmitted beam at distances of 0, 10, 20 and 30 µm from the exit surface of the material.

In this case the effect on beam divergence is more significant than for NE102 due to the higher atomic number and density of the scattering material. In this case a thickness of 10 µm of scintillator will result in an increase in the beam diameter by 1.4 µm at 10 µm from the surface of the ZnS(Ag) crystal and by 3.4 µm at 30 µm from the scintillator surface.

4.6 Conclusions

When considering the optimum material for the detection of protons the factors of efficiency and particle scatter must be weighed against each other. In addition, the geometries available for each material must also be considered since this will effect the collection of emitted photons in the restricted space imposed by the microbeam apparatus. With these considerations in mind attempts have been made to develop a scintillation detector using a variety of scintillator materials. The attempts made, and the construction of a functional detection system are described in Chapter 5.

Chapter 5 : The Development of a Charged Particle Scintillation Transmission Detector

5.1 Introduction

The mean numbers of photons which are produced by the traversal of a 3.5 MeV proton through 1 μm of NE102a and through 1 μm of ZnS(Ag) were calculated in Sections 4.4 and 4.5. However, to use these materials to produce an efficient particle detector the emitted photons must be collected and then converted into an electrical signal for analysis. The preferred position for a particle detector was shown in Section 4.1 to be between the collimator and the base of the cell dish. In this position the geometry of the microbeam imposes severe restrictions on the collection of photons from the scintillator, due to the proximity of the collimator, cell dish and objective lens. The collection of light from the scintillator is possible in two directions, horizontally out from beneath the cell dish or vertically through its base and the overlying cell culture media. The latter is used in the PNL microbeam, using a 7 μm foil of plastic scintillator over the collimator with a photomultiplier tube in place of or surrounding the objective lens.

The proposed design for the transmission detector developed in this work was to collect the light emitted from the scintillator by the use of small diameter optical fibres close to the scintillator material. The efficient transmission of the fibres in the visible part of the spectrum may then be used to transfer the collected photons to a photomultiplier tube for conversion into a charge pulse. If the diameter of the fibre is sufficiently small it will not compromise the proximity of the collimator to the target cell. In addition, by arranging for light collection close to the point of scintillation the solid angle for the collection of the emitted photons will be large. The combination of a large solid angle for the collection of the emitted light and the high transmission of the optical fibre will result in a high counting efficiency for particle detection.

In addition, since the emitted light is non-directional it will be possible to use more than one fibre coupled to the scintillator in order to collect a greater proportion of the

photons produced. If the amount of light collected in each channel is sufficiently large it will be possible to use a two-channel, two-photomultiplier tube system, allowing the use of a coincidence counting approach. The use of coincident counting allows the use of a low discriminator level which includes some of the single photoelectron noise distribution. Although the distribution of noise pulses will result in single channel noise counts, a coincident count will only be produced by simultaneous events in both channels. If the noise level is sufficiently low then the probability of a false count due to random coincidence will also be low. Since the discriminator level may be set close to the single photoelectron level the size of the light signal collected at the photomultiplier tube may be small relative to that required for a single channel counting approach in which the distribution of noise counts and signal counts must be well separated.

The development of a detection systems developed, using both NE102a and ZnS(Ag) scintillators, and the results obtained will be described here.

5.2 The Development of an NE102a Particle Detector

5.2.1 Initial tests

In order to verify that a thickness of 10 μm of NE102a plastic scintillator would give an adequate signal for the detection of 3.5 MeV protons, a preliminary test was performed using an ^{241}americium alpha particle source. The emitted 5.3 to 5.5 MeV alpha particles were used to irradiate a 10 μm thick polymer foil of NE102a mounted at 1 mm from the source. The apparatus used is shown in Figure 5.1.

The output from the photomultiplier tube was amplified using a 50 μs shaping constant, charge-sensitive pre-amplifier designed and built in-house (Vojnovic, unpublished). The pulses obtained from ZnS(Ag) inorganic crystals were emitted over ~ 100 μs due to the slow process of fluorescence and so were unsuitable for analysis using standard nucleonics. In order to compare the light signals from various scintillating materials a digitising oscilloscope (DSA 602, Tektronix USA) with the ability to count the number of pulses above a discriminator level with a fixed absolute voltage was used to record the heights of the pulses obtained from the various samples of scintillator material.

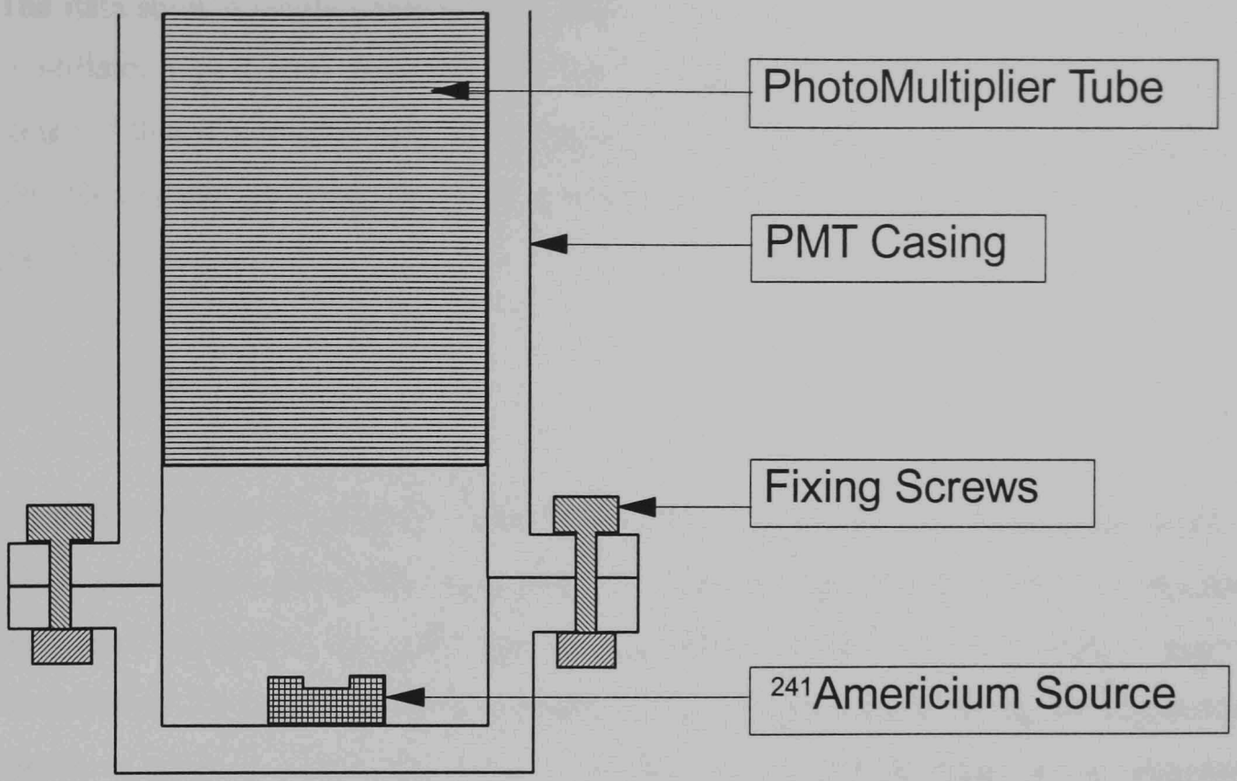

Figure 5.1 Test apparatus for the evaluation of the light output from various scintillator materials, resulting from irradiation by Americium alpha particles.

Timed irradiations were performed using a range of discriminator levels and for each discriminator level the number of pulses above the discriminator level was recorded. A pulse height analysis of the signals obtained from the NE102a is shown in Figure 5.2.

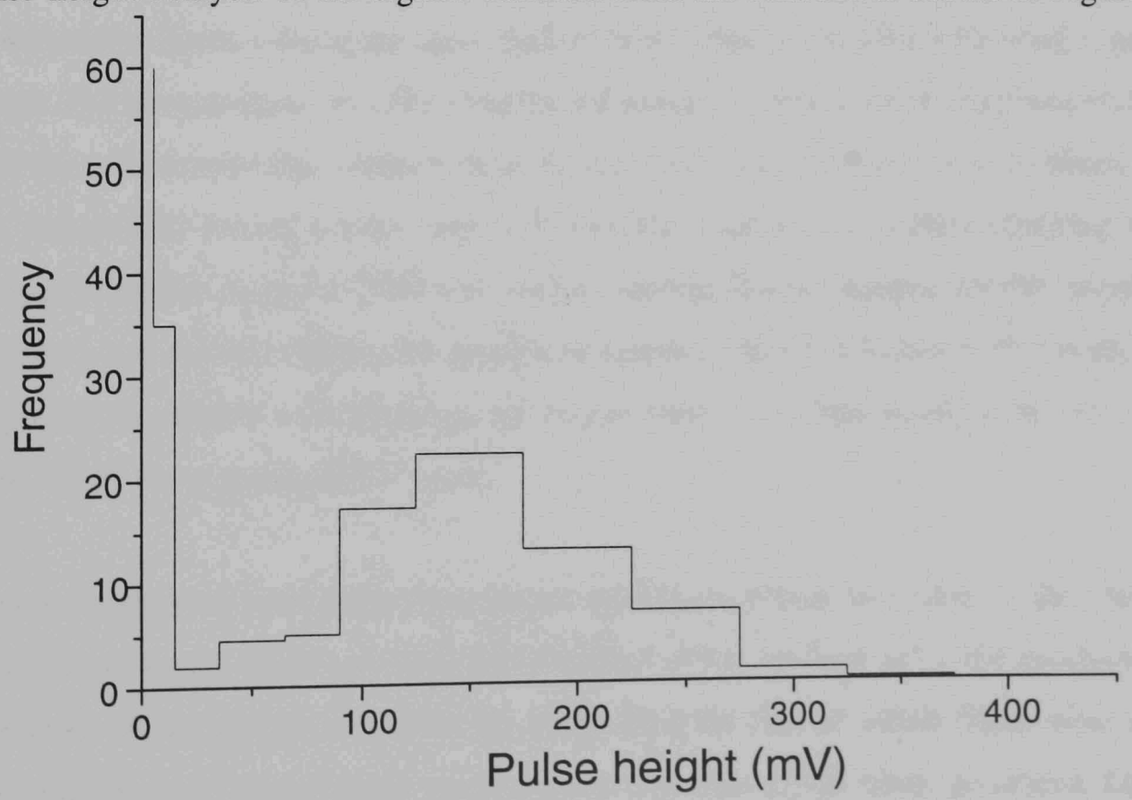

Figure 5.2 Pulse height spectrum obtained for the light emitted by the irradiation of a 10μm thick sheet of NE102a plastic scintillator with 5.3 to 5.5 MeV alpha particles. Signal analysis was by a digitising oscilloscope.

The data show a single photoelectron noise signal below 40 mV with a well separated scintillator signal peak from the NE102a having a maximum at 210 mV. The signal suggests that if a similar light collection efficiency can be achieved by the design of a suitable detector geometry then proton detection using this thickness of NE102a will be possible.

5.2.2 Design

In order to couple the NE102a scintillator to the optical fibres as proposed in Section 5.1 a convenient geometry of scintillator material was required. The calculations performed in Section 4.4, and the work described in Section 5.2.1, suggest that a thickness of 10 μm of NE102a is sufficient for proton detection with an acceptable degree of particle scatter. In order to provide adequate light collection a proposed geometry was the co-axial alignment of a 10 μm diameter fibre of plastic scintillator between two optical fibres with coupling of the components using an optical cement.

In addition to the high solid angle of acceptance of the optic fibre to the scintillator, the use of optical fibres abutted onto the fibre of NE102a allowed the transmission of light by internal reflection along the inner surface of the plastic scintillator fibre into the optic fibres. The photon signal was then transferred along the optical fibre to a photomultiplier tube for conversion into a charge pulse. Commercial optical fibres were obtained (Type A2, Schott UK) having a glass core of 27 μm diameter, a 1.5 μm thick cladding and no protective buffer material. This was within the size limits imposed by the microbeam geometry and the calculations for particle scatter described in Chapter 4. However, fibres of plastic scintillator with diameters of 10 μm were not commercially available and so these fibres were produced in-house.

Two methods were used to produce plastic scintillator fibres. In each case the fibre was drawn from liquid NE102a which was liquified either by heat or by the production of a solution of the plastic in xylene. By controlling the rate at which fibres were drawn from the liquid it was possible to control the diameter of the fibres produced. Lengths of fibre were cut using a sharp blade and resulted in lengths as short as 150 μm being produced.

5.2.3 Construction

In order to test the efficiency of particle detection using this approach a scintillation fibre assembly was constructed. The assembly consisted of two optical fibres with a short length of NE102a fibre connected between them. The optical fibres were then coupled to two photomultiplier tubes using commercial fibre optic connectors (ST-type, The Fibre Optic Centre, UK) which were mounted into the metal housing of the two photomultiplier tubes. The assembly was supported on a frame constructed using glass microscope slides to relieve any stress on the connections between the detector elements.

The detector assembly was constructed under the 10× objective lens of an epi-fluorescence microscope. Each element of the detector was positioned using a three-direction micro-positioning block (Photon Control, UK) which gave the ability to position the detector components to better than 0.1 μm in each direction. The positioning elements were clamped to an in-house constructed plate mounted in the place of the commercial microscope stage and illumination from below through a central hole in the plate was used to provide sufficient light by which to construct the assembly. Ultraviolet light curing optical coupling cement (Type 350, Loctite, UK) was used to hold the individual components together and was cured using ultraviolet epi-illumination via the objective lens. The arrangement of the positioning elements used to construct the detector assembly is shown in Figure 5.3.

The image of a completed detector, obtained using the imaging system of the microbeam apparatus, is shown in Figure 5.4.

Detectors of this type were constructed using fibres from both melted and dissolved NE102a scintillator, however, those fibres drawn from xylene solution proved the more efficient. In the case of the melting technique it is likely that the heating applied to the NE102a denatured or vaporised the molecules of the scintillator from the polyvinyl toluene base polymer of the NE102a scintillator.

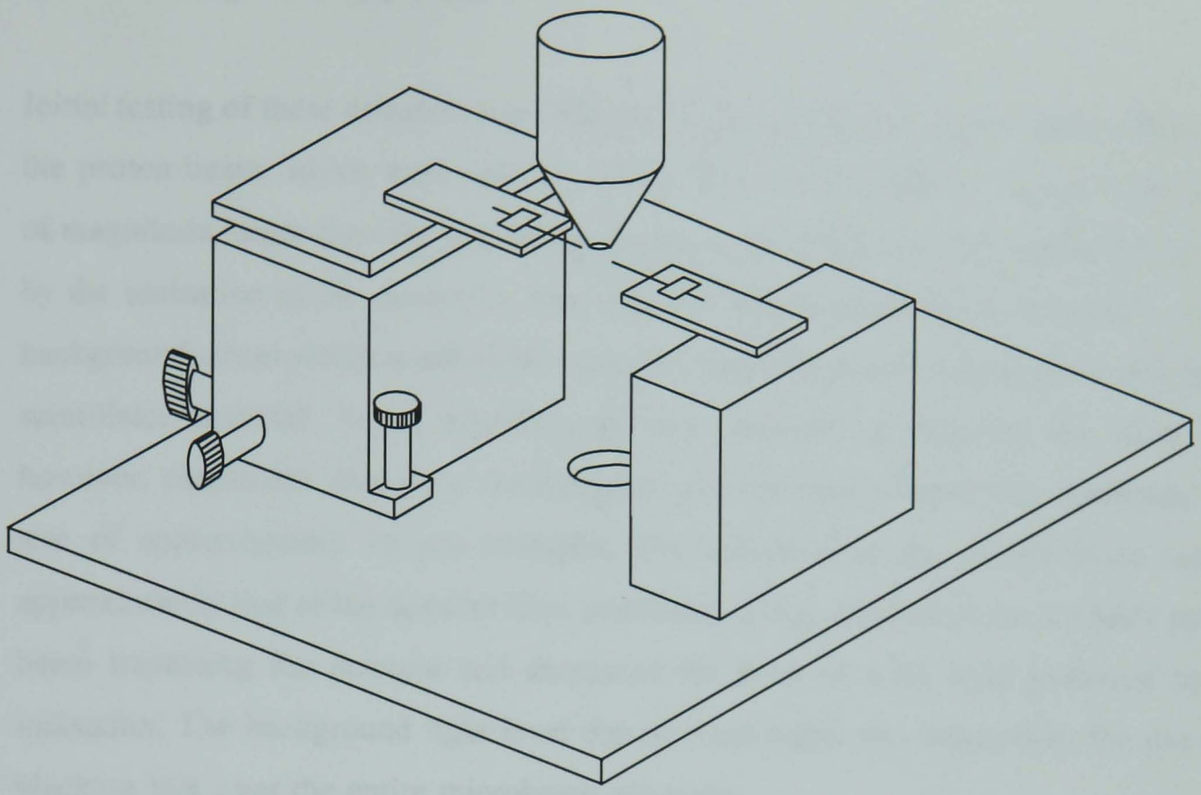

Figure 5.3 The arrangement of the positioning elements used in the construction of the detector assemblies.

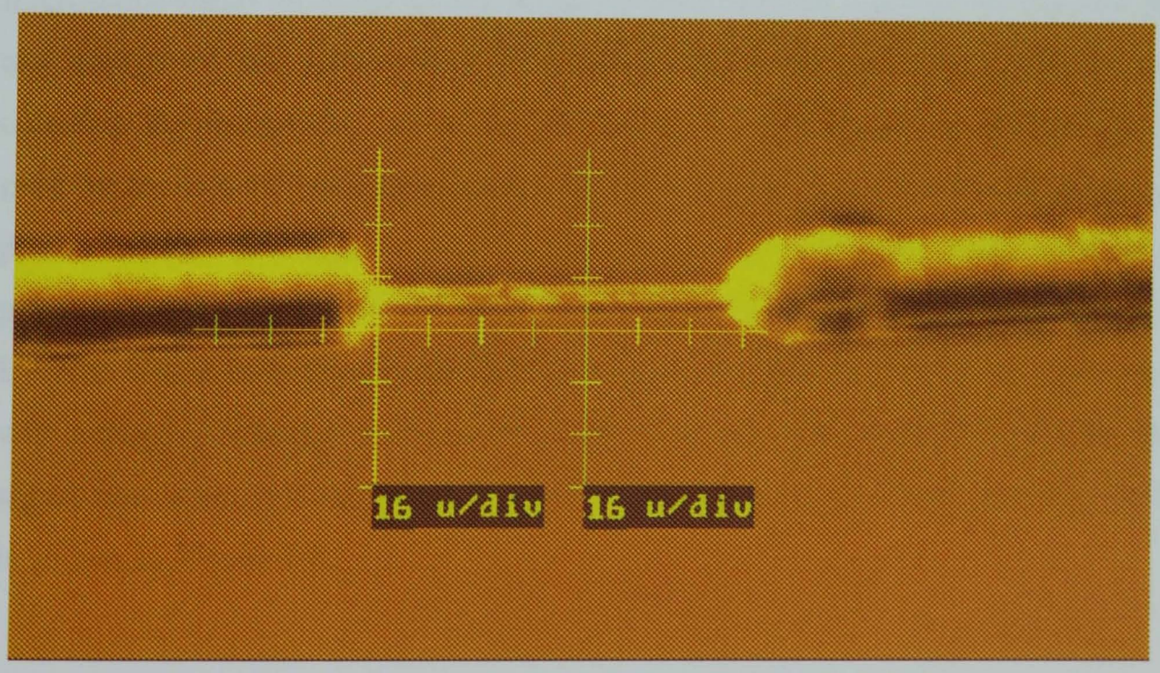

Figure 5.4 A 10 μm diameter plastic scintillator fibre mounted between two 30 μm diameter optic fibres using ultraviolet light curing optical cement.

5.2.4 Counting Efficiency Data

Initial testing of these detectors was difficult since the polonium alpha particle beam and the proton beam, which were used to test the detector assemblies, were several orders of magnitude larger than the size of the detector fibre diameter. The production of light by the ionisation of air molecules, due to the charged particle beam, resulted in a high background count which masked the relatively low number of signals produced by the scintillator material. Some improvement was obtained by reducing the beam size, however, conclusive data were not obtained until the proton beam was collimated to a size of approximately 10 μm diameter. The reduction of the proton beam size to approximately that of the detector fibre resulted in a high fraction of the 3.5 MeV proton beam traversing the detector and decreased the level of stray light produced by air ionisation. The background light level due to room lights was reduced by the use of a blackout box over the entire microbeam apparatus.

The fibre detectors were tested using a proton beam produced by a drawn capillary pipette collimator having an exit aperture diameter of 10 μm. Using an automated microscope stage it was possible to align the detector to a resolution of 0.25 μm. A microscope-turret mounted silicon surface barrier detector was used to monitor the flux and energy of the proton beam. The energy measurements could then be used to calculate the energy loss due to the fibre detector. The production of a single energy peak for the transmitted protons indicated the accurate alignment of the detector over the proton beam. The light signal emitted from the scintillator was detected using photomultiplier tubes having bi-alkali photocathodes and operating at a voltage of 1.1 kV. The signal from the photomultiplier tubes was then amplified using a pre-amplifier with a shaping constant of 50 μs (Vojnovic, personal communication) and the resulting signal was processed using standard nucleonics units. A schematic of the system used is shown in Figure 5.5.

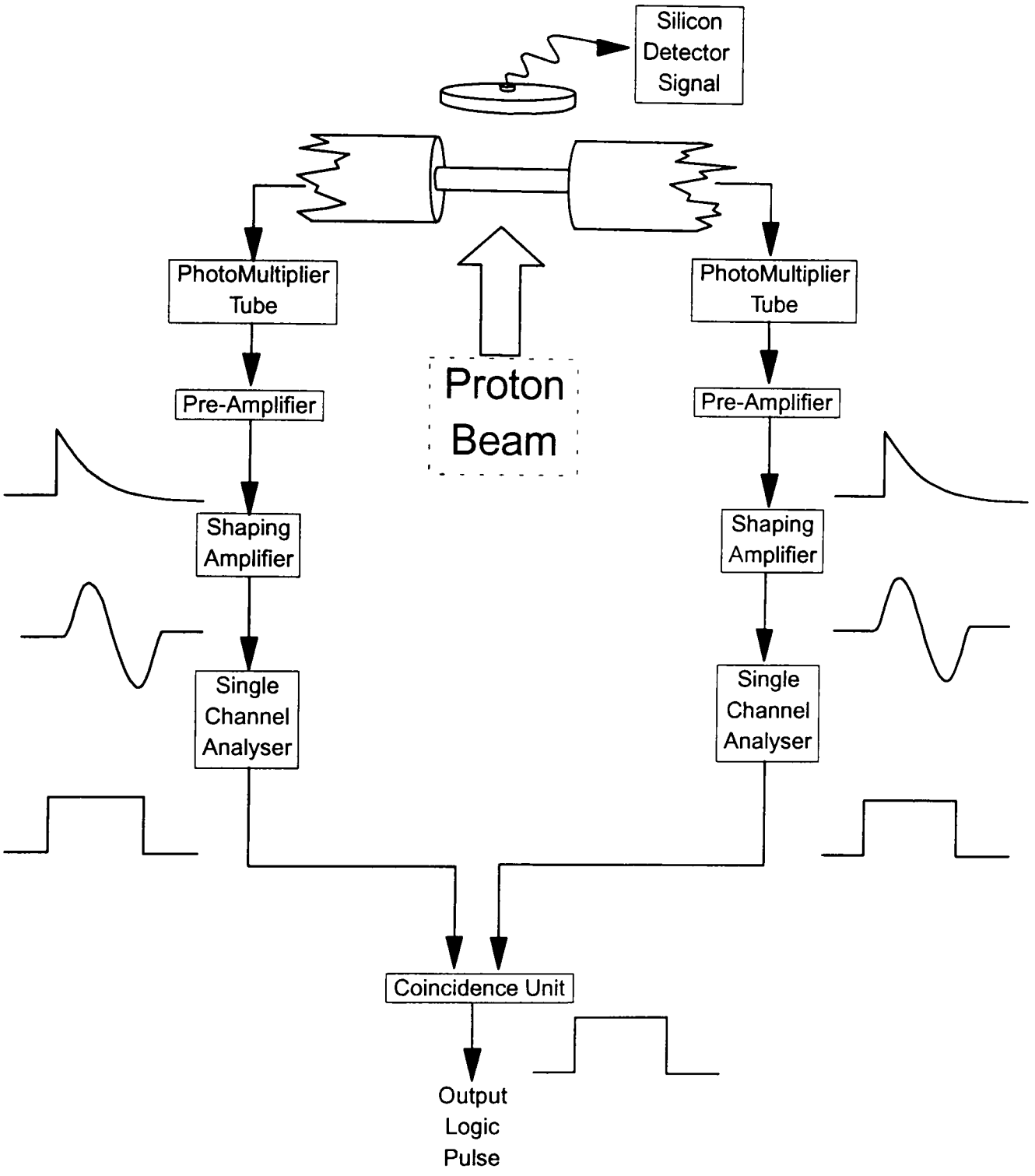

Figure 5.5 A schematic of the detector and signal processing arrangement used to test the plastic scintillant fibre detector assembly.

NE102a fibre detectors with diameters of 7, 14 and 30 μm were tested. For each fibre diameter the discriminator level of the single channel analyzer was set to eliminate electronic noise but to include single photon counts due to stray light. The broad particle beams used previously resulted in light production by the ionisation of air molecules which contributed to an increase in the background counts. An assessment of the effect of air ionisation produced by the collimated beam was therefore performed. A fibre was placed at 50 μm from the collimator aperture and the number of pulses over the

discriminator was recorded. The output showed no increase in the amount of stray light due to the presence of the proton beam and therefore any increase in the number of single photon counts when a detector was present over the collimator aperture was not due to ionisations in the air.

Using a 7 μm diameter scintillating fibre detector the increase in the single channel count rate due to the proton beam was from 6000 counts per minute (cpm) with no beam to 12000 cpm with beam present. However, when the logic pulses from each channel independently were used as the inputs to a coincidence counting unit, the increase in count rate due to the proton beam was only 600 cpm. Therefore for each pulse of at least one photoelectron produced in a single channel, the probability of a pulse of at least one photoelectron being emitted simultaneously in the second channel was only 10 %. The overall detector efficiency in coincidence counting mode was therefore $(10\ \%)^2$ = 1 %.

An increase in the diameter of the NE102a fibre to 14 μm resulted in a single channel counting efficiency of 28 % and therefore an overall coincidence counting efficiency of $(28\ \%)^2 = 7.8\ \%$.

A fibre of 30 μm diameter also showed disappointing results, having a single channel efficiency of only 50 % and therefore an overall counting efficiency of $(50\ \%)^2 = 25\ \%$.

Pulse height analysis of the signal produced was performed using the signal obtained from the 14 μm diameter fibre. The results are shown in Figure 5.6.

The upper curve shows the counts obtained from the photomultiplier tube of a single channel of the detector including both noise signals and scintillator pulses. The lower curve shows data from the same channel but using a coincident signal from the surface barrier detector and therefore including only pulses which were coincident with the transmission of a proton through the scintillator fibre. Since the count rate due to noise pulses was 100 s^{-1}, the probability of a random coincidence occurring within the 10 μs coincidence pulse generated by the surface barrier detector pulse was only 0.001. The data show that when no coincident signal was used the pulse height spectrum consisted

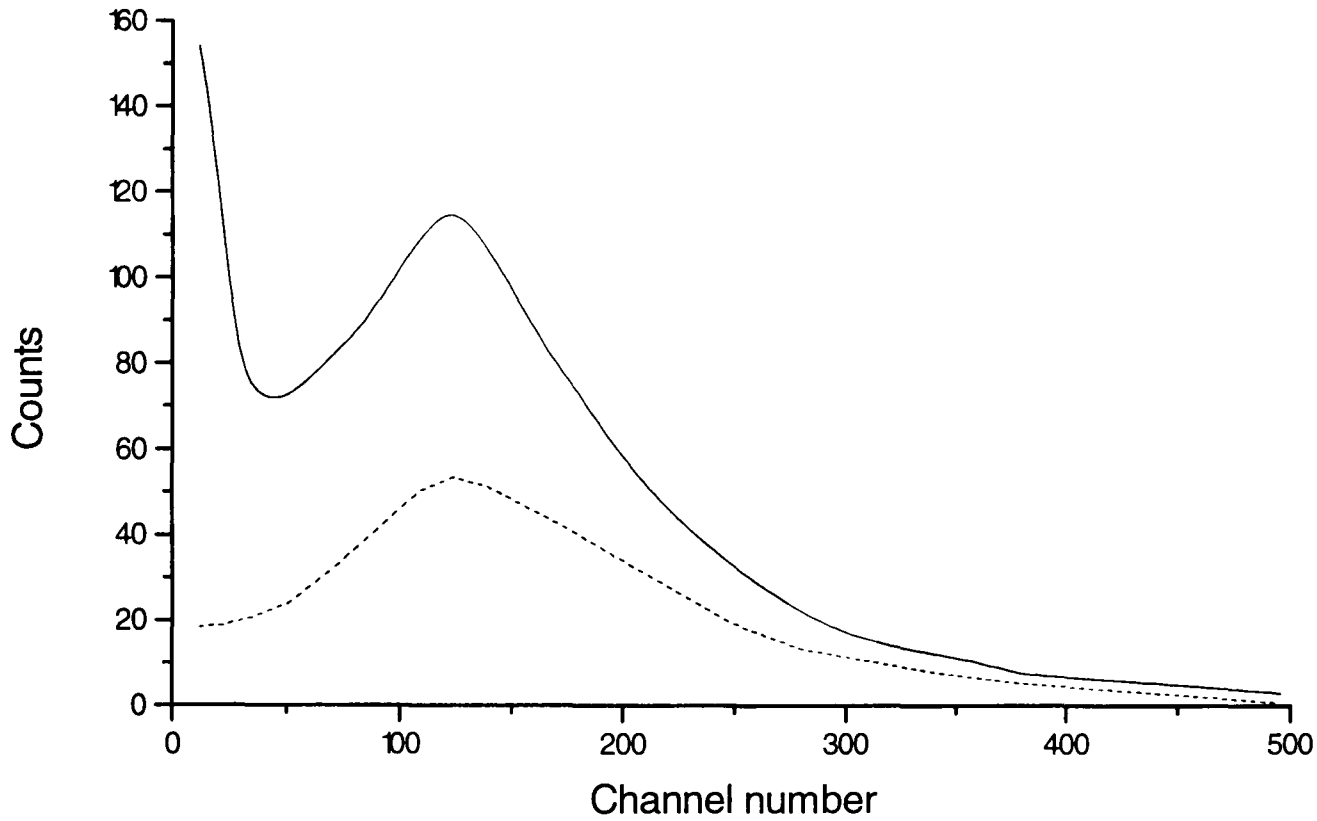

Figure 5.6 Pulse height analysis of the signal obtained from a 14 μm diameter plastic scintillator fibre assembly for an incident beam of 3.5 MeV protons, **a)** without and **b)** with a coincidence pulse from the silicon detector.

of electronic noise below channel 40 with a single photoelectron peak having a maximum at channel 120. Using a coincidence pulse from the surface barrier detector gave a peak at the single photon level with a height of approximately 50 % of that for the single channel, non-coincidence peak height. This data correlate well with the absolute count rates of 6000 cpm due to stray light with no proton beam and 12000 cpm with beam. The signal produced in this channel was therefore due exclusively to single photoelectron events at the photocathode.

5.2.5 Conclusions

The data show that a detector constructed using a polymer scintillator fibre with a diameter of up to 14 μm would be ineffective in the detection of 3.5 MeV protons.

There are two possible explanations for the small signal sizes obtained, and the resulting lack of detector efficiency. The first is that the scintillating material may have lost its efficiency by the use of xylene as a solvent. This could be due to a differential solubility between the scintillator molecules and the toluene polymer base material, resulting in

the scintillating molecules remaining in solution whilst the toluene fibre was drawn out. The second possible explanation is that the process by which the emitted photons were transmitted to the photomultiplier was inefficient. The process of photon collection and transmission to the photomultiplier tube consisted of several stages; transmission of emitted photons along the scintillating fibre, coupling of the scintillator to the optical fibre, transmission along the optic fibre, and illumination of the photocathode. At each stage some loss will be introduced into the detection process. Some of these losses will be considered here.

The total internal reflection angle for NE102a is 39.3° from normal incidence and therefore the half-angle for light transmission along the fibre is 50.7°. It is however the acceptance angle of the optical fibre which will limit the collection of the emitted photons. The geometrical arrangement is shown in Figure 5.7.

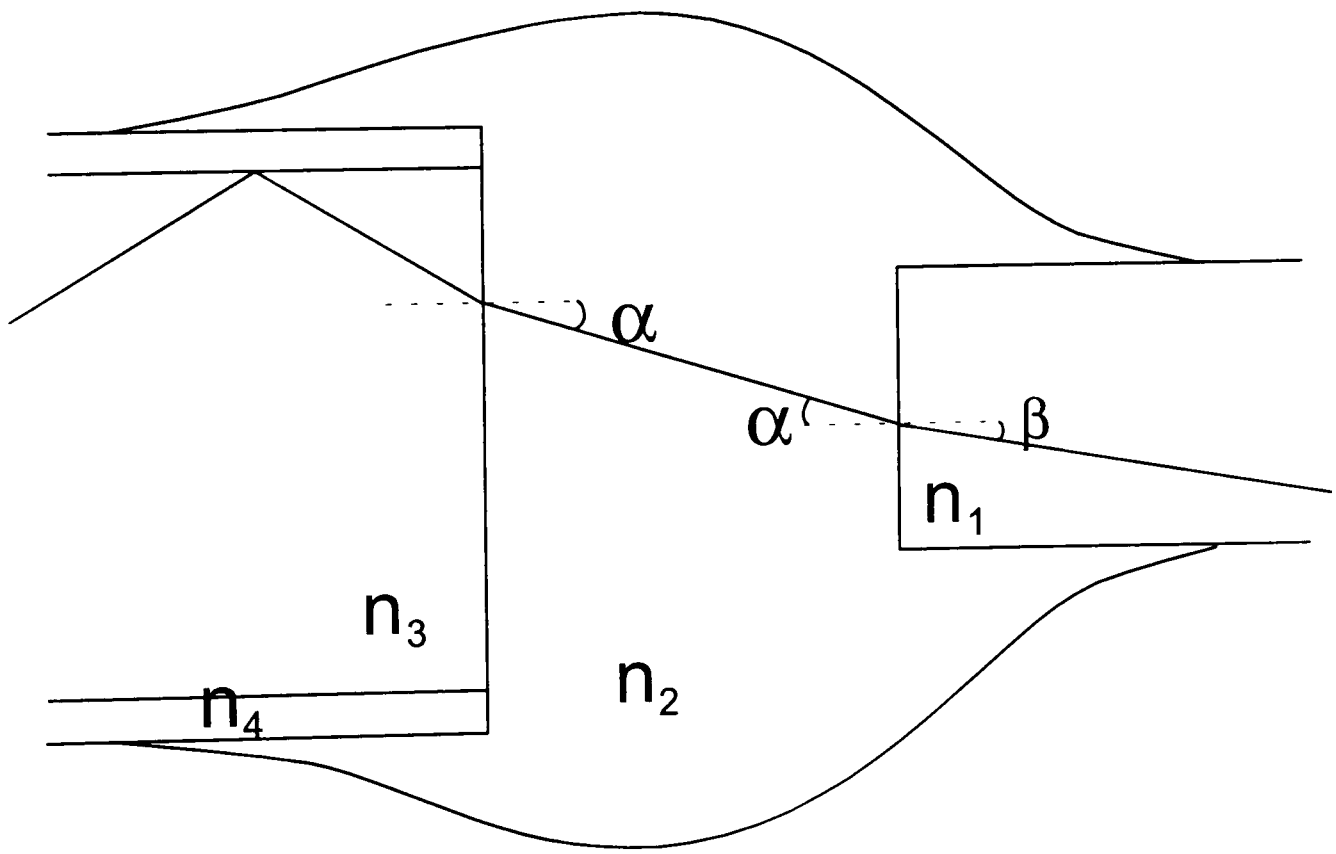

Figure 5.7 A schematic defining the angles involved in the transmission of light from the plastic fibre scintillator through the optical cement to the optic fibre.

The numerical aperture of the fibre, $\mathbf{NA = n_2 \sin(\alpha_{max}) = n_1 \sin(\beta_{max})}$

where $\mathbf{n_1}$ and $\mathbf{n_2}$ are the refractive indices of the scintillator and coupling cement and α_{max} and β_{max} are the angles within the optical cement and scintillating fibre which correspond to the angle for total internal reflection in the optic fibre.

Therefore, $\sin(\beta_{max}) = NA / n_1$

and, $\beta_{max} = \sin^{-1}(NA / n_1)$

For the 30 μm fibre used the numerical aperture is 0.64 and for the NE102a the refractive index is 1.58,

therefore, $\beta_{max} = \sin^{-1}(0.64 / 1.58)$

giving, $\underline{\beta_{max} = 28.9^{o}}$

Using this angle and the calculation of the proportion of the solid angle subtended at a point, given in Appendix III, the maximum percentage of the emitted photons accepted directly into the optical fibre is **6.23 %**. Since the mean number of photons produced by 10 μm of NE102a is 1874, the number which are emitted at an angle which allows transmission into the optical fibre with an angle less than that for total internal reflection is $1874 \times 0.0623 = 117$ photons. Since the quantum efficiency of the photocathode is 24 %, the maximum mean number of photoelectrons which may in theory be produced by the transmission of a 3.5 MeV proton is $117 \times 0.24 = 28$ photoelectrons.

For a fibre length of 75 μm, corresponding to half the length of the scintillating fibre, photons emitted at the maximum angle for acceptance of 28.8° will undergo approximately four internal reflections within the scintillator material. This process will introduce losses into the system which will be dependent on the surface properties of the scintillator fibre. Any dirt or surface defects in the polymer will cause a loss in the reflection efficiency at the surface. In addition, at the entrance and exit of the fibre there will be some loss due to reflection at each change of refractive index. A further loss of efficiency will occur due to the internal reflections of the optic fibre not being 100 % efficient and this loss will be compounded by any curves in the fibre. Finally for a wavelength of 423 nm the fibre and optical coupling cement are near to the high energy transmission cut off and transmission will be less efficient for light of shorter wavelengths in the emission spectrum of the scintillator.

These losses in photon collection and in the transfer of the light emitted from the scintillator together with a possible reduction in the efficiency of the plastic scintillator are likely to result in the low photoelectron number produced in the photomultiplier tube.

5.3 The Development of a ZnS Particle Detector

5.3.1 Initial tests

Using the apparatus shown in Figure 5.1 it was possible to irradiate a sample of ZnS(Ag) crystals, having dimensions of ~ 5 μm, mounted on a 2.5 μm thick layer of mylar. The light signal produced by the traversal of an americium alpha particle was emitted from the crystal over ~ 100 μs. The shape of a typical light pulse, after amplification by a pre-amplifier with a 50 μs shaping constant, was obtained using a 1 GHz digitising oscilloscope (DSA 602, Tektronix) and is shown in Figure 5.8. The upper trace shows the signal after processing by the charge-sensitive pre-amplifier and the lower trace shows the corresponding unamplified signal output from the photomultiplier tube.

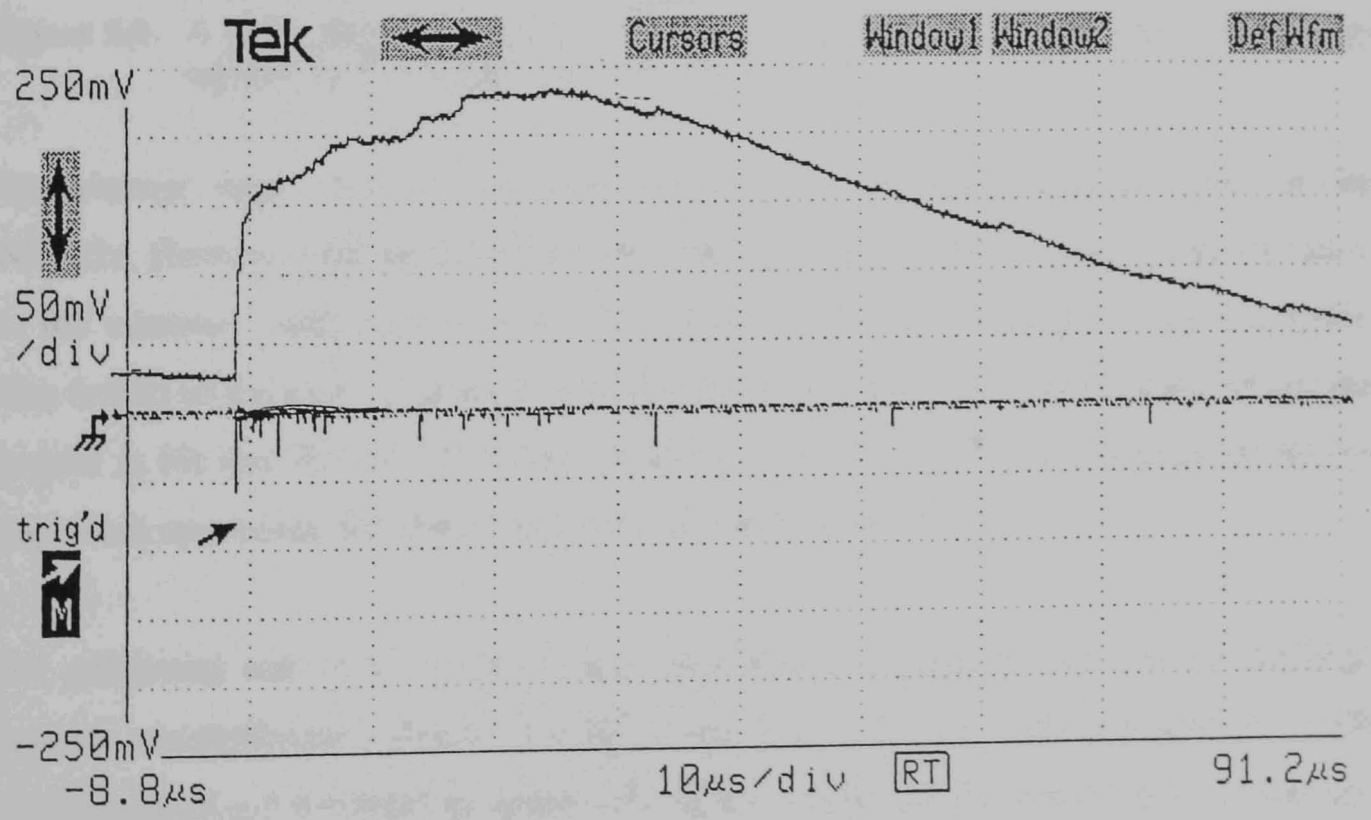

Figure 5.8 Characteristic light pulse produced in ZnS(Ag) by the traversal of a 5.2 to 5.5 MeV alpha particle.

As for the NE102a plastic scintillator a set of timed irradiations were performed using a digitizing oscilloscope to count the number of pulses over a set absolute voltage level. The results are shown in Figure 5.9.

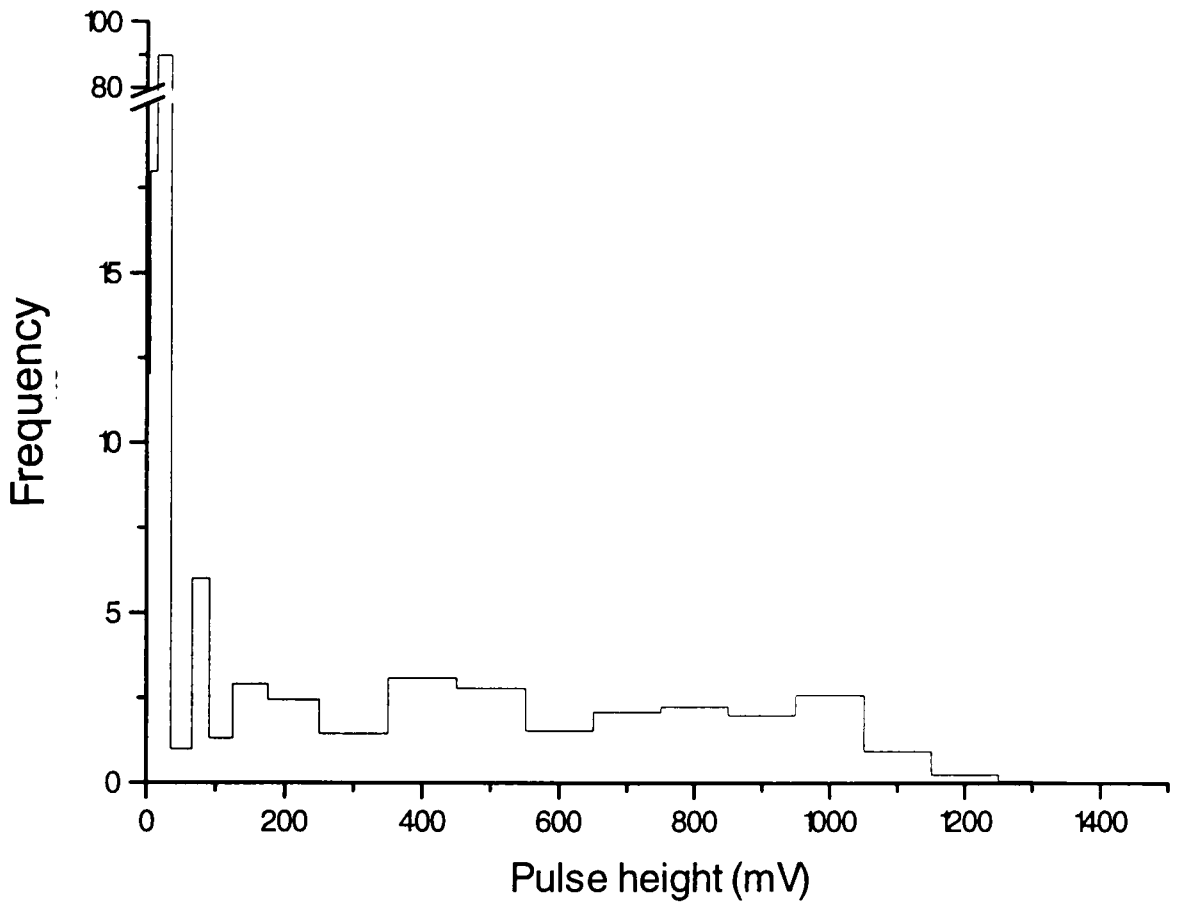

Figure 5.9 A pulse height analysis of the signals obtained by the irradiation of ZnS(Ag) crystals with ^{241}Americium alpha particles.

On average larger signals were obtained from the inorganic crystals than for the NE102a. However, the data obtained from the ZnS(Ag) crystals show a large variation in the measured peak heights, due to the presence of many irregularly shaped crystals. The length of the path of an alpha particle though a crystal will depend upon where the crystal is hit and this will therefore produce a large spread in the amount of energy deposited and hence the size distribution of the pulse produced.

An additional test of the pulse heights produced by ionising radiation in ZnS(Ag) crystals was performed using a ^{238}Pu alpha particle source. Five crystals of ZnS(Ag) with dimensions of ~ 5 μm were mounted onto the end surface of an optic fibre having a core diameter of 50 μm. The other end of the fibre was coupled to a photomultiplier tube using a commercial fibre connector. An attempt was made to use standard nucleonics to analyze the signals, by the use of a coincidence pulse generated from the pre-amplified signal. The pre-amplified signal was used as the input to an Ortec 571 pulse shaping amplifier, designed to produce bipolar output pulses. The resulting output signal consisted of a large bipolar pulse with additional trailing pulses of smaller amplitude due to the delayed component of the scintillation pulse. In order to isolate the primary

bipolar signal from the secondary peaks a coincidence pulse was generated using the original shaped pulse as the input to an Ortec 551 single channel analyzer, producing a 5 volt logic pulse. An in-house designed pulse stretcher was then used to adjust the length of the 5 volt logic pulse. The signal processing is shown in Figure 5.10.

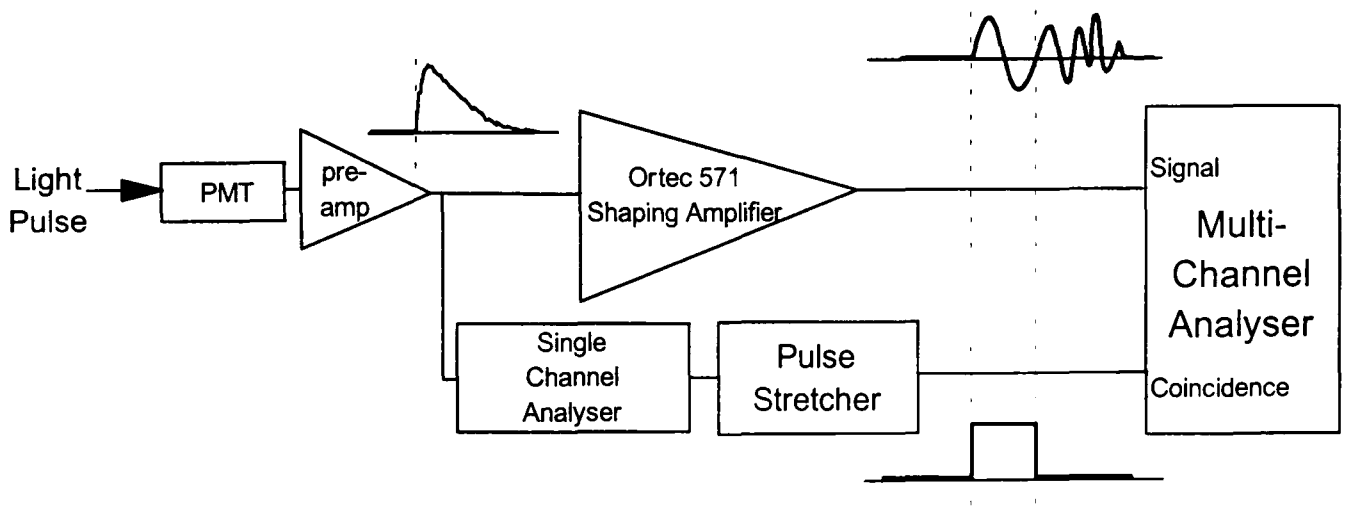

Figure 5.10 The signal processing used to apply standard nucleonics units to the analysis of ZnS(Ag) scintillator pulses.

The pulse height analysis of the signals obtained by the irradiation of the five ~ 5 μm ZnS(Ag) crystals by a beam of ^{238}Plutonium α-particles of ~ 3.2 MeV is shown in Figure 5.11.

As with the data obtained from the irradiation of NE102a, the number of background counts due to air ionisation was considerable. However, the pulse heights of the signals obtained from the ZnS(Ag) crystals were significantly greater than the single photoelectron noise peak. Although the relationship between the number of photons emitted by the ZnS(Ag) and the height of the bipolar pulse from the shaping amplifier was not proportional, due to the irregular shape of the initial amplified signal, the data indicate that the mean pulse height obtained was considerably higher than that of the single photoelectron peak. The double peak shown suggests the presence of crystals with two different sizes, having correspondingly different pulse heights. To verify that sufficiently large signals were also obtained by irradiation with protons of 3.5 MeV, a 10 μm ZnS(Ag) crystal was mounted onto a 50 μm core optical fibre which was coupled to a photomultiplier tube by an ST type commercial fibre connector mounted into the housing of the photomultiplier tube. The results of the pulse heights obtained are shown in Figure 5.12.

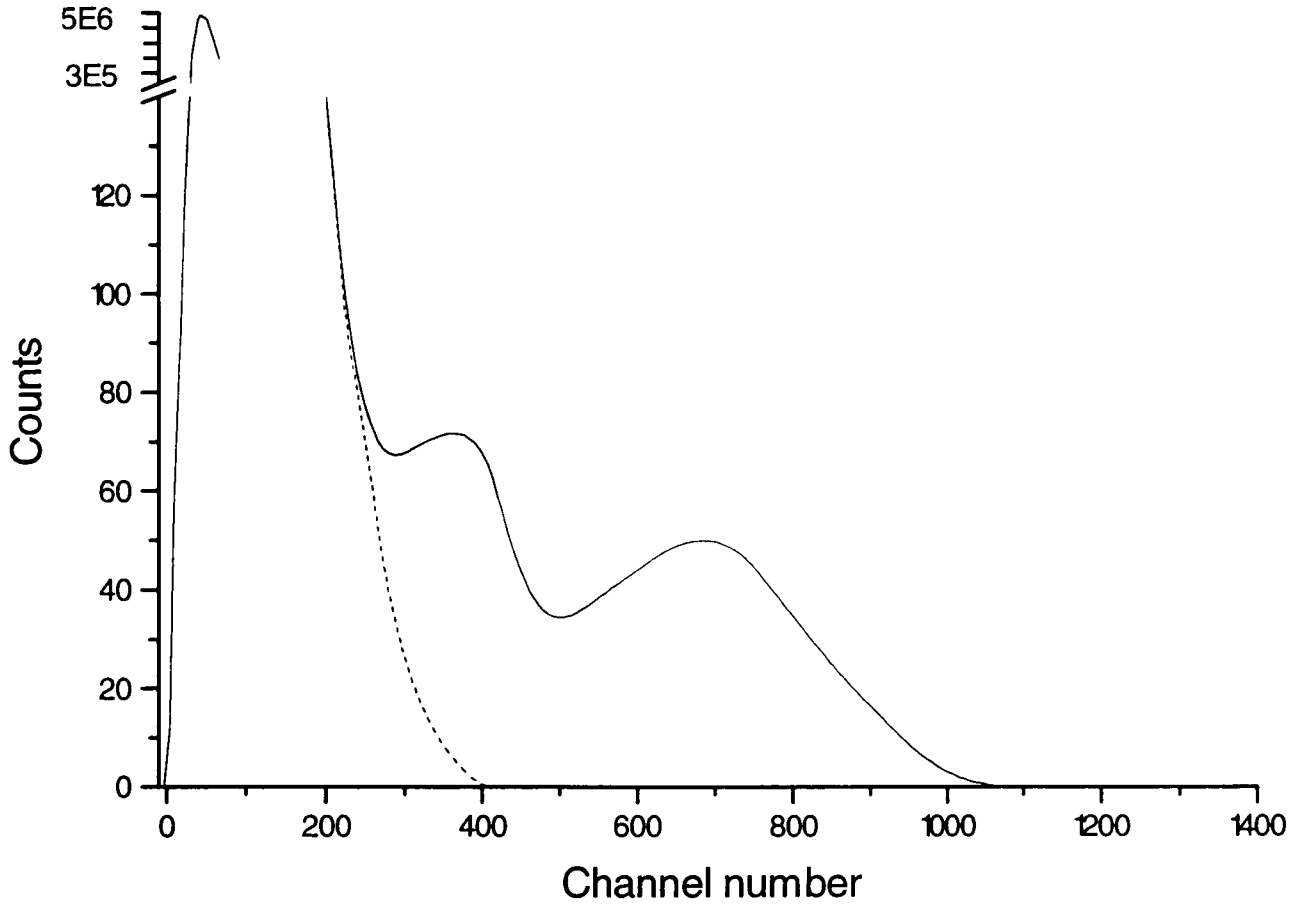

Figure 5.11 Pulse height analysis of the signals obtained from the irradiation of ZnS(Ag) crystals by ^{238}Pu α-particles (Solid Line) and of the level of background signal (Dashed Line).

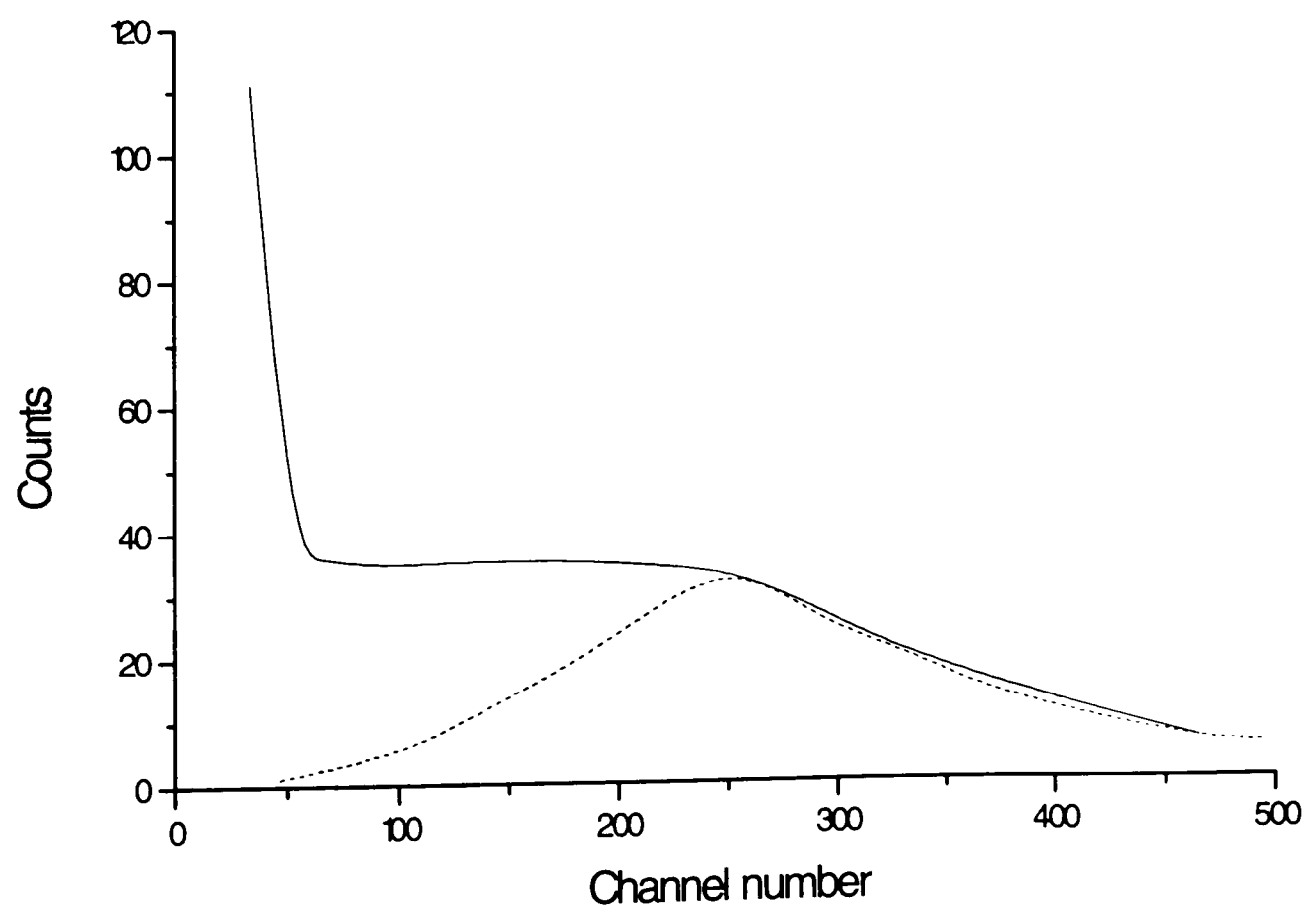

Figure 5.12 Pulse height analysis of the signals obtained from the irradiation of ZnS(Ag) crystals by 3.5 MeV protons with (Dashed Line) and without (Solid Line) the use of a coincidence pulse from a silicon detector mounted over the crystal.

The upper curve of Figure 5.12 shows the spread of pulse heights obtained by a broad beam irradiation of ZnS(Ag) crystals. It shows single photon noise present below channel 60 with a large spread of pulse heights above the single photon noise level. The lower curve of Figure 5.12 shows the pulse height spectrum obtained using a coincidence pulse from a surface barrier detector positioned above the ZnS(Ag) crystal and so includes only those pulses which coincide with the passage of a proton. The data show that the pulses produced by the transmission of 3.5 MeV protons through the ZnS(Ag) crystals have a maximum near channel 250. The pulses due to single photon noise and the erratic pulses caused by the processing of an irregular signal are eliminated using this approach. Since the crystal was irradiated by a broad beam of particles it is likely that the lowest signals in the distribution were due to particles which passed through the edge of the crystal and so did not traverse the full 10 μm thickness of the ZnS(Ag) crystal. The highest energy pulses may be attributed to the deposition of large amounts of energy by scattered particles which were fully stopped within the crystal. The peak heights of the signals produced suggested that, if a detector geometry could be designed to collect a comparable proportion of the emitted photons, then ZnS(Ag) could be used in the development of a proton transmission detector.

In order to test the efficiency of the proposed geometry, using a crystal of ZnS(Ag) between two optic fibres for proton detection, it was necessary to develop a system in which all of the incident proton beam traversed the crystal. This required the collimation of the proton beam to a diameter of less than 10 μm. The methods used to achieve this resolution are discussed in Chapter 3.

5.3.2 Detector assembly 1

5.3.2 (a) Construction

An initial attempt was made to construct an assembly in which all of the particles in the beam traversed the detector, using a drawn borosilicate glass capillary collimator having a 10 μm diameter exit aperture and covered by a 2.5 μm thick mylar window. The detector was constructed using a similar method to that for the construction of a scintillating fibre detector. A crystal of ZnS(Ag) (N E Technology Ltd, UK) was

mounted over the collimator exit aperture and the fibres abutted to it. In order to produce a rigid and durable assembly the crystal, fibres and collimator tip were embedded in UV-curing optical cement. The surface of the optical cement was then polished using 5 μm grain size optical polishing paper until the detector was visible below the surface of the polymer. A diagram of the assembly is shown in Figure 5.13.

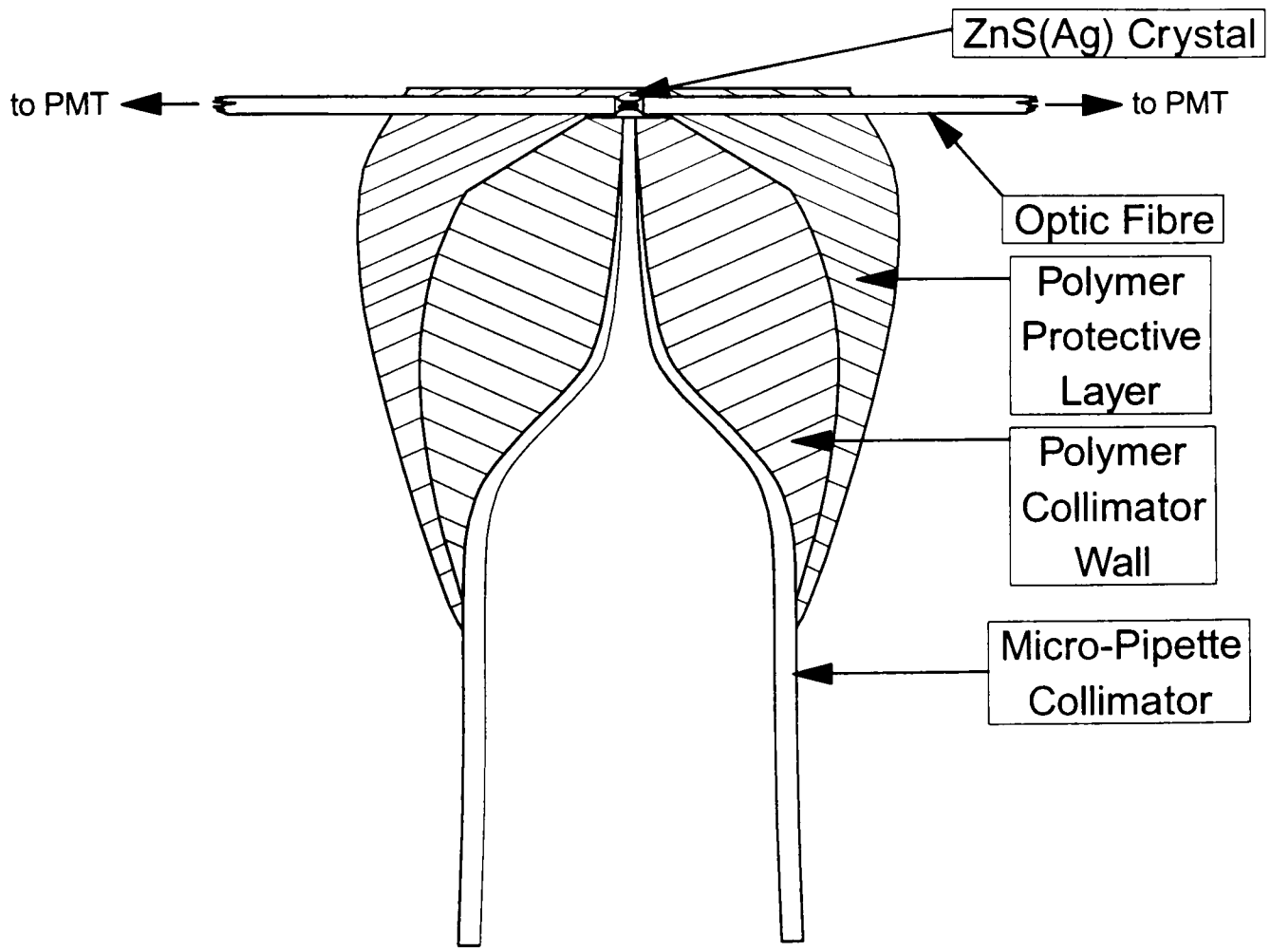

Figure 5.13 The collimator-detector arrangement constructed to test a ZnS(Ag) crystal scintillator detector by arranging for all particles to traverse the crystal.

5.3.2 (b) Energy Data

The energy spectrum of the particle beam transmitted by this assembly was obtained using a silicon surface barrier detector and is shown in Figure 5.14 with the spectrum of the beam produced by the collimator alone. The data were obtained for an incident beam of 3.5 MeV protons.

The highest energy curve, (a), shows the energy spectrum for the collimator with no detector mounted over it and therefore the highest energy protons in this curve are at 3.5 MeV. As shown in Section 3.4 this type of collimator introduced significant scatter into the proton beam and so there were also a considerable number of protons present with lower energies. The largest of the two lower energy curves, (b), shows the energy of the protons which were transmitted through the detector and the polymer layer. The peak value in the spectrum occurs at 1.3 MeV and therefore shows a mode energy loss for the incident 3.5 MeV protons of 2.2 MeV. The presence of two components in this spectrum is suggested by a change in curvature at 1.1 MeV. The smaller of the low energy curves, (c), was obtained by using a coincident signal from the ZnS(Ag) detector and so includes only those protons which have traversed the detector. This shows that

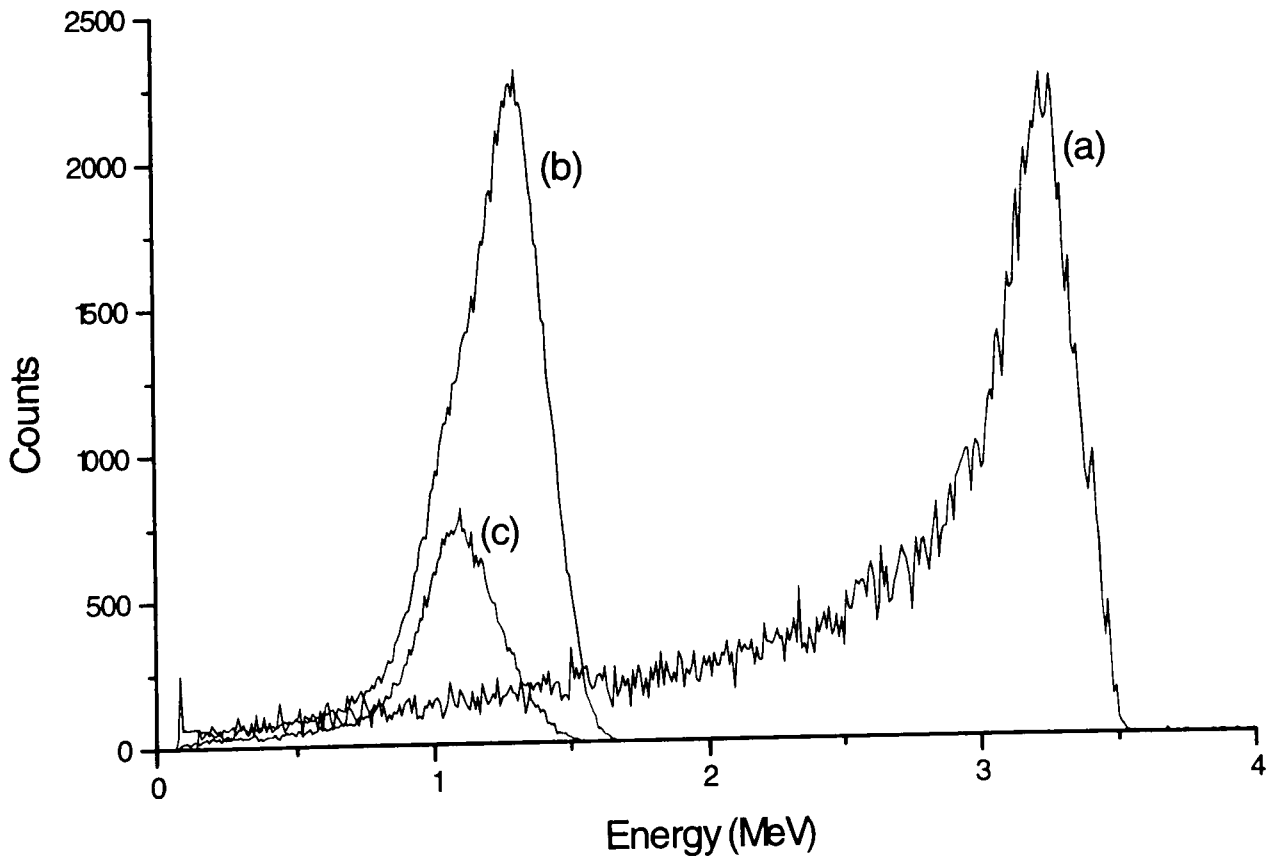

Figure 5.14 Energy spectra for the transmitted beam produced by **a**) a drawn borosilicate glass capillary collimator alone, and by a capillary collimator with a ZnS(Ag) detector mounted over the exit aperture, **b**) without and **c**) with a coincidence count from the ZnS(Ag) detector.

those particles which produce a photon pulse in both channels of the detector are also the protons which suffer the highest energy loss. This effect is due to the higher stopping power of ZnS(Ag) compared to that of the polymer layer. The peak position confirms the presence of the two components in the peak for the transmitted proton beam indicating that many of the transmitted protons did not traverse the ZnS(Ag)

crystal. This indicates that either the collimated beam was larger than the exit hole of the collimator or that the crystal was misaligned with the exit aperture.

In addition, by the analysis of the signals produced in each channel and those from the surface barrier detector, using a digitising oscilloscope, it was apparent that 10 % of the events which produced pulses in both channels of the ZnS(Ag) detector did not have a coincident pulse produced in the surface barrier detector. This indicates that some of the protons were fully stopped within the crystal and polymer layer. This agrees well with the initial energy spectrum produced by this collimator, showing a large number of low energy, scattered particles present in the proton beam. The data also show that an excess of polymer is present over the detector resulting in an unacceptable degree of energy loss.

Although large signals were observed in each channel of the detector no attempt was made to characterise the detection efficiency because of the problems of excessive energy loss and crystal misalignment. An attempt to improve this assembly by further polishing of the polymer layer resulted in damage to the optic fibres and a loss of signal due to a failure of the fibre to internally reflect the emitted photons.

5.3.3 Detector assembly 2

5.3.3 (a) Construction

Improvements which were made to the quality of the collimation of the microbeam system resulted in a highly collimated proton beam of 5 μm diameter with few scattered particles. The production of this beam using hplc tubing is described in Section 3.5 and allowed the construction of a modified detector assembly which eliminated many of the problems encountered in Assembly 1. A 15 μm thick ZnS(Ag) crystal (Lumilux blue, Hoechst UK) was mounted over the 5 μm exit aperture and two 30 μm diameter optical fibres were positioned abutting onto the crystal. The ZnS(Ag) crystals were obtained from a different manufacturer to those used in Assembly 1 and were used in all further detectors constructed. The geometry of the crystals is more plate-like rather than irregular and the crystal appear to be more transparent to visible light than the

previously used samples. Optical coupling cement was used to bond the crystal to the optical fibres and also to attach the optic fibres to the mylar window covering the collimator. A schematic diagram of the assembly is shown in Figure 5.15.

An image of the assembly, looking vertically down onto the collimator surface, obtained using the solid state microscope attached to the microbeam facility, is shown in Figure 5.16.

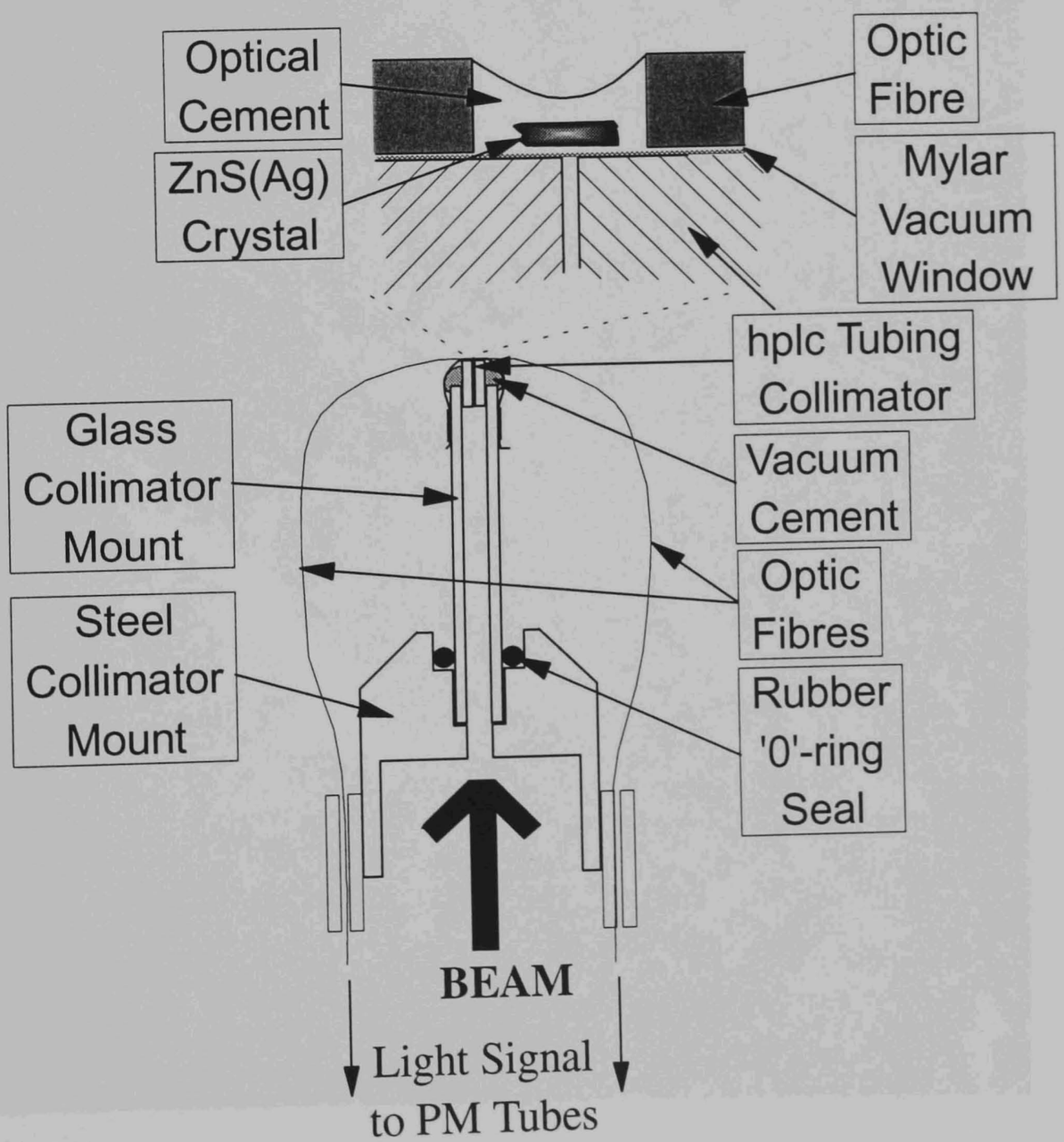

Figure 5.15 Diagram showing the arrangement of the elements used to construct Detector Assembly 2, using a 15 μm thick ZnS(Ag) crystal mounted between two optic fibres.

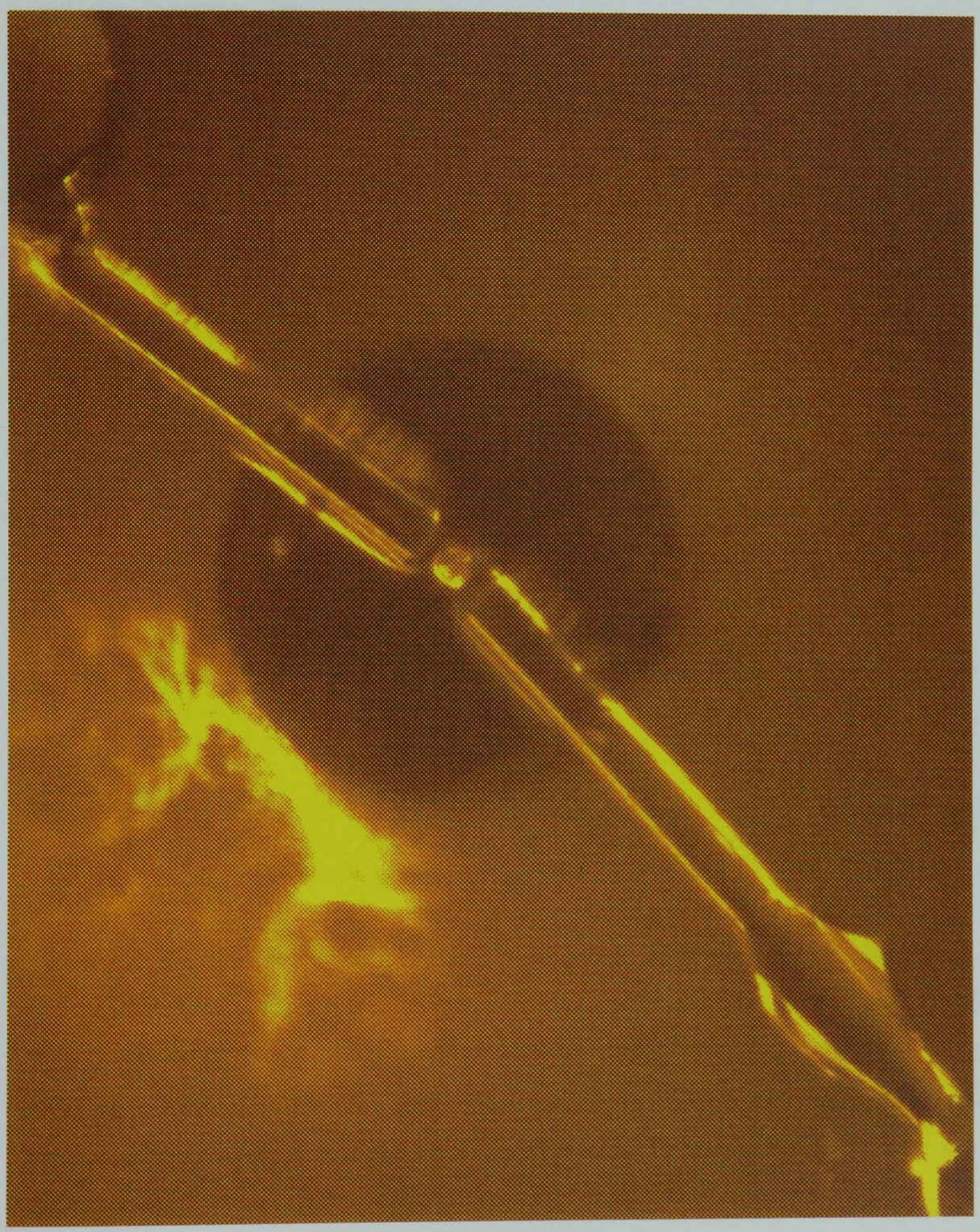

Figure 5.16 Image from a solid state microscope of Detector Assembly 2 as seen from above, showing the hplc tubing collimator, ZnS(Ag) crystal and 30 μm diameter optical fibres.

5.3.3 (b) Energy data

The initial energy spectra of the collimator prior to the addition of the detector assembly and the spectrum obtained after the addition of the detector assembly above the collimator are shown in Figure 5.17.

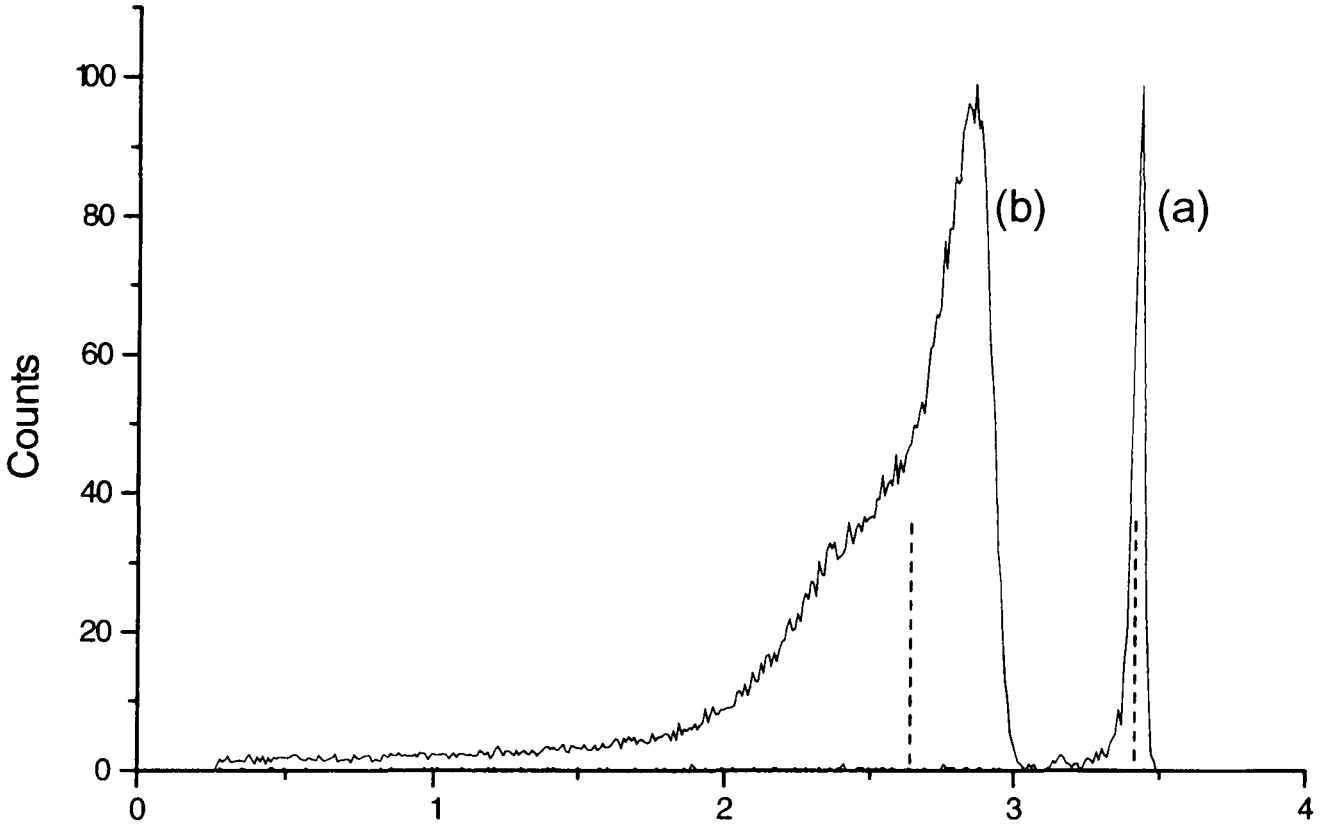

Figure 5.17 Energy spectra for the transmitted beam produced by **a**) an hplc fused silica tubing collimator alone, and **b**) by an hplc tubing collimator with a ZnS(Ag) detector mounted over the 5 μm exit aperture, for an incident beam of 3.5 MeV protons.

The mode energy loss for this assembly, calculated as the peak-to-peak distance, is 573 keV. The mean energy loss is 780 keV, calculated by the integration of the two peaks to find the mean energy value for each spectrum, which divides the area of the peaks into two equal areas. The data again show an indication of a two component peak for the transmitted protons, suggesting a misalignment of the ZnS(Ag) crystal with the collimator.

5.3.3 (c) Counting efficiency data

A two channel, coincidence counting signal analyzer system was designed and built in-house for use with this assembly (Vojnovic, personal communication). The signal analyzer takes the outputs from two photomultiplier tubes and amplifies them using an

amplifier with a shaping constant of 50 μs, resulting in the pulse shape shown in Figure 5.8, in each channel. If either channel reaches the level of a user defined discriminator voltage then a logic pulse is produced in that channel. If the second channel also reaches the discriminator level and produces a second logic pulse within the duration of the first then a third, coincidence logic pulse is produced. The coincident logic pulses are then used as the input to an internal digital counter with a numeric display. The user defined parameters on the signal analyzer are the input signal gain, the balance of gains between the two channels, the discriminator level, and the width of the single channel logic pulse. In order to test the efficiency of the detector this counter was used in conjunction with a pulse counter and a multi-channel analyzer used as a counter. A schematic of the signal processing used in testing the detector efficiency is shown in Figure 5.18.

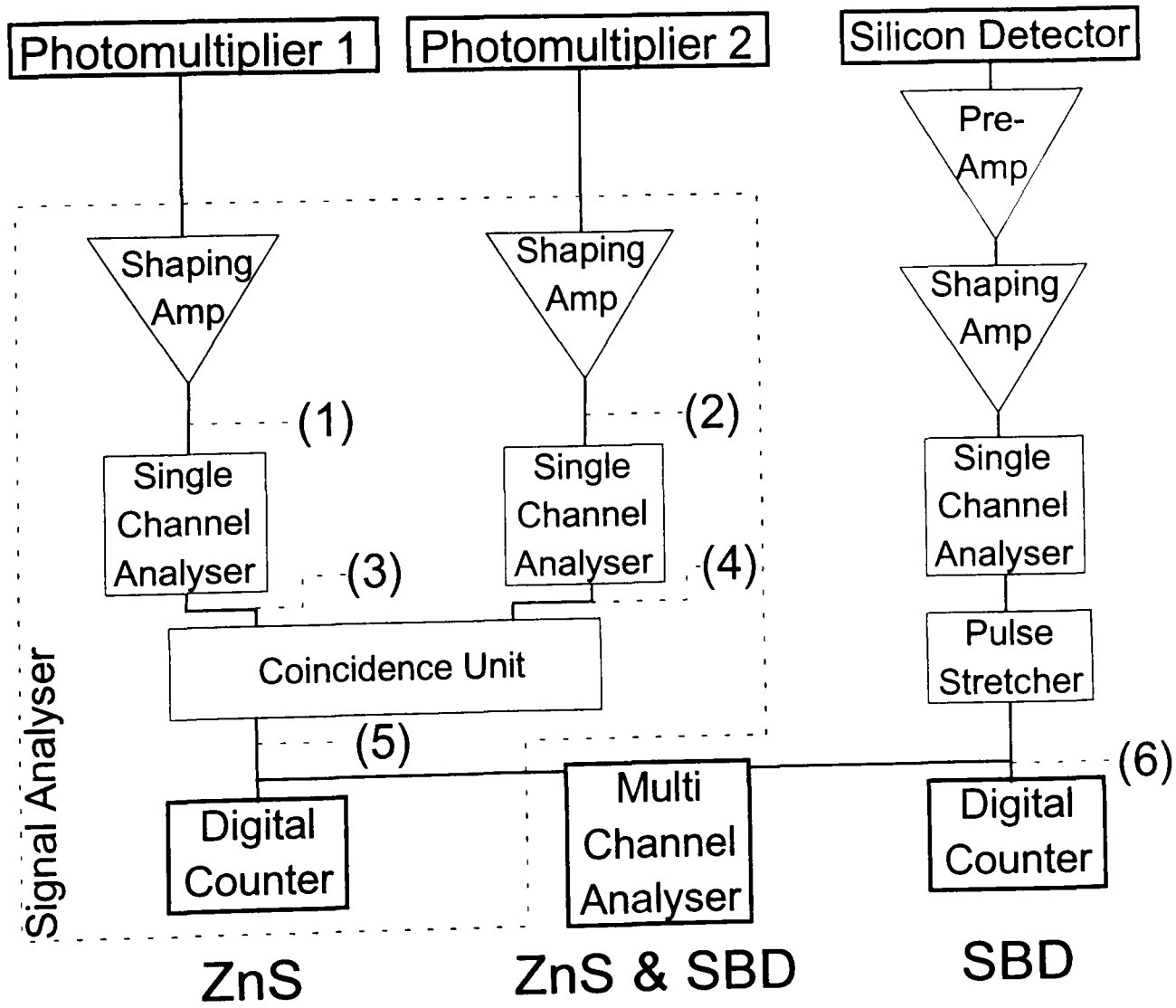

Figure 5.18 The signal processing used to test the efficiency of the detector assembly 2, constructed using a ZnS(Ag) detector.

An example of typical output signals from the six positions marked in Figure 5.18 is given in Figure 5.19.

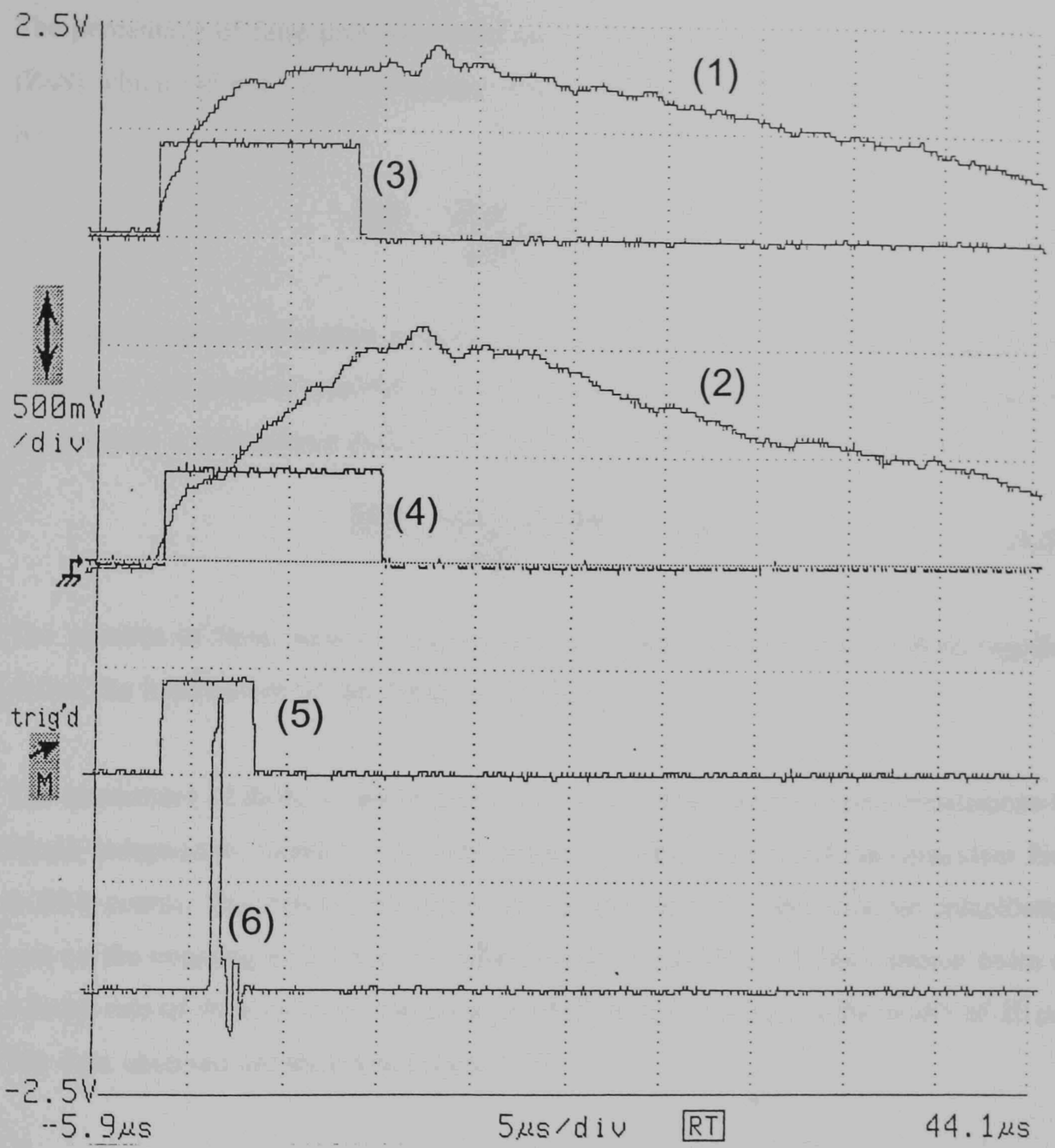

Figure 5.19 The signals produced by the passage of a proton through the ZnS(Ag) detector at the various stages of the signal processing numbered in Figure 5.18.

The output pulses from the surface barrier detector, (**SBD**), and the ZnS(Ag), (**ZnS**), coincidence unit can be used to give :-

i) the number of protons transmitted through the hole (**SBD**), given by the surface barrier detector,

ii) the number of coincident counts (**ZnS**), given by a signal from the in-house built signal processing unit,

iii) the number of events in which a count is registered on both the surface barrier detector and the ZnS(Ag) coincidence unit (**ZnS & SBD**), by using the two logic pulses as the input to a second coincidence counter.

The percentage of false positive counts i.e. a count from the in-house coincidence unit (**ZnS**) which did not have a coincident count from the surface barrier detector, is given by :-

$$\frac{ZnS - (ZnS \ \& \ SBD)}{SBD} \times 100\ \% \qquad \text{- (5.1)}$$

The percentage of uncounted protons i.e. a proton which was transmitted through the collimator and detector assembly and was detected in the surface barrier detector but did not produce a coincidence pulse in the ZnS(Ag) detector system, is given by :-

$$\frac{SBD - (ZnS \ \& \ SBD)}{SBD} \times 100\ \% \qquad \text{- (5.2)}$$

The number of false positive counts and the number of uncounted protons together define the inefficiency of the detection system.

The assessment of detector performance was made using multiple timed irradiations to obtain independent values for the **ZnS** counts, the **SBD** counts and the coincident **ZnS & SBD** counts. The effect of the discriminator level setting of the in-house coincidence unit on the counting efficiency was measured for an incident 3.5 MeV proton beam at a count rate of 40 protons s^{-1} and a single channel analyzer logic pulse width of 20 μs. The data obtained are shown in Figure 5.20.

The data show that an optimum efficiency was obtained for a discriminator level setting of 1.3 (see Figure 5.20). Below this level the contribution of single-photon noise due to air ionisation, stray background light, photocathode noise, and delayed fluorescence of the crystal, increased the level of random coincidences between the two channels and so increased the number of false positive counts. As the number of logic pulses produced increased this also resulted in the introduction of dead-time into the system and so increased the number of uncounted protons. Above this discriminator level the number of random coincidences due to noise in each channel was reduced. However, raising the discriminator above the optimum level of 1.3 also increased the number of uncounted protons by increasing the probability that a signal pulse height was less than the discriminator level. A contribution to the false positive counts was also present due to low energy, scattered particles present in the collimated beam which were fully

stopped in the scintillator crystal. An improvement in the quality of collimation would reduce the source of these false positive counts.

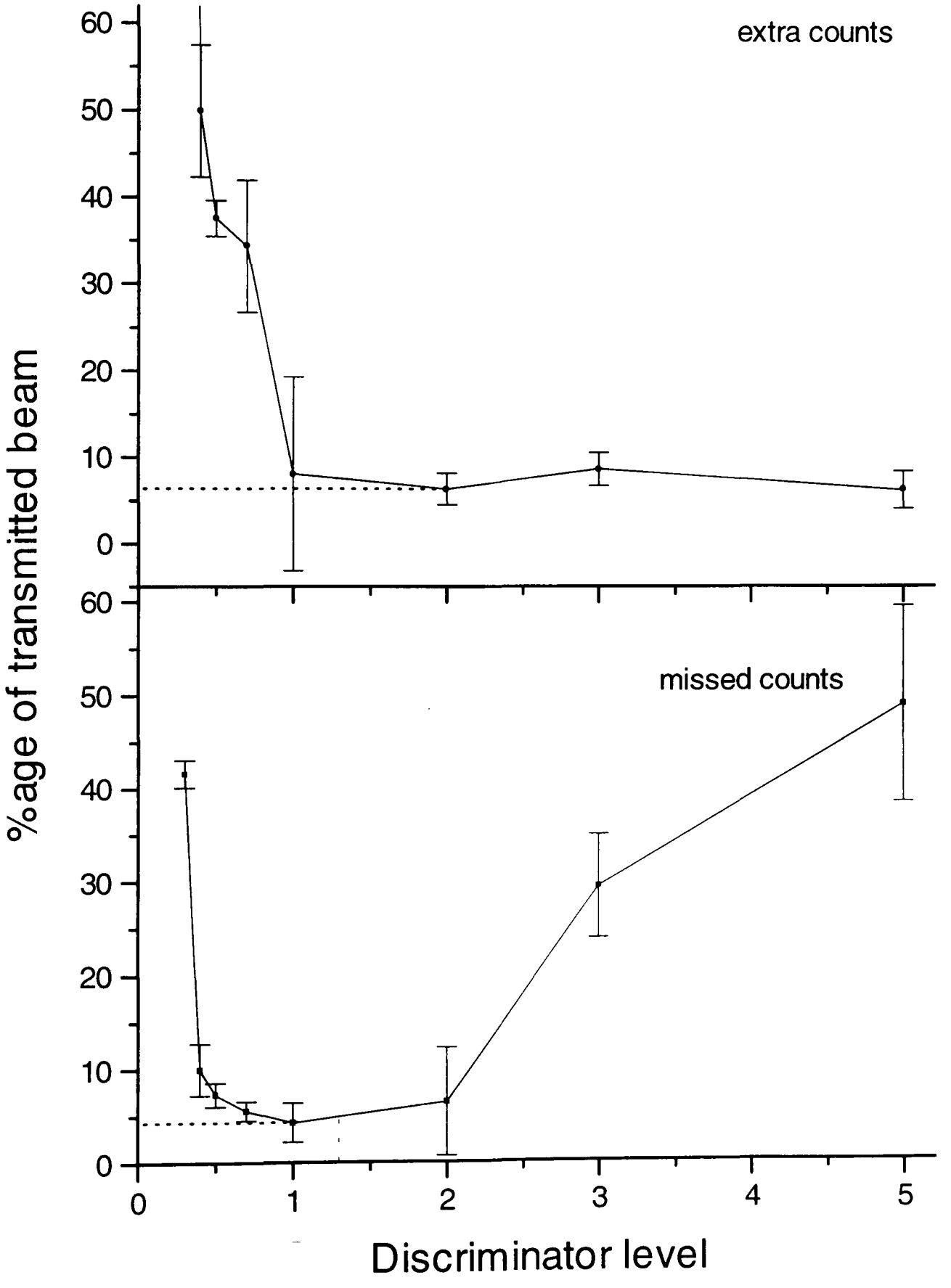

Figure 5.20 Data showing the effect of the discriminator level on the efficiency of detector assembly 2, for a count rate of 40 s^{-1} and a logic pulse width of 20 μs.

Having determined the optimum discriminator setting at a count rate of 40 s^{-1} it was necessary to investigate how this detector would function over the range of count rates

which may be used in a microbeam experiment. Efficiency data for count rates of 7 to 1200 s^{-1} were therefore obtained, using a discriminator setting of 1.3 and a single channel logic pulse width of 20 μs. The results are shown in Figure 5.21.

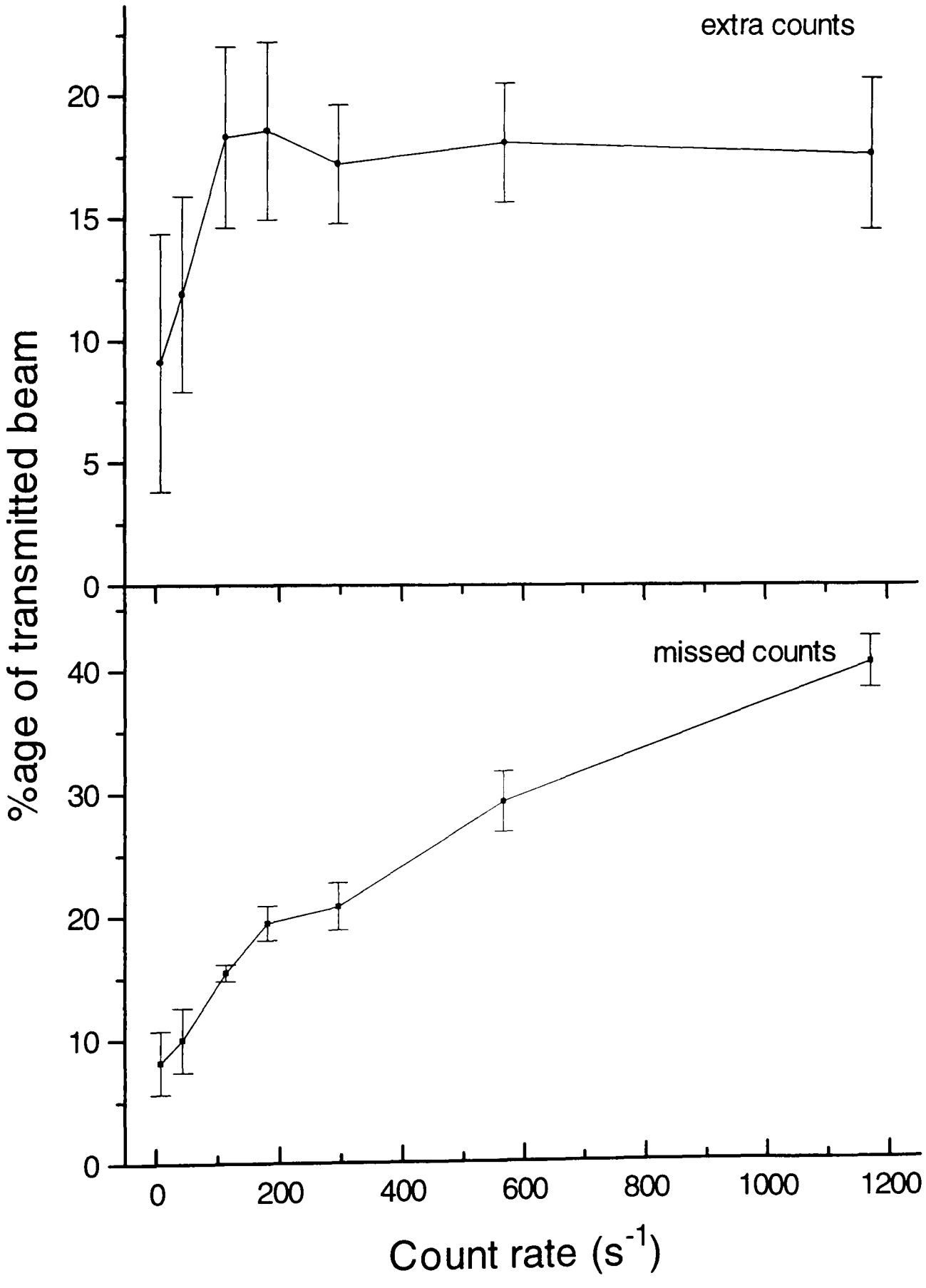

Figure 5.21 Data showing the effect of count rate on the efficiency of detector assembly 2, for a discriminator setting of 1.3 and a logic pulse width of 20 μs.

The data show that the optimum detector efficiency was obtained at the lowest count rate. The loss in efficiency by increasing the count rate to 1000 protons s^{-1} was considerable, resulting in 36 % uncounted protons and 20 % false positive counts. The level of false positive counts reaches a plateau at 300 counts s^{-1} and is perhaps indicative of a saturation in the delayed fluorescence process in the ZnS(Ag) crystal.

5.3.3 (d) Conclusions

The detector system shows an overall inefficiency of 7 % for uncounted protons and 7 % for false positive counts, using a fixed discriminator level of 1.3 and a fixed logic pulse width of 20 μs. Although this is a lower detection efficiency than is desired for the Gray Laboratory microbeam, the signal sizes obtained show that the approach is an appropriate one. Some of the loss in the detector efficiency may be due to a misalignment of the crystal over the collimator, resulting in protons traversing the edge of the crystal rather than its central region. This will result in smaller signal sizes since the crystal is likely to be thinner at its edges. Some protons may even be missing the crystal entirely. The presence of two elements in the energy spectrum of the transmitted protons suggests that this may be a possibility.

A second problem that exists in this assembly was that the mode energy loss was 573 keV, measured from peak-to-peak. This energy loss was equivalent to a ZnS(Ag) layer having a thickness of 23 μm (Ziegler, 1985). Although the layer was a combination of ZnS(Ag) and optical cement, the contribution of this amount of scattering material would add significantly to the divergence of the transmitted beam. Because of the fragility of this detector arrangement it was not possible to use the detector assembly to irradiate CR39 track etch plastic, which would have allowed the efficiency measurements and beam diameter to be verified.

5.3.4 Detector assembly 3

5.4.3 (a) Construction

In the case of the previous detectors assembled the energy loss within the ZnS(Ag) and

optical cement was too large. An attempt was therefore made to construct a detector, again mounted over a 5 μm diameter hplc tubing collimator, using a minimum amount of UV-curing optical cement and using a thinner crystal of ZnS(Ag). In addition, care was taken to obtain the optimum cleave from each end of the optical fibres in order to maximise the light acceptance and emittance.

5.3.4 (b) Energy data

The spectrum of the collimator with no detector mounted over it and the spectrum of the detector-collimator assembly are shown in Figure 5.22.

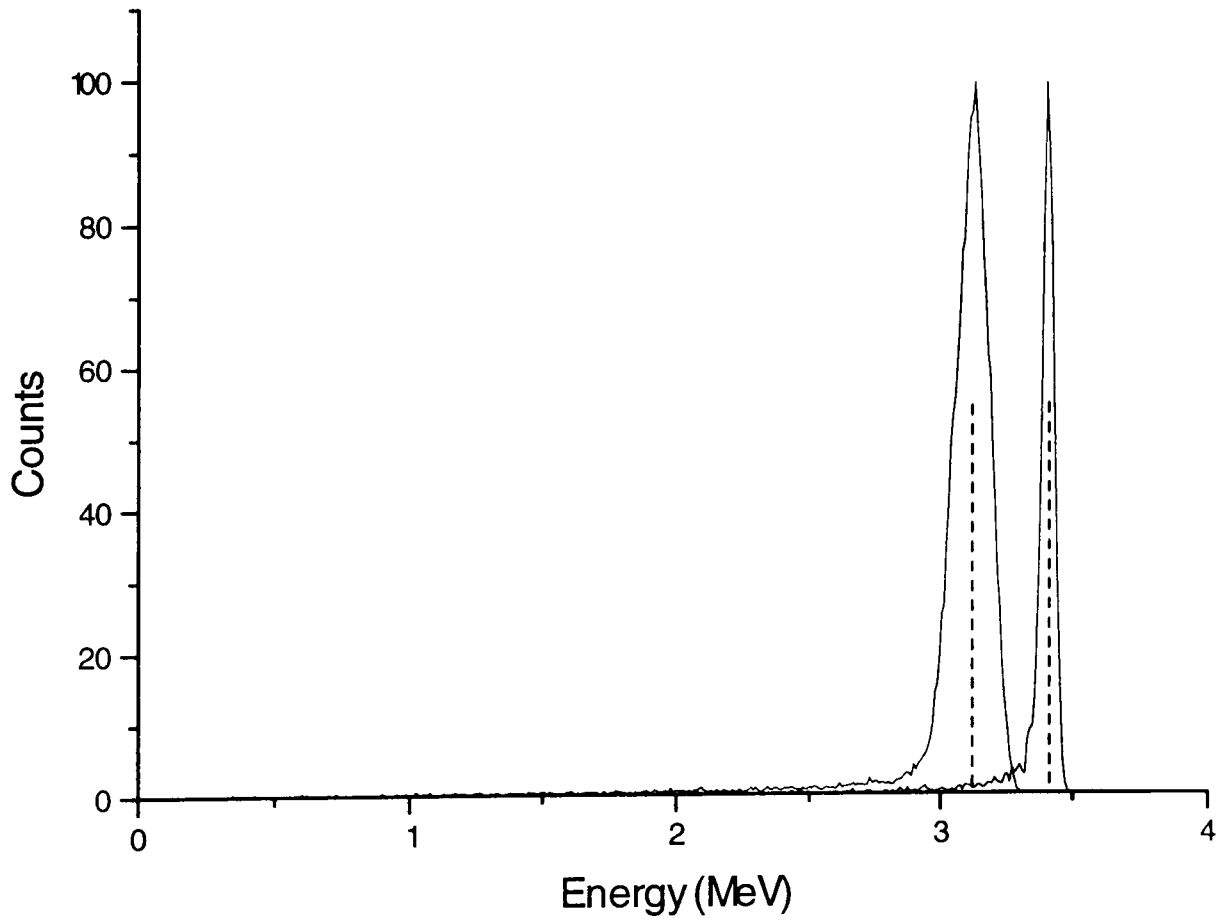

Figure 5.22 Energy spectra for the 5 μm exit hole diameter hplc tubing collimator alone and for the collimator plus detector assembly.

The mode energy loss of the incident beam, measured from peak to peak was 276 keV and the mean energy loss for the two spectra was 293 keV. The energy loss in this detector was therefore considerably less than that of the previous detectors constructed. Since the energy loss of 3.5 MeV protons in ZnS is 24.8 keV μm^{-1} (Ziegler, 1985), the energy loss in this detector assembly corresponds to a crystal thickness of ~ 11 μm. However, some of the energy loss was due to the optical cement at the top and bottom surfaces of the crystal suggesting a ZnS(Ag) thickness of less than 11 μm.

5.3.4 (c) Counting efficiency data

Modifications were made to the system used for testing the efficiency of the detector system to enable the simultaneous counting of the ZnS pulses, the surface barrier detector pulses (SBD) and the level of coincidence between the two detectors (ZnS & SBD). This has reduced the standard deviation of the data considerably since statistical errors and variations in count rate were eliminated from the measurements.

The components of the electronic system used to test the efficiency of the detector are described in Section 5.3.3(c). Although the two channels of the detector were constructed using identical components an imbalance in the average pulse heights between the channel existed due to a difference in the overall efficiencies of the separate components. Since the discriminator level was the same for each channel it was important that the channels were balanced to produce equal pulse heights from the pre-amplifier. To correct for possible errors the first step was to set the input gain and relative gain of the two channels to give pulse heights of 200 mV in each channel. In order to find the optimum discriminator setting the single channel logic pulse width was again set at 20 μs and the count rate set at 20 transmitted protons per second. Three data points were collected for each discriminator setting using 1000 protons for each point. The data obtained are shown in Figure 5.23.

The data show that for this detector the counting efficiency was 99 % at the optimum discriminator setting. Both the number of false positive counts and the number of uncounted protons reached levels of less than 1 % at a discriminator setting of 3.5. As the discriminator level was reduced to less than 3.0 it reached the height of single photoelectron noise event signals and so the number of false positive counts increased dramatically due to an increase in the number of random coincidences between single channel logic pulses produced by single photoelectron events. As the discriminator level was raised it re-crossed the decaying edge of the detector pulse closer to the peak of the photon pulse. Since the number of emitted photons was large in this position relative to a later portion of the decaying pulse it was likely that a second coincident pulse would be generated at this time. This resulted in a rise in the number of false positive counts as the discriminator was raised. In addition, there may have been a contribution to this

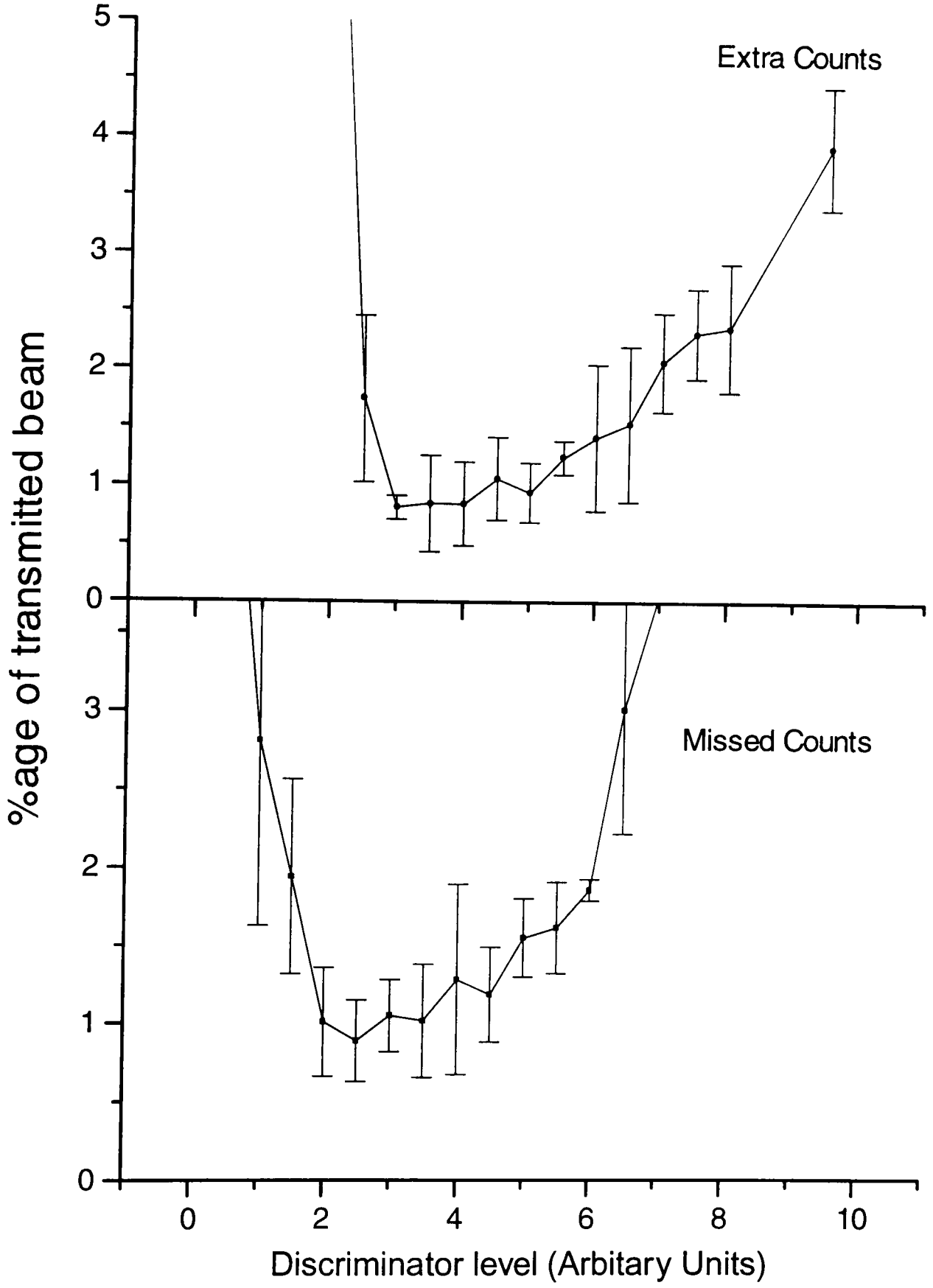

Figure 5.23 Data showing the effect of the discriminator level on the efficiency of detector assembly 3, for a logic pulse width of 20 μs and a count rate of 20 s^{-1}.

rise in the number of false positive counts due to the pulse generated by the ZnS(Ag) detector not coinciding with the pulse generated by the surface barrier detector since a higher discriminator resulted in a later logic pulse. The rise in the number of uncounted protons at lower discriminator settings could also indicate a lack of coincidence between

the surface barrier detector pulse and the signal from the ZnS(Ag) detector.

Having determined the optimum discriminator setting of 3.5 this level was then used to assess the effect of the single channel logic pulse width at a count rate of 30 s^{-1}. The electronics used and the number of protons counted in this experiment was identical to that used for finding the optimum discriminator level. The data obtained are shown in Figure 5.24.

The data show that the number of false positive counts increased by an absolute value of 1 % as the logic pulse width was increased from 2 to 200 μs, at a count rate of 30 s^{-1}. As the logic pulse width was increased the likelihood of two independent noise pulses overlapping increased and so caused a slight increase in the percentage of extra counts recorded. The increase in the dead-time of the detector by this process was not sufficiently significant to increase the number of missed counts by preventing the scoring of a true event. The apparent reduction in the number of false positive counts at logic pulse widths of between 100 and 150 μs may be a real effect since this time interval corresponded to the approximate length of the decaying photon pulse. At logic pulse widths of less than 100 μs it was possible for a second coincident pulse to occur, due to photons emitted late in the signal from the scintillator. By the use of a logic pulse which was as long as the signal pulse no second coincident pulse was possible. The use of long logic pulses would however have resulted in an increase in the number of false counts as the dose rate was raised.

Since the leading edge of the signal from the ZnS(Ag) rose over 10 μs, short logic pulse widths of less than 6 μs resulted in a loss in counting efficiency by an increase in the likelihood that although pulses were generated in each channel they were not coincident. Above this value the number of uncounted protons remained approximately constant at this count rate. The optimum single channel logic pulse width at this count rate was therefore between 10 and 20 μs.

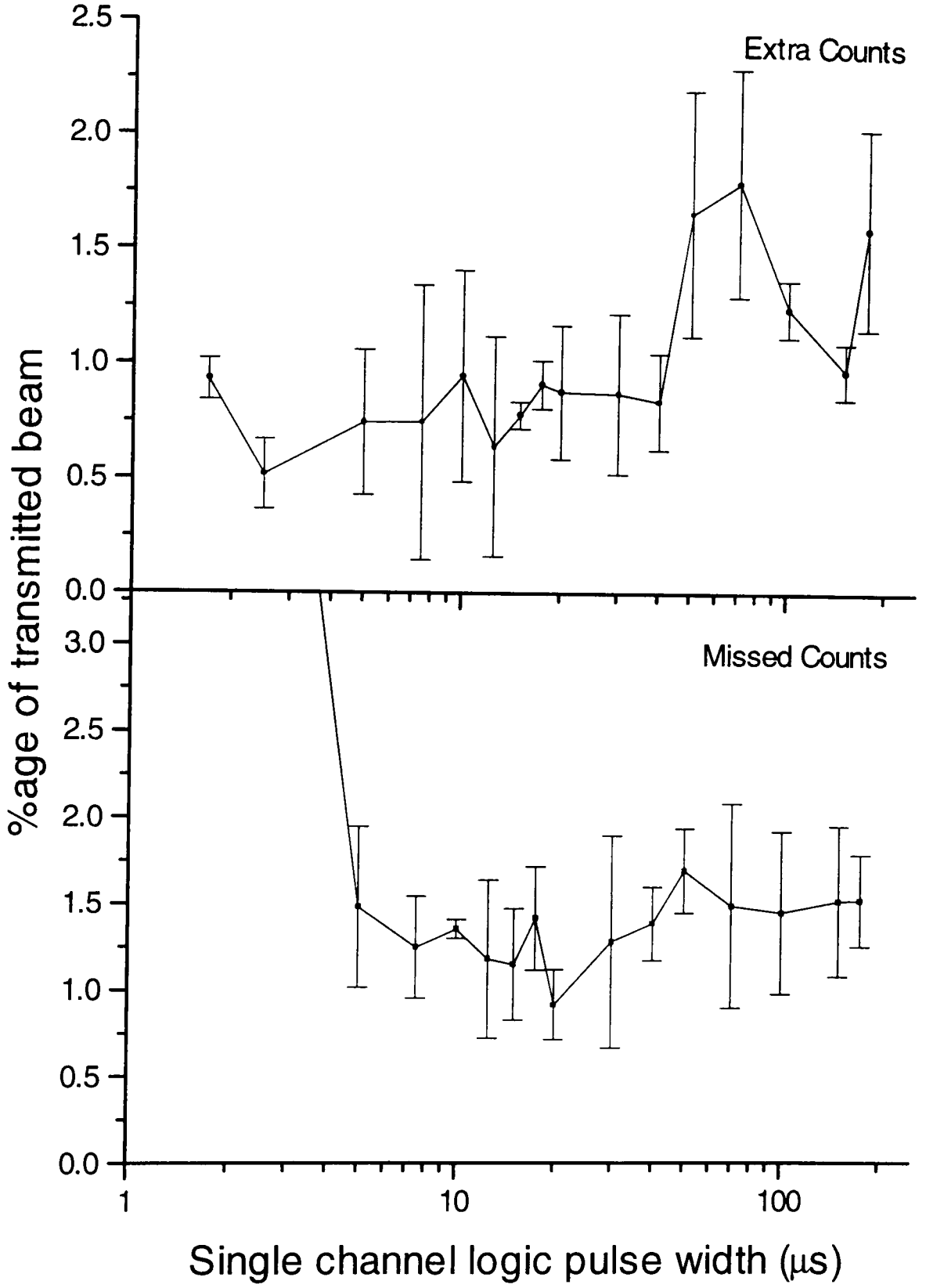

Figure 5.24 Data showing the effect of the single channel logic pulse width on the efficiency of detector assembly 3, for a discriminator setting of 3.5 and a count rate of 30 s^{-1}

Having determined the optimum discriminator level and logic pulse width for a count rate of 30 s^{-1} it was also necessary to investigate how a variation in the count rate would effect the detector efficiency. The discriminator setting used was 3.5 and the logic pulse width used was 20 μs. The data were obtained using an identical method to that used to determine the optimum values of the previous parameters. Results were obtained for count rates between 17 and 1000 s^{-1} and are presented in Figure 5.25.

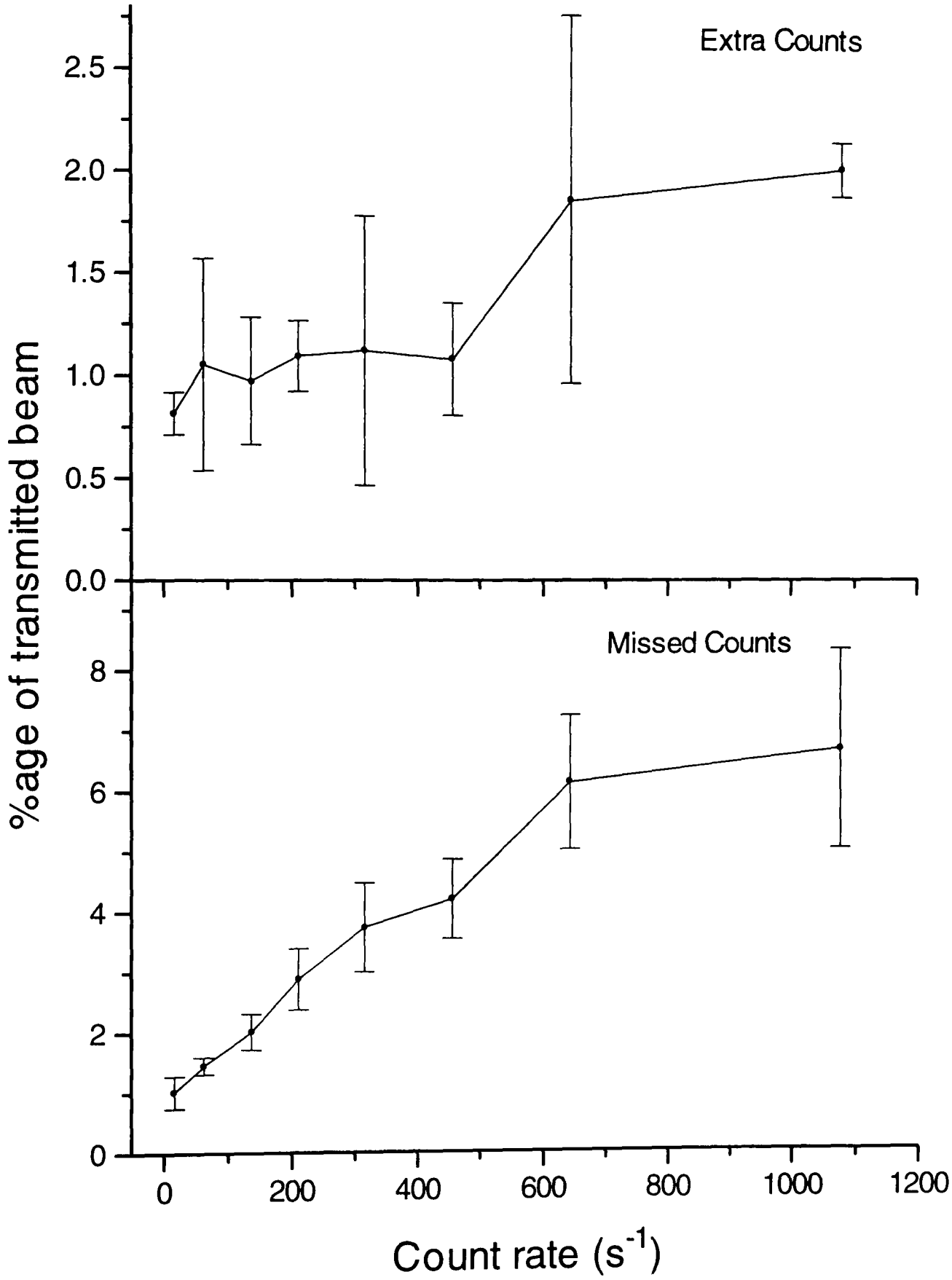

Figure 5.25 Data showing the effect of the count rate of the transmitted proton beam on the efficiency of detector assembly 3, for a discriminator setting of 3.5 and a single channel logic pulse width of 20 μs.

Clearly the count rate had a significant effect upon the detector performance, resulting in an increase in the number of uncounted protons to 7 % and an increase in the number of false positive counts to 2 % at a count rate of 1000 s^{-1}. At a high count rate the

amount of light produced by the delayed fluorescence in the ZnS(Ag) crystal will have increased due to the continuous excitation of the crystal. This will have resulted in both false positive counts due to random coincidences between noise events and also an increase in the number of uncounted protons due to counts occurring in the dead-time caused by an increase in the number of single channel pulses. The optimum count rate for this type of particle detector is therefore as low as possible. In practice the count rate used will be determined by the limitations imposed by the experiment for which the detector is to be used.

5.3.4 (d) Conclusions

This work has demonstrated the applicability of a scintillation transmission detector approach to particle counting for the Gray Laboratory microbeam. The third collimator - detector assembly shows a detector performance which attains the target specified in Section 1.1. Although the counting efficiency is reduced at increased count-rates, the proposed biological experiments will use a count-rate which is well below 100 s^{-1} and so the counting efficiency will be sufficiently high in this range. The thickness of scintillator used is near to the maximum which may be used without the introduction of an unacceptable degree of particle scatter. However, the size of signal obtained indicates that it will be possible to reduce the thickness of scintillator considerably with no significant loss in the detector efficiency.

Chapter 6 : Development of a Collimator-Detector Assembly for the Irradiation of Cells

6.1 Introduction

The possibility of constructing a detector assembly mounted onto the surface of a particle collimator was demonstrated in Chapter 5. However, in order to be of experimental value the Gray Laboratory microbeam required the design and construction of a durable collimator-detector assembly which would withstand repeated pressure as a result of contact with the mylar base of the cell dish, without damage. The assembly was required to perform predictably for a variety of exposure times and to maintain its performance with prolonged irradiations.

The work described in Chapter 3 showed the development of a collimator capable of reducing a 3.5 MeV proton beam to a diameter of ~ 2.3 μm diameter. The work described in Chapter 5 described the development of a transmission particle detector capable of detecting 3.5 MeV protons with an efficiency of better than 99 %. By the combination of these two elements it was possible to produce a useful collimator-detector assembly for the production of a proton microbeam. This chapter describes the production of a ruggedised collimation and detection system and the analysis of its performance.

6.2 Construction

In order to bring the two elements of collimation and detection together in a durable assembly it was necessary to re-design the steel end-cone to accommodate an hplc tubing collimator, vacuum window and ZnS(Ag) detector. The design was internally similar to that shown in Figure 3.7 and was externally as shown in Figure 6.1. The design consisted of a pivoting end-cone with a removable steel disc mounted to form the upper surface of the assembly. The disc was held in position by screws, which applied pressure to a rubber O-ring positioned between the disc and the body of the end-cone to form a vacuum seal. A 280 μm diameter hole was drilled at the centre of the disc to

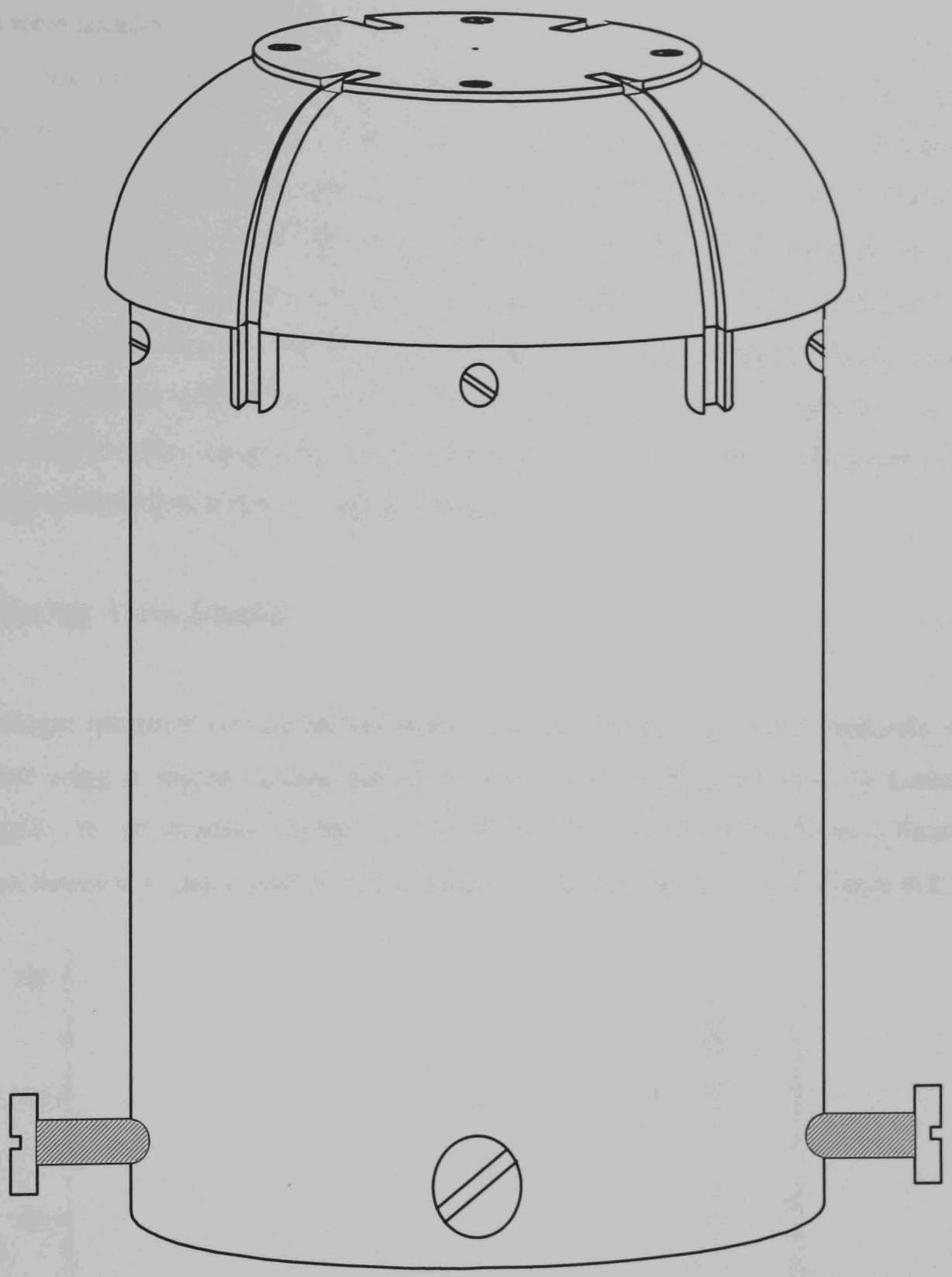

Figure 6.1 End-cone designed for the production of a rugged collimator-detector assembly using an hplc tubing collimator and a ZnS(Ag) crystal.

accommodate the collimator. To produce a vacuum window for the collimator a 2.5 µm thick mylar sheet was glued to a 40 µm thick, 3 mm diameter nickel disc with a 600 µm laser drilled hole at its centre (Ealing Electro-Optics Ltd., UK). This was then mounted over the hplc tubing and was held in position using adhesive. A single ZnS(Ag) crystal was then mounted onto the mylar window over the collimator aperture and two optical

fibres were attached to the crystal. Across the surface of the disc the fibres were bonded to the metal using optical cement giving a solid support for the fibre from the edge of the disc to the crystal itself. It was this support which gave the assembly its durability, by maintaining a rigid fibre position under physical pressure from above. The fibre direction was turned through 90° from horizontal to vertically downwards at the edge of the disc through a radius of curvature of 5 mm. The fibres were then transferred into black PVC tubing through fibre guides, where they were held in place using a mixture of silicone rubber and black paint. The optic fibres were again connected to the photomultiplier tubes using plug-in optic fibre connectors. A complete description of the method of construction is described in Appendix V.

6.3 Energy Loss Studies

The energy spectrum for the proton beam produced by the completed assembly was obtained using a silicon surface barrier detector, with signal processing by standard nucleonics, for an incident 3.5 MeV proton beam. The spectra for the 5 μm collimator with no detector in place and for the completed assembly are shown in Figure 6.2.

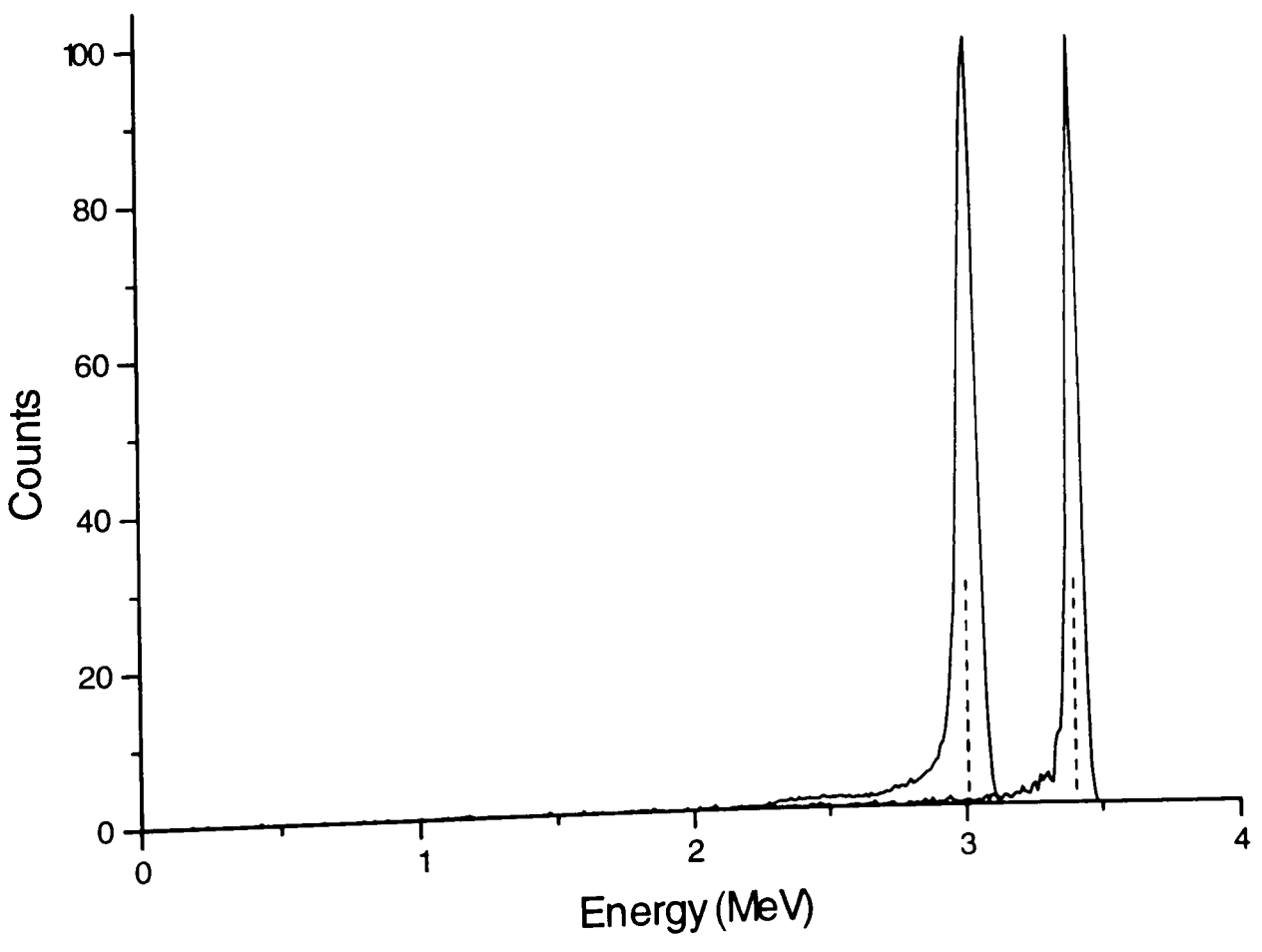

Figure 6.2 Energy spectra for the hplc tubing, 5 μm diameter exit aperture, collimator alone and for the collimator plus detector assembly.

The data show a peak-to-peak energy loss of 380 eV and a mean energy loss, measured between the means of the spectra, of 393 eV. This energy loss corresponds to an equivalent ZnS crystal thickness of 15 μm, assuming an energy loss of 24.8 keV μm^{-1}, for 3.5 MeV protons in ZnS (Ziegler, 1977). This thickness was similar to that measured by light microscopy for the crystal used, which was large in order to preserve a high counting efficiency for this assembly.

6.4 Spatial Resolution Studies

To measure the experimental spatial resolution of the proton beam resulting from traversal through the ZnS(Ag) crystal, irradiations of CR39 track etch plastic were performed. Results for single irradiations of 10, 50 and 100 protons are shown in Figure 6.3. These irradiation experiments were also used as a test of the durability of the assembly since the detector was driven into the CR39 sheet during initial alignment and irradiation. No damage to the assembly was apparent after the experiment.

The beam diameters were measured using the software of the solid-state microscope attached to the Gray Laboratory microbeam. The data show that for a 10 proton irradiation the mean beam diameter was 5.8 ± 1.6 μm, for 50 protons was 8.3 ± 1.7 μm and for 100 protons was 8.7 ± 1.7 μm. The calculations in Section 3.7 show that the best representation of the 90 % beam width is given by the mean diameter of the 10 - proton irradiations.

In order to understand the relationship between the degree of scatter within the detector and the final beam size, a two dimensional computer simulation code was written. The beam distribution from the collimator was modelled by a rectangular, 'top-hat', probability distribution with a width determined by the exit aperture diameter of the collimator. The scatter due to the detector was modelled by a Gaussian distribution. The code for the simulation programme is shown in Appendix IV. Simulations were performed for collimator apertures of 1.5, 5 and 10 μm, corresponding to the available diameters of hplc tubing, and with Gaussian scatter peak widths of between 0 and 10 μm. The width of the Gaussian peak was defined as the full width which contained 90 % of the area of the distribution and corresponded to the parameter used to describe the

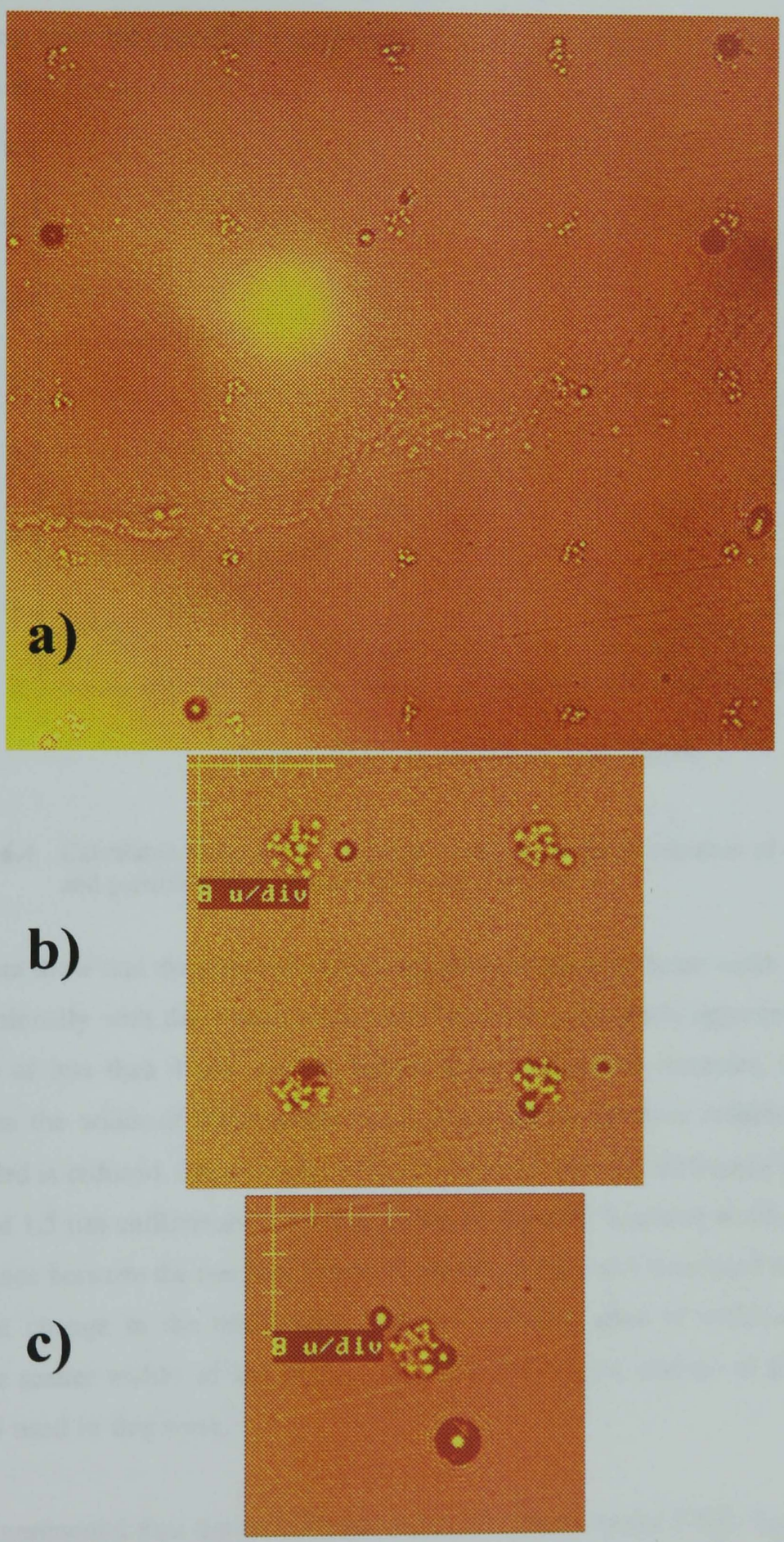

Figure 6.3 Data showing the spatial resolution of the transmitted proton beam produced by a rugged collimator detector assembly using irradiations of **a)** 10, **b)** 50 and **c)** 100 protons in a 50 μm spacing grid, in CR39 track etch plastic.

scatter widths calculated for various thicknesses of ZnS in Section 4.5. The beam widths resulting from the specified degree of scatter, for each collimator width, are shown in Figure 6.4.

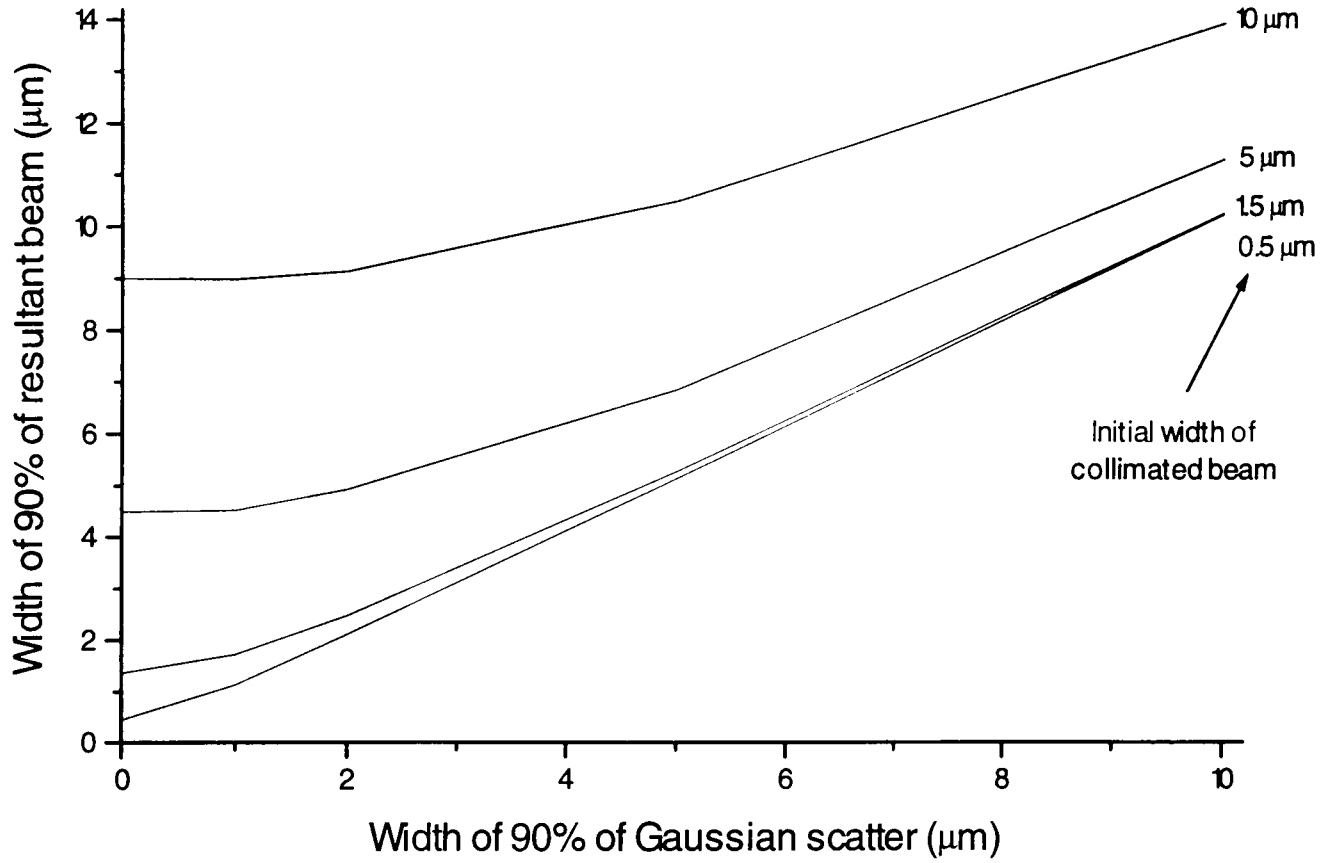

Figure 6.4 Calculated beam widths showing the effect of the combination of collimator size and particle scatter on the final beam produced.

The data show that the effect of particle scatter upon the final beam width does not vary proportionally with the scatter width and that this is particularly apparent at scattering widths of less than 4 µm. As the degree of particle scatter increases, the difference between the width of the resultant beam produced by the three collimator diameters modelled is reduced. For example, with no particle scatter the difference between the 5 µm and 1.5 µm collimators is 3.5 µm, however, for a 90 % scatter width of 10 µm the difference between the resultant beams of the two collimators is reduced to 1.9 µm. The greatest change in the relationship between the three sizes of collimators exists at particle scatter widths of less than 4 µm which is a region relevant to the thicknesses of ZnS used in this work.

The experimental data shown in Figure 6.3 for the irradiation of CR39 track etch plastic by single, timed exposures indicate a 90 % beam diameter of 5.8 µm. The Gaussian scatter width indicated by Figure 6.4, for this beam diameter from a 5 µm exit aperture

collimator, is 3.2 μm. From the data, shown in Figure 4.5, showing the effect of various thicknesses of ZnS on a 3.5 MeV proton beam, a scatter width of 3.2 μm corresponds to the 90 % beam width of a 3.5 MeV proton beam at 20 μm from the surface of a 12 μm thick ZnS crystal. This result is a good approximation to the 15 μm thickness of ZnS calculated by the energy loss calculations in Section 6.3.

6.5 Counting Efficiency Studies

The performance of the collimator-detector assembly was analyzed using the methods described in Section 5.3.3(c). Counts from the silicon surface barrier detector and ZnS(Ag) crystal were counted simultaneously in determining the number of false positive and missed counts to minimise counting errors. The initial parameter tested was that of the discriminator level, using a count rate of 60 s^{-1} and a single channel logic pulse width of 17 μs. The results are shown in Figure 6.5.

The data show that the optimum discriminator setting was 2.0, and corresponded to a detector inefficiency of 0.27 ± 0.22 % for false positive counts and 1.7 ± 0.4 % for missed counts. As for the detectors tested in Chapter 5 the number of missed counts and false positive counts increased as the discriminator reached the height of the background noise signal and increased due to the presence of second coincident signals from the decaying edge of the signal pulse at high discriminator settings. An additional contribution to the number of missed counts and false positive counts may have been present due to a movement in the relative positions of the surface barrier pulse and the ZnS(Ag) pulse, causing a loss of coincidence between the signals from the two detectors. The data show a small increase in the number of missed counts and a small reduction in the number of false positive counts, relative to the results obtained for detector assembly 3 in chapter 5. This may be explained by an overall reduction in the amount of both signal and background light entering the photomultiplier tube and so may indicate a lower efficiency for the transmission of emitted light in either one or both channels of the detector.

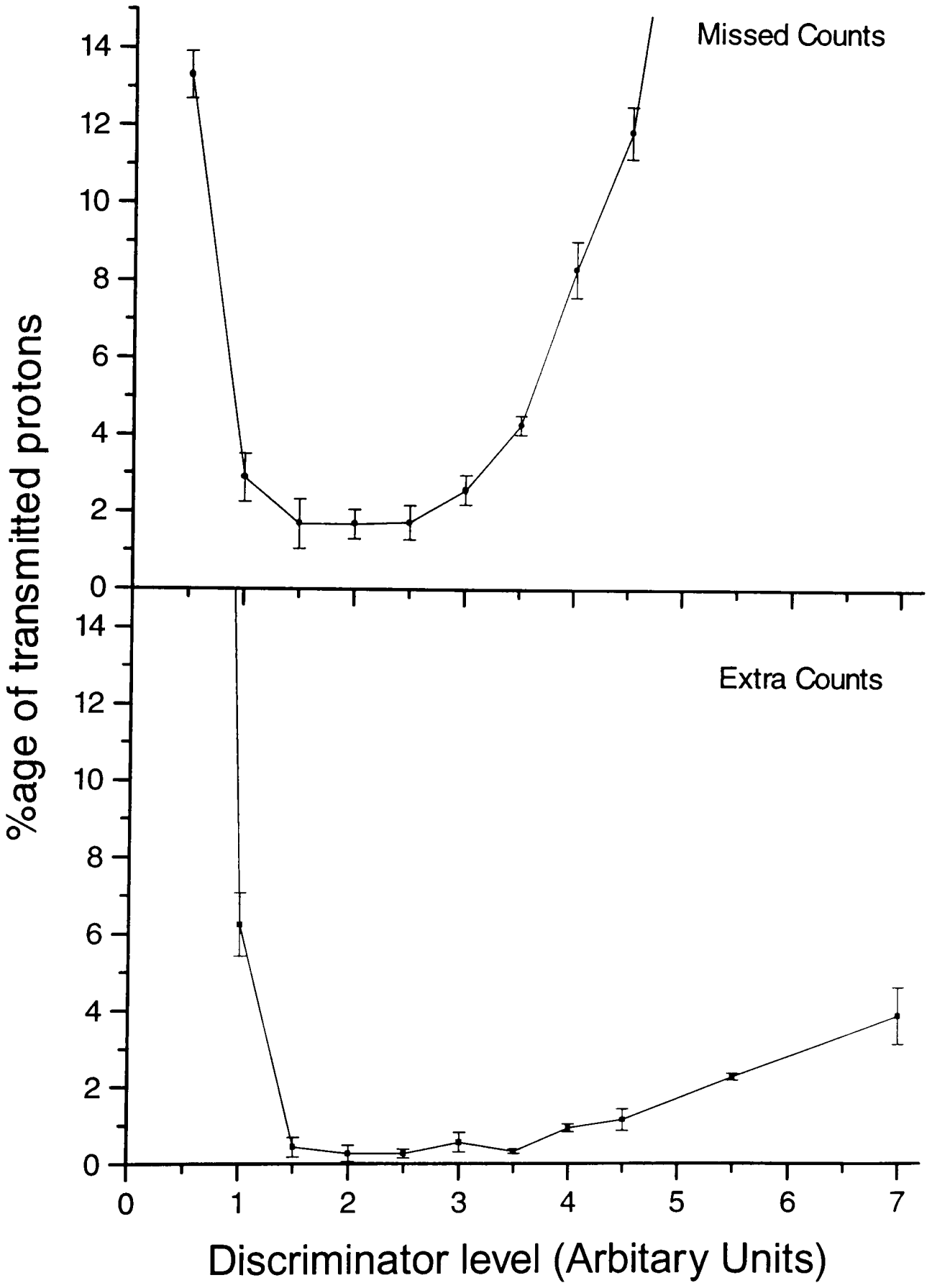

Figure 6.5 Data showing the effect of the discriminator level on the efficiency of a rugged detector assembly, for a count rate of 60 s^{-1} and a single channel logic pulse width of 17 μs.

Having determined the optimum discriminator level, the effect of the count rate upon the detector efficiency was then investigated. It was assumed that the timing characteristics of the light pulse produced was identical for all ZnS(Ag) crystals and so

the previously obtained optimum single channel logic pulse width of 17 μs was used throughout this study. The effect of a variation in the beam intensity was investigated at count rates of between 1 and 1000 protons s^{-1}. The results are shown in Figure 6.6.

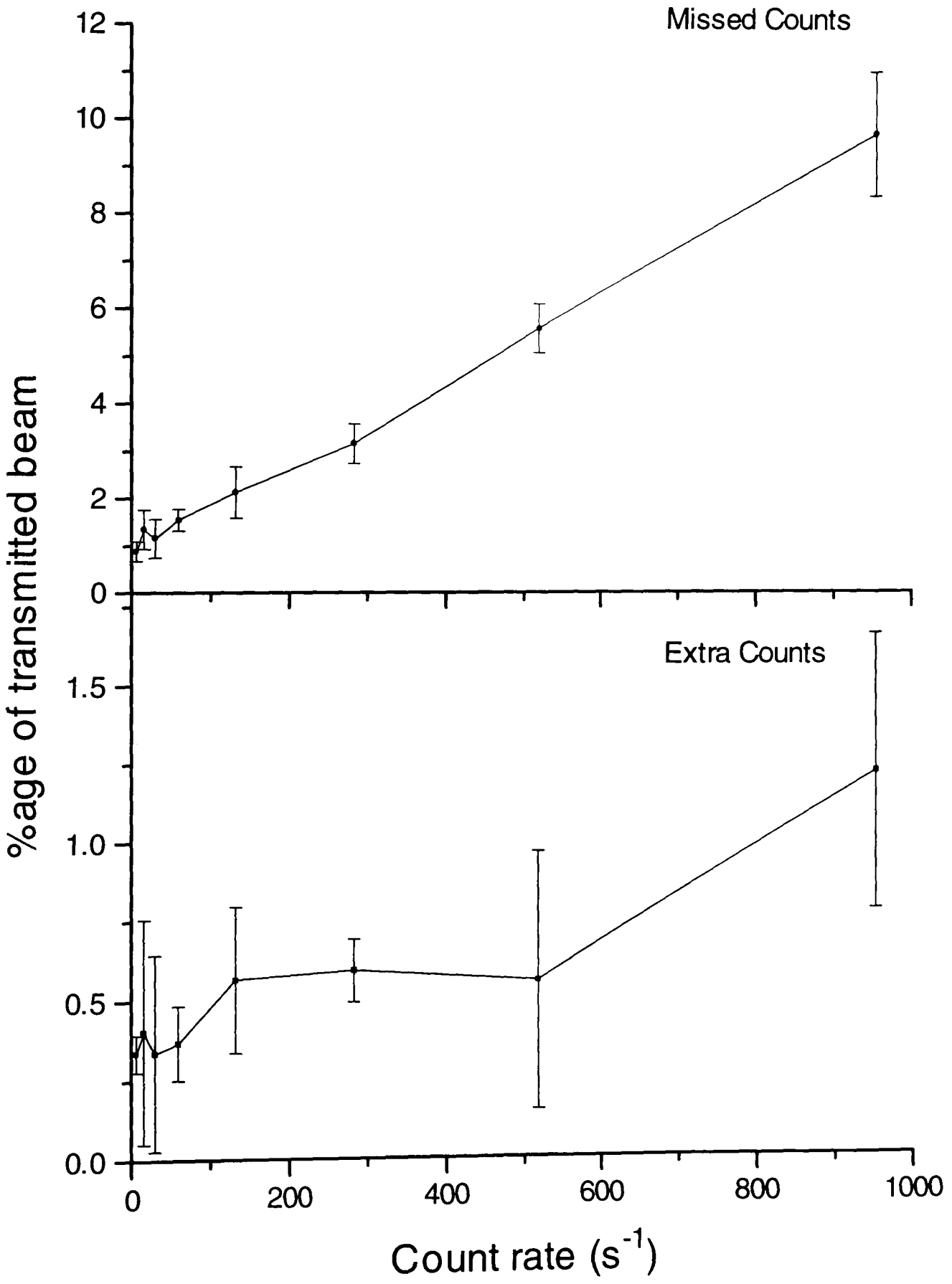

Figure 6.6 Data showing the effect of the count rate on the efficiency of a rugged detector assembly, for a discriminator level of 2.0 and a single channel logic pulse width of 17 μs.

As shown in the results of previous assemblies both the number of false positive counts and the number of missed counts increased as the count rate increased. This was due to an increase in the amount of delayed fluorescence from the crystal, resulting in an increase in the background light and therefore in the dead-time of the detector. At a count rate of 950 s^{-1} the number of false positive counts increased to 1.2 ± 0.4 % and the number of missed counts increased to 9.8 ± 1.3 %.

In order to verify the detector efficiencies obtained in the previous section, studies were performed using CR39 track etch plastic. Single proton irradiations were used to produce two, 10 × 10 point grids with a spacing of 50 μm between points. The irradiations were controlled using a mechanical shutter (Folkard, private communication) using a signal from the detector electronics after a single count to turn off the beam. The shutter had an operating time of 50 ms and so at several points the shutter did not close rapidly enough to prevent a second proton traversing the detector. The number of detector counts was therefore manually recorded for each irradiation. A section of the grid of point irradiations produced on the plastic is shown in Figure 6.7.

As the figure shows, the grid of protons can be clearly seen against the background of the CR39 due to the production of bright spots at the site of a proton irradiation by the lensing effect of the pits in the plastic. A number of pits are visible between the points of irradiation due to background irradiation during the several years storage period of the CR39. The beam diameter was shown to be ~ 9 μm in Section 6.4 and so any protons outside of this diameter from the irradiation point are assumed to be due to background already present on the CR39. The background radiation was also visible on non-irradiated control samples and was not of a sufficiently high density to obscure the proton hits. Several points of the grid must be eliminated from the counting statistics since physical marks on the plastic have obscured the site of the hit, as can be seen in the top row of Figure 6.7. Also visible in the figure are two double hits, in the second and third row, due to the slow shutter speed, which were counted as two protons by the detector, and a point with no proton hit, in the second row, due to a false count.

By counting the number of hits at each site the total number of protons was calculated to be 204. There were 9 false positive counts, i.e. a count in the ZnS detector but no

Figure 6.7 The results, in CR39 track etch plastic, of repeated single irradiations of 1 proton per point in a 50 μm spacing grid.

mark on the CR39, and 2 missed counts, i.e. two marks on the CR39 for a single ZnS detector count. These figures correspond to 1.0 ± 0.7 % for missed counts and 4.4 ± 1.5 % for false positive counts. The results show a larger percentage of false positive counts than obtained using signal analysis by electronics. A possible source of this error in the experiment is in the imaging of the CR39. There is some variation in the size of the pits which were produced by development of the CR39 plastic and it is possible that some less well developed pits, combined with a low contrast in the image, have not appeared in the image obtained from the solid state microscope. A second possible source of the discrepancy in the number of false positive counts is user error when performing the irradiations. For each irradiation the collimator-detector assembly was lowered 1 mm, the CR39 moved to the next position and the assembly returned to the irradiation position at the next point in the grid. If the irradiation was performed with the assembly in the lowered position then the proton would not be detected at that position in the grid. An automated irradiation procedure would remove this source of potential error.

6.6 Conclusions

In conclusion, the collimator-detector assembly constructed has proved sufficiently rugged to perform several hundred irradiations of CR39 plastic. Multiple irradiations of 10 protons show a mean beam diameter of 5.8 ± 1.6 μm and irradiations of 100 protons show a mean beam diameter of 8.7 ± 1.7 μm. The maximum counting inefficiency of the system, as measured electronically by signals analysis, is 1.7 ± 0.4 % for missed counts and 0.27 ± 0.22 % for false positive counts.

The desired specification of the Gray Laboratory microbeam is a spatial resolution of < 1 μm and a counting efficiency of 99 %. The beam produced in this work has a detection efficiency which achieves this specification, however with a beam diameter which is significantly larger than the desired specification. The beam produced will nevertheless be of use in biological experiments conducted with the Gray Laboratory microbeam. If used at count rates of less than 100 s^{-1} the detector counting efficiency is within the targets defined for use in the Gray Laboratory microbeam.

Chapter 7 : Conclusions and Further Work

7.1 Microbeam Performance

The use of various materials and methods in the manufacture of particle collimators is described in detail in Chapter 3. The optimum collimation obtained in this work was for a 3.5 MeV proton beam using a 1500 μm long fused silica collimator having parallel walls and a circular exit aperture with a diameter of 1.5 μm. This collimator produced a beam with a diameter of 2.3 ± 0.9 μm and an energy spectrum, for an incident 3.5 MeV proton beam, for which 75 % of the beam was contained within a Gaussian fit to the full energy peak and 90 % of the beam had an energy of > 3.0 MeV.

Chapter 5 described the development of a transmission particle detector using an ~ 10 μm thick single ZnS(Ag) crystal coupled to two 30 μm diameter optic fibres. The fibres transmitted the emitted scintillation light to two photomultiplier tubes, the signals from which were analyzed in a coincidence counting configuration, using in-house designed and built electronics. The resulting detector had a confidence of detection for a transmitted 3.5 MeV proton, of > 99 % and a likelihood of producing a false count of < 1 %.

The use of a 5 μm diameter fused silica collimator and an ~ 15 μm thick ZnS(Ag) crystal to produce a rugged microbeam assembly capable of cellular irradiations was described in Chapter 6. The parameters of the beam produced by this assembly were a diameter of 5.8 ± 1.6 μm containing 90 % of the transmitted protons, and a diameter of 8.3 ± 1.7 μm containing 99 % of the transmitted protons. The detection efficiency for the system, measured using irradiations of CR39 track etch plastic, was a confidence of particle detection of 99.0 ± 0.7 %, and a likelihood of producing a false count of 4.4 ± 1.5 %.

By comparison, the early proton microbeam of Zirkle and Bloom (1957) had a spatial resolution of ~ 5 μm in diameter with a maximum energy at 1.1 MeV and a highly degraded energy spectrum containing many scattered protons, see Section 1.4.7. The recently constructed microbeam at Columbia Laboratory has been characterised, using

alpha particles, as having a beam diameter of ~ 6 μm with 90 % of the transmitted particles lying within the full-energy peak. The overall spatial resolution, including mechanical tolerances, has been measured to be 8 μm (Randers-Pehrson *et al.*, 1993;1994). A similar alpha particle beam performance has been reported for the apparatus constructed at Pacific Northwest Laboratories (Braby, 1993).

This initial attempt to produce a ruggedized collimator-detector assembly at the Gray Laboratory has therefore produced a proton microbeam which has parameters comparable to those of microbeams produced by other experimenters in this field, although comparison between the alpha particle and proton beam performances is difficult.

7.2 Biological Relevance of the Microbeam

The usefulness of the proton beam produced is determined by its relationship to the size of the relevant target. A picture of V79 hamster fibroblast cells is shown in Figure 7.1 overlaid by concentric circles of 5.8 and 8.3 μm diameter, representing the 90 % and 99 % beam diameters respectively.

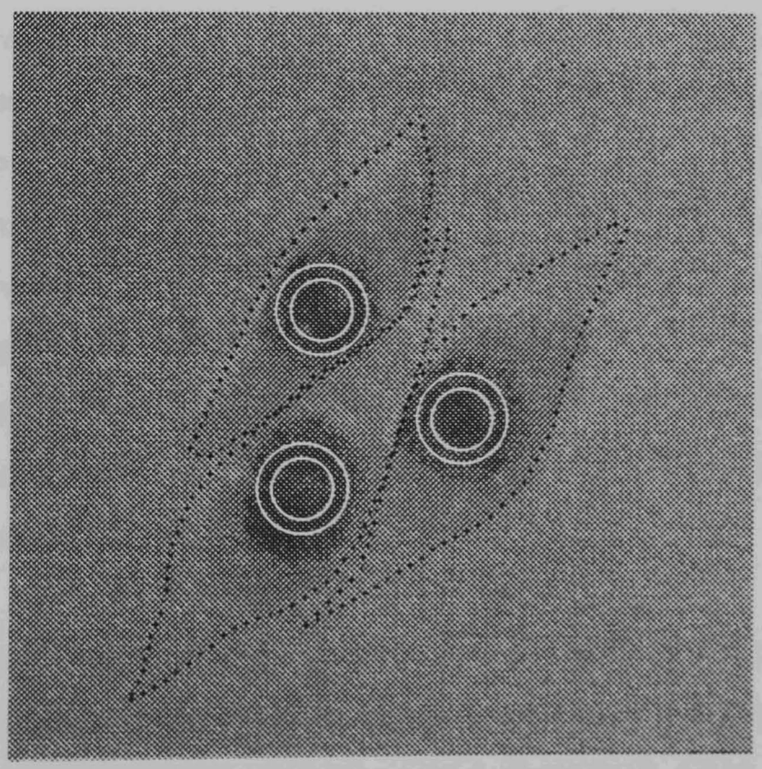

Figure 7.1 Demonstration of the 90 % beam diameter, inner circles, and 99 % beam diameter, outer circles, of the microbeam produced, relative to the size of V79 hamster fibroblast cells.

In addition, the dimensions of five cell lines attached to mylar plastic have been made by Raju (1991). The values for the mean nuclear diameter, calculated from the mean nuclear area by making the simplification of assuming a circular nucleus are shown in Table 7.1.

Cell Type	Mean Nuclear Diameter (μm)	Mean Nuclear Thickness (μm)
CHO-10B	11.43 ± 1.67	3.7
HSTE-23	9.00 ± 1.34	7.1
C3H10T½	15.96 ± 1.96	2.1
V79	9.77 ± 1.63	3.8
AG1522	13.37 ± 2.15	1.2

Table 7.1 Mean nuclear diameters of several cultured cell lines, calculated from Raju (1991) using the assumption of a circular nucleus.

The cell lines shown all have mean nuclear diameters which are larger than the diameter of the beam produced by the collimator-detector assembly. Many biological experiments will therefore be possible using this assembly. Of particular interest will be the low-dose response of various cell lines for a variety of end-points such as, survival to a defined number of cell divisions, micronucleus formation, levels of DNA damage as measured by the comet assay and chromosome damage measured by fluorescence in-situ hybridisation, protein expression in the low-dose region by single cell anti-body staining, ion regulation, and the effect of a priming dose of protons upon low-dose responses to further doses of protons or other radiations.

However, the spatial resolution of the microbeam is not sufficient, in this assembly, to investigate the difference in dose response due to a spatial variation of the energy deposition across the cell. This capability would be particularly useful in investigating the differential in the responses of the cell to cytoplasmic, membrane, or nuclear irradiations. It would, however, be possible to perform experiments using timed

irradiations with the 1.5 μm diameter collimator alone, producing a 2.3 μm beam with the error in the delivered dose determined by Poisson statistics. If the dose required for a specific end-point was large, for instance irradiations of > 100 protons, then the Poisson error in the dose delivered to each target would be tolerably small. Initial experiments of this kind have been performed to establish the various assays of biological end-points required for this work (Prise *et al.*, personal communication).

7.3 Further Work

There are two methods by which the spatial resolution of the microbeam produced by the collimator-detector assembly developed in this work may be improved. Either by reducing the size of the beam emerging from the collimator or by reducing the degree of scatter between the exit aperture and the target. These developments will be discussed separately in Sections 7.3.1 and 7.3.2 with a consideration of how improvements in the performance of these elements will effect the final microbeam diameter in Section 7.4.

7.3.1 Improvements in collimation

Improvements in the collimation of the Gray Laboratory microbeam may be made by a reduction of the dimensions of the current collimator designs, by designing new collimator geometries or by improving the characteristics of the incident particle beam. Consideration of possible improvements in these three elements are given in the following sections.

7.3.1 a) Reduced collimator dimensions

Of the collimators developed in this work, those of the hplc tubing and of the silicon micro-manufactured collimators show potential for an improvement in the diameter of proton collimation achieved.

A progression to smaller exit aperture collimators using silicon manufacturing techniques requires an improvement in the manufacturing techniques used to produce these collimators, perhaps by an alternative manufacturer. The minimum size of the silicon

collimators produced by Applied Microengineering Ltd. was 3 μm, resulting in a proton beam of ~ 5 μm across. Manufacturing techniques have been developed in the semi-conductor industry which allow the production of structures with dimensions of significantly less than 1 μm, the main limitation being the production costs involved. The possibility still exists therefore to use this approach in improving the collimation of the Gray Laboratory microbeam. An improvement in the performance of this type of collimator may also be obtained by the design of new collimator geometries, this option is discussed in Section 7.3.1 b).

The production of a smaller diameter collimator of the hplc tubing type is also a feasible possibility. Off-the-shelf commercial hplc tubing with an internal diameter of 5 μm was used to produce a 90 % beam size of 4.7 ± 1.2 μm. The initial attempt by SGE Ltd. (Australia) to produce tubing with a diameter of less than this value resulted in fused silica tubing with a bore diameter of 1.5 μm, producing a microbeam with 90 % of the transmitted protons within a diameter of 2.3 ± 0.9 μm. Given the apparent ease with which tubing of this diameter was produced it is likely that further attempts by this manufacturer to produce tubing with a diameter of less than 1 μm would be successful. The use of hplc tubing collimators in more complex designs may be possible by the removal of a section of rigidly mounted tubing to create two collinear collimators with the inclusion of a void.

The advantages of low-cost and the high quality of the beam produced by the hplc tubing make this approach the most likely to yield a proton beam of less than 1 μm in the future.

7.3.1 b) Improved collimator designs

The simulations performed to predict the performance of various collimators were tailored to the specific parameters of the incident beam and collimator used in this work. The long computing time required for these studies precluded a more detailed investigation of the possible effects of other collimator and beam parameters on the beam performance. A more lengthy investigation, or a significant reduction in the computing time required to obtain sufficient data, would allow the further consideration

of the many variable parameters present in this problem and therefore to discover possible improvements in collimator design.

Preliminary attempts to design more complex collimators were made by the simulation of single voids in 1 μm wide collimators. These designs predicted improvements of ~ 2 % in both the energy and spatial resolutions of the collimated beam, relative to the results obtained for a single, straight-sided collimator of an equal total length. These initial results show the potential for performance gain by the use of multiple collimator assemblies and suggest that further modelling of more complex collimator geometries, for example using non-parallel sides, may show potential improvements in collimator performance.

The variables considered in the simulation work were the collimator length and width, and the incident beam divergence and misalignment. In addition to further work using these parameters to improve the design of collimators in silicon, it would be useful to consider how collimators constructed from alternative materials would affect the quality of the transmitted beam and how collimators that were designed for a specific incident proton beam would perform for an incident beam of a different energy or particle type.

The use of curved collimators was also modelled, using a modification to the original simulation code to incorporate the effects of a uniform magnetic field. The simulation of collimators with a radius of 289.1 mm, in a 1 Tesla field, for an incident 4 MeV proton beam, showed improvements of more than 10 % in both energy and spatial resolution parameters, relative to straight collimators of an equivalent length. The limitation in this approach is the considerable complexity involved in the construction of a collimator, with a circular path, and within a tunable magnetic field which is both uniform and perpendicular to the plane of curvature of the collimator.

7.3.1 c) Improvements in the simulation of collimator performance

The collimators modelled, using the computer simulation programme developed, were of a relatively simple geometry, based upon straight-sided collimators, some with the inclusion of voids. It is likely that the use of different collimator designs and alternative

collimator materials will produce an improvement in the spatial resolution of the transmitted beam. However, in order to design more complex systems it is important that the predictions made by the computer simulation programme are accurate, since considerable cost is likely to be involved in the production of these more complex collimator structures. Several improvements may be made to increase the accuracy of the collimator simulations.

The current version of the programme uses a Gaussian distribution as an approximation to the scatter introduced by a defined depth of the collimator material, equal to the step size per iteration. The use of a Gaussian distribution to model particle scattering is an approximation and does not include high angle scattering events. The same principle of simulation using fixed step sizes but with a more accurate distribution for the particle scattering angle, including the tail of particles scattered at high angles, would improve the accuracy of the data obtained. Alternatively the particle scatter may be considered by the construction of a lattice of atoms through which the particle track can be calculated mechanistically. This approach is under development (Gohla, 1995).

A simplification has been made in the simulation programme by the tracking of particles through the collimator in only two dimensions. The inclusion of three-dimensional modelling of particle trajectories may show a variation in the results obtained from the programme. The effect of changing from two to three dimensions was shown in Section 2.7 to reduce the ratio of the exit aperture to the collimator wall by a factor of two. This may result in an increase in the relative proportion of scattered particles in the transmitted beam, so reducing the performance predicted by the collimator modelled.

The inclusion of these two elements into the simulation programme will be a complex task but may prove valuable in the design of new collimator geometries. It is likely that these refinements will increase the length of time required to obtain sufficient data and it would therefore require the use of a considerably faster computer than the 486PC used in this study to retain a run-time which was practical.

7.3.1 d) Improvements in the incident particle beam

It was shown in Chapter 3 that a reduction in the divergence of the incident beam would significantly improve the performance of collimation for a straight-sided collimator. The incident proton beam at the Gray Laboratory had an estimated full-width divergence of 0.067°. This value would be reduced by an improvement in the control, alignment and performance of the focusing elements in the accelerator system to produce a more parallel beam. However, since the focusing elements have many variables, the complexity of this task is considerable. The second alternative is that of pre-collimating the incident beam by the use of small apertures having a large separation and positional adjustability in two directions. This may be achieved by the installation of a second set of adjustable X-Y slits at a position below that of the existing slits installed in the beam line, see Figure 1.12.

A second possibility to improve the spatial resolution of the microbeam by a modification of the incident particle beam would be by the use of α-particles rather than protons. The reduced penetration of these particles may reduce the number of particles which emerge through the collimator exit surface and would therefore improve the performance of the collimator. This consideration, and that of using $^{3}He^{2+}$ ions, may be further investigated using the computer simulation programme developed.

Both the reduction of the incident beam divergence and the development of smaller diameter hplc tubing collimators are most likely to lead to an improvement in the quality of collimation for the Gray Laboratory microbeam. The design of more complex geometries, and the use of alternative materials and methods in collimator production, will require further development including an increase in the accuracy of the computer simulation.

7.3.2 Improvements in detection

Although the detection efficiency of the system developed in this work is within the initial specification for the Gray Laboratory microbeam, the degree of scatter introduced by the thickness of ZnS used is high. The aim of improving the detection system is

therefore to obtain a sufficiently large signal from a reduced thickness of ZnS, and so reduce the amount of scatter of the transmitted particles.

7.3.2 a) Modifications to the current design

The signal size obtained using the current design is large relative to that of single photon noise and shows efficient light collection, however, significant improvements may be made to increase the efficiency of the detector assembly.

Transmission of light from the crystal into the fibre optics may be made more efficient in several ways. The light emitted reaches the fibres either directly or by internal reflection from the faces of the crystal. This process requires a smooth crystal surface in order to be efficient, and irregularities present in the ZnS surface will result in light loss. However, an alternative to the use of specular reflection from the surfaces would be to use diffuse reflection. By coating the crystal with an optically dense layer of a diffuse scatterer such as silver the efficiency of light reflection through the crystal to the fibre would be increased. Further improvements may be obtained by also coating the underside of the crystal or the upper surface of the collimator assembly. This however poses more difficult technical problems for the construction of complete collimator-detector assemblies.

An additional way to increase the light transmission from the crystal to the optic fibre is to match the refractive indices of the optical coupling cement (1.62) and the crystal (2.36). Since the edge of the crystal is uneven, refraction of light at the angled surface of the crystal may result in some of the emitted light being bent to angles which are too large for internal reflection within the fibre optic, resulting in light loss. An index-matched optical coupling cement will remove these effects of refraction at the edge of the crystal. The optical cement used was chosen for its physical strength and its ease of curing, however further investigation may yield ultraviolet light curing cements which can be index-matched to the ZnS crystal.

In addition to improving the collection of light by optical fibres it will also be possible to increase the efficiency of transmission of light to the photomultiplier tubes. The

current design includes a 90° curve with a radius of 5 mm which will result in some light loss within the fibre. The curve in the fibre may be eliminated by the use of a 45° mirror reflecting light from the fibre which is connected to the crystal into a second fibre connected to the photomultiplier tube. This arrangement would also allow the use of a shorter length of 30 μm diameter fibre from the crystal and to use a larger fibre, with better light conduction properties, for the longer length to the photomultiplier tube.

The fibres at present couple to photomultiplier tubes which have an effective photocathode size of 23 mm. Since the area of the photocathode illuminated by the cone of light from the fibre optic is much less than this diameter, the single photoelectron noise level is higher than is necessary. By the use of smaller photocathodes the level of single photoelectron noise could be reduced in proportion to the reduction in the area of the photocathode. Since the occurrence of random coincidences limits the level at which the discriminator may be set, a reduction in the amount of background noise will allow the use of a lower discriminator level, and therefore allow a reduction in the thickness of ZnS(Ag) used.

At the photomultiplier tube another improvement in efficiency may be obtained by the use of an optical coupling gel between the fibre end and the glass window of the photomultiplier tube. This will reduce both the internal reflection from the exit face of the optic fibre and the transmission of light to the photocathode.

7.3.2 b) Redesign of the current assembly

Further design modifications to the assembly constructed will also lead to an increase in the efficiency of light collection and detection and so will allow a thinner crystal of ZnS(Ag) to be used.

The assembly constructed uses two optic fibres attached to the edge of the crystal at 180° to each other. It would be possible to construct an assembly using four fibres around the ZnS(Ag) crystal, attached at 90° to each other. The fibres would then be coupled in pairs into the photomultiplier tubes. This approach alone may, by simple geometry, yield as much as 100 % more light from the crystal and consequently allow

at least a 50 % reduction in the thickness of ZnS(Ag) used.

The design of the current assembly results in a completed unit which is not removable from the stainless steel end-cone. It would be necessary therefore to machine a separate end-cone for each collimator-detector assembly constructed. This approach is impractical since the use of different particles or particle energies may require different combinations of collimator diameter and detector thickness. A more adaptable approach would be to construct the collimator-detector assembly on a single stainless steel disc, which may be removed from the end-cone. The 30 μm fibres would terminate at the edge of the disc and by careful machining could be made to couple to a second set of fibres transmitting the light to the photomultiplier tubes. This approach would allow the use of larger diameter fibres to conduct the light to the photomultiplier tubes, as previously considered.

A problem encountered by using ZnS(Ag) as a scintillator material was the irregular shape of the signal generated. This results in the need for a long single-channel logic pulse, with an optimum of ~ 17 μs, in order to produce coincidence in the two channels. The use of a long coincidence pulse increases the likelihood of random coincidences occurring. In addition, the trailing edge of the shaped pulse is 'toothed' by the intermittent production of single photons over a period of ~ 100 μs. This then increases the probability of a second coincidence pulse occurring in each channel near to the discriminator level on the trailing edge of the pulse. One solution may be to use a shaping pre-amplifier with a shorter shaping constant of 5 μs. The result of this would be to reduce the absolute height of the signal pulse, however, the trailing edge would decay to less than the discriminator level within the time of the coincidence pulse, eliminating the possibility of a second, false count. Spurious photons collected after this time would only produce pulses equivalent to a single photoelectron in height.

Another problem encountered in the use of ZnS(Ag) as a scintillator was the high level of delayed fluorescence which caused a significant increase in the level of single photon noise. This then prevented the use of a discriminator level set at the single photon noise level and so reduced the advantage gained by the use of a coincidence counting method of detection. An alternative design for use with the ZnS(Ag) scintillator would be a

detection system using a single photomultiplier tube with multiple optic fibre connector inputs in a single-channel mode. The increase in signal resulting from the coupling of all the optic fibres into a single photomultiplier tube may allow the use of a discriminator level set significantly above the single photon noise.

An alternative to compensating for the problems inherent in the use of a ZnS(Ag) detector would be to use a different scintillator material with better timing properties. The choice of ZnS(Ag) was made because of its high light output and the crystal shape being ideal for coupling to small diameter fibres. Other materials were tested in this configuration, however, ZnS(Ag) crystals gave the best results in terms of total light output. By the growth of crystals of other materials in more favourable geometries or the design of alternative detector geometries with superior light collection it may be possible to develop a system using a scintillator with a faster light output. The scattering introduced by an alternative material may be less than that of ZnS(Ag) if the atomic numbers of the elements in the scintillator are lower than those of zinc and sulphur.

A further reduction in the effect of particle scattering may be achieved by the use of smaller diameter fibres coupled to the scintillator crystal. Although the fibres used were the smallest diameter commercially available at the time, there may now be smaller fibres available with comparable light collection and transmission properties. Alternatively fibres may be custom-made for the application. The use of smaller fibres would reduce the distance between the scintillator and the target cell and so would decrease the beam enlargement due to particle scatter within the detector.

A small contribution to a reduction in the degree of scatter would also be made by the reduction of the collimator exit window thickness. This could be achieved by the use of a thinner polymer window or by the use of alternative materials available in extremely thin form, such as beryllium or silicon nitride.

The use of a diffuse scatterer coating, the refractive index matching of the optical coupling cement to the crystal, and an increase in the number of optic fibres coupled to the crystal are the modifications which may most easily be implemented to increase the efficiency of light collection. In addition, the use of modified electronics may be used

to improve the processing of the signal produced by the scintillator and consequently to reduce the percentage of false counts. The high level of single-photon noise due to delayed fluorescence in the ZnS(Ag) crystal may result in a higher detection efficiency by the use of a single-channel counting method rather than the two-channel, coincidence counting approach adopted in this work. The applicability of the two approaches will require further investigation to determine which gives the optimum performance.

7.4 Potential Future Performance

Using data from Figure 4.5, describing the degree of scatter resulting from various thicknesses of ZnS, and data from Figure 6.4, describing the transmitted beam resulting from the combination of a collimated beam with various degrees of particle scatter, it was possible to calculate the effects of improvements in the parameters describing collimation and detection separately upon the resulting beam diameter. Since the target is fixed at 30 μm from the exit aperture of the collimator, due to the size of the optic fibres currently used, and the ZnS crystal is mounted in contact with the exit surface of the collimator, consideration of the distance from the exit surface of the scatterer to the target cell must also be included in the calculations of beam performance. The resultant beam diameters were predicted for various thicknesses of ZnS scatterer, using collimator diameters of 5, 1.5 and 0.5 μm, and are given in Table 7.2.

Experimental data were obtained for a thickness of ~ 15 μm of ZnS over a collimator with an exit aperture of 5 μm. The resulting 90 % beam diameter was measured to be 5.8 ± 1.6 μm and is in good agreement with the calculated value of 5.6 μm obtained from the simulation. Further comparison with experimental data would be obtained by the construction of more collimator detector assemblies and would be necessary to validate the data obtained.

The data show that an assembly constructed using 1.5 μm rather than 5 μm diameter bore hplc tubing, with an equal thickness of ZnS, results in a reduction in the final beam diameter from 5.6 μm to 3.4 μm. The improvements suggested to increase the efficiency of light collection should allow at least a 50 % reduction in the thickness of ZnS used. A reduction in the thickness of ZnS from 15 μm to 7 μm, and using the 1.5 μm

ZnS thickness (μm)	Beam diameter containing 90 % of protons for a 5.0 μm diameter exit aperture (μm)	Beam diameter containing 90 % of protons for a 1.5 μm diameter exit aperture (μm)	Beam diameter containing 90 % of protons for a 0.5 μm diameter exit aperture (μm)
1	4.5	1.6	1.0
2	4.6	1.9	1.3
5	4.9	2.3	1.9
7	5.0	2.5	2.1
10	5.2	2.9	2.5
15	5.6	3.4	3.1

Table 7.2 The effect of reducing the collimator diameter and degree of particle scatter in the detector on the transmitted beam diameter.

diameter hplc tubing, would result in a further reduction in the resulting beam diameter from 3.4 μm to 2.5 μm.

The above improvements are gains which may be realised in the short term. Although these modifications would create the smallest existing operational microbeam designed for single-particle irradiation of biological samples, they do not attain the 1 μm beam diameter which was the design objective for the Gray Laboratory microbeam. The data suggest that, for the range of collimator and detector parameter values used, a beam diameter of 1 μm is only attainable by using the optimum parameters simulated of a 0.5 μm diameter collimator with a 1 μm thick layer of ZnS as the transmission particle detector. Whether either of these parameters is realisable will only be discovered by further experimentation.

In conclusion, this work has resulted in the production of a 3.5 MeV proton microbeam with a mean diameter of 5.8 ± 1.6 μm, containing 90 % of the transmitted particles, and having a particle detection efficiency of 99 %. Small modifications to the current

assembly will allow the production of a microbeam of ~ 2.5 μm, containing 90 % of the scattered particles, and having an equally high detection efficiency. Further improvements in both collimation and detection using the principles developed here will result in a proton microbeam which approaches the 1 μm diameter design objective for the Gray Laboratory microbeam.

Appendix I : Listing of Collimator Simulation Programme KJH7.BAS

```
' program proton tracking
'
' The program simulates a single Silicon collimator
' with entrance and exit parameters given as inputs.
' Incident beam is a proton beam , Energy, Spatial distribution, Alignment,
' and Angular resolution are given as inputs.
' Most parameters are as "Inputs", start X,Y,Angle are "Hardwired".
' Particle tracks through the material in steps of 0.5 um with an approximation
' to energy loss and multiple scattering at each step.
' The particle is extrapolated to the collimator surface both initially
' and every time it leaves the material.
' Output is to file.
' Programme ends when defined number of particles have been transmitted
'
' physical parameters
'
M = 938.279                                          ' proton mass
IEFF = .000172                                       ' ionisation potential
ME = .511                                            ' electron mass
DELTA = .5                                           ' step size (um)
X0 = 9.36                                            ' radiation length in cm's
DELTA2 = DELTA * .0001                               'convert step size into cm's
'
CLS
'
INPUT "START ENERGY (MeV)"; TSTART                   ' incident proton energy
INPUT "HOW MANY TRANSMITTED PROTONS"; N
INPUT "RANDOM SEED (A -IVE ODD NUMBER)"; seed
INPUT "FILE NAME FOR DATA STORAGE"; B$               ' results go to this file
INPUT "ENTRANCE HOLE (UM)"; ENT                      "
INPUT "EXIT HOLE (UM)"; EXI                          " collimator dimensions
INPUT "LENGTH (UM)"; LENG                            "
INPUT "SPREAD OF INPUT BEAM (UM)"; yin               ' beam spread at entrance hole
INPUT "BEAM MISALIGNMENT (DEG)"; MISA                ' beam misalignment
INPUT "BEAM DIVERGENCE (DEG)"; DIV                   ' 1/2 FWHM of angular distribution
'
CLS
'
mis = MISA * (3.1415 / 180)                          'convert misalignment to radians
'
' DELTAMIN SHOULD BE 1E-3 OF X0
' MAKE THIS SOME MULTIPLE OF DELTA
'
DELTAMIN = .00005                                    'minimum distance over which multiple scattering is OK
'                                                    ' MSC is used in calculation of scattering angle
```

```
MSC = (1 + (1 / 9) * LOG(DELTAMIN / X0)) * SQR(DELTAMIN / X0)
'
' approx normal distribution
'
DEF FNNORM
     SUM = -6!
     FOR J = 1 TO 12
     SUM = SUM + RND
     NEXT J
     FNNORM = SUM
END DEF
'
OPEN B$ FOR OUTPUT AS #1                                    'open file for output
'
PRINT #1, "START ENERGY ="; TSTART          ' '
PRINT #1, "TOTAL NO. OF PROTONS ="; N       ' 'write
PRINT #1, "SEED ="; seed                    ' 'initial
PRINT #1, "ENTRANCE ="; ENT                 ' 'parameters
PRINT #1, "EXIT ="; EXI                     ' 'to
PRINT #1, "LENGTH ="; LENG                  ' 'output
PRINT #1, "BEAM SPREAD ="; yin              ' 'file
PRINT #1, "MISALIGNMENT ="; MISA            ' '
PRINT #1, "DIVERGENCE ="; DIV               ' '
'
' definition of graphics
'
SCREEN 8                                    ' screen pixels 640 by 200
WINDOW (0, -10)-(5500, 10)                  'set values for the window limits (um)
'
X1 = 5000 - LENG                            '
Y1 = 30                                     '
X2 = 5000 - LENG                            '
y2 = ENT / 2                                ' define
X3 = 5000                                   ' the
Y3 = EXI / 2                                ' eight
X4 = 5000                                   ' corners
Y4 = 30                                     ' of
X5 = 5000 - LENG                            ' the
Y5 = -30                                    ' collimator
X6 = 5000 - LENG                            ' walls
y6 = -1 * ENT / 2                           '
X7 = 5000                                   '
Y7 = -1 * EXI / 2                           '
X8 = 5000                                   '
Y8 = -30                                    '
'
DEF FNCOLL                                  ' Function to draw the collimator
     LINE (0, 30)-(5500, -30), 2, B
     LINE (X1, Y1)-(X2, y2), 2
     LINE (X2, y2)-(X3, Y3), 2
```

```
      LINE (X3, Y3)-(X4, Y4), 2
      LINE (X5, Y5)-(X6, y6), 2
      LINE (X6, y6)-(X7, Y7), 2
      LINE (X7, Y7)-(X8, Y8), 2
      'LINE (5000, 30)-(5000, -30)
      'LINE (5010, 30)-(5010, -30)
      FNCOLL = 1
END DEF
'
DONE = FNCOLL                                    'call fncoll to draw collimator
'
LOCATE 1, 2
PRINT "WINDOW (0,-10) (5500,10) DIMENSIONS IN MICRONS, 4MEV P,
SILICON"
'
' initialise parameters
'
AVRANGE = 0!
NTRANS = 0
'
' loop over n particles
'
'
FOR IP = 1 TO 100000000
    IF IP = 2 THEN                          ' set seed for random number generator
        seed = -1 * seed                ' to a positive number second time around it will
    END IF                              ' then continue in sequence from the initial seed
    x = 5000 - LENG - 1000          ' set first x value, 1000 um in front of collimator
    msangle = (FNNORM * DIV * (3.1416 / 180!))          'random start msangle
    y = ((RND(seed) - .5) * yin)                        'set y value at entrance surface
    '
    y = y - (1000 * TAN(mis + msangle))        ' extrapolate back to start y position
    '
    msangle = msangle + mis                    ' initial random angle + misalignment
    XS = x                                                      ' store start values
    ys = y                                                        '  "
    TS = msangle                                                  '  "
    T = TSTART                                                  ' set initial energy
    '
    EOLD = 0                    'eold is a safety parameter in case elav goes negative
    '
    ' extrapolate to the collimator
    '
    yext = y + (((5000 - LENG) - x) * TAN(msangle))
    IF (yext > y2 OR yext < y6) THEN
      LINE (x, y)-((5000 - LENG), yext), 1
      y = yext
      x = 5000 - LENG
      MU = (Y3 - y2) / (X3 - X2)
      CU = y2 - (MU * (5000 - LENG))
```

```
      ML = (Y7 - y6) / (X7 - X6)
      cl = y6 - (ML * (5000 - LENG))
      MP = TAN(msangle)
      cp = y - (x * MP)
      GOTO 10
    ELSE
      LINE (x, y)-((5000 - LENG), yext), 1
      x = 5000 - LENG
      y = yext
    '
    ' set up equations of the collimator walls
    ' suffix U = upper collimator surface
    ' suffix L = lower collimator surface
    ' suffix P = particle
    '
    MU = (Y3 - y2) / (X3 - X2)
    CU = y2 - (MU * (5000 - LENG))
    ML = (Y7 - y6) / (X7 - X6)
    cl = y6 - (ML * (5000 - LENG))
40  MP = TAN(msangle)
    cp = y - (x * MP)
    '
    ' extrapolate to the position of the next wall hit
    '
    yend = y + ((5000 - x) * TAN(msangle))
    IF (yend > Y7 AND yend < Y3) THEN
        YTERM = y + (5000 - x) * MP
        LINE (x, y)-(5000, YTERM), 4
        y = YTERM
        x = 5000
        GOTO 50
ELSE
IF yend >= Y3 THEN
        xhit = (CU - cp) / (MP - MU)
        Yhit = (MU * xhit) + CU
        LINE (x, y)-(xhit, Yhit), 5
        yext = Yhit
        XEXT = xhit
ELSE
IF yend <= Y7 THEN
        xhit = (cl - cp) / (MP - ML)
        Yhit = (ML * xhit) + cl
        LINE (x, y)-(xhit, Yhit), 3
        yext = Yhit
        XEXT = xhit
ELSE
        PRINT "IT AIN'T GONE NOWHERE MAN!"
        GOTO 20
END IF
END IF
```

```
        END IF
    END IF
    '
    ' finished extrapolating-Phew!
    '
    MAT = 1                    ' particle is in the collimator wall unless told otherwise
    y = yext
    x = XEXT
    '
10  ' track through the material
    '
    E = T + M                  '
    P = E * E - M * M          '
    '                          '
    IF P > 0! THEN             '
        P = SQR(P)             ' calculate beta
        BETA = P / E           '
    ELSE                       '
        P = 0!                 '
        BETA = 0!              '
    END IF                     '
    '
    ' now put in energy loss
    '
    GAMMA = 1 / SQR(1 - BETA * BETA)
    ELM = .0000178 / (BETA * BETA)
    ELAV = 2 * ELM * (LOG((2 * ME * BETA * BETA * GAMMA * GAMMA)
                                                    /IEFF)-BETA*BETA)
    IF ELAV <= 0! THEN
        ELAV = EOLD
        PRINT "ELAV GOING NEGATIVE", T, ELACV, THICK, BETA
        GOTO 20
    ELSE
        EOLD = ELAV
    END IF
    T = T - ELAV * DELTA * MAT                    'subtract energy loss
    '
    ' put in multiple scattering.....gaussian approximation
    '
    MSANGLEP = ((14 * MSC) / (BETA * P)) * FNNORM
    msangle = MSANGLEP * MAT + msangle
    THICK2 = 0!
    '
    x = x + DELTA * COS(msangle)                          'new x
    y = y + DELTA * SIN(msangle)                          'new y
    PSET (x, y), 1                                    'draw dot at (x,y)
    '
    ' now loop !!!
    '
    '
```

```
    THICK = THICK + DELTA                                   'add step to total path length
    '
50
    ' is the particle in the collimator?
    '
    MAT = 1!                                                'initialise mat
    '
    IF x >= 5000 END                                        ' end of collimator reached
       PRINT #1, XS, ys, TS, x, y, msangle, T       ' write particle parameters to file
       yend = y + ((5500 - x) * TAN(msangle))' extrapolate to 500 um from surface
       NTRANS = NTRANS + 1      'NTRANS monitors no. of transmitted particles
       LINE (x, y)-(5500, yend), 4                          ' draw extrapolation on the screen
       y = yend
       x = 5500
       GOTO 20
    END IF
    '
    ' if it hasn't reached the end where is it?
    '
    IF x >= X2 AND x < 5000 THEN  ' if still in the collimator by its x co-ordinate
      Y1U = MU * x + CU       ' work out the y co-ordinates of the collimator walls
      Y1L = -Y1U
         IF y > Y1L AND y < Y1U THEN                        ' if its in the void
           MAT = 0!
           GOTO 40
         END IF
    '
    ELSE
      MAT = 0!                                              ' not in collimator so set mat=0
      GOTO 40
    END IF
    '
    IF T > 0! THEN                                  ' check that energy has not gone negative
      GOTO 10
    END IF
    '
20                                                          '  finished
    '
    AVRANGE = AVRANGE + THICK                               ' total range of all particles
    '
    LOCATE 2, 50
    PRINT NTRANS; "/"; IP; " / "; N      ' keep track of where simulation has got to
    '
    IF NTRANS >= N THEN                                     ' we've got enough particles so end
      GOTO 60
    END IF
    '
    NEXT IP
'
60
```

```
'
DONE = FNCOLL                                          ' redraw collimator
AVRANGE = AVRANGE / N                                  ' mean particle range
LOCATE 1, 2
PRINT "WINDOW (0,-10) (5500,10) DIMENSIONS IN MICRONS, 4MEV P.
SILICON"'
LOCATE 2, 2
PRINT N; " TRACKS IN TOTAL, "; NTRANS; " TRANSMITTED,"
'PRINT "AV. RANGE IN COLLI = "; AVRANGE          ' interesting but not used
LOCATE 2, 40
INPUT "FINISHED"; A$          ' hold picture on screen for screen dump if needed
CLOSE #1
END
```

Appendix II : Summary of Collimator Simulations Programme

KJH2.BAS was developed to model the performance of drawn capillary collimators. The programme simulates a single straight sided Silicon collimator of fixed geometry with an entrance hole of 30 μm, an exit hole of 5 μm and a length of 4000 μm. The incident beam is a proton beam with the energy and incident proton number given as inputs. The spatial distribution is defined as 40 μm and the divergence as 0.067 degrees FWHM. The particle tracks through the material in steps of 0.5 μm with an approximation to energy loss and multiple scattering at each step. The particle is extrapolated to the collimator surface both initially and every time it leaves the material. Transmitted particle parameters are saved to file at 500 μm from the exit surface of the collimator.

KJH3.BAS was developed to include variable dimensions of single straight sided collimators. The program simulates a single straight sided Silicon collimator with entrance and exit parameters given as inputs. The incident beam is a proton beam with energy, spatial distribution and incident proton number given as inputs. Most parameters are as user defined inputs with start X, Y, and angle defined within the code. The particle traverses the material in steps of 0.5 μm with an approximation to energy loss and multiple scattering at each step. The particle is extrapolated to the collimator surface both initially and every time it leaves the material. Transmitted particle parameters are saved to file at 500 μm from the exit surface of the collimator.

KJH4.BAS was written as a demonstration program. It is a pictorial simulation of the irradiation of either nucleus or cytoplasm by a single collimator.

KJH5.BAS was developed from KJH3.BAS to include the effect of beam misalignment. The program simulates a single straight sided Silicon

collimator with entrance and exit parameters given as inputs. The incident beam is a proton beam with energy, spatial distribution, beam misalignment and incident proton number given as inputs. Most parameters are as user defined inputs with the start X, Y, and angle defined within the code. The particle tracks through the material in steps of 0.5 with an approximation to energy loss and multiple scattering at each step. The particle is extrapolated to the collimator surface both initially and every time it leaves the material. Transmitted particle parameters are saved to file at 500 μ m exit surface of the collimator.

KJH6.BAS was developed to investigate the effect of voids in collimators. The programme simulates a two collimator assembly in Silicon with the entrance, exit and length of each collimator given as inputs. The incident beam is a proton beam with energy, spatial distribution and incident proton number are given as inputs. The beam divergence is defined as 0.067 degrees FWHM. Most parameters are user defined inputs with start X, Y, and angle defined within the code. The particle tracks through the material in steps of 0.5 μm with an approximation to energy loss and multiple scattering at each step. The particle is extrapolated to the collimator surface both initially and every time it leaves the material. Transmitted particle parameters are saved to file at 500 μm from the exit surface of the collimator.

KJH7.BAS was developed as an all purpose programme for the simulation of single straight sided collimators in Silicon. All collimator and proton beam parameters are given by user defined inputs. The programme simulates a single Silicon collimator with entrance, exit and length parameters given as inputs. The incident beam is a proton beam with energy, spatial distribution, alignment, angular resolution and number of transmitted protons given as user defined inputs. The particle tracks through the material in steps of 0.5 μm with an approximation to energy loss and multiple scattering at each step. The particle is extrapolated to the collimator surface both initially and every time it leaves the material.

Transmitted particle parameters are saved to file at the exit surface of the collimator. The programme ends when a defined number of particles have been transmitted.

KJH8.BAS was developed to investigate the performance of multiple collimator assemblies. The program simulates a three collimator assembly in Silicon with entrance, exit and length parameters of each collimator given as inputs. The incident beam is a proton beam with energy, spatial distribution and incident proton number given as inputs. The divergence is defined within the code as 0.067 degrees FWHM. Most parameters are as user defined inputs with the start X, Y, and angle defined within the code. The particle tracks through the material in steps of 0.5 μm with an approximation to energy loss and multiple scattering at each step. The particle is extrapolated to the collimator surface both initially and every time it leaves the material. Transmitted particle parameters are saved to file at 500 μm from the exit surface of the collimator.

KJH9.BAS was developed to investigate the performance achieved by aligning two 500 μm straight sided collimators each side of a 1 Tesla magnetic field as an alternative to a curved collimator within a magnetic field. The program simulates five collimators, with a field of 1 Tesla on the centre collimator and with the entrance, exit and length parameters of each collimator given as inputs. Collimators 1 and 5 are angled to conicide with the effect of the field for an unscattered proton. The incident beam is a proton beam with the energy, spatial distribution and incident proton number given as inputs. The divergence is defined within the code as 0.067 degrees FWHM. The particle is extrapolated to the collimator surface both initially and every time it leaves the material. Transmitted particle parameters are saved to file at 500 μm from the exit surface of the collimator.

KJH50.BAS was developed to investigate the performance of a curved collimator in a magnetic field. The programme simulates a single curved collimator in Silicon and within a uniform field of 1 Tesla. The collimator dimensions

are defined within the code as 1 μm wide and 5000 μm long. The incident beam is a 4 MeV proton beam with a spatial distribution and incident proton number given as user defined inputs. The incident beam divergence is defined within the code as 0.067 degrees FWHM. Transmitted particle parameters are saved to file at 500 μm from the exit surface of the collimator.

Appendix III : Calculation of the Fraction of Solid Angle Subtended by a Disc at a Point.

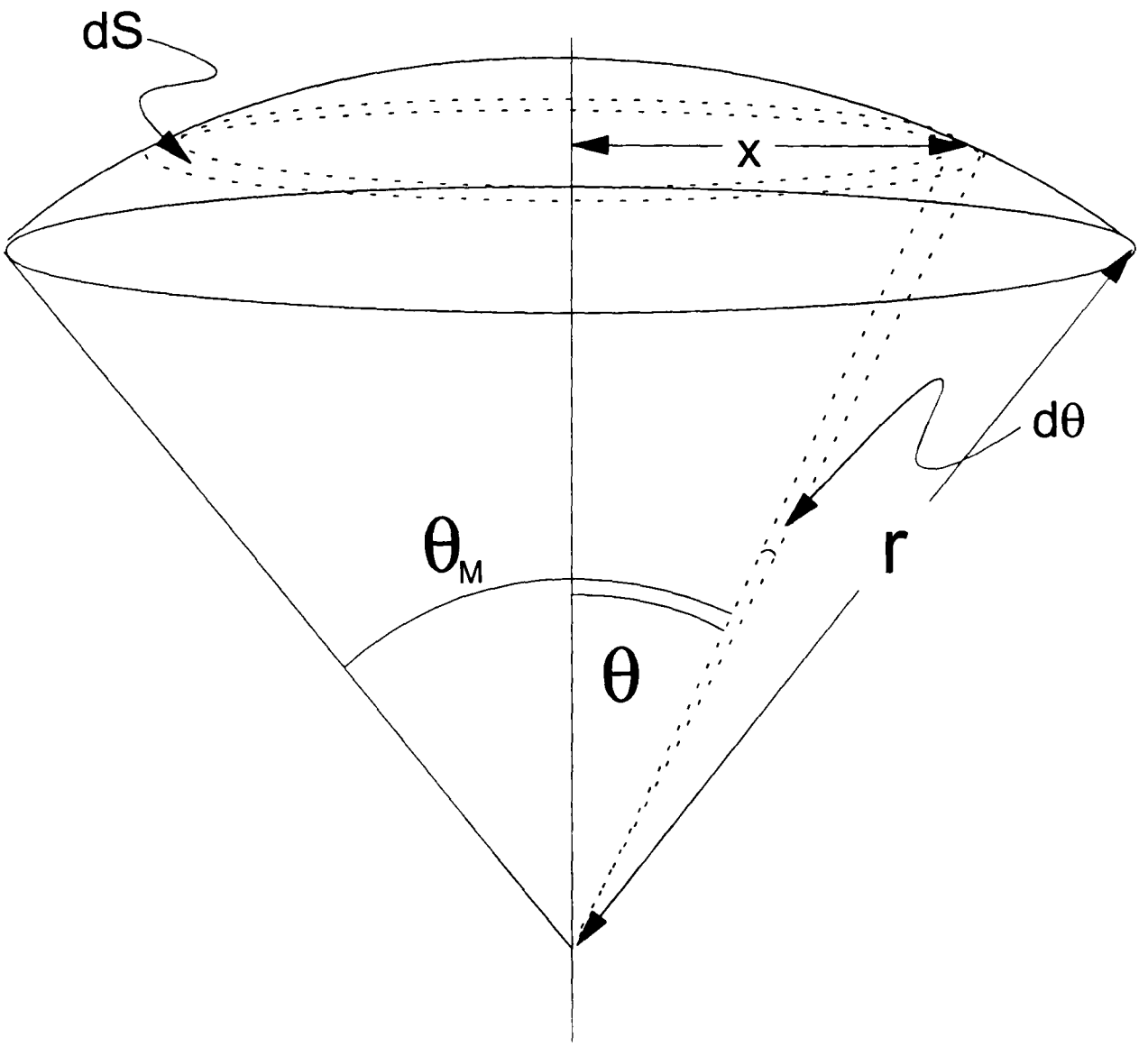

The area of the annulus dS is given by :-

$$dS = 2\pi x\, r d\theta$$

Since $\mathbf{x = \sin\theta}$:-

$$\rightarrow \quad dS = 2\pi r \sin\theta\, r d\theta$$

$$\rightarrow \quad dS = 2\pi r^2 \sin\theta\, d\theta$$

$$\rightarrow \quad S = 2\pi r^2 \int_0^{\theta_m} \sin\theta\, d\theta$$

$$\rightarrow \quad S = 2\pi r^2 \left[-\cos\theta \right]_0^{\theta_m}$$

The solid angle subtended at the center of the sphere is therefore :-

$$\frac{S}{r^2} = 2\pi \left[-\cos\theta \right]_0^{\theta_m}$$

The percentage of the total solid angle which this represents is therefore :-

$$\frac{1}{4\pi}\frac{S}{r^2} = \frac{2\pi}{4\pi}\left[-\cos\theta \right]_0^{\theta_m}$$

$$\rightarrow \quad \frac{S}{4\pi r^2} = -\frac{1}{2}\left[\cos\theta \right]_0^{\theta_m}$$

$$\textit{for } \theta_m = 39.3^o \rightarrow \frac{S}{4\pi r^2} = -\frac{1}{2}\left[0.774 - 1 \right] = 0.113 \equiv \underline{11.3\ \%}$$

$$\textit{for } \theta_m = 25.1^o \rightarrow \frac{S}{4\pi r^2} = -\frac{1}{2}\left[0.905 - 1 \right] = 0.0472 \equiv \underline{4.72\ \%}$$

Appendix IV : Programme to Simulate the Effect of ZnS Scatter on Beam Spatial Resolution

```
Program to combine the effects of a gaussian on a square function
'
CLS
INPUT "Input Square width"; SqrWidth
INPUT "Input Gaussian 90% of full width (diameter)"; GaussWidth
INPUT "Input Number of Numbers"; m
INPUT "Filename"; b$
'
OPEN b$ FOR OUTPUT AS #1
PRINT #1, "Gaussian Width = "; GaussWidth
PRINT #1, "Square   Width = "; SqrWidth
'
FOR n = 1 TO m
'
' Generate a random number from a square function
'
     Square = (RND - .5) * SqrWidth
'
' Generate a random number from a gaussian function
'
     Gauss = 0
     FOR J = 1 TO 12
          Gauss = Gauss + RND
     NEXT J
     Gauss = Gauss - 6
     Gauss = GaussWidth * Gauss / 3.2
'
' Add the two random numbers
'
     sum = Gauss + Square
'
' Save result to file
'
     PRINT #1, sum
'
' Keep track of the iterations
'
     LOCATE 2, 30
     PRINT ; n; "/"; m
NEXT n
CLOSE #1
END
```

Appendix V : Construction of a Ruggedised Collimator - Detector Assembly

The method of production of this detector assembly is given below.

1) Place the steel disc across the surface of two blocks of equal height.
2) Strip the plastic coating from the hplc tubing using a scalpel blade.
3) Feed an ~ 30 mm length of hplc tubing through the hole in the disc with at least 5 mm of tubing remaining above the surface of the disc.
4) Using a pin place a small quantity of vacuum cement around the hplc tubing to fix it to the lower, vacuum side of the disc.
5) Cleave the hplc tubing each side of the disc and as close to the two surfaces of the disc as possible.

6) Tape a piece of clean mylar plastic out into a flat sheet of ~ 40 mm square.
7) Using vacuum cement glue several laser drilled discs onto the surface of the mylar, using a small enough quantity of glue that the centre of the hole in the disc remains clear of glue.
8) Place the steel disc under a low power binocular microscope.
8) Cut the discs out from the plastic so that each disc has a firmly attached mylar sheet across the hole.
9) Using an absolute minimum of super-glue, fix the laser-drilled disc over the hplc collimator so that the short length of protruding hplc tubing stretches the mylar tight across its surface.
10) Test the collimator with window for the quality of collimation using the energy spectrum obtained after alignment with an incident proton beam.

11) Mount the end-cone on an ~ 30 mm high pole fixed to a firm base and hold the cone in position using its mounting screws.
12) Align the collimator in the centre of the objective lens and in focus.
13) Wet the tip of a drawn micro-capillary tube with optical cement and attach the

capillary to the micropositioning block.

14) Use the micro-capillary to place a very small amount of optical cement onto the mylar window above the collimator position. Do not cure the optical cement. Remove the assembly.

15) Dip a thin wire into ZnS(Ag) powder, attach the wire to a microscope slide and attach the microscope slide to the aluminium block.

16) Align the wire, which will have many ZnS(Ag) crystals attached, under the objective lens and in focus.

17) Using a second drawn micro-capillary tip, attached to a microscope slide on the micropositioning block, remove a single crystal of suitable geometry from the wire. The surface interaction will hold the crystal to the drawn micro-capillary.

18) Remove the aluminium block and the micropositioning block with micro-capillary and ZnS(Ag) crystal attached.

19) Place the end-cone under the microscope objective lens (UV off) and align with the centre of the field of view.

20) Lower the microscope stage and collimator by ~ 3 mm.

21) Replace the micropositioning block with the ZnS(Ag) crystal over the centre of the collimator.

22) Focus and align the crystal in the centre of the field of view.

23) Slowly lower the crystal and then raise the microscope stage until the crystal re-appears in focus. Repeat this process until both the collimator position and the crystal can be seen with only small adjustments of the microscope z-drive.

24) Align the crystal over the exit aperture of the collimator using the micropositioning block adjustment.

25) Carefully lower the crystal onto the wet mylar over the collimator aperture. The glue will act to pull the crystal from the micro-capillary.

26) Use the micro-capillary to position the crystal exactly over the collimator hole, rotation of the end-cone may be needed to give movement in all directions.

27) When the crystal is in position remove the micro-capillary and cure the optical cement for ~ 10 minutes.

28) Remove the end-cone.

29) Cut an ~ 0.3 m length of 30 μm optical fibre.

30) Cleave one end of the fibre using a single blade fibre cleaver. Optimum cleaves were obtained by laying the fibre across the pad of a finger and gently drawing the blade across the fibre, perpendicular to its length.

31) Check the quality of the cleave under the objective. The fibre will appear black if a good cleave has been obtained and will light brightly if the uncleaved end is placed near to a light source.

32) Mount the fibre onto the microposiitoning block by lying the fibre along an attached microscope slide and lying a second microscope slide across the first. Ensure that the fibre lies clear of the mechanisms of the microscope and micropositioning block. Align the fibre with the centre of the microscope field of view.

33) Attach an ~ 30 mm length of fibre to the aluminium block, wet the fibre with optical cement and align under the objective lens.

34) Using this short fibre length place a small quantity of optical cement onto the cleaved fibre.

35) Remove the short length of fibre and move the cleaved fibre to the side. Position the collimator and crystal under the objective lens ensuring that the fibre guides are parallel with the fibre direction. Focus on the centre of the collimator.

36) Lower the microscope stage.

37) Align the cleaved fibre over the collimator.

38) Slowly lower the fibre down to the surface of the collimator at a distance a little away from the collimator aperture by focusing between the fibre and the collimator.

39) Using the fine adjustments of the micropositioning block abut the fibre onto the crystal.

40) When sufficient glue has flowed between the fibre, the crystal and the mylar window open the shutter to the ultraviolet light and cure the optical cement for ~ 10 mins.

41) Lower the optic fibre onto the surface of the disc. Run a limited amount of UV curing cement between the fibre and the metal surface an cure.

42) Remove the half made assembly from the microscope stage.

43) Lie the uncleaved fibre end through in the fibre guide.

44) Feed the uncleaved end of the fibre through the PVC sleeving and through the ST connector and attach the black sleeving to the ST connector.

45) Fix the optic fibre into the fibre guide using silicon rubber mixed with plack paint. Ensure that the entrance to the PVC tubing is also filled by the blackened silicon rubber to prevent light entering the photomultiplier tube by this route.

46) Apply a blob of optical polymer to the fibre near to the connector and cure using the UV from the objective lens.

47) Cut the uncleaved fibre near to the blob.

48) Polish the fibre using a high speed carborundum polishing wheel (Narishige Ltd.) and cover the end with an ST connector cap for protection.

49) Repeat steps 17 to 39 for the second fibre.

References:

Aghamohammadi, S. Z., Goodhead, D. T., & Savage, J. R. K. (1988) Induction of sister chromatid exchanges (SCE) in G_0 lymphoctyes by plutonium-238 α-particles
Int. J. Radiat. Biol., **53**, 909-915.

Aguilar-Benitez, M., *et al.* (Particle Physics Group). (1992) Review of particle properties
Physical Review, **D45**.

Alper, T. (1968) Low oxygen enhancement ratios for radiosensitive bacterial strains, and two types of primary lesion
Nature, **217**, 862-863.

Alper, T. (1974) The role of membrane damage in irradiated cells
Proceedings of the British Institute of Radiology, **47**, 240.

Alper, T. (1987) The cell as single-hit detector
British Journal of Cancer, **55**, 32-38.

Belli, M. (1993) Some applications of microbeam probes in basic radiation biology and biophysics, In B. D. Michael, M. Folkard, & K. M. Prise (Ed.), *Microbeam Probes of Cellular Radiation Response*, (pp. 9.1.1-9.1.3). C.R.C. Gray Laboratory, London, UK.

Berns, M. W. (1971) A simple versatile argon laser microbeam
Experimental Cell Research, **65**, 470-473.

Berns, M. W. (1974). *Biological Microirradiation : Classical and Laser Sources* (1st ed.). New Jersey: Prentice-Hall.

Berns, M. W., & Cheng, W. K. (1971) Are chromosome secondary constrictions nucleolar organizers? *A re-examination using a laser microbeam*
Experimental Cell Research, **1971**, 185-192.

Berns, M. W., Cheng, W. K., Floyd, A. D., & Ohnuki, Y. (1971) Chromosome lesions produced with an argon laser microbeam without dye sensitization
Science, **171**, 903-905.

Berns, M. W., Olson, R. S., & Rounds, D. E. (1969) *In vitro* production of chromosomal lesions with an argon laser microbeam
Nature, **221**, 74-75.

Berns, M. W., Wright, W. H., & Steubing, R. W. (1991) Laser microbeam as a tool in cell biology
International Review of Cytology, **129**, 1-44.

Bettega, D., Calzolari, P., Chiorda, G. N., & Tallone-Lombardi, L. (1992) Transformation of C3H $10T^{1}/_{2}$ cells with 4.3 MeV α particles at low doses : Effects of single and fractionated doses
Radiation Research, **131**, 66-71.

Bloom, W. (1959) Cellular responses
Reviews of Modern Physics, **31**, 21-29.

Bloom, W. (1960a) Changes in the fine structure of parts of chromosomes after localized ultraviolet irradiation
Annals of the New York Academy of Sciences, **90**, 353-356.

Bloom, W. (1960b) Submicroscopic changes in "paling" of irradiated chromosomes (Abstract)
Science, **131**, 1316.

Bloom, W., & Leider, R. J. (1962) Optical and electron microscopc changes in ultraviolet-irradiated chromosomes segments
Journal of Cell Biology, **13**, 269-301.

Bond, V. P., Varma, M. N., Sondhaus, C. A., & Feinendegen, L. E. (1985) An alternative to absorbed dose, quality, and RBE at low exposures
Radiation Research, **104 Supplement**, S52-S57.

Braby, L. A. (1993) A microbeam system for targeted single particle irradiation of cells, In B. D. Michael, M. Folkard, & K. M. Prise (Ed.), *Microbeam Probes of Cellular Radiation Response*, (pp. 4.1.1-4.1.2). C.R.C. Gray Laboratory, London, UK.

Braby, L. A., & Ellett, W. H. (1972) Ionization in solid- and grid-walled detectors
Radiation Research, **51**, 569-580.

Brenner, D. J. (1993) Unfolding the Poisson distribution: Can mathematical tricks do as well as a single-particle microbeam?, In B. D. Michael, M. Folkard, & K. M. Prise (Ed.), *Microbeam Probes of Cellular Radiation Response*, (pp. 1.3.1-1.3.4). C.R.C. Gray Laboratory, London, UK.

Brenner, D. J., Miller, R. C., Huang, Y., & Hall, E. J. (1995) The biological effectiveness of radon-progeny alpha particles. *III Quality factors*
Radiation Research, **142**, 61-69.

Brenner, D. J., & Ward, J. F. (1992) Constraints on energy deposition and target size of multiply damaged sites associated with DNA double-strand breaks
Int. J. Radiat. Biol., **61**, 737-748.

Bridges, B. A., Cole, J., Arlett, C. F., Green, M. H. L., Waugh, A. P. W., Beare, D., Henshaw, D. L., & Last, R. D. (1991) Possible association between mutant frequency in peripheral lymphocytes and domestic radon concentrations
The Lancet, **337**, 1187-1189.

Brooks, A. L., Nelson, J. M., Khan, M. A., Duncan, A., & Braby, L. A. (1994) The induction of micronuclei by the exposure of CHO cells to alpha particles from the single particle irradiator, In L. A. Braby (Ed.), *Particle Microbeam Workshop*, (pp. 18). Pacific Northwest Laboratory,
Richland, Washington, USA.

Brown, D. Q., & Zirkle, R. E. (1967) Action spectra for mitotic spindle destruction and anaphase delay following irradiation of the cytoplasm with an ultraviolet microbeam
Photochemistry and Photobiology, **6**, 817-828.

Charlton , D. E. (1986) The range of high LET effects from ^{125}I decays
Radiation Research, **107**, 163-171.

Chatterjee, A., Maccabee, H. D., & Tobias, C. A. (1973) Radial cutoff LET and radial cutoff dose calculations for heavy charged particles in water
Radiation Research, **54**, 479-494.

Chatterjee, A., & Schaefer, H. J. (1976) Microdosimetric structure of heavy ion tracks in tissue
Radiation and Environmental Biophysics, **13**, 215-227.

Chmelevsky, D., & Kellerer, A. M. (1982) Maximum likelihood estimation of the prevalence of nonlethal neoplasms - An application to radon-daughter inhalation studies
Radiation Research, **91**, 589-614.

Colautti, P., Talpo, G., & Tornielli, G. (1993) Proposal for a single-particle-single-cell in flight impact experiment, In B. D. Michael, M. Folkard, & K. M. Prise (Ed.), *Microbeam Probes of Cellular Radiation Response*, (pp. 5.3.1). C.R.C. Gray Laboratory, London, UK.

Cole, A. (1969) Absorption of 20-eV to 50,000-eV electron beams in air and plastic
Radiation Research, **38**, 7-33.

Cole, A., Cooper, W. G., Shonka, F., Corry, P. M., Humphrey, R. M., & Ansevin, A. T. (1974) DNA scission in hamster cells and isolated nuclei studied by low-voltage electron beam irradiation
Radiation Research, **60**, 1-33.

Cole, A., Humphrey, R. M., & Dewey, W. C. (1963) Low-voltage electron beam irradiation of normal and 5-bromouridine deoxyriboside-treated L-P_{59} mouse fibroblast cells *in vitro*
Nature, **199**, 780-782.

Corcoran, G. B., & Ray, S. D. (1992) The role of the nucleus and other compartments in toxic cell death produced by alkylating hepatotoxicants
Toxicology and Applied Pharmacology, **113**, 167-183.

Cornforth, M. N., Schillaci, M. E., Goodhead, D. T., Carpenter, S. G., Wilder, M. E., Sebring, R. J., & Raju, M. R. (1989) Radiobiology of ultrasoft X rays. III. Normal human fibroblasts and the significance of terminal track structure in cell inactivation *Radiat Res*, **119**, 511-22.

Datta, R., Cole, A., & Robinson, S. (1976) Use of track-end alpha particles from ^{241}Am to study radiosensitive sites in CHO cells
Radiation Research, **65**, 139-151.

Davis, M., & Smith, C. L. (1957) The irradiation of individual parts of single cells in tissue culture with a microbeam of α-Paricles *I. Apparatus*
Experimental Cell Research, **12**, 15-34.

Dean, R. T. (1987) Free radicals, membrane damage and cell-mediated cytolysis
British Journal of Cancer, **55**, 39-45.

Eastman, A., & Barry, M. A. (1992) The origins of DNA breaks: A consequence of DNA damage, DNA repair, or apoptosis?
Cancer Investigation, **10**, 229-240.

Errera, M., & Vanderhaeghe, F. (1957) Effets des rayons U.V. sur *Acetabularia Mediterranea*
Experimental Cell Research, **13**, 1-10.

Facius, R., Bucker, H., Hildebrand, D., Horneck, G., Holtz, G., Reitz, G., Schafer, M., & Toth, B. (1978) Radiological results from the *Bacillus Subtilis* biostack experiments within the Apollo and the ASTP space flights
Life Sciences and Space Research, **XVI**, 151-156.

Facius, R., Schafer, M., Baltschukat, K., & Bucker, H. (1983) Inactivation probability of heavy ion-irradiation *Bacillus Subtilis* spores as a function of the radial distance to the particle's trajectory
Advances in Space Research, **3**, 85-94.

Fain, J., Monnin, M., & Montret, M. (1974) Spatial energy distribution around heavy-ion path
Radiation Research, **57**, 379-389.

Fernow, R. (1986). *Introduction to Experimental Particle Physics.*
Cambridge University Press.

Folkard, M., Prise, K. M., Vojnovic, B., Hollis, K. J., & Michael, B. D. (1993) Development of the Gray Laboratory charged particle microbeam, In B. D. Michael, M. Folkard, & K. M. Prise (Ed.), *Microbeam Probes of Cellular Radiation Response*, (pp. 4.2.1-4.2.4). C.R.C. Gray Laboratory, London, UK.

Gilmore, G. (1992). *Single particle detection and measurement* (1st ed.). London: Taylor & Francis Ltd.

Glass, W. A., & Braby, L. A. (1969) A wall-less detector for measuring energy deposition spectra
Radiation Research, **39**, 230-240.

Gohla, H. (1995) Final year project 1994/1995
Brunel University of West London, Detector Physics Group, Internal Publication.

Goodhead, D. T. (1989) The initial physical damage produced by ionizing radiations
Int. J. Radiat. Biol., **56**, 623-634.

Goodhead, D. T., & Nikjoo, H. (1989) Track structure analysis of ultrasoft X-rays compared to high- and low-LET radiations
Int. J. Radiat. Biol., **55**, 513-529.

Gray, L. H. (1956). Primary sites of energy deposition associated with radiobiological lesions. In G. E. W. Wolstenholme & C. M. O'Conner (Eds.), CIBA Foundation Synposium on Ionizing Radiation and Cell Metabolism (pp. 255-274). London: J. & A. Churchill Ltd.

Hatfield, J. M. R., Dendy, P. P., Meyskens, F., & Rickinson, A. B. (1973) Importance of the nucleolus in the initiation of DNA synthesis in mammalian cells. *Studies with an ultraviolet microbeam and low concentrations of actinomycin D*
Experimental Cell Research, **78**, 214-224.

Haynes, R. H., & Zirkle, R. E. (1960) An alpha particle microbeam for partial cell irradiation (Abstract)
Radiation Research, **12**, 442.

Hickman, A. W., Jaramillo, R. J., Lechner, J. F., & Johnson, N. F. (1994) α-Particle-induced p53 protein expression in a rat lung epithelial cell strain
Cancer Research, **54**, 5797-5800.

Hofer, K. G., Harris, C. R., & Smith, J. M. (1975) Radiotoxicity of intracellular *67*Ga, *125*I and *3*H nuclear versus cytoplasmic radiation effects in murine L1210 leukemia
Int. J. Radiat. Biol., **28**, 225-241.

Hofer, K. G., van Loon, N., Schneiderman, M. H., & Charlton, D. E. (1992) The paradoxical nature of DNA damage and cell death induced by ^{125}I decay
Radiation Research, **130**, 121-124.

Hofmann, W., Katz, R., & Chunxiang, Z. (1986) Lung cancer risk at low doses of α particles
Health Physics, **51**, 457-468.

Jacobi, W., & Paretzke, H. G. (1985) Risk assessment for indoor exposure to radon daughters
The Science of the Total Environment, **45**, 551-562.

Jagger, J., Prescott, D. M., & Gaulden, M. E. (1969) An ultraviolet microbeam study of the roles of nucleus and cytoplasm in division delay, killing, and photoreactivation of *amoeba proteus*
Experimental Cell Research, **58**, 35-54.

James, S. J., Enger, S. M., & Makinodan, T. (1991) DNA strand breaks and DNA repair response in lymphocytes after chronic *in vivo* exposure to very low doses of ionizing radiation in mice
Mutation Research, **249**, 255-263.

Kadhim, M. A., Macdonald, D. A., Goodhead, D. T., Lorimore, S. A., Marsden, S. J., & Wright, E. G. (1992) Transmission of chromosomal instability after plutonium α-particle irradiation
Nature, **355**, 738-740.

Kanai, T., & Kawachi, K. (1987) Radial dose distribution for 18.3 Mev/n α particle beams in tissue-equivalent gas
Radiation Research, **112**, 426-435.

Kirkpatrick, P., & Pattee, H. H. J. (1953) Approaches to X-ray microscopy
Advances in Biological and Medical Physics, **3**, 247-282.

Kitzes, M., Twiggs, G., & Berns, M. W. (1977) Alteration of membrane electrical activity in rat myocardial cells following selective laser microbeam irradiation
Journal of Cellular Physiology, **93**, 99-104.

Kobayashi, K., & Iida, A. (1993) Current status of X-ray microbeam technology development at the Photon Factory in relation to radiobiology, In B. D. Michael, M. Folkard, & K. M. Prise (Ed.), *Microbeam Probes of Cellular Radiation Response*, (pp. 6.2.1-6.2.4). C.R.C. Gray Laboratory, London, UK.

Kozubek, S., & Krasavin, E. A. (1984) Cell sensitivity to irradiation and DNA repair processes. *II The cell sensitivity to ionizing radiation of different LETs*
Neoplasma, **31**, 685-695.

Kraft, G., Kramer, M., & Scholtz, M. (1992) LET, track structure and models : *A review*
Radiation and Environmental Biophysics, **31**, 161-180.

Kraske, F., Ritter, S., Scholz, M., Schneider, M., Kraft, G., Weisbrod, U., & Kankleit, E. (1990) Directed irradiation of mammalian cells by single charged particles with a given impact parameter
Radiation Protection Dosimetry, **31**, 315-318.

Kuzin, A. M., & Wainson, A. A. (1966) Effect of α-particle microbeam irradiation on the synthesis of deoxyribonucleic acid in tissue culture
Nature, **212**, 819-820.

Lambin, P., Marples, B., Fertil, B., Malaise, E. P., & Joiner, M. C. (1993) Hypersensitivity of a human tumour cell line to very low radiation doses
Int. J. Radiat. Biol., **63**, 639-650.

Leuthold, G., & Burger, G. (1988) Mathematical simulation of proton tracks in water vapor and their microdosimetric analysis
Radiation and Environmental Biophysics, **27**, 177-187.

Lin, T. P., & Chan, J. Y. (1984) Effects of laser microbeam irradiation of the nucleus on the cleavage of mouse eggs in culture
Radiation Research, **98**, 549-560.

Mackie, T. R., Gould, M., MacKay, J., Pearson, D., Fowler, J., Kennan, W., Deasy, J. O., Shulman, P., Hill, C., Nelms, B., & DeLuca, P. J. (1993) A sychrotron-produced ultrasoft X-ray microbeam, In B. D. Michael, M. Folkard, & K. M. Prise (Ed.), *Microbeam Probes of Cellular Radiation Response*, (pp. 2.2.1-2.2.4). C.R.C. Gray Laboratory, London, UK.

Marin, G., & Bender, M. A. (1963) A comparison of mammalian cell-killing by incorporated ^{3}H-thymidine and ^{3}H-uridine
Int. J. Radiat. Biol., **7**, 235-244.

Marples, B., & Joiner, M. C. (1993) The response of chinese hamster V79 cells to low radiation doses: Evidence of enhanced sensitivity of the whole cell population
Radiation Research, **133**, 41-51.

Martin, S. G., Miller, R. C., Geard, C. R., & Hall, E. J. (1995) The biological effectiveness of radon-progeny alpha particles. *IV. Morphological transformation of syrian hamster embryo cells at low doses*
Radiation Research, **142**, 70-77.

Metting, N. F. (1994) Specific transcription and protein localization of cell-cycle regulators after α-particle irradiation, In L. A. Braby (Ed.), *Particle Microbeam Workshop*, (pp. 09). Pacific Northwest Laboratory,
Richland, Washington, USA.

Michael, B. D., Folkard, M., Prise, K. M., Hollis, K. J., & Vojnovic, B. (1994) Development and applications at the Gray Laboratory of microbeam irradiation of individual cells, In L. A. Braby (Ed.), *Particle Microbeam Workshop*, (pp. 02). Pacific Northwest Laboratory,
Richland, Washington, USA.

Michette, A. G., Foster, G. F., & Folkard, M. (1993) Focuses X-ray probes, In B. D. Michael, M. Folkard, & K. M. Prise (Ed.), *Microbeam Probes of Cellular Radiation Response*, (pp. 6.1.1-6.1.4). C.R.C. Gray Laboratory, London, UK.

Miller, R. C., Marino, S. A., Brenner, D. J., Martin, S. G., Richards, M., Randers-Pehrson, G., & Hall, E. J. (1995) The biological effectiveness of radon-progeny alpha particles. *II Oncogenic transformation as a function of linear energy transfer*
Radiation Research, **142**, 54-60.

Montgomery, P. O., & Hundley, L. L. (1961) Ultraviolet microbeam irradiation of the nucleoli of living cells
Experimental Cell Research, **24**, 1-5.

Moreno, G., & Salet, C. (1985) Cytotoxic effects following micro-irradiation of cultured cells sensitized with haematoporphyrin derivative
Int. J. Radiat. Biol., **47**, 383-386.

Munro, T. R. (1958a) Alpha irradiation of parts of single cells in tissue cultures *I. Techniques*
Experimental Cell Research, **15**, 529-536.

Munro, T. R. (1958b) Alpha irradiation of parts of single cells in tissue cultures *II. Dosimetry*
Experimental Cell Research, **15**, 537-550.

Munro, T. R. (1959) Alpha irradiation of parts of single cells in tissue culture *III. Irradiation of chick fibroblasts during metaphase and anaphase*
Experimental Cell Research, **18**, 76-99.

Munro, T. R. (1961) Irradiation of selected parts of single cells
Annals of the New York Academy of Sciences, **95**, 920-932.

Munro, T. R. (1970) The site of the target region for radiation-induced mitotic delay in cultured mammalian cells
Radiation Research, **44**, 748-757.

Nagasawa, H., & Little, J. B. (1992) Induction of sister chromatid exchanges by extremely low doses of α-particles
Cancer Research, **52**, 6394-6396.

Nagasawa, H., Little, J. B., Inkret, W. C., Carpenter, S., Raju, M. R., Chen, D. J., & Strniste, G. F. (1991) Response of X-ray-sensitive CHO mutant cells (xrs-6c) to radiation *II Relationship between cell survival and the induction of chromosomal damage with low doses of α particles*
Radiation Research, **126**, 260-288.

Nagasawa, H., Little, J. B., Inkret, W. C., Carpenter, S., Thompson, K., Raju, M. R., Chen, D. J., & Strniste, G. F. (1990a) Cytogenetic effects of extremely low doses of plutonium-238 alpha-particle irradiation in CHO K-1 cells
Mutation Research, **244**, 233-238.

Nagasawa, H., Robertson, J., & Little, J. B. (1990b) Induction of chromosomal aberrations and sister chromatid exchanges by alpha particles in density-inhibited cultures of mouse $10T^{1}/_{2}$ and 3T3 cells
Int. J. Radiat. Biol., **57**, 35-44.

Naruse, S., Yatani, R., & Takeda, S. (1967) Morphological changes following ultraviolet microbeam irradiation of parts of nuclei of living cells
Radiation Research, 32, 849 - 860

Nicotera, P., McConkey, D. J., Dypbukt, J. M., Jones, D. P., & Orrenius, S. (1989) Ca^{2+}-activated mechanisms in cell killing
Drug Metabolism Reviews, **20**, 193-201.

Nikjoo, H., Goodhead, D. T., Charlton, D. E., & Paretzke, H. G. (1991) Energy deposition in small cylindrical targets by monoenergetic electrons
Int. J. Radiat. Biol., **60**, 739-756.

Ohnuki, Y., Rounds, D. E., Olson, R. S., & Berns, M. W. (1972) laser microbeam irradiation of the juxtanucleolar region of prophase nucleolar chromosomes
Experimental Cell Research, **71**, 132-144.

Orton, C. G. (1986). *Radiation Dosimetry : Physical and Biological Aspects*. New York: Plenum Press.

Paretzke, H. G., Turner, J. E., Hamm, R. N., Ritchie, R. H., & Wright, H. A. (1991) Spatial distributions of inelastic events produced by electrons in gaseous and liquid water
Radiation Research, **127**, 121-129.

Perry, R. P. (1957) Changes in the ultraviolet absorption spectrum of parts of living cells following irradiation with an ultraviolet microbeam
Experimental Cell Research, **12**, 546-559.

Perry, R. P. (1960) On the nucleolar and nuclear dependence of cytoplasmic RNA synthesis in HeLa cells
Experimental Cell Research, **20**, 216-220.

Peto, J., & Darby, S. (1994) Radon risk reassessed
Nature, **368**, 97-98.

Raju, M. R., Eisen, Y., Carpenter, S., Jarrett, K., & Harvey, W. F. (1993) Radiobiology of alpha particles: *IV. Cell inactivation by alpha-particles of energies 0.4-3.5 MeV*
Radiation Research, **133**, 289-296.

Ramakrishnan, N., McClain, D. E., & Catravas, G. N. (1993) Membranes as sensitive targets in thymocyte apoptosis
Int. J. Radiat. Biol., **63**, 693-701.

Randers-Pehrson, G. (1994) Columbia alpha particle microbeam, In L. A. Braby (Ed.), *Particle Microbeam Workshop*, . Pacific Northwest Laboratory, Richland, Washington, USA.

Randers-Pehrson, G., Geard, C., Marino, S., & Johnson, G. (1993) Development of the RARAF microbeam, In B. D. Michael, M. Folkard, & K. M. Prise (Ed.), *Microbeam Probes of Cellular Radiation Response*, (pp. 4.3.1). C.R.C. Gray Laboratory, London, UK.

Rink, H. (1975) Radiation damage to membrane-bound sulphydryl groups and permeability to yeast cells
Int. J. Radiat. Biol., **27**, 305-310.

Rogers, R. W., & von Borstel, R. C. (1957) Alpha-particle bombardement of the *Habrobracon* egg I. Sensitivity of the nucleus
Radiation Research, **7**, 484-490.

Seed, J. (1960) Inhibition of nucleic acid synthesis caused by X-irradiation of the nucleolus
Proceedings of the Royal Society, **B152**, 387-396.

Shimomura, T., Naruse, S., & Takeda, S. (1967) Stomatogenesis and cell division in *Euplotes* inhibited by ultra-violet microbeam irradiation
Nature, **215**, 91-92.

Singh, B., Arrand, J. E., & Joiner, M. C. (1994) Hypersensitive response of normal human lung epithelial cells at low radiation doses
Int. J. Radiat. Biol., **65**, 457-464.

Smith, C. L. (1964) Microbeam and partial cell irradiations
International Review of Cytology, **16**, 133-153.

Szekely, J. G., Copps, T. P., & Morash, B. D. (1980) Radiation-induced invagination of the nuclear envelope
Radiation Research, **83**, 621-632.

Tait, W. H. (1980). *Radiation Detection* (1st ed.).
London: Butterworth & Co.

Thacker, J., Stretch, A., & Goodhead, D. T. (1982) The mutagenicity of α particles from plutonium-238
Radiation Research, **92**, 343-352.

Tobleman, W. T., & Cole, A. (1974) Repair of sublethal damage and oxygen enhancement ratio for low-voltage electron beam irradiation
Radiation Research, **60**, 355-360.

Trump, B. F., & Berezesky, I. K. (1992) The role of cytosolic Ca^{2+} in cell injury, necrosis and apoptosis
Current Opinion in Cell Biology, **4**, 227-232.

Uretz, R. B., Bloom, W., & Zirkle, R. E. (1954) Irradiation of individual cells *II. Effects of an ultraviolet microbeam focused on parts of chromosomes*
Science, **120**, 197-199.

Uretz, R. B., & Perry, P. B. (1957) Improved ultraviolet microbeam apparatus
The Review of Scientific Instruments, **28**, 861-866.

Vojnovic, B., Locke, R. J., & Gilbey, J. (1993) Micro-imaging and cell recognition, In B. D. Michael, M. Folkard, & K. M. Prise (Ed.), *Microbeam Probes of Cellular Radiation Response*, (pp. 7.4.1-7.4.4). C.R.C. Gray Laboratory, London, UK.

von Borstel, R. C., & Rogers, R. W. (1958) Alpha-particle bombardement of the *Habrobracon* egg I. Response of the cytoplasm
Radiation Research, **8**, 248-253.

Warters, R. L., & Hofer, K. G. (1977) Radionuclide toxicity in cultured mammalian cells, elucidation of the primary sites for radiation-induced division delay
Radiation Research, **69**, 348-358.

Warters, R. L., Hofer, K. G., Harris, C. R., & Smith, J. M. (1977) Radionuclide toxicity in cultured mammalian Cells: Elucidation of the primary site of radiation damage
Current Topics in Radiation Research Quarterly, **12**, 389-407.

Watanabe, H., Kobayashi, Y., Kamiya, T., & Arakawa, K. (1993) Apparatus for microbeam irradiation of cell in TIARA, In B. D. Michael, M. Folkard, & K. M. Prise (Ed.), *Microbeam Probes of Cellular Radiation Response*, (pp. 4.4.1-4.4.4). C.R.C. Gray Laboratory, London, UK.

Weisbrod, U., Bucker, H., Horneck, G., & Kraft, G. (1992) Heavy-ion effects on bacterial spores: The impact parameter dependence of the inactivation
Radiation Research, **129**, 250-257.

Wheeler, K. T., Hickman, R., Nelson, G. B., Moore, S. K., & Wallen, C. A. (1992) Relationship between DNA damage, DNA repair, metabolic state and cell lethality
Radiation and Environmental Biophysics, **31**, 101-115.

Williamson, J. F. (1987) Monte Carlo evaluation of kerma at a point for photon transport problems
Medical Physics, **14**, 567-576.

Wilson, W. E., & Paretzke, H. G. (1980) Calculation of ionization frequency distributions in small sites
Radiation Research, **81**, 326-335.

Zaider, M., Brenner, D. J., & Wilson, W. E. (1983) The application of track calculations to radiobiology. *I Monte Carlo simulation of proton tracks*
Radiation Research, **95**, 231-247.

Zermeno, A., & Cole, A. (1969) Radiosensitive structures of metaphase and interphase hamster cells as studied by low-voltage electron beam irradiation
Radiation Reasearch, **39**, 669-684.

Ziegler, J. F., & Biersack, J. P. (1985) *The Stopping and Ranges of Ions in Solids (TRIM).* New York: Pergamon Press.

Zirkle, R. E. (1932) Some effects of alpha radiation upon plant cells
Journal of Cellular Comp. Physiology, **2**, 251-274.

Zirkle, R. E. (1957)
Advances in Biological and Medical Physics, **5**, 104-106.

Zirkle, R. E. (1970) Ultraviolet-microbeam irradiation of newt-cell cytoplasm: Spindle destruction, false Anaphase, and delay of true anaphase
Radiation Research, **41**, 516-537.

Zirkle, R. E., & Bloom, W. (1953) Irradiation of parts of individual cells
Science, **117**, 487-493.

Zirkle, R. E., & Uretz, R. B. (1960) Energy relations in chromosomes paling by ultraviolet microbeams (Abstract)
Science, **131**, 1316.

Zirkle, R. E., Uretz, R. B., & Haynes, R. B. (1960) Disappearance of spindles and phragmoplasts after microbeam irradiation of cytoplasm
Annals of the New York Academy of Sciences, **90**, 435-439.

Declaration

This thesis has been composed by Kevin John Hollis and is a report of work performed by Kevin John Hollis.

It has not been accepted in any previous application for a degree.

All quotations have been distinguished by quotation marks and sources of information have been acknowledged.

Signed

K J Hollis

for the 38 keV.μm^{-1} proton data, it is probable that a small fraction of the protons are fully stopped within each cell. For this reason, it is difficult to estimate the volume average LET reliably when the highest LET protons are used. Also, it is evident that track segment conditions do not apply in this instance.

It can be seen that the RBE increases with increasing LET over the range studied, and that a single line adequately fits the trend for both protons and deuterons. This is expected because LET-matched protons and deuterons have the same charge and velocity and therefore, the same track structure. However, this result contrasts with a preliminary report by Cherubini *et al*[6] who find unexpectedly that below 31 keV.μm^{-1}, deuterons are less effective than protons with the same LET. When the data are compared to that for α particles, it is evident that above 20 keV.μm^{-1} singly charged particles become increasingly more effective than α particles of the same LET. This is in agreement with previous work by ourselves[2] and other workers[3-5]. This finding is currently being substantiated, firstly by exploiting the extra penetration that is available using deuterons to measure the RBEs at still higher LETs, and secondly by measuring the effectiveness of He^{3++} ions using the experimental arrangement described here so that the differences between singly and doubly charged particles can be more critically evaluated.

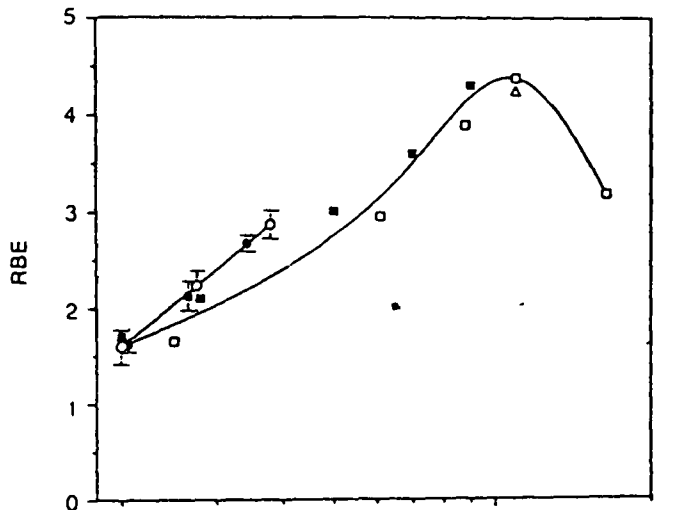

Figure 1. The RBE for cell survival at 10% surviving fraction for protons (open circles) and deuterons (closed circles). Also plotted are data for α particles from Barendsen[11] (open squares) and Thacker[10] (closed squares). Data obtained by us using 110 keV.μm^{-1} α particles are also shown (open triangles). The errors bars are ±1 standard error. The lines through the data are drawn by eye.

Table 1. The volume average LET and RBE at 10% surviving fraction for protons, deuterons and α particles.

Particle	Incident energy (MV)	Volume average LET (keV.μm^{-1})	RBE at 10% SF
Proton	1.8	19.9	1.59
Proton	1.0	27.6	2.23
Proton	0.7	38	2.87
Deuteron	3.4	20.6	1.61
Deuteron	2.1	26.6	2.12857
Deuteron	1.4	34.3	2.67333
α particles	3.9	110	4.23

Evaluation of the charged particle microbeam

Although the Gray Laboratory charged particle microbeam is mostly operational, a few key components (specifically, those concerning collimation and detection) are not yet performing to the required specification. The best collimation to date has been obtained using commercially available fine bore glass capillaries. CR39 etchable plastic has been used to evaluate a 2 mm by 5 μm diameter internal bore glass capillary. At the sample position (about 10 μm from the exit of the capillary) about 90% of the protons are still within a 5 μm diameter. Measurements using the surface barrier detector show that 95% of the protons have an energy close to the full energy value. A transmission scintillation detector of the type described earlier has been constructed, however an attempt to evaluate its performance by comparing its output to that from the surface barrier detector operating in coincidence gave inconclusive results. This was most likely because the collimators used did not have sufficient performance for this measurement. A critical evaluation will take place now that improved collimators are available. The expectation is that these features will meet their target criteria in the near future, and while development of these components continues, other aspects of the microbeam have been evaluated.

The computer-automated cell recognition and irradiation system is now operational, although improvements continue to be implemented. It takes about 8–10 min to raster scan a 5 mm square region of the cell dish and to identify and log the positions of all objects (ideally just single cells, but divided cells and debris may also be logged) within that region. At present, all the found objects are re-visited manually to 'flag' single cells suitable for experimentation, however, the intention is that the image analysis software will fulfill this requirement automatically. Cells are automatically positioned over the collimator with an accuracy of 1–3 μm (this is being improved), while the re-visiting accuracy after an extended period (i.e. after removal, and subsequent relocation of the cell dish on the stage) is about 5–15 μm, which is at present sufficient for assaying purposes. The irradiation sequence for each cell (i.e. the alignment of the cell with the collimator, then the delivery of the dose) takes about 6–10 s per cell. The implementation of single cell survival with

CH5SSS044P 18 04 95 08 45 05

reasonable statistics is therefore quite feasible at this speed.

CONCLUSIONS

Using the broad field arrangement, the expected similarity in effectiveness between photons and deuterons has been demonstrated and in agreement with earlier work, about 20 keV.μm^{-1} singly charged particles are more effective than α particles of the same LET, demonstrating that LET is not the best indicator of biological effectiveness. One aspect important to risk estimation is the effectiveness of single charged particles interacting with cells. The Gray Laboratory charged particle microbeam will be capable of addressing this, and other questions regarding the spatial distribution of sensitive sites within the cell.

ACKNOWLEDGEMENTS

This work is supported by the Cancer Research Campaign and by grants from the Radiation Protection Action Programme of the European Community and the UKCCCR. The authors should like to thank the staff of the Gray Laboratory mechanical and electrical workshops and Rosalind Locke from the data processing group for their considerable involvement in these projects.

REFERENCES

1. Prise, K. M., Folkard, M., Davies, S. and Michael, B. D. *The Irradiation of V79 Mammalian Cells by Protons with Energies below 2 MeV. Part II: Measurement of Oxygen Enhancement Ratios and DNA Damage.* Int. J. Radiat. Biol. 58, 261–277 (1990).
2. Folkard, M., Prise, K. M., Vojnovic, B., Davies, S., Roper, M. J. and Michael, B. D. *The Irradiation of V79 Mammalian Cells by Protons with Energies below 2 MeV. Part I: Experimental Arrangement and Measurement of Cell Survival.* Int. J. Radiat. Biol. 56, 221–237 (1989).
3. Belli, M., Cera, F., Cherubini, R., Ianzini, F., Moschini, G., Sapora, O., Simone G., Tabocchini, M. A. and Tiveron, P. *RBE-LET Relationship for Survival and Mutation Induction of V79 Cells Irradiated with Low-energy Protons: Re-evaluation of the LET Values at the LNL Facility.* Int. J. Radiat. Biol. 61, 145–146 (1992).
4. Goodhead, D. T., Belli, M., Mill, A. J., Bance, D. A., Allen, L. A., Hall, S. C., Ianzini, F., Simone, G., Stevens, D. L., Stretch, A., Tabocchini, M. A. and Wilkinson, R. E. *Direct Comparison of Biological Effectiveness of Protons and α-particles of the Same LET. I. Irradiation Methods and Inactivation of Asynchronous V79, HeLa and C3H 10T½ Cells.* Int. J. Radiat Biol. 61, 611–624 (1992).
5. Perris, A., Pialoglou, A. A., Katsanos, A. A. and Sideris, E. G. *Biological Effectiveness of Low Energy Protons. I. Survival of Chinese Hamster Cells.* Int. J. Radiat. Biol. 50, 1093–1101 (1986).
6. Cherubini, R., Cera, F., Haque, A. M. I., Tiveron, P., Moschini, G., Simone, G. and Tabocchini, M. A. (1992) and Belli M., Ianzini, F., Sapora, O. and Tabocchini, M. A. *Mutation Induction of Low Energy Protons in V79 Cells.* In: Abstracts of papers for the 41st Annual Meeting of the Radiation Research Society (1992) and the 13th Annual Meeting of the North American Hyperthermia Society, Dallas, Texas, p. 135 (1993).
7. Raju, M. R., Eisen, Y., Carpenter, S., Jarrett, K and Harvey, W. F. *Radiobiology of α-particles. IV. Cell Inactivation by α particles of Energies 0.4–3.5 MeV.* Radiat. Res. 133, 289–296 (1993).
8. Cole, A., Meyn, R. E., Chen, R., Corry, P. M. and Hittleman, W. *Mechanisms of Cell Injury.* In: Radiation Biology in Cancer Research, Eds R. E. Meyn and H. R. Withers (New York: Raven Press) pp. 33–58 (1980).
9. Michael, B. D., Folkard, M. and Prise, K. M. *Meeting Report: Microbeam Probes of Cellular Radiation Response* In: Proc. 4th L. H. Gray workshop, 8–10 July 1993. Int. J. Radiat. Biol. 65, 503–508 (1994).
10. Thacker, J., Stretch, A. and Stephens, M. A. *Mutation and Inactivation of Cultured Mammalian Cells Exposed to Beams of Accelerated Heavy Ions. II. Chinese Hamster V79 Cells.* Int. J. Radiat. Biol. 36, 137–148 (1979).
11. Bardensen, G. W. *Responses of Cultured Cells, Tumors and Normal Tissues to Radiations of Different Linear Energy Transfer.* In: Current Topics of Radiation Research, Vol. IV. Eds M. Ebert and A. Howard (Amsterdam: North-Holland) pp. 293–356 (1968).
12. ICRU. *Stopping Powers and Ranges for Protons and α-particles.* Report 49 (Washington, DC: International Commission on Radiation Units and Measurements) (1993).

CHSSSS0440 18:04 95 08 45 05

Radiation Protection Dosimetry
Vol 00, No. 0, pp 0–0 (1995)
Nuclear Technology Publishing

CONVENTIONAL AND MICROBEAM STUDIES USING LOW ENERGY CHARGED PARTICLES RELEVANT TO RISK ASSESSMENT AND THE MECHANISMS OF RADIATION ACTION

M. Folkard, K. M. Prise, B. Vojnovic, H. C. Newman, M. J. Roper, K. J. Hollis and B. D. Michael
Cancer Research Campaign, Gray Laboratory
PO Box 100, Mount Vernon Hospital
Northwood, Middx, HA6 2JR, UK

Abstract — A study of the effectiveness of low energy charged particles has shown that in the LET range 20–38 keV.μm^{-1}, protons and deuterons are more effective than α particles of equivalent LET. These differences may reflect dissimilarities in the track structures and have important consequences both for mechanistic studies and risk assessment. This work will underpin investigations into mechanisms of radiation action and extreme low dose responses using a charged particle microbeam. This facility will enable cells to be irradiated individually using singly and doubly charged particles. Using this approach it is possible to devise *in vitro* models that are a more realistic representation of the situation relevant to environmental exposures to charged particles where single particle effects predominate. With sufficient spatial resolution (at present 5 μm, but with ~1 μm in prospect) the microbeam will also be useful in addressing observations related to cellular spatial sensitivity, for example, the identification of critical sub-cellular targets.

INTRODUCTION

Two contrasting, but complementary techniques have been developed at the Gray Laboratory to study the effectiveness of protons and deuterons (and in the future He^{3++} and He^{4++}) close to their track-ends. The first technique uses a broad field of low energy, near mono-energetic charged particles to irradiate mammalian cells supported as a monolayer. The second technique is to irradiate cells singly, and with a high spatial resolution using counted particles. This, the so-called microbeam, is currently in the final stages of development.

For low energy singly and doubly charged particles, the biological effectiveness for a number of functional endpoints exhibits a strong dependence on LET (although, significantly, not for DNA double strand break induction[1] which has an RBE of 1 for all LETs studied). Previous work by ourselves[2], and by other workers[3–5] has demonstrated that protons with LET between about 20–30 keV.μm^{-1} are more effective at killing cells than doubly charged particles of the same LET. At high LETs (>30 keV.μm^{-1}), protons have a very short range in tissue and in these circumstances it may be preferable to use deuterons which are also singly charged, but have about twice the range of protons with the same LET. Using a new experimental arrangement, it has been possible to compare the effectiveness of protons and deuterons over the 20–38 keV.μm^{-1} LET range. In particular it has been possible to match part of the range covered by Cherubini *et al*[6] where their preliminary studies have indicated differences in the effectiveness of protons and deuterons. This result is surprising because the track structures of LET-matched protons and deuterons are considered to be identical.

These findings have important consequences both for mechanistic studies and for the assessment of risk associated with exposures to α particles and neutrons. Further information regarding the risk associated with exposure to charged particles can be gained by using the microbeam approach. For example, it is possible to devise *in vitro* models that are a more realistic representation of the situation relevant to environmental and occupational exposures to charged particles (e.g. with radon and with neutrons). The situation common at protection levels *in vivo* is that virtually no cell receives more than one charged particle traversal and neither epidemiological studies of Japanese bomb survivors and uranium miners nor conventional (i.e. broad-field) *in vitro* cell experiments can address this point.

Both of the experimental arrangements used here are useful for studying mechanistic effects. The increased effectiveness of singly charged particles compared to doubly charged particles of the same LET suggests that the energy deposited by the secondary electrons is important in determining biological effect. The microbeam will be particularly useful for addressing observations related to cellular spatial sensitivity. For example, a particle crossing the nucleus will (in theory) intersect the DNA many times and it is unclear how some cells are able to survive this insult. Also, a study by Raju *et al*[7], has shown that α particles which completely traverse the nucleus are more effective per unit average dose, than those terminating within it. This finding differs from the earlier work of Cole[8] which showed that the DNA close to the nuclear membrane is the most sensitive. The spatial control that a microbeam offers may be able to clarify the true nature of these effects

METHODS

In recent years there has been a revival of interest in the use of microbeams in several key areas of radiobiology[7], partly because modern technological developments now make it possible to devise experiments that were previously unfeasible. Nevertheless, the development of a versatile single cell, single particle irradiation system with high spatial resolution still presents a major technological challenge. The Gray Laboratory charged particle microbeam has been designed to meet the following specifications: Firstly, the particle should traverse a predetermined target with a positional accuracy ~1 μm. Secondly, the number of particles hitting the target should be under the control of the experimenter. Thirdly, the process of identifying, aligning and irradiating each cell should be rapid and accurate. Finally, the ability to re-visit cells after incubation, or other long-term treatments is necessary.

For both the broad field and the microbeam experiments energetic protons and deuterons (and in the future, He^{3++} and He^{4++} ions) are produced using the Gray Laboratory Van de Graaff accelerator, which can operate at any accelerating voltage between 2 and 4.2 MV and is equipped with conventional beam analysing and bending magnets.

For broad field irradiations, each sample was prepared by spreading a 20 μl suspension of V79-379A Chinese hamster cells (concentrated to $1 \times 10^7 ml^{-1}$) onto a 13 mm diameter polyvinylidine difluoride filter, which rests on 1.0% (w/v) agar. A new arrangement based on a facility described previously[2] was used for the irradiations. Further details will be given in a future publication.

The charged particle microbeam: collimation and detection

Initially microcollimators were constructed by drawing down fine glass capillaries. This has achieved collimation of protons to about 10 μm at the sample position. Our efforts to draw finer capillaries have not, in general, been successful. However, commercially available fine bore glass capillaries have been tested recently and found to collimate to about 5 μm.

To achieve collimation approaching 1 μm, a design based on silicon technology is being developed in collaboration with a microengineering company (Applied Microengineering Ltd, UK). By etching a (100) silicon wafer with potassium hydroxide, it is possible to form a 'V' shaped groove the sides of which are the (111) planes of the crystal lattice. A second piece can then be used to form a three-sided hole. A range of collimators based on this principle have been manufactured with microchannel apertures from 1 μm upwards and of various lengths.

A transmission type of detector based on a thin scintillator located between the microcollimator and the sample is being developed but is not yet fully operational. The scintillator (currently zinc sulphide) is coupled via fine optical fibres to a pair of photomultipliers operating in coincidence. Additionally, a gas-filled proportional counter detector which will be sited on the far side of the cell has been developed for use in situations where the particle has sufficient energy to emerge from the cell.

Cell recognition and alignment

Preliminary experiments are being carried out on V79 cells attached to 50 mm diameter mylar based dishes. Cells are visualized using an epifluorescence, solid state microscope, sited such that it can view the collimator and the attached cells. An arrangement of motorised and computer controlled micropositioning elements is used to align the cells with the collimator. Prior to irradiation, cells are stained with a low concentration (down to 5 nM) of the DNA stain Hoeschst 33258. Under fluorescence illumination a selected area of the dish is raster scanned. Using image analysis software, cells (specifically, their nuclei) are identified and their coordinates logged. When this has been completed, it is possible to position each cell in turn over the collimator and irradiate it. The identification of cells, and their subsequent irradiation are both fully automated and each is initiated by a single computer command. To ascertain the fate of each cell, the dish is re-scanned after the appropriate incubation time.

RESULTS

RBEs for cell survival using the broad field irradiator

The RBE for cell survival at the 10% surviving fraction level relative to LET is shown in Figure 1, and tabulated in Table 1. Three proton and three deuteron data points are shown. For comparison, the RBEs at 10% surviving fraction for α particles are also indicated. These are taken from the tabulated data of Thacker *et al*[10] for V79 cells and re-calculated from the data of Barendsen[11] for T1 cells. Additionally, the RBE for 110 $keV.\mu m^{-1}$ α particles obtained using our cell line[2] is shown to confirm that the comparison is valid. The LET value attributed to each data point is the calculated volume averaged LET within the cell nucleus. To derive this quantity, the LET spectrum within a typical cell nucleus is generated using the measured incident energy spectrum and tabulated stopping power data[12]. The energy of the particles incident on the cells is reasonably monoenergetic; the full width at half maximum is <100 keV in all cases. At low LETs the spread of LETs within the nucleus is small and the measurements correspond reasonably to a track segment type of experiment. The spread in LET for the 34.3 $keV.\mu m^{-1}$ deuteron points is significant however (about ±5 $keV.\mu m^{-1}$) and

CHSSSS044P 18 04 95 08 45 05